Active matter in silico:
phase behaviour of attractive, repulsive and anisotropic self-propelled particles

Cover: A simulation snapshot of self-propelled and attractive particles in a percolating clustered state.

PhD thesis, Utrecht University, the Netherlands, July 2017.

ISBN: 978-90-393-6806-0

Printed by Gildeprint.

The work described in this thesis was performed in the Soft Condensed Matter group, part of the Debye Institute for Nanomaterials Science, at Utrecht University.

A digital version of this thesis is available at http://web.science.uu.nl/SCM/

Active matter in silico:
phase behaviour of attractive, repulsive and anisotropic self-propelled particles

---

Actieve materie in silico:
fasegedrag van aantrekkende, afstotende en anisotrope zelfvoortstuwende deeltjes

(met een samenvatting in het Nederlands)

Proefschrift

ter verkrijging van de graad van doctor aan de Universiteit Utrecht op gezag van de rector magnificus, prof. dr. G. J. van der Zwaan, ingevolge het besluit van het college voor promoties in het openbaar te verdedigen op woensdag 13 september 2017 des middags te 2.30 uur

door

Vasileios Prymidis

geboren op 30 oktober 1988 te Veroia, Griekenland

Promotor: Prof. dr. ir. M. Dijkstra
Copromotor: Dr. L. C. Filion

Contents

1

Introduction

In this introductory chapter we present the reader with content needed in order to understand and assess the research presented in this thesis. We define active matter and present examples of active matter systems, with a focus on the colloidal and granular scale. We then give a theoretical description of active matter and outline the simulation methods we use throughout this thesis. Moreover, after discussing two important theoretical models of active matter and their statistical properties, we briefly review the latest advancements in the statistical description of active matter and explain the contribution of the present thesis in this context.

1.1 Active matter

In this thesis we study, using computer simulations, collective properties of many-body systems whose individual components are *self-propelled*, *i.e.* the different units are able to convert energy into motion. Apart from the self-propulsion, another crucial characteristic common to the investigated systems is the presence of *interactions* between the different components. As such, the model systems under study can be viewed as simplified versions of synthetic systems with locomotive components or even of living systems.

There is typically a vast difference between living and inanimate matter when studying the self-propulsion of individual units; a difference that stems from the distinctive origins of movement for units that belong to the two different sets. Namely, a grain of sand moves only when an external force is exerted on it while an animal and a bacterium are able to choose a direction of motion *via* an internal process and subsequently relocate themselves towards that direction, using energy that is stored in their bodies. Therefore, a detailed description of the motion of a living organism requires a complete understanding of the decision making process, which is, for the time being, out of reach for most living beings.

Despite these complications, the collective motion of large groups of living organisms can often be reproduced by means of simple models [1–3]. These models involve elementary rules that can be seen as heuristics of the decision making process, and dictate the movement of the individual units and the interactions between them. Moreover, actual realizations of such simple models are becoming increasingly common in scientific laboratories, as we shall discuss shortly. These realizations involve systems of many inanimate objects that are equipped with a propulsion mechanism, and often present complex collective motion on a par with the collective motion of living systems. A question which then naturally arises is whether large populations of living and self-propelled inanimate objects share the same statistical properties.

One field that hopes to describe under one theoretical framework the statistical properties of objects which can move autonomously, both living and inanimate, is active matter physics [4–10]. An active matter system (or an active system for short) comprises units which can individually transform internal or external energy into directed motion or forces exerted on their local environment. In all realizations of active matter, the source of the consumed energy can be considered as external to the system itself, so an active matter system is intrinsically out of thermal equilibrium as there is constant energy input into it. Having given a generic definition, let us proceed to discuss different examples of active systems.

Naturally, the most diverse and populous group involves living organisms that can propel themselves. Animals such as birds or fish tend to assemble and move together in flocks or schools, insects create swarms, and even crowds of humans often behave in patterns [2, 11–13]. A commonality in all of the above is that the collective motion of the system emerges despite the absence of central coordination. In contrast, collective motion in active matter emerges simply as a result of the synergy between the autonomous movement of the individual unit and its mechanical or biological interaction with the other units. This synergy often produces exotic, in a statistical physics view, as well as beautiful, in an aesthetics view, patterns, such as fish tornadoes (vortices) and turbulent motion of bacteria colonies [14, 15].

Another class of biological systems which are put under the umbrella of active matter are active gels [16]. These are internally driven systems with a network structure. The most important and studied active gel is the cytoskeleton of cells, which is a network of cross-linked filaments and motor proteins [17, 18]. The cytoskeleton is the backbone of a cell and determines the movement of the cell, its adhesion and division. Subsequently, the mechanical properties of the cytoskeleton naturally affect the macroscopic behaviour of tissues as well.

Even though the study of living active matter can probably be dated back to the dawn of man, in the last few decades a new approach and formalism for its description has begun to emerge. This approach consists of viewing these systems as out of thermal equilibrium soft condensed matter systems, and therefore using statistical physics to describe and make predictions for their macroscopic and statistical properties. This novel effort is largely driven by experimental advances in the synthesis of artificial swimmers and walkers on the colloidal ($1-1000\ nm$) and granular ($1\ \mu m$ and larger) scale, which we will proceed to review.

1.2 Synthetic swimmers

Besides the living systems described in the previous section, the term active matter also includes systems of colloidal or granular particles that can self-propel, rotate or perform some kind of autonomous motion.

Thomas Graham was the first to identify colloids in the early 1860s. The term "colloid" is derived from the Greek word "κόλλα" which translates to "glue", as colloidal particles would not go through a membrane that Graham used in his early experiments [19]. Colloids are particles made out of several atoms or small molecules and are typically immersed in another substance, which is in most cases a fluid phase. Everyday examples of colloidal suspensions include milk, paint and ink.

Due to their immersion, colloidal particles incessantly collide with the surrounding phase and their velocities are constantly changing. In a statistical physics language, the colloids are said to be subject to thermal fluctuations. The resulting non-uniform motion of colloids is called Brownian motion, after the botanist Robert Brown who was one of the first to study and report the phenomenon. Brownian motion and the interactions between colloids are the two essential ingredients for the rich phases of the colloidal world, as colloids can among others be found in gas, liquid and solid states.

On the other hand, granular matter is made of larger particles which should not undergo Brownian motion. Granular materials range in size from powder ($\sim 1\ \mu$m) and coffee beans up to icebergs and asteroids. The different states of a granular system can be similar to a colloidal system, namely they are typically found in gas, liquid or solid states, but the properties of the states of the two classes are different. For example, a gas composed of granular matter typically contains many clusters of grains, as the collisions between grains are dissipative, while colloids in a gaseous state will form only short-lived clusters.

Colloidal systems and many granular matter systems belong to soft condensed matter, a subfield of condensed matter where physics, chemistry and often biology meet. Soft

matter includes all systems whose state behaviour is rich close to room temperature. This property entails that soft matter systems typically involve length scales of the colloidal to the lower end of the granular scale, are subject to temperature fluctuations and also tend to assemble into structures at room temperature. Hence the classification also includes gels, polymers and biological materials [20, 21]. Phenomena in soft matter can in most cases be described by classical physics, in contrast to hard condensed matter, which studies the statistical properties of systems where quantum effects play a major role.

Nowadays, chemists can produce an astounding number of different shapes of colloids with different interactions, ranging from simple hard spheres to flexible chains and patchy particles, where different kinds of interactions take place at different parts of the particle (*e.g.* [22]). The same can also be argued for the world of granular materials, where, due to the larger sizes involved, one can design a myriad of shapes and interactions between particles, as nowadays even small robots can be programmed to behave according to a certain set of instructions [23].

A recent development in the synthesis and construction of artificial colloidal and granular particles is the addition of propulsive mechanisms to individual units. When self-propelled particles have sizes in the colloidal range, they are called microswimmers. Perhaps the earliest example of synthetic microswimmers is the system of self-propelled rods of Paxton and collaborators [24]. These rods consisted of a platinum and a gold segment and, when immersed in an aqueous solution which contained hydrogen peroxide, would move autonomously. This autonomous motion resulted from a catalytic reaction taking place only on the platinum end of the rod. The same catalytic reaction was also employed in order to create spherical active particles [25]. A different mechanism of self-propulsion was introduced by Bricard and collaborators, who took advantage of Quincke rotation, an electrohydrodynamic phenomenon, in order to rotate spherical particles on a surface. The particles' rotation resulted then in self-propulsive motion [26]. Another system involved granular discs with a polar asymmetry such that, when vertically vibrated, a disc would self-propel towards a given direction [27]. A similar strategy was adopted for a system of self-propelled granular rods [28]. Other prominent examples can be found in Refs. [29–40].

Artificial active systems have attracted a lot of scientific interest for several reasons. First of all, systems of synthetic swimmers often present individually or collectively patterns of motion which resemble living systems [6]. Hence, they can be used as models that will help us deepen our understanding of living systems' complex behaviour. Moreover, they have been employed to useful applications such as targeted cargo delivery [41, 42] and cleansing of polluted water [43] as well as building elements for novel types of materials [40]. Therefore in the near future they may well play an important role in industry and medicine. For these reasons, there is extreme interest in active matter and in particular in a theoretical framework which can describe and predict the phase behaviour of these out-of-equilibrium systems.

Computer simulations have proven to be an extremely valuable tool in the study of soft matter, and this is the approach we will use throughout this thesis in order to study active matter. By performing computer simulations, we investigate and shed light on generic aspects of the collective behaviour of different systems as well as test and expand on recent theoretical descriptions. Before initiating our investigation, we will proceed

in the following section to describe how one can simulate active matter. We will focus on artificial systems and, when appropriate, we will comment on possible extensions to biological systems.

1.3 Methods: Simulating artificial active matter

As we have seen in the previous section, in experimental realizations there is a large number of different propulsion mechanisms that may be used in combination with particles which have different properties, and the whole active system may also be placed in very different environments. So, to truly replicate such a complicated system in a computer simulation one would need a theoretical description of all the above: a model for the interaction between particles, a model for the environment (which can be for example a surface that absorbs energy, a surrounding fluid, or both), a model for the propulsion mechanism, as well as an estimation of the effect all the above have on one another. We are currently far from such a detailed understanding of all these parameters, and especially of the interplay between them [44].

As a consequence, when it comes to studying the collective behaviour of active colloidal and granular systems, the most popular route that has been followed so far is to ignore the exact propulsion mechanism. Instead, self-propulsion is approximated by either a given slip velocity of the particle across its boundaries or a constant force that acts on the particles' center of mass. We will discuss both approaches in the following sections.

1.3.1 Active particles in a solvent

A microswimmer that swims in a fluid generates flow in order to move [4]. Consequently, this flow field affects the translational and rotational movement of other microswimmers, leading to an involved long-range hydrodynamic interaction between them. A brute force approach to simulate active colloids in a solvent would thus be to solve iteratively the full equations of motion (Newton's 2^{nd} law) for every swimmer and solvent molecule, by taking into account all interactions between them. Such an approach is essentially impossible at the moment, when one wishes to simulate a reasonable number of colloids. The reason is that the typical difference in sizes between colloids and solvent molecules results in a prohibitively large number of solvent molecules that need to be simulated.

Nevertheless, since in the study of active matter we are mostly interested in the self-assembly and collective properties of the microswimmers rather than the surrounding solvent, one way to circumvent the above difficulty is to coarse-grain the solvent. This can be done by simulation techniques such as multi-particle collision dynamics (MPCD), where a number of solvent molecules are explicitly considered and modified equations of motion are solved for them [45, 46]. Another technique is the lattice Boltzmann (LB) model, where the discrete Boltzmann equation is solved in order to acquire the flow of the solvent [47, 48]. A different approach is to solve the Stokes equation with the colloids acting as sources of fluid flow, by calculating the modes of the velocity and force fields for each swimmer [49, 50]. Once the numerical mode numbers converge, one approaches the full hydrodynamics of the system.

For all of the above simulation techniques, in order to incorporate the effects of activity on the movement of particles one has to assume either a given velocity profile of the fluid on the boundary of the colloidal particles or constant momentum transfer from the solvent to the swimmers. In any case, the linear and angular momentum of the system must be conserved. However, as we will see in the next section, one may adopt a simpler approach and model activity as an explicit force and torque that directly acts on the swimmer, such that the linear and angular momentum of the system are not conserved. Ten Hagen and collaborators argued that such a simplification can indeed be made for arbitrarily-shaped particles, even in the presence of external fields, when the flow field that is generated by particles does not significantly affect their dynamics [51]. Unfortunately, whether this approximation can also be used when hydrodynamic effects are important remains an unresolved question.

1.3.2 Implicit solvent and dry active matter: the Langevin equation

A different way to coarse-grain the solvent of colloidal suspensions is to completely ignore the hydrodynamic interactions between swimmers and only assume an effective equation of motion for the individual particles. Naturally, this equation of motion should reproduce the Brownian motion of individual particles in the absence of interparticle interactions. In 1908, Paul Langevin introduced such a stochastic differential equation [52]. The equation is named after him and is the equation of motion that we will be using throughout this thesis. Therefore we will now proceed to describe it in detail.

Let us assume that a colloidal particle labeled i is suspended in a solvent that consists of particles which are much smaller in size than the colloidal particle. The position of the particle is given by the vector $\boldsymbol{r}_i$ and time is denoted by t. The Langevin equation then dictates

$$m\frac{d^2\boldsymbol{r}_i}{dt^2} = -\eta\frac{d\boldsymbol{r}_i}{dt} + \sqrt{\frac{2\eta}{\beta_s}}\boldsymbol{\xi}_i^{tr}, \tag{1.1}$$

where m is the particle's mass, η is the particle's damping coefficient which quantifies the viscosity of the solvent and β_s is the inverse temperature of the solvent such that $\beta_s = 1/k_B T_s$ with k_B the Boltzmann constant and T_s the solvent's temperature. Note that T_s should not be identified with the temperature of the active system itself, a quantity which we discuss in Section 1.5. The forces that appear on the right-hand side of Eq. 1.1 are, from left to right, the drag force and a stochastic force that is also referred to as a noise term. These two forces account for the continuous collisions between the colloidal particles and the molecules of the solvent. The vector $\boldsymbol{\xi}_i^{tr}$ is a unit-variance random vector, with mean value and variation

$$\left\langle \boldsymbol{\xi}_i^{tr}(t) \right\rangle = 0 \tag{1.2}$$

$$\left\langle \boldsymbol{\xi}_i^{tr}(t)\boldsymbol{\xi}_j^{tr}(t') \right\rangle = \mathbb{I}_d\,\delta_{ij}\,\delta(t-t'), \tag{1.3}$$

where $\mathbb{I}_d$ is the unit matrix in d dimensions. The brackets denote here an average with respect to a Gaussian probability distribution of the realizations of the stochastic components of the vectors.

If one follows the displacement of the particle with time, one finds that

$$\langle \boldsymbol{r}_i(t) - \boldsymbol{r}_i(0) \rangle = 0 \tag{1.4}$$

$$\langle (\boldsymbol{r}_i(t) - \boldsymbol{r}_i(0))^2 \rangle = 2dt/\beta_s\eta, \tag{1.5}$$

where the brackets denote again an average over many different noise realizations. Equations 1.4 and 1.5 then describe a particle that undergoes Brownian motion with diffusion coefficient $D_{tr} = 1/\beta_s\eta$, which coincides to the famous Einstein-Smoluchowski relation [53–55], and confirms the validity of the Langevin equation for our purposes.

Let us now include more particles in our system that will interact with particle i *via* a pairwise potential $U(r)$. Also, let us make our particles self-propelled. A simple way to do this is by associating a d-dimensional unit vector $\boldsymbol{u}_i$ to particle i. This unit vector identifies the direction in which the self-propelling force propels the particle at any given time. We also assume that the self-propelling force has a constant magnitude f_0. The modified Langevin equation is then given by

$$m\frac{d^2\boldsymbol{r}_i}{dt^2} = -\sum_{j\neq i}\frac{\partial U(\boldsymbol{r}_{ij})}{\partial \boldsymbol{r}_i} - \eta\frac{d\boldsymbol{r}_i}{dt} + f_0\boldsymbol{u}_i + \sqrt{\frac{2\eta}{\beta_s}}\boldsymbol{\xi}_i^{tr}, \tag{1.6}$$

where $\boldsymbol{r}_{ij} = \boldsymbol{r}_j - \boldsymbol{r}_i$ and the sum runs over all distinct particle pairs. The forces that appear on the right-hand side of Eq. 1.6 are, from left to right, the force due to particle interactions, the drag force, the self-propelling force and a stochastic force. Note that here the self-propelling force is implemented as an explicit force that directly acts on the swimmer such that momentum conservation in the system can be violated, contrary to the implementations we described in Section 1.3.1 where the presence of the solvent ensures the conservation of linear and angular momentum.

In a typical colloidal system the ratio of inertial forces to viscous forces is very small [8]. This ratio is referred to as the Reynolds number and is a crucial quantity in fluid mechanics. A low Reynolds number means that one can neglect the inertial term in the equation of motion, that is the term on the left hand side in the case of Eq. 1.6. Applying this simplification to Eq. 1.6 we are left with the overdamped Langevin equation

$$\frac{d\boldsymbol{r}_i}{dt} = -\frac{1}{\eta}\sum_{j\neq i}\frac{\partial U(r_{ij})}{\partial \boldsymbol{r}_i} + \upsilon_0\boldsymbol{u}_i + \sqrt{2D_{tr}}\boldsymbol{\xi}_i^{tr}, \tag{1.7}$$

where the self-propulsion speed $\upsilon_0 = f_0/\eta$. The term overdamped refers to the fact that the inertia is negligible when compared to the drag force. Accordingly, one can refer to Eq. 1.6 as the underdamped Langevin equation.

Apart from the two Eqs. 1.6 and 1.7 that describe translational motion one should also consider the rotational motion of the particles. We will only consider the overdamped case here. For spherical particles that do not exert torques on one another, the overdamped rotational Langevin equation can be written as

$$\frac{d\boldsymbol{u}_i}{dt} = \sqrt{2D_r}\,(\boldsymbol{u}_i \times \boldsymbol{\xi}_i^r)\,, \tag{1.8}$$

where D_r denotes the rotational diffusion coefficient and the random vector $\boldsymbol{\xi}_i^r$ satisfies relations analogous to Eqs. 1.2 and 1.3. For spherical particles in the low-Reynolds

number regime, the translational and rotational diffusion coefficients are linked *via* the relation $D_r = 3D_{tr}/\sigma^2$ [56]. Nevertheless, the rotational diffusion coefficient is considered as an independent parameter in many studies of active matter [57–59]. The reason for this extra degree of freedom is that individual particles in experimental active systems, such as bacterial colonies [60], are often also subject to athermal rotational diffusion which can depend on the propulsion mechanism.

Even though we have introduced Eqs. 1.6, 1.7 and 1.8 for the case of colloidal particles immersed in a solvent, these equations could be slightly modified in order to apply to dry active matter as well. The term dry active matter refers to particles that are not immersed in a solvent. Consequently, dry matter most commonly refers to granular particles or living organisms such as birds or sheep [6]. Note that for these systems the translational noise in Eqs. 1.6 and 1.7 is not caused by thermal fluctuations and is in many cases absent, and the same holds for the term associated with friction. Nonetheless, particles whose motion satisfies Eqs. 1.6 or 1.7 and 1.8 are referred to in literature as active Brownian particles (ABPs) [5].

We conclude this section by commenting on the importance and applicability of the ABP model to active matter. First of all, the model has the advantage that it is a reasonable approximation for wet systems, where the propulsion and the bare interactions between particles dominate any hydrodynamic effects, and can also be used as a model for dry active matter under the right conditions. Thus, results that are obtained using this model are potentially applicable to both worlds as the essential interplay between activity and interactions is captured. Also, when one wishes to study collective phenomena of wet systems such as clustering and phase separation without requiring a direct mapping to experiments, neglecting the hydrodynamics can be a reasonable first approach. Moreover, the computational cost of this model is much less than any of the current techniques to model hydrodynamics. As an example, simulations of ABPs can include up to millions of particles [61, 62], while simulations that include coarse-grained hydrodynamics typically include a few hundred to mostly a few thousand particles [46, 50]. Nonetheless, one should keep in mind that hydrodynamics can have important consequences even on the collective behaviour of active systems, as has been explicitly shown in Refs. [47] and [50].

1.4 Prominent theoretical models of active matter

Of the various theoretical models of active matter that can be found in literature, there are two that have emerged as its most prominent and as a result have been immensely studied. These are the Vicsek model, which constitutes a cornerstone model for active matter, and the model of self-propelled, purely repulsive discs, which is mostly relevant to colloidal active matter. The importance of these two models lies in the novel types of phase transitions that they undergo, despite their apparent simplicity. Below we briefly discuss the models and their phase behaviour.

1.4.1 The Vicsek model: flocking transition

The Vicsek model is arguably the most studied model of active matter and was introduced by Tamás Vicsek *et al.* in 1995 [63]. The original Vicsek model assumes an off-lattice, two-dimensional system of self-propelled, point-like particles. The time-discretized translational equation of motion of particle i is simply

$$\boldsymbol{r}_i(t + \Delta t) = \boldsymbol{r}_i(t) + v_0 \boldsymbol{u}_i(t)\Delta t, \tag{1.9}$$

where $\boldsymbol{r}_i$ denotes the position of particle i, Δt is the numerical integration time step, v_0 is the self-propulsion speed (which is the same for all particles) and $\boldsymbol{u}_i = (\cos(\theta_i), \sin(\theta_i))$ denotes the direction of self-propulsion for particle i, as θ_i is the azimuthal angle of self-propulsion with a predefined axis. The direction of self-propulsion is updated according to the equation

$$\theta_i(t + \Delta t) = \langle \theta_i(t) \rangle_s + \Delta\theta_i, \tag{1.10}$$

where $\langle \theta_i(t) \rangle_s$ denotes the average direction of self-propulsion of all particles that are within a distance s from particle i, including particle i. As a result, this term tends to align the direction of self-propulsion, or speed, of neighboring particles. The term $\Delta\theta_i$ introduces noise into the model and is chosen from the interval $[-\xi/2, \xi/2]$ with a uniform probability.

The free parameters of the model that determine its state behaviour are the density of particles, the speed of self-propulsion v_0, the distance s and the magnitude of the noise ξ. Snapshots of the system in different characteristic states are shown in Fig. 1.1.

The novelty of the model lies in the contrast between Figs. 1.1(a) and (d), which suggest that the system transitions from a homogeneous state, where the positions and velocities of the particles are not correlated, to an ordered state, where all particles move coherently in the same direction, as the density and v_0/ξ ratio are increased. The mechanism that drives the transition is well understood: the alignment interaction initially creates small groups that move coherently. Since the resulting groups will have very different directions of movement, they will frequently collide with one another. Thus, the transport of information from one part of the system to another happens faster than diffusive transport. This increased speed of exchanging information, due to the large spatial fluctuations of the velocity field, is what ultimately suppresses the fluctuations themselves and drives the system to an ordered state [64].

The transition is referred to as the flocking transition and has been studied in depth using different simulation models as well as mean-field and hydrodynamics theories [64–71]. The flocking transition has also a universal character as it is found in many different active systems such as groups of birds and active rods [72, 73]. The Vicsek model has played a pivotal role for active matter since it incorporates the essential ingredients of many biological and artificial systems that exhibit the universal flocking transition, despite its apparent simplicity.

As a final remark, note that the equations of motion for the Vicsek model are similar to the overdamped Langevin Eqs. 1.7 and 1.8 of the ABP model: the translational equation of motion Eq. 1.9 is the integration of Eq. 1.7 using the Euler method while omitting particle interactions and translational noise, while Eq. 1.10 is different from an

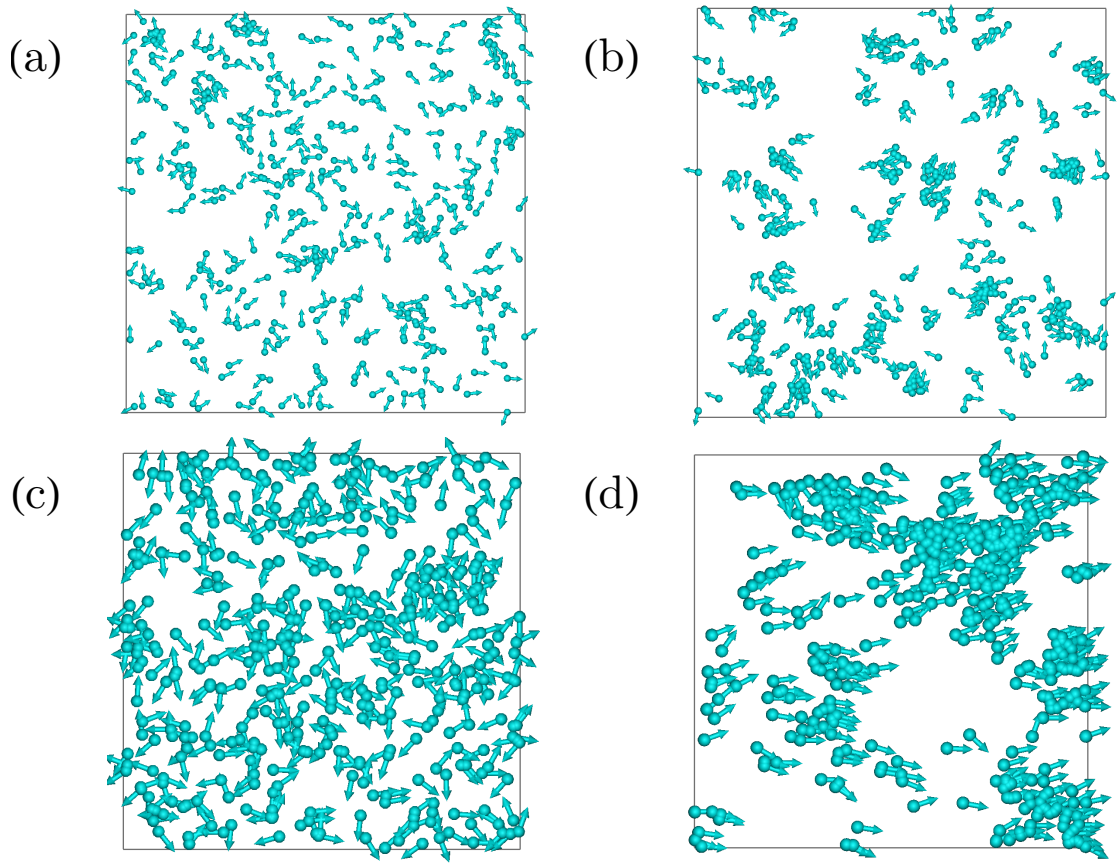

Figure 1.1: Snapshots of different states of the Vicsek model. The systems contains 400 particles and periodic boundary conditions are applied. The center of the particles is denoted by a sphere while the arrows attached to the spheres indicate the instantaneous direction of the self-propulsion speed. (a) The system is in a homogeneous state for low density and small ratio v_0/ξ. The particles' positions and velocities are randomly distributed. (b) The particles assemble in small groups that move coherently for low density of the system and large ratio v_0/ξ. (c) For high density and small ratio v_0/ξ the system is in a homogeneous state and the velocities of the particles are correlated only locally. (d) All particles move coherently in the same direction for high density and large ratio v_0/ξ.

Euler integration of Eq. 1.8 as it includes an aligning interaction between particles and also the noise results from a uniform distribution instead of a Gaussian one. Variations of the original Vicsek model that include a steric repulsion between particles and Gaussian translational and rotational noise reproduce the same phenomenology, as the only necessary ingredients for the flocking transition are self-propulsion and aligning interactions between particles [66].

1.4.2 Self-propelled repulsive discs: motility-induced phase separation

As hard spheres and discs are the cornerstone models of soft matter physics, it comes as no surprise that hard or purely repulsive self-propelled discs and spheres are among the most studied models of active matter. Nonetheless, it took almost twenty years after the first publication of the flocking transition of the Vicsek model for the report of a similarly novel phase transition for self-propelled discs.

In 2012 Yaouen Fily and Cristina Marchetti were the first ones to report that a system of purely repulsive discs would separate into a dense and a dilute phase for high enough density and speed of self-propulsion, a phenomenon that is referred to as motility-induced phase separation [74]. The two-dimensional ABP model that they studied was composed of particles of radius σ that follow the equations of motion Eqs. 1.7 and 1.8. A simple harmonic potential was used as the interparticle repulsive potential such that $U(r) = \frac{\kappa}{2}(2\sigma - |\boldsymbol{r}|)^2$, where κ tunes the strength of the interaction and $\boldsymbol{r}$ denotes the interparticle distance vector.

For fixed translational and rotational diffusion parameters as well as interaction strength κ, the remaining free parameters of this model are the density of particles and the self-propulsion speed v_0. A series of characteristic snapshots that summarize the phase behaviour of the system can be found in Fig. 1.2.

The striking contrast between the panels of the bottom row suggests that a high density system of purely repulsive discs undergoes a phase transition from a homogeneous state to a phase separated state as the speed of self-propulsion is increased. Or equivalently, the right column of the figure suggests that a system of self-propelled discs with a sufficiently high speed of self-propulsion undergoes a phase transition as its density is increased. The phase separated state consists of a low-density fluid and a high density phase that shows local crystalline order. The mechanism driving the phase transition is the following [61, 74]: particles that collide with one another slow down significantly and create small clusters. Shortly after, and before they are able to escape their cluster, more particles from the dilute phase bump into them and slow down themselves. If the propulsion speed of the particles and the density are high enough, this leads to a positive feedback loop which grows the cluster until there is an equilibrium between the number of particles that join the cluster from the dilute phase and the number of particles that escape it.

Note that the transition described by this process is very different from the order-disorder transition of passive ($v_0 = 0$) hard or purely repulsive discs which is driven by entropy, and is instead caused by the combination of the motility of particles and the steric repulsions. The phenomenon is thus justifiably called motility-induced phase separation (MIPS), and also takes place in the three-dimensional analogue of the system [62]. It has

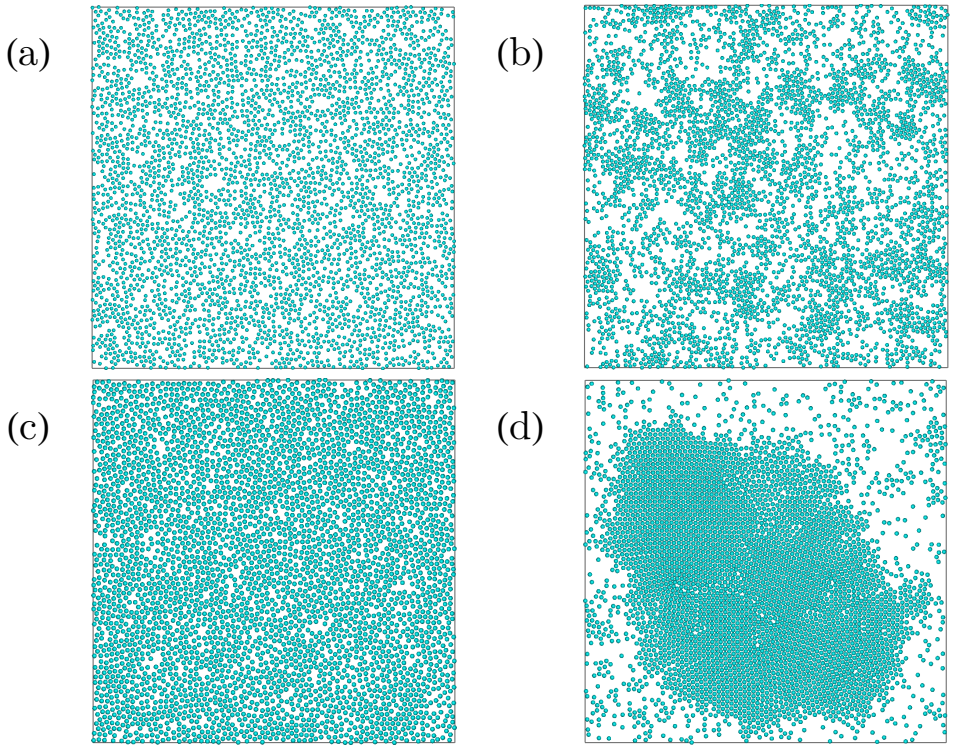

Figure 1.2: Snapshots of different states of a system of self-propelled and purely repulsive discs. The system contains approximately 4000 particles and periodic boundary conditions are applied. (a) The system is in a homogeneous state for low density and low propulsion speed. (b) The system shows pronounced clustering for low density and high propulsion speed. (c) For high density and low propulsion speed the system is in a homogeneous state. (d) The system phase separates into a dense and a dilute region for high density and high propulsion speed.

been shown by simulations that MIPS takes place for a wide range of different particle shapes and that the specific potential details do not matter as long as particles posses a repulsive core [75–78]. However, particle geometry seems to affect the stability as well as other collective properties of MIPS, as studies of active anisotropic particles revealed [76–78]. We also study the effect of particle geometry on MIPS for a specific system in Chapter 6.

Surprisingly, even though MIPS is a genuinely non-equilibrium phase transition, the phase diagram of MIPS for spherical active particles can be mapped onto a fairly equilibrium-like phase diagram [61]. This unexpected mapping hinted on the possible description of active matter in an extended thermodynamics and statistical mechanics framework and is also the motivation for much of the work presented in this thesis, specifically in Chapters 5, 6 and 7.

Due to the generality and the purely out-of-equilibrium nature of MIPS, a full understanding of the physics behind it would be extremely valuable for the development of a statistical theory for soft active matter. As such, it has been studied in a great number of theoretical studies that involve computer simulations, continuum models, and field theories [61, 62, 74, 79–81]. Even though MIPS has not explicitly been found experimentally, many experiments have reported on the enhanced clustering due to the same mechanism that drives MIPS [34–36]. For a more general review on MIPS see Ref. [82].

1.5 Thermodynamics and statistical mechanics of active matter

The statistical properties of a soft system in thermal equilibrium can be understood using classical thermodynamics and statistical mechanics. These two theoretical frameworks were formulated by the early 20^{th} century and were brought together by the work of Willard Gibbs [83, 84]. Thermodynamics is based on four empirical laws and describes a system that contains a very large number of units using macroscopic observables that can be measured in the laboratory, such as temperature and pressure. Statistical mechanics uses mathematical constructions such as the partition function and the free energy to demonstrate how the thermodynamics emerges as a consequence of many-particle statistics. Thus, it links the microscopic properties of a system to its macroscopic behaviour. Among others, it also assesses the stability of a system and links phase transitions to the concepts of energy minimization or entropy maximization.

As we have described earlier, active matter is intrinsically out of equilibrium. As a result, equilibrium statistical mechanics is naturally not directly applicable to it. However, the applicability of equilibrium notions such as entropy, pressure, temperature and surface tension to active matter and its associated phase transitions has been an area of intense study in recent years [62, 80, 85–98]. Note that a large fraction of the studies on the statistical physics of active matter has so far focused on isotropic active particles, *i.e.* particles that do not experience any torques due to interactions. In fact, a large part of the present thesis also focuses on such systems (see Chapters 2-5). Apart from the obvious simpler nature of isotropic particles, an important reason for this focus is that the addition of anisotropic interactions between particles due to, *e.g.* the anisotropic shape of particles,

alters significantly the physics of active matter. We discuss the complications that arise from particle geometry below, when appropriate. Below we give a short review of the rapidly growing field of thermodynamics and statistical mechanics of active matter.

First of all, the notion of an effective temperature of active matter is still a topic of discussion among scientists. Experimental and theoretical results suggest that many properties of an active system can be directly mapped onto an equilibrium system of a higher effective temperature, for dilute as well as very dense (glassy) systems (see *e.g.* Refs. [99, 100]). Moreover, one can also map the complete equation of state of chemically powered colloids onto an equilibrium equation of state using an effective temperature [101]. However, entirely non-equilibrium phenomena such as MIPS obviously cannot be captured by such a description. Consequently, the extent as to where this mapping is valid is not clear yet.

Apart from temperature, the mechanical pressure of active matter has attracted a lot of attention as well. It is now understood that the pressure of dry active matter is a function of its state, in the complete absence of torques, but surprisingly the same cannot be said for particles with an anisotropic shape and particles that experience torques in general [90]. Furthermore, Julian Bialké and his collaborators showed that, even for isotropic particles, the accepted definition for the mechanical pressure of active matter leads to a negative surface tension between coexisting phases in the case of MIPS [91]. Even though the definition of active pressure is already being used in more general theories that aspire to predict phase coexistences [86, 102], it is evident that its interpretation will remain a topic of intense study in the near future. In this thesis, we test and use the definition of pressure for active matter in Chapters 3, 4, 5 and 7.

The last of the intensive variables of a traditional thermodynamical system, the chemical potential, has also been defined and even measured for particle simulations in a series of papers [62, 86, 103]. However, another work dismisses the idea of a chemical potential for active systems, as it proposes that active systems are, contrary to passive systems, not extensive [97]. Given that if all the intensive variables of a system can be measured one can predict the phase coexistence of different phases, or even define a free energy of the system, the quest for a definition of a chemical potential will surely attract much more attention. In Chapters 5 and 7 we study chemical equilibrium between phases of active matter as well as attempt an implicit definition of a chemical potential.

Other efforts have focused on creating an approximate method to describe active matter with the help of an effective equilibrium theory. For example, Farage and collaborators [88] constructed a framework that maps a system of self-propelled particles with short reorientation times to an equilibrium system with effective interactions. Moreover, Maggi and his collaborators [87] treated active particles which are subject to coloured Gaussian noise with a multidimensional version of the Unified Coloured Noise Approximation, and Preisler and Dijkstra argued that the distribution of configurations of a system of purely repulsive self-propelled discs can be mapped onto an equilibrium system with a modified Boltzmann distribution and an effective temperature [97]. Additionally, Solon and collaborators constructed a generalized free energy that quantitatively accounts for the phase diagram of MIPS [102].

From the above brief review it is evident that there is a plethora of different approaches to the physics of active matter as well as a variety of results that may currently even

appear contradicting to one another. Even though at present we cannot know whether a thermodynamics and statistical physics for active matter can be built, there will certainly be intense theoretical research towards that goal in the coming years which will be based and expand on these first promising attempts.

1.6 Scope of this thesis

As we have discussed so far in this introductory chapter, particularly in Sections 1.4 and 1.5, the synergy between interparticle interactions and self-propulsion determines the collective properties and the phase behaviour of active matter systems. With this important observation in mind, in this thesis we set to perform two separate tasks. On the one hand, using computer simulations we chart the phase behaviour of active matter systems and attempt to understand how the interplay between the self-propulsion and the interactions gives rise to the observed collective behaviour. On the other hand, we investigate whether there exist universal tools that can be used to describe and predict phenomena of active matter systems, such as phase transitions, without being restricted to a specific type of interaction. These tools would naturally be part of a statistical physics description of active matter. Below we discuss briefly the contribution of the following chapters to each task.

The first three research chapters of this thesis are devoted to the study of the same system, namely a system of attractive self-propelled spherical particles. In Chapter 2 we focus on the self-assembly of the system and present its phase diagram along with a description of the structural and dynamical properties of the different phases that we identify. In Chapters 3 and 4 we apply statistical physics and critical phenomena language to study, in the former chapter, the vapour-liquid transition of the system and, in the latter chapter, the vapour-liquid interface. In both chapters we make use of equilibrium statistical physics notions such as the mechanical pressure and the surface tension and determine the extent of their possible application to the system.

Chapter 5 can be grouped together with the three previous Chapters 2-4 since it concerns systems with purely isotropic interactions among its constituent particles. In this chapter we study two binary mixtures, one of attractive and one of purely repulsive self-propelled particles that undergo vapour-liquid and motility-induced phase separation respectively. The purpose of this chapter is to demonstrate the existence of two quantities, equivalent to the mechanical pressure and the chemical potential of equilibrium systems, and their application to the construction of phase diagrams for active matter systems.

In Chapters 6 and 7 we study systems with anisotropic interactions between particles. Chapter 6 contains a description of the phase behaviour and the dynamics of a system of self-propelled squares, where the anisotropic interactions result solely from the anisotropic shape of the particles. We find that certain properties of the phase diagram are in accordance with equilibrium scaling laws, even though we have departed from isotropic interactions. Motivated by this finding, in Chapter 7 we test the machinery of Chapter 5 for a system of purely repulsive self-propelled particles with explicit anti-aligning interactions that can undergo motility-induced phase separation. In this way we

examine whether our method to predict phase diagrams of systems with purely isotropic interactions can be extended to active systems in general.

Acknowledgments

Tommaso Comparin, Wessel Vlug and Berend van der Meer are gratefully acknowledged for a critical reading of this chapter.

2

Self-assembly of active attractive spheres

In this chapter we study the self-assembly of a system of self-propelled, Lennard-Jones particles. We examine the state diagrams of the system for different rotational diffusion coefficients of the self-propelled motion of the particles. For fast rotational diffusion, the state diagram strongly resembles the phase diagram of the equilibrium Lennard-Jones fluid. As we decrease the rotational diffusion coefficient, the state diagram is slowly transformed. Specifically, the liquid-gas coexistence region is gradually replaced by a highly dynamic percolating network state. We find significant local alignment of the particles in the percolating network state despite the absence of explicit aligning interactions, and propose a simple mechanism to justify the formation of this novel state.

2.1 Introduction

As we have described in Chapter 1 of this thesis, one of the most intriguing and important theoretical results of active matter is the phase separation of self-propelled particles with purely repulsive interactions, which is driven by the motility of the particles and is appropriately called motility-induced phase separation [61, 62, 74, 79, 81]. At the same time, motility-induced phase separation has not been observed in experimental realizations of active matter, even though the phenomenon can be partially linked to the clustering of particles reported in many experiments [34–36]. One of the reasons for this are of course the interactions between particles, which are more complex than simple steric interactions.

A simple step towards complexity is the addition of attractive interactions between the particles, which was shown to also lead to clustering of self-propelled particles. Specifically, Palacci *et al.* showed in a numerical study that phoretic attraction between self-propelled hard discs gives qualitative agreement between the clustering properties of their model and their experiments [35]. A more elaborate numerical study on the interplay between attraction and self-propulsion was done by Redner *et al.* [75]. The authors studied a two-dimensional ensemble of self-propelled particles that interact *via* Lennard-Jones interactions. By varying the strength of the attraction and the swimming velocity of the particles, they showed that the self-propulsion can have two opposing effects for a given strength of attraction: for slow swimmers it can break aggregations caused by the attractive force, while it can induce aggregation for fast enough swimmers. For intermediate swimming velocities, the steady state of the system was identified as a homogeneous fluid phase. A first study of a similar model in three dimensions was done by Mognetti *et al.* [104]. The focus of this paper was mainly on the clustering properties of the system - as the strength of attraction is increased, the system passes from a homogeneous state to a clustered state caused by the attractive interactions. A state of rotating clusters has also been reported in Ref. [32] for active attractive dumbbells.

However, the transition from homogeneity to clustering in active and attractive systems has not yet been clearly linked with the known phase behaviour of the corresponding equilibrium systems. Moreover, structural properties of the clustered state have not been examined and compared to the well-studied gas-liquid phase separation.

In the present chapter we study a three-dimensional model of self-propelled Brownian particles that interact *via* a Lennard-Jones potential. This model was chosen since the phase behaviour of the equilibrium system is well characterized and can be readily verified by computer simulations [105, 106]. Moreover, the Lennard-Jones potential roughly accounts for the steric repulsion and the short range attraction that is present in many colloidal systems. By tuning the rotational diffusion rate of the particles, we are able to continuously move the system from the regime of fast rotational diffusion, where strong similarities with the equilibrium behavior are expected [58], to small values of the diffusion rate where non-equilibrium features arise. Thus, we are able to construct a series of state diagrams that evolve from a diagram similar to the well-established Lennard-Jones phase diagram to diagrams with novel properties.

Moreover, we find that the interplay between attraction and self-propulsive motion in three dimensions gives rise to a highly dynamic, percolating network. As we will show in this chapter, this percolating network has many similarities to living clusters, observed in

Ref. [104]. It is, however, a system spanning structure. This new state is accompanied by an unexpected result - the emergence of local alignment of the axes of self-propulsion of the particles despite the absence of an aligning mechanism.

In Section 2.2 we describe the model, the dynamics implemented for our simulations and the analysis methods used in the subsequent parts of the chapter. In Section 2.3.1 we present the state diagrams of the system, and in Section 2.3.2 we focus on properties of the percolating network state. Lastly, we compare our work with the results of Ref. [104] in Section 2.3.3 and give a short discussion of our results in Section 2.4.

2.2 Methods

2.2.1 Model

In this chapter we examine the behaviour of self-propelled, attractive particles immersed in a solvent. We consider a three-dimensional system consisting of N spherical particles (colloids) in a periodic cubic box of length L. The position of the center of mass of the i-th particle at time t is given by the vector $\boldsymbol{r}_i(t)$. To each particle i, we associate a three-dimensional unit vector $\boldsymbol{u}_i(t)$ that identifies the direction in which the self-propelling force propels the particle at a given time t. The particles interact with each other *via* a Lennard-Jones potential

$$\beta_s U(r_{ij}) = 4\beta_s\epsilon\left[\left(\frac{\sigma}{r_{ij}}\right)^{12} - \left(\frac{\sigma}{r_{ij}}\right)^{6}\right], \tag{2.1}$$

truncated and shifted at 2.5σ where σ is the particle length scale, $r_{ij} = |\boldsymbol{r}_j - \boldsymbol{r}_i|$, ϵ is the strength of the interaction and $\beta_s = \frac{1}{k_B T_s}$ is the inverse temperature of the surrounding solvent, with k_B the Boltzmann constant and T_s the solvent temperature.

2.2.2 Dynamics

We do not model the solvent explicitly, but rather only include it implicitly. We use two distinct expressions to describe the translational motion of the individual colloidal particles inside the solvent, namely the underdamped and overdamped Langevin equations. The underdamped Langevin equation is given by

$$m\frac{d^2\boldsymbol{r}_i}{dt^2} = -\sum_{j\neq i}\frac{\partial U(r_{ij})}{\partial \boldsymbol{r}_i} - \eta\frac{d\boldsymbol{r}_i}{dt} + f_0\boldsymbol{u}_i + \sqrt{\frac{2\eta}{\beta_s}}\boldsymbol{\xi}_i^{tr}, \tag{2.2}$$

where m is the particle's mass, η is the particle's damping coefficient and f_0 denotes the magnitude of the self-propelling force. Note that $\boldsymbol{\xi}_i^{tr}$ is a unit-variance random vector, with mean value and variation

$$\left\langle \boldsymbol{\xi}_i^{tr}(t)\right\rangle = 0 \tag{2.3}$$

$$\left\langle \boldsymbol{\xi}_i^{tr}(t)\boldsymbol{\xi}_j^{tr}(t')\right\rangle = \mathbb{I}_3\,\delta_{ij}\,\delta(t-t'), \tag{2.4}$$

where $\mathbb{I}_3$ is the unit matrix in three dimensions. The forces that appear on the right-hand side of Eq. 2.2 are, from left to right, the force due to particle interactions, the drag force, the self-propelling force and a stochastic force. The drag and stochastic forces account for the constant collisions between the colloidal particles and the molecules of the solvent.

In the regime of low Reynolds numbers (typical of a colloidal system) one can neglect the inertial term, and thus the translational motion of each particle follows from the overdamped Langevin equation

$$\frac{d\boldsymbol{r}_i}{dt} = -\frac{1}{\eta}\sum_{j\neq i}\frac{\partial U(r_{ij})}{\partial \boldsymbol{r}_i} + \upsilon_0 \boldsymbol{u}_i + \sqrt{2D_{tr}}\boldsymbol{\xi}_i^{tr}, \tag{2.5}$$

where the translational diffusion coefficient is given by the Einstein-Smoluchowski relation $D_{tr} = 1/(\beta_s \eta)$ and the self-propulsion speed by $\upsilon_0 = f_0/\eta$. We define the unit of time $\tau = \sigma^2 D_{tr}^{-1}$.

The axis of self-propulsion is subject to rotational diffusion and for the simulations presented in this chapter its motion always obeys the overdamped rotational Langevin equation

$$\frac{d\boldsymbol{u}_i}{dt} = \sqrt{2D_r}\left(\boldsymbol{u}_i \times \boldsymbol{\xi}_i^r\right), \tag{2.6}$$

where D_r denotes the rotational diffusion coefficient and the random vector $\boldsymbol{\xi}_i^r$ satisfies relations analogous to Eqs. 2.3 and 2.4. Note that after each iteration of Eq. 2.6 we normalize the unit vectors $\boldsymbol{u}$ in order to prevent their drift. For spherical particles in the low-Reynolds number regime, the translational and rotational diffusion coefficients are linked *via* the Stokes-Einstein relation $D_r = 3D_{tr}/\sigma^2$. Nevertheless, the rotational diffusion coefficient is considered as an independent parameter in our study, similar to previous theoretical work [57–59]. The reason for this extra degree of freedom is that individual particles in experimental active systems, *e.g.* bacteria [60], are often subject to athermal rotational diffusion.

In order to implement the aforementioned equations of motion, Eqs. 2.5 and 2.6, we used the Euler-Maruyama integration scheme [107]. To implement the underdamped Langevin Eq. 2.2, we employed the integration scheme proposed by Grønbech-Jensen and Farago [108]. We have verified that simulations in the overdamped regime give indistinguishable results with ones in the highly viscous underdamped regime. A time step of $dt = 3 \times 10^{-5}\tau$ was used for the numeric integration of the equations of motion in both the underdamped and the overdamped regime and the simulations ran for at least $10^6\tau$, so that we get sufficient statistics for the system.

The behavior of the system was probed as the following dimensionless parameters were systematically varied: the magnitude of the propulsion force $\beta_s f_0 \sigma$ or speed $\upsilon_0\tau/\sigma$, the rotational diffusion coefficient $D_r\tau$, the density of the system $\rho\sigma^3 = \frac{N\sigma^3}{L^3}$ and the strength of the Lennard-Jones potential $\beta_s\epsilon$. In order to facilitate direct comparison to the equilibrium Lennard-Jones system, we define $T = 1/\beta_s\epsilon$ as the dimensionless temperature of our system. In the case of the underdamped system, we also varied the (dimensionless) damping coefficient $\tilde{\eta} = \beta_s\eta\sigma^2/\tau$. Following Ref. [104], we quantified the ratio between the strength of attraction and the magnitude of self-propulsion by the aggregation propensity

$$P_{\text{agg}} = \frac{\beta_s\epsilon}{\beta_s f_0 \sigma} = \frac{\epsilon}{f_0\sigma} = \frac{\epsilon}{\eta\upsilon_0\sigma}. \tag{2.7}$$

The number of particles for all simulations in the underdamped regime was 1728, in order to compare directly our results with Ref. [104], while for the overdamped regime was 4917, unless stated otherwise. The effects of the finite size of the system on our results are discussed, when considered relevant, in the respective sections.

2.2.3 Steady state and initial configurations

Due to the self-propelling force there is constant energy input in the system. Nevertheless, by following the evolution of the total potential energy of the system with time, we observed that after a short transient period there was no energy drift in our simulations. After this period the potential energy of the system fluctuated around a mean value. We identified this regime of quasi-constant energy with the steady state of the system. For our measurements we considered configurations from the steady state only. Furthermore, for each point in the parameter space, a minimum of two simulations were performed, starting from two different initial configurations: one where the particles were on a cubic lattice that spanned the entire system, and one where all the particles were part of a dense liquid slab. These two initial conditions were chosen in order to study any possible effect the starting configuration could have on the steady state of the system. We found that after the transient period, the average potential energy in both simulations converged to the same value, which indicates that the system indeed relaxed at the same state and we can safely identify the regime of quasi-constant potential energy with the steady state. For a limited number of simulations we also looked at the time evolution of the degree of clustering and the local density histograms, both of which are described in detail later in this chapter, and we found that in the regime of quasi-constant energy these structural functions were also only subject to fluctuations and there were no major changes. Once again the results obtained for different initial configurations coincided. All the above ensure that the potential energy is a reasonable indicator of when the system reaches the steady state.

For sets of parameters where the system is close to crystallization, the system was additionally initialized from a gaseous state that contains a large (face-centered-cubic) crystalline cluster. The cluster contained approximately 25% of the system's particles. We observed high crystallization and melting barriers in many cases, which caused difficulties in identifying the true steady state of the system, as the simulations would have to run for a very long time. We found that these difficulties were enhanced by finite size effects. Nevertheless, the results for the parameter space points presented in this chapter have been thoroughly verified.

2.2.4 Analysis methods

We used a Voronoi construction to construct local density histograms of the system [109]. By calculating the volume of the Voronoi cells we were able to estimate the local density of particles. Furthermore, the identification of surface particles was performed by means of the cone algorithm [110].

In order to distinguish the percolating network state from bulk gas-liquid coexistence we use the following criterion. First, we considered two particles as clustered when their

center of mass distance was less than 1.2σ. Note that in our system, the first minimum in the radial distribution function is typically between 1.3σ and 1.6σ. We chose 1.2σ as the cutoff distance in order to both be consistent with that used in Ref. [104] and ensure that we did not overestimate the amount of connectedness in our system.

Second, we calculated the probability of having a cluster percolating simultaneously in all three dimensions in the system. To determine whether a cluster percolates in a given direction we duplicated the system in that direction, doubling the number of particles. If the number of particles in the cluster doubled as well, then the cluster percolated. When the probability of percolation was found higher than a certain threshold that was density-dependent, we identified the system as being in the percolating cluster state. This threshold was used for the necessary distinction between strong fluctuations of the liquid phase that can temporarily percolate in three dimensions and the percolating network structure. The probability threshold was set at 35%, 90% and 95% for total densities $\rho\sigma^3 = 0.191, 0.382$ and 0.445 accordingly. However, for a total density higher than $\rho\sigma^3 = 0.5$ this criterion failed as the liquid cluster always percolated in all three dimensions.

2.3 Results

2.3.1 State diagrams

Passive Lennard-Jones particles have been extensively studied and their phase behaviour is well-characterized (see *e.g.* Ref. [105]). At high temperatures, Lennard-Jones systems exhibit a single first-order phase transition from a fluid to a face-centered-cubic crystal as the density of the system is increased. Upon lowering the temperature, a critical temperature is reached where a second phase transition appears separating the fluid phase into gas and liquid phases. At even lower temperatures a triple point appears below which the liquid phase disappears and only the gas and crystal remain.

When the passive particles are replaced by active particles by introducing self-propulsion, deviations from the equilibrium behaviour are expected. To explore these deviations, we study the behaviour of the system as a function of the rotational diffusion coefficient $D_r\tau$ while keeping the self-propulsion force (speed) f_0 (v_0) and temperature T fixed. Note that in the limit of fast rotational diffusion, $D_r\tau \to \infty$, the persistence length of the particles goes to zero and the active force acts effectively as translational diffusion [58]. As a result, we expect the behaviour in this limit to coincide with the behaviour in the equilibrium (passive) system, but with a modified interaction strength. However, as $D_r\tau$ is decreased, the non-equilibrium effects should become more evident.

In this section we use overdamped Brownian dynamics simulations to explore the behaviour of systems with $D_r\tau$ between 0.3 and 30 and densities $\rho\sigma^3$ between 0.191 and 0.764. In all cases, the magnitude of the self-propelling speed is fixed at $v_0\tau/\sigma = 50$.

For all values of $D_r\tau$ we consider, we find that the system is in a fluid state for a sufficiently high value of temprature $T = 1/\beta_s\epsilon$ (see Fig. 2.1(a)). As the temperature decreases and the strength of the attraction is increased, the particles tend to aggregate. The structure of the aggregate depends strongly on the rotational diffusion coefficient. For high rotational diffusion coefficient, the aggregated phase appears as the liquid in a

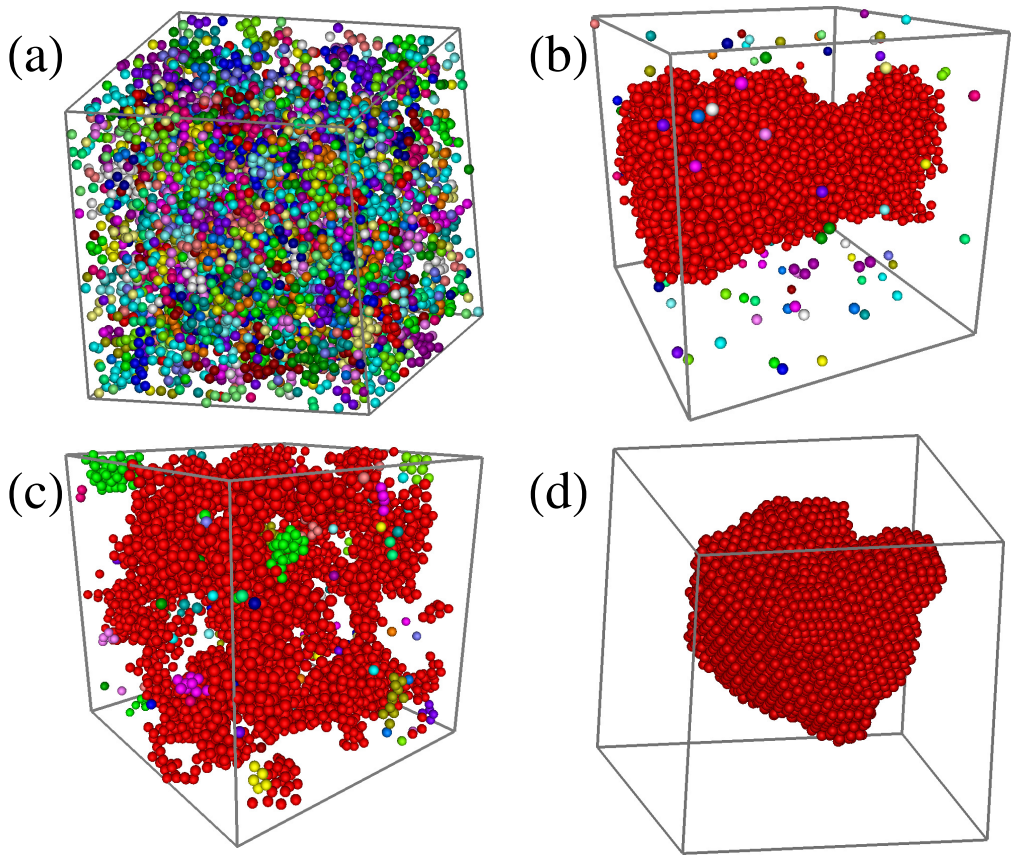

Figure 2.1: Snapshots of different states of the system. In (a) the system is in a homogeneous fluid state, in (b) there is liquid-gas coexistence, in (c) a percolating network state is found, and in (d) a crystal coexists with a gas. Particles that belong to different clusters have different colours. The values of the parameters are $\rho\sigma^3 = 0.191$, $v_0\tau/\sigma = 50$, $T = 0.2$ for (a) and 12.5 for (b)-(d) and $D_r\tau = 30, 4.2, 0.01, 30$ for (a)-(d) respectively.

classical liquid-gas phase separation, namely, the liquid phase is organized such that the surface of the cluster is minimal (Fig 2.1(b)). However, for slower rotational diffusion, the aggregated phase is much less compact as shown in Fig. 2.1(c), and frequently spans the entire system or forms "living" clusters as described in Ref. [104].

In order to better quantify the aggregation of particles, we obtained density histograms for the systems we examined. We found that in most cases the density histograms transitioned from a unimodal to a bimodal curve as the temperature is decreased, a transition that typically indicates passing from a homogeneous state into coexistence. Examples of such histograms are presented in Fig. 2.2. We subsequently used the local maxima of the density histograms, which we identify as the local densities of the coexisting phases ρ_l, to construct the state diagram of the system for different rotational diffusion coefficients, see Fig. 2.3. Note that in Fig. 2.2 some of the peaks in the gas phase are very low compared to the peaks of the liquid phase, indicating that only a small fraction of our system consisted of gas particles. We identified as fluid the regime where only a single peak is visible in the local density histogram. States which exhibited two peaks but showed no signs of global phase separation were identified as percolating network states, and states which exhibited a clear phase separation were marked as either gas-liquid or gas-crystal, depending on whether the high density phase is crystalline. Note that we have not probed the exact positions of the critical or triple points in any of the diagrams presented in Fig. 2.3. Additionally, the boundaries presented in black dashed lines are simply approximate state boundaries.

As shown in Fig. 2.3(a), for a rotational diffusion coefficient $D_r\tau = 30$ (ten times larger than the value dictated by the Stokes-Einstein relation), the behaviour of the system is very similar to the phase diagram seen for passive systems. The system transitions with decreasing temperature T from a homogeneous fluid state to a gas-liquid coexistence and eventually to a gas-crystal coexistence. Moreover, the binodal envelope is similar to that of the equilibrium system, in the sense that the value of temperature alone dictates the densities of the two coexisting phases. The low-density curves do not fall exactly on top of each other for low values of temperature due to surface effects that are discussed at the end of this section.

Decreasing the rotational diffusion to $D_r\tau = 9$ (Fig. 2.3(b)) results in the emergence of a new state, which we refer to as a percolating network. This new state consists of a dynamic network of clustered particles coexisting with a gas phase and in static images resembles an equilibrium system which has undergone spinodal decomposition. However, in contrast to such a state, the percolating network we observe is clearly not kinetically trapped. From Fig. 2.3(b) we see that the system now transitions with decreasing temperature from a homogeneous fluid state to a percolating network and then to gas-liquid coexistence.

Setting the rotational diffusion coefficient to the value dictated by the Stokes-Einstein relation, namely $D_r\tau = 3$, results in the state diagram shown in Fig. 2.3(c). Here, we find that the region where the percolating network state occurs, is increased at the expense of the gas-liquid coexistence region. Additionally, in the percolating network region, attraction does not solely dictate the densities of the coexisting states anymore. In contrast, the peaks in the local density histograms also depend on the total density

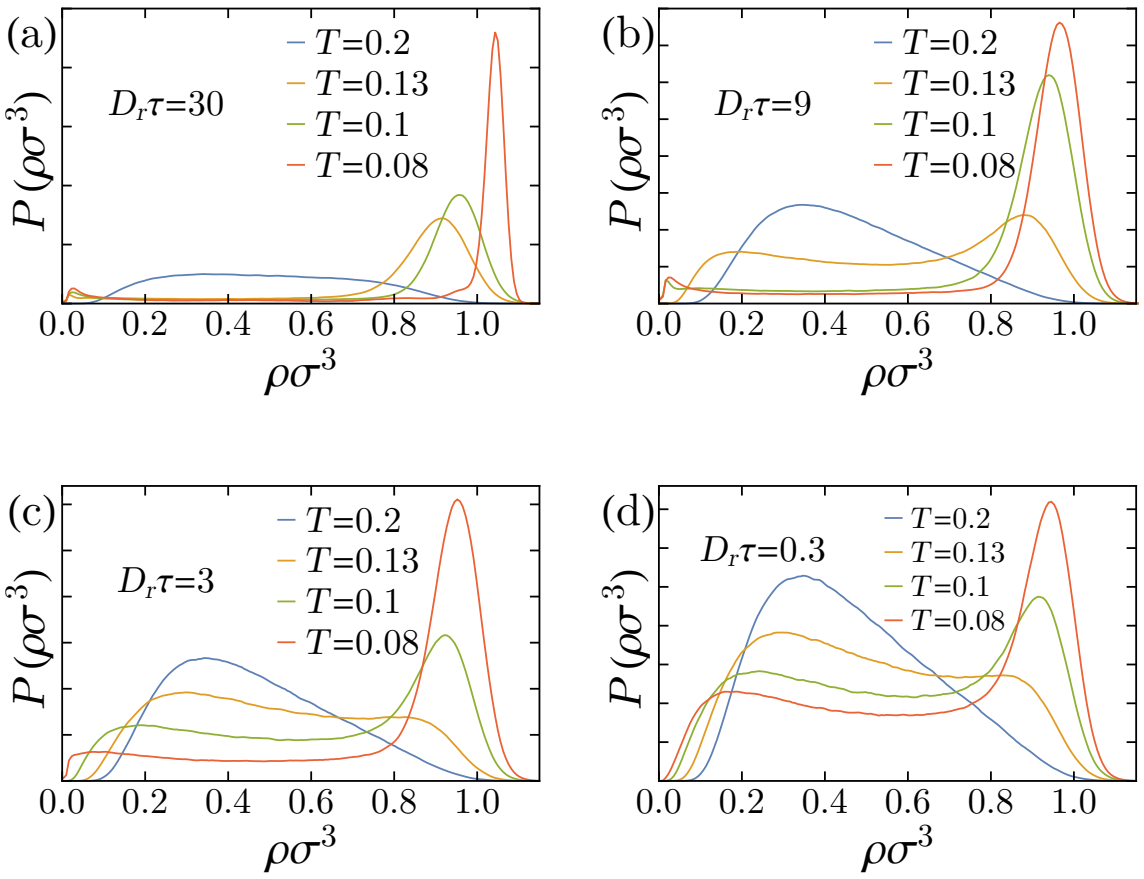

Figure 2.2: Local density histograms for a system with total density $\rho\sigma^3 = 0.381$ and magnitude of self-propulsion $v_0\tau/\sigma = 50$. $P(\rho\sigma^3)$ denotes the probability to find a particle with local density $\rho\sigma^3$. The subfigures (a)-(d) correspond to different rotational diffusion coefficients as indicated.

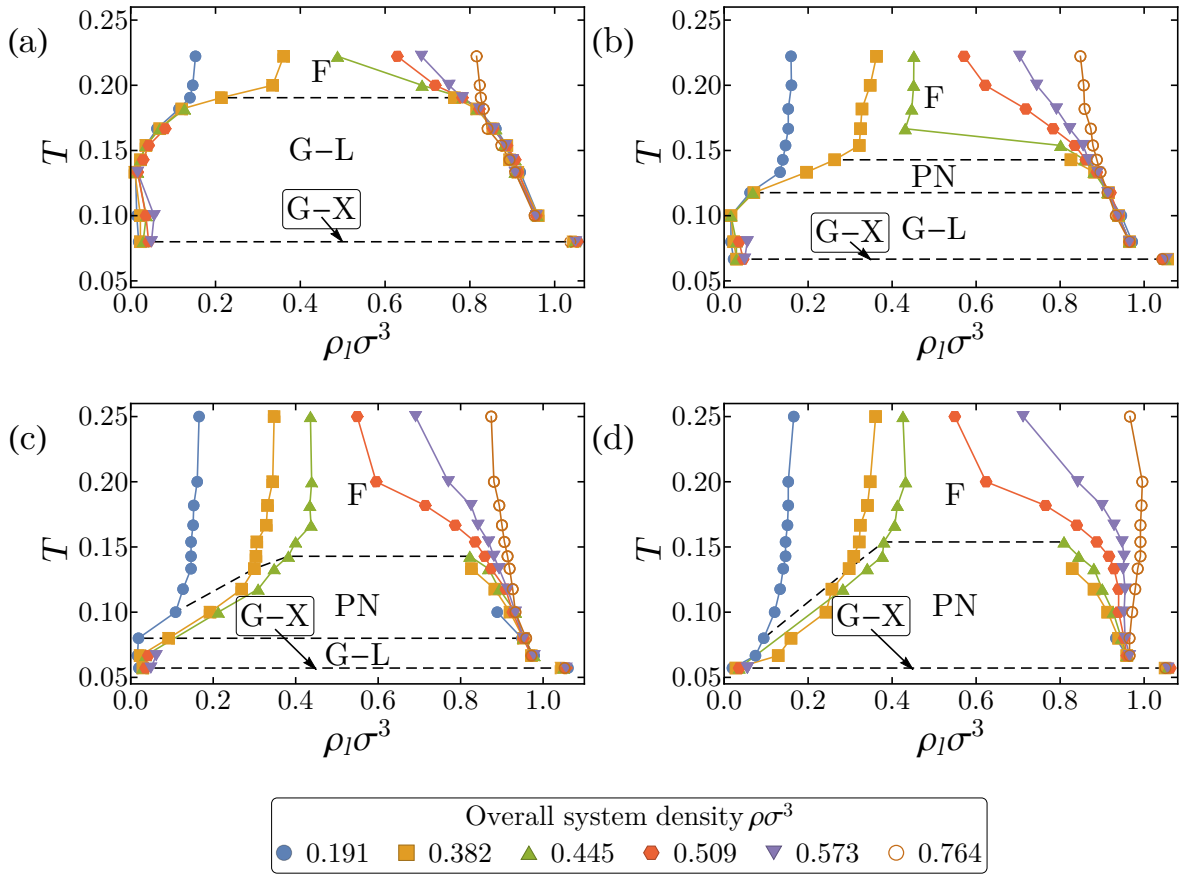

Figure 2.3: (a)-(d) State diagrams of the active Lennard-Jones system with rotational diffusion coefficients $D_r\tau = 30, 9, 3$, and 0.3 respectively. On the y-axes T denotes the temperature of the system. Data points correspond to local maxima of density histograms, which we identify as the local densities ρ_l of the coexisting phases. Different symbols correspond to different overall densities of the system. The black dashed lines indicate approximate state boundaries. Labels are as follows: F indicates the fluid, G-L gas-liquid coexistence, G-X gas-crystal coexistence and PN the percolating network state.

of the system. We note that this non-collapse was validated for various system sizes as described below.

For very low rotational diffusion ($D_r\tau = 0.3$) the state diagram continues to evolve (Fig. 2.3(d)). The percolating network has now completely replaced the gas-liquid region - according to our simulations, the system transitions directly from the percolating network state to a gas-crystal coexistence state.

We conclude this section by commenting on finite size effects. In order to ensure that the behaviour we observed in Fig. 2.3 was robust with respect to system size, we simulated a few state points for larger and smaller systems, consisting of $N = 21952$ and 2197 particles respectively. First of all, we found that the identification of the states does not change, *e.g.* we observe fluid, liquid-gas, crystal and the percolating network independent of system size. Additionally, the density of the dense phase (percolating network of liquid clusters, liquid or crystal) was only slightly affected by the system size. Substantial deviations occurred only for the low-density phase. These deviations are expected, since the first peak of the local density histogram is complicated by the presence of surface particles in addition to the gas particles. Nevertheless, this effect does not affect the conclusions drawn above.

2.3.2 Percolating cluster state

One of the most striking differences between a gas-liquid coexistence and the novel percolating network state is the compactness of the dense clusters. In a gas-liquid coexistence, the system evolves in order to minimize the surface area of the dense cluster, resulting in compact spherical or cylindrical geometries. In the percolating network, the active system appears to almost attempt to maximize the surface area, resulting in a highly branched network. One way to characterize this difference is by looking at the ratio of surface to volume of these large aggregates. In Fig. 2.4 we plot the average ratio N_S/N_V of surface particles over the total number of particles for the largest cluster, as a function of the rotational diffusion coefficient. In all cases, the density $\rho\sigma^3 = 0.191$, self-propelling force $v_0\tau/\sigma = 50$ and interaction strength $T = 0.08$ are chosen such that nearly all particles are part of one large cluster ($> 90\%$). We have found that for the parameters used in Fig. 2.4 the fluctuations of the number of particles in the biggest cluster N_V as well as the ratio N_S/N_V are small. Thus, the size of the largest cluster does not fluctuate significantly, and the dynamic changes in the shape of the percolating network do not seem to affect the presented results.

In the fast rotational diffusion regime, the liquid cluster is indeed compact, resulting in a small surface-to-volume ratio, which decreases further with increasing system size, as expected. On the other hand, for low rotational diffusion, *i.e.* in the percolating network state, we observe a much larger fraction of surface particles, which is independent of the system size. For the system parameters studied in Fig. 2.4 we find that the transition between the network state and the gas-liquid separation occurs at a rotational diffusion of around $D_r\tau \sim 2$.

To gain further insight into the properties of the percolating network state, we study the pairwise correlations between particles. In Fig. 2.5(a), we plot the radial distribution function g(r) for four different values of $D_r\tau$, at the same density and interaction strength

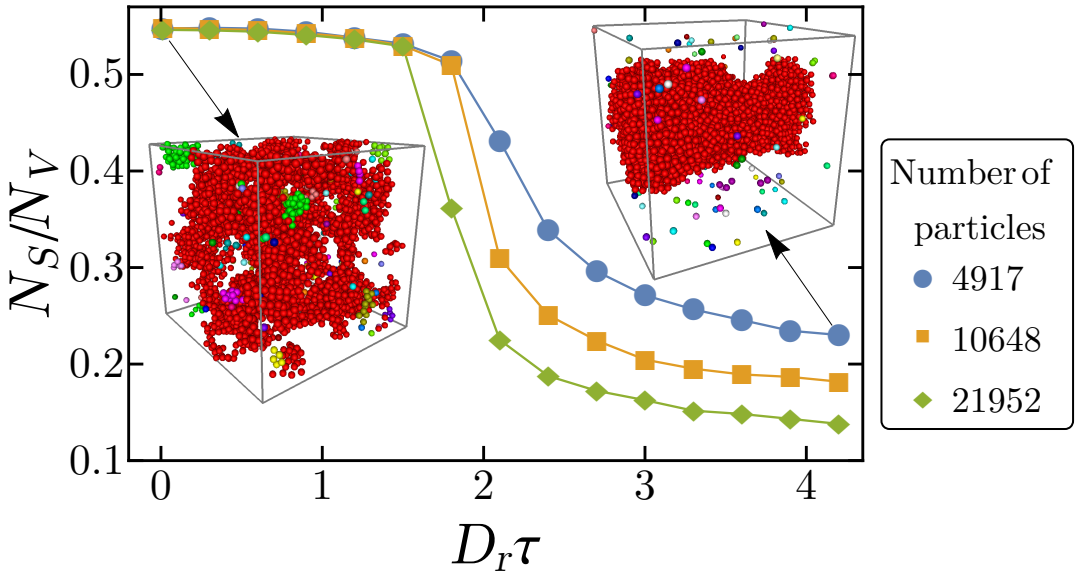

Figure 2.4: Average ratio of the number of surface particles N_S over the number of particles N_V in the biggest cluster of the system, as a function of the rotational diffusion coefficient $D_r\tau$. For all points, $v_0\tau/\sigma = 50$, $T = 0.08$, and $\rho\sigma^3 = 0.191$. The insets show snapshots of the system for the corresponding values of $D_r\tau$. Particles that belong to different clusters have different colours.

as was used for Fig. 2.4. For the highest value of $D_r\tau$, the system exhibits a gas-crystal phase separation, and the radial distribution function shows sharp peaks characteristic of the crystalline order. For $D_r\tau = 9$ and 3, the system exhibits a gas-liquid separation, resulting in much weaker peaks in $g(r)$. Finally, for $D_r\tau = 0.3$, we observe the percolating network state, for which the radial distribution function looks essentially the same as that of the gas-liquid separation.

Additionally, we calculate the normalized orientation correlation function $C_1(r)$, defined as

$$C_1(r) = \frac{\left\langle \sum_{i=1}^{N} {\sum_{j=1}^{\prime N}} \delta\left(r - r_{ij}\right) \boldsymbol{u}_i \cdot \boldsymbol{u}_j \right\rangle}{\left\langle \sum_{i=1}^{N} {\sum_{j=1}^{\prime N}} \delta\left(r - r_{ij}\right) \right\rangle}, \tag{2.8}$$

where the prime on the summation sign indicates that terms for which $i = j$ are not included. The angular brackets indicate a configurational average. This function is equal to unity if all the axes of self-propulsion of particles are aligned and zero if all particle orientations are uncorrelated. We plot $C_1(r)$ in Fig. 2.5(b). In all cases, we see that for $r < \sigma$, there is a negative correlation between the orientations of the particles. This is expected, as the only way for particles to be significantly closer than $r = \sigma$ is for them to be pushing towards each other. Moreover, as expected, the crystalline state shows significant statistical noise, due to small values of the denominator in Eq. 2.8. The most important result in Fig. 2.5 is the strong local alignment of particles in the percolating state in comparison to the other states. As there is no explicit aligning torque in the

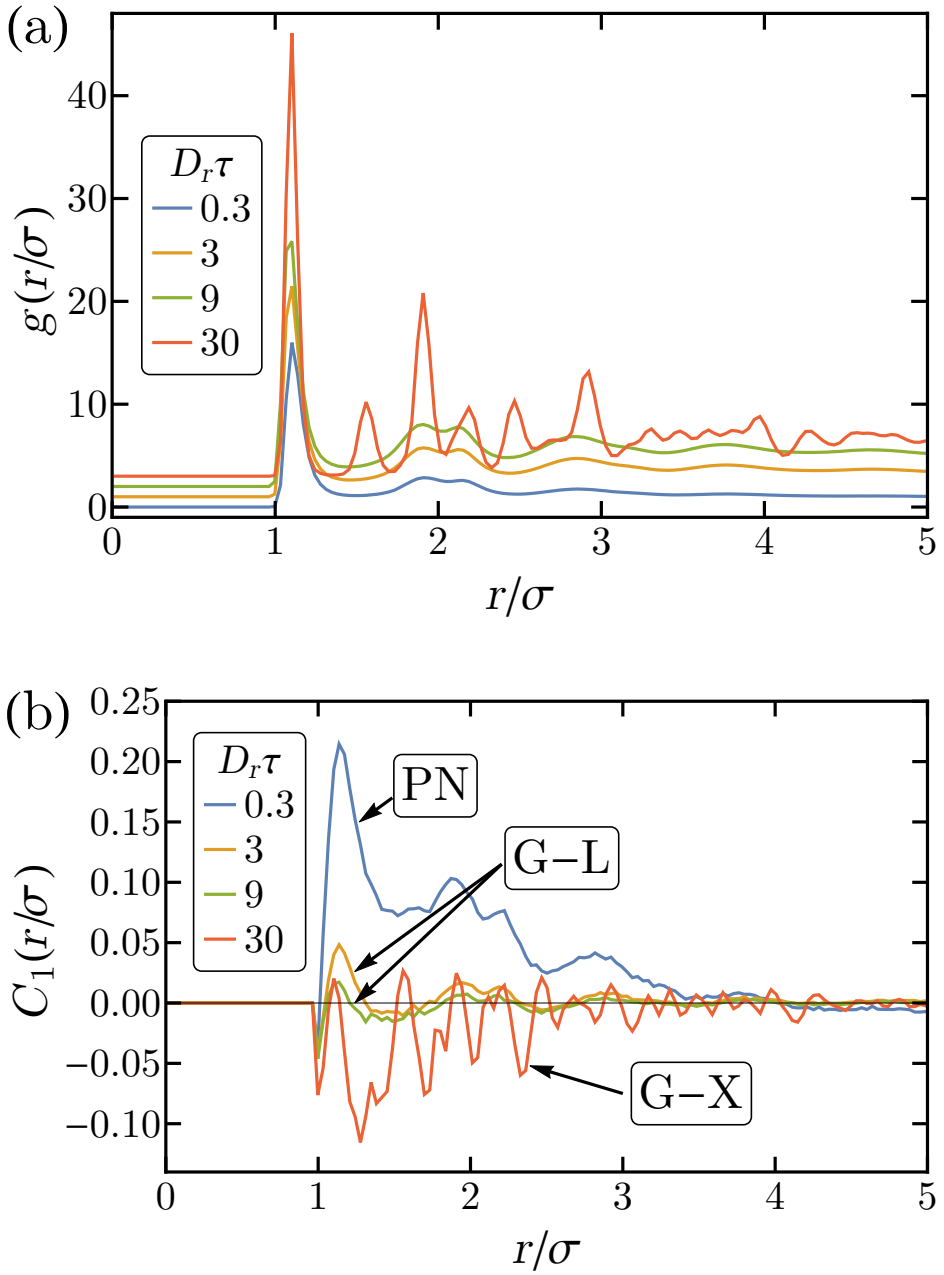

Figure 2.5: (a) Radial distribution function g(r), and (b) normalized orientation correlation function $C_1(r)$ for different values of the rotational diffusion coefficient. All curves correspond to values of the parameters $\rho\sigma^3 = 0.191$, $v_0\tau/\sigma = 50$ and $T = 0.08$. For $D_r\tau = 30$ crystal and gas coexist, for $D_r\tau = 9, 3$ liquid and gas coexist and for $D_r\tau = 0.3$ the system is in the percolating network state. Note that in subfigure (a) the radial distribution functions are offset for clarity.

model, this is surprising, and indicates that particles with similar orientations tend to stay in closer proximity in the percolating network.

In light of the above conclusions, we propose here a possible mechanism that accounts for the formation of the percolating network state. Consider a dilute system of self-propelled particles with an attraction strength at least strong enough to cause gas-liquid phase separation in the absence of self-propulsion. Now assume that the magnitude of self-propulsion is stronger than the attractions $\beta_s f_0 \sigma > \beta_s \epsilon$, and that the axis of self-propulsion associated with each particle is pointing in a fixed, random direction ($D_r \tau = 0$). When two particles collide there are two possible scenarios - if their axes of self-propulsion are pointing in a similar direction, then the attraction will cause them to aggregate and travel together. In contrast, if the axes of self-propulsion are pointing in sufficiently different directions, the particles will overcome the attraction and move away from each other. After a large number of collisions, this process will ultimately create a collection of clusters, with each cluster containing particles with similar orientations. By performing a small number of simulations (not shown in the present chapter) in very low densities $\rho\sigma^3 = 0.001 - 0.01$ and for $\beta_s f_0 \sigma > \beta_s \epsilon > 1$, we have indeed verified that the above process creates a collection of small clusters in which particle orientations are highly correlated.

Now, if we increase the density and instead of a fixed direction of self-propulsion we allow the particles to slowly rotate (corresponding to a low rotational diffusion coefficient), then this argument should continue to hold, *e.g.* particles that have similar orientations aggregate more easily than particles pointing in opposite directions. This results in highly dynamic aggregates with groups of particles frequently attaching and detaching, and neighboring particles displaying high degrees of orientational correlation as seen in Fig 2.5. For sufficiently high density (as those studied in this chapter), these aggregates become completely system spanning, and the majority of particles are connected to a single network, as seen in our simulations. This picture agrees well with movies from our simulations and accounts for both the local alignment of particles (Fig. 2.5) and the lack of system size dependence of the structural properties of the percolating network (Fig. 2.4).

As $D_r \tau$ increases, the persistence length of the self-propelled motion of the particles decreases. In this case, the attractive force is able to aggregate particles with larger differences in the orientation of the axes of self-propulsion. This process ultimately leads to a transition to the (bulk) gas-liquid phase coexistence region (Fig. 2.4). A similar transition from the percolating network state to gas-liquid coexistence can take place by fixing the persistence length of the particles and increasing the attraction (Fig. 2.3(b) and (c)).

2.3.3 Clustering properties

In a recent publication, Mognetti *et al.* [104] showed that the aggregation, *i.e.* clustering, in a system of self-propelled attractive particles depended only on the ratio $P_{\text{agg}} = \epsilon / f_0 \sigma$. To examine whether this collapse also occurs in our system, we calculated the degree of clustering Θ, introduced in Ref. [104], as

$$\Theta = 1 - \frac{\langle N_{clusters} \rangle}{N}, \tag{2.9}$$

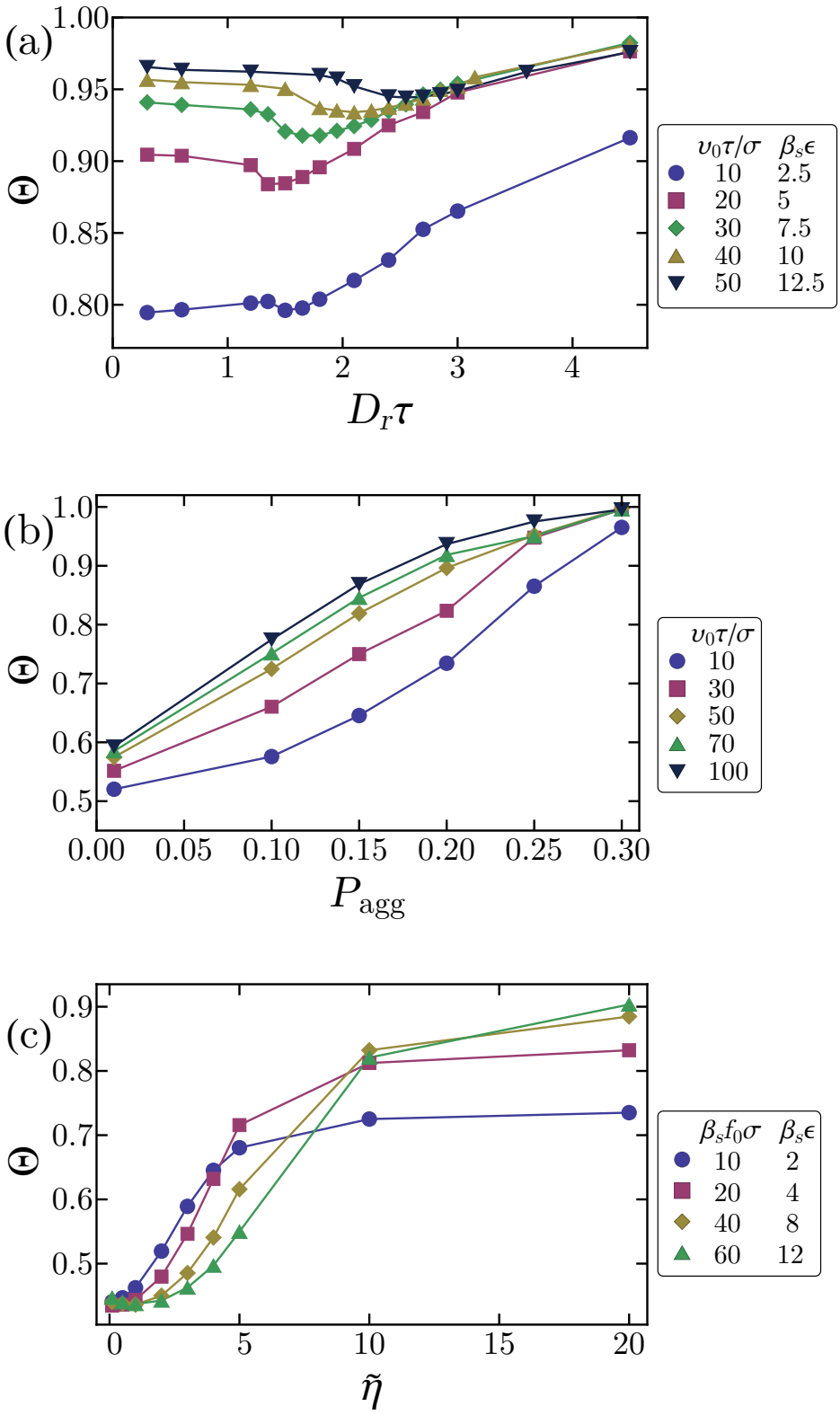

Figure 2.6: Degree of clustering Θ as a function (a) of the rotational diffusion coefficient $D_r\tau$ for different values of $v_0\tau/\sigma$ and $\beta_s\epsilon$, but constant ratio P_{agg}=0.25, (b) of P_{agg} for different values of $v_0\tau/\sigma$ and fixed $D_r\tau = 3$ and (c) of the dimensionless damping parameter $\tilde{\eta}$ for different values of $\beta_s f_0\sigma$ and $\beta_s\epsilon$, but constant ratio P_{agg}=0.20 and constant $D_r\tau = 3$. The density of the system is $\rho\sigma^3 = 0.191$, same as in Ref. [104].

where $\langle N_{clusters} \rangle$ is the average number of clusters in the system. We considered particles clustered when their center of mass distance is less than 1.2σ [104]. Thus, $\Theta \to 0$ when the system is in the dilute gas phase where $\langle N_{clusters} \rangle \simeq N$, while $\Theta = 1 - \frac{1}{N} \simeq 1$ when all particles belong to the same cluster. The results are plotted in Fig. 2.6.

In Fig. 2.6(a) we plot the degree of clustering Θ as a function of the rotational diffusion coefficient $D_r\tau$ at constant $P_{\rm agg}$ near the percolating network to gas-liquid transition. We do not see a collapse in the degree of clustering here. Similarly, in Fig. 2.6(b) we do not see a collapse when plotting Θ as a function of $P_{\rm agg}$ at fixed rotational diffusion $D_r\tau$ for a wider range of state points. Finally, we checked to see if the collapse would occur if we use underdamped dynamics in place of overdamped dynamics for the translational degrees of freedom. As shown in Fig. 2.6(c), we also do not find a value of the damping parameter $\tilde{\eta}$ for which a collapse occurred. We conclude that the data collapse found by Mognetti *et al.* [104] does not occur in our system. We attribute this discrepancy to the difference in the applied dynamics, and more specifically to the different mechanisms that rotate the particles in the two different systems.

2.4 Conclusions

In the present chapter, we employed computer simulations to study the self-assembly of a system of self-propelled, Brownian particles, that interact *via* the truncated and shifted Lennard-Jones potential.

We determined state diagrams of the overdamped system for various rates of rotational diffusion of the self-propelled motion of the particles. We found that for fast rotational diffusion, the properties of the state diagram bore strong similarities to the phase diagram of the equilibrium Lennard-Jones system. However, as the rotational diffusion was decreased, new features arose due to the interplay between self-propulsion and attraction. That is, a new state was observed between the fluid phase and gas-liquid coexistence, which we identified as a highly dynamic, percolating network state. That state consisted of interconnected but motile clusters that created a system-spanning network. Finally, for slow rotational diffusion the (bulk) gas-liquid coexistence disappeared and the system transitioned from the percolating network state directly to gas-crystal coexistence.

We subsequently discussed the unique properties of the percolating state, and presented evidence of a transition from gas-liquid coexistence to percolating network with decreasing rotational diffusion. By examining the correlations between the orientations of the axes of self-propulsion of the particles, we found significant local alignment in the percolating state. A possible mechanism was proposed in order to explain the formation of the percolating network.

Finally, we noted that the ratio of the strength of the attraction over the magnitude of self-propulsion does not solely characterize our system. This is in contrast to what was found in Ref. [104], and may be due to differences in the applied dynamics.

We would like to comment here on the significance of the percolating network state. First, we note once more that this state is caused by the synergy between attraction and self-propulsion, so we expect it to be present in three-dimensional systems for a wide variety of attractive potentials and propulsion mechanisms. Moreover, our simulations

suggest that this novel state is present for low density systems and experimentally relevant rotational diffusion, so a search for this state in real colloidal systems is feasible. As earlier work has shown, hydrodynamic interactions may also cause local alignment of particles, an effect that may enhance the formation of the percolating network state in experimental systems [47].

Last but not least, as demonstrated in Section 2.3.3, the exact dynamics of a theoretical model are of importance not only for the quantitative but also for the qualitative results it generates. Detailed comparisons between different theoretical models, as well as actual experimental systems, such as Ref. [111], are thus extremely valuable and needed, in order to deepen our understanding of active matter systems.

Acknowledgments

The work presented in this chapter was performed in collaboration with Harmen Sielcken, an undergraduate student. Harmen performed simulations and analysis of results that are part of Figs. 2.4 and 2.6(a). We also thank Zdeněk Preisler for useful discussions.

3

Vapour-liquid coexistence of an active Lennard-Jones fluid

In this chapter we study the vapour-liquid transition of a three-dimensional system of self-propelled Lennard-Jones particles. Using recent theoretical results for active matter, we calculate the pressure and report equations of state for the system. Additionally, we chart the vapour-liquid coexistence and show that the coexistence densities can be well described using simple power laws. Lastly, we demonstrate that our out-of-equilibrium system shows deviations from both the law of rectilinear diameters and the law of corresponding states.

3.1 Introduction

One of the most interesting yet still not fully developed aspect of active matter physics is the applicability of equilibrium statistical physics concepts, such as free energy, pressure and chemical potential, to describe the phase behaviour of active matter systems and the associated phase transitions [62, 80, 85–88, 90–95]. One of the few systems where a phase transition has been thoroughly explored, even in the context of critical phenomena, is the Vicsek model together with its modifications [63, 67, 68, 73, 112]. In this chapter, we study a different, yet also highly relevant model system for active matter, namely a system of attractive, self-propelled, and spherical Brownian particles [5, 113]. We investigate theoretically a vapour-liquid phase transition and present an extensive study of the out-of-equilibrium phase transition.

One of the most well-studied equilibrium model systems which undergo such a vapour-liquid phase transition is the Lennard-Jones (LJ) fluid [105, 106]. In this chapter, we modify this model by introducing a self-propulsion force to each particle, and treat the motion using Brownian dynamics. This model was chosen since the phase behaviour of the equilibrium system is well characterized and can be readily verified by computer simulations. In particular, since the LJ particles interact *via* a short-range attractive potential, the second-order vapour-liquid phase transition of the system belongs to the Ising universality class [114–116]. Moreover, the LJ fluid obeys both the law of rectilinear diameters when in phase coexistence, which is obeyed by a myriad of real substances as well as active matter systems [116–118] (see also Chapter 6), and the Noro-Frenkel law of corresponding states, which maps the thermodynamic properties of different spherically symmetric attractive potentials onto each other [119, 120].

In the case of the active LJ fluid preliminary studies of the vapour-liquid phase transition have hinted on the deviation of the transition properties from equilibrium [75, 104, 121] (see also Chapter 2). Most interestingly, as we have shown in Chapter 2, when the direction of the self-propulsion of the particles diffuses in a sufficiently slow rate, a dynamic percolating state is found between the fluid and the vapour-liquid coexistence. Herein we expand on these results by measuring the equation of state for the system and by studying the behaviour of the pressure in the vapour-liquid coexistence regime. Additionally, we map out the phase diagram for different combinations of the propulsion speed and rotational diffusion rate. We compare the behaviour of the binodals of the active system with that of the equilibrium system by exploring whether the laws of rectilinear diameters and corresponding states hold. Moreover, we examine whether the binodals can be fitted *via* simple power laws.

In Section 3.2 we introduce the model and the dynamics and also present the method that we used to calculate the equation of state. Equations of state are presented in Section 3.3.1, followed by a close study of the phase coexistence in Section 3.3.2. This study includes the power law and exponential scaling of the order parameter and the critical temperature respectively in Section 3.3.3, a test of the law of rectilinear diameters and the scaling of the critical density in Section 3.3.4 and ultimately a test of the law of corresponding states in Section 3.3.5. Our conclusions are summarized in Section 3.4.

3.2 Methods

3.2.1 Model and dynamics

We consider a three-dimensional system consisting of self-propelled spherical particles (colloids) immersed in a molecular solvent, in a periodic box with dimensions L_x, L_y and L_z. The position of the center of mass of the i-th particle at time t is given by the vector $\boldsymbol{r}_i(t)$. With particle i, we associate a three-dimensional unit vector $\boldsymbol{u}_i(t)$ that indicates the direction of the self-propelling force. The particles interact with each other *via* a Lennard-Jones potential

$$U(r_{ij}) = 4\epsilon \left[\left(\frac{\sigma}{r_{ij}} \right)^{12} - \left(\frac{\sigma}{r_{ij}} \right)^{6} \right], \tag{3.1}$$

truncated and shifted at 2.5σ, where σ is the particle length scale, $r_{ij} = |\boldsymbol{r}_j - \boldsymbol{r}_i|$ and the parameter ϵ controls the strength of the interaction.

To describe the translational and rotational motion of the individual colloidal particles inside the solvent we use the overdamped Langevin equations

$$\frac{d\boldsymbol{r}_i}{dt} = -\frac{1}{\eta} \sum_{j \neq i} \frac{\partial U(r_{ij})}{\partial \boldsymbol{r}_i} + v_0 \boldsymbol{u}_i + \sqrt{2D_{tr}}\boldsymbol{\xi}_i^{tr}, \tag{3.2}$$

$$\frac{d\boldsymbol{u}_i}{dt} = \sqrt{2D_r}\,(\boldsymbol{u}_i \times \boldsymbol{\xi}_i^{r})\,. \tag{3.3}$$

Note that after each iteration of Eq. 3.3 we normalize the unit vectors $\boldsymbol{u}$ in order to prevent their drift. The translational diffusion coefficient is given by the Einstein-Smoluchowski relation $D_{tr} = 1/(\beta_s \eta)$, with η the damping coefficient and β_s the inverse temperature of the surrounding solvent. D_r denotes the rotational diffusion coefficient and v_0 the propulsion speed. The vectors $\boldsymbol{\xi}_i^{tr}$ and $\boldsymbol{\xi}_i^{r}$ are unit-variance random vectors, with mean value and variation

$$\langle \boldsymbol{\xi}_i^{tr,r}(t) \rangle = 0, \tag{3.4}$$

$$\langle \boldsymbol{\xi}_i^{tr,r}(t) \boldsymbol{\xi}_j^{tr,r}(t') \rangle = \mathbb{I}_3\, \delta_{ij}\, \delta(t - t'), \tag{3.5}$$

where $\mathbb{I}_3$ is the unit matrix in three dimensions.

We implemented the aforementioned equations of motion (Eqs. 3.2 and 3.3) using an Euler-Maruyama integration scheme [107]. A maximum time step of $dt = 2 \times 10^{-5} \sigma^2 / D_{tr}$ was used for the numeric integration of the equations of motion. The number of particles in our simulations was approximately $N = 2500$. We have verified that the measurements presented in this chapter are robust by repeating a limited number of measurements on a system of 5000 particles.

Lengths are given in units of σ, time in units of $\tau = \sigma^2/D_{tr}$, and energy in units of $1/\beta_s$. We also denote $T = 1/\beta_s \epsilon$ as the dimensionless temperature of our system. This notation is adopted as it facilitates direct comparison to a passive LJ system.

3.2.2 Pressure

In order to measure the pressure of our active system we use the results of Winkler *et al.* [122] (see also Appendix A). Specifically, the pressure P of a system of self-propelled and spherical particles in a periodic box is calculated using

$$P = P_{id} + P_{vir} + P_{swim}. \tag{3.6}$$

In this expression, the ideal gas pressure P_{id} is given by

$$P_{id} = \rho/\beta_s, \tag{3.7}$$

with ρ the number density. Additionally, P_{vir} is the standard virial pressure given by

$$P_{vir} = -\frac{1}{3V}\left\langle \sum_{i=1}^{N-1}\sum_{j=i+1}^{N} \frac{\partial U(r_{ij})}{\partial \boldsymbol{r}_i}\cdot(\boldsymbol{r}_i - \boldsymbol{r}_j)\right\rangle, \tag{3.8}$$

where V is the volume of the system. Finally, P_{swim} is the "swim pressure", *i.e.* the direct contribution of the self-propulsive forces to the pressure, and is given by

$$P_{swim} = \frac{\rho\eta v_0^2}{6D_r} - \frac{\eta v_0}{6VD_r}\left\langle \sum_{i=1}^{N-1}\sum_{j=i+1}^{N} \frac{\partial U(r_{ij})}{\partial \boldsymbol{r}_i}\cdot(\boldsymbol{u}_i - \boldsymbol{u}_j)\right\rangle. \tag{3.9}$$

Note that the brackets in Eqs. 3.8 and 3.9 denote a time average over the steady state. The steady state of the system was identified following Ref. [121] (see also Chapter 2).

3.3 Results

3.3.1 Equations of state

Recent theoretical work has established the existence of an equation of state for self-propelled particles with purely isotropic interactions, such as our model [90, 92, 122, 123]. In this section we calculate equations of state for an active LJ system in a periodic cubic box. Our goal is to examine the behaviour of the equation of state as the active system transitions from a homogeneous state to vapour-liquid phase coexistence, and compare it with the behaviour of a passive LJ system.

In Fig. 3.1(a) we show characteristic equations of state for the system. As in the passive system, lowering the temperature causes the equation of state to become non-monotonic, a behaviour associated with phase separation into a gas and a liquid. From these equations of state, we observe no qualitative differences from the passive LJ system.

In order to examine the equations of state in more detail, we study the different contributions to the pressure. In Fig. 3.1(b) we plot the swim pressure as a function of the density for different temperatures. We find that for high temperatures, where no coexistence takes place, the swim pressure has a roughly parabolic shape. However, once phase separation occurs in the system, the swim pressure grows linearly with the density in the phase coexistence regime. This linear growth in the coexistence region is present for all other parameter space points that we have examined. We find that the swim pressure

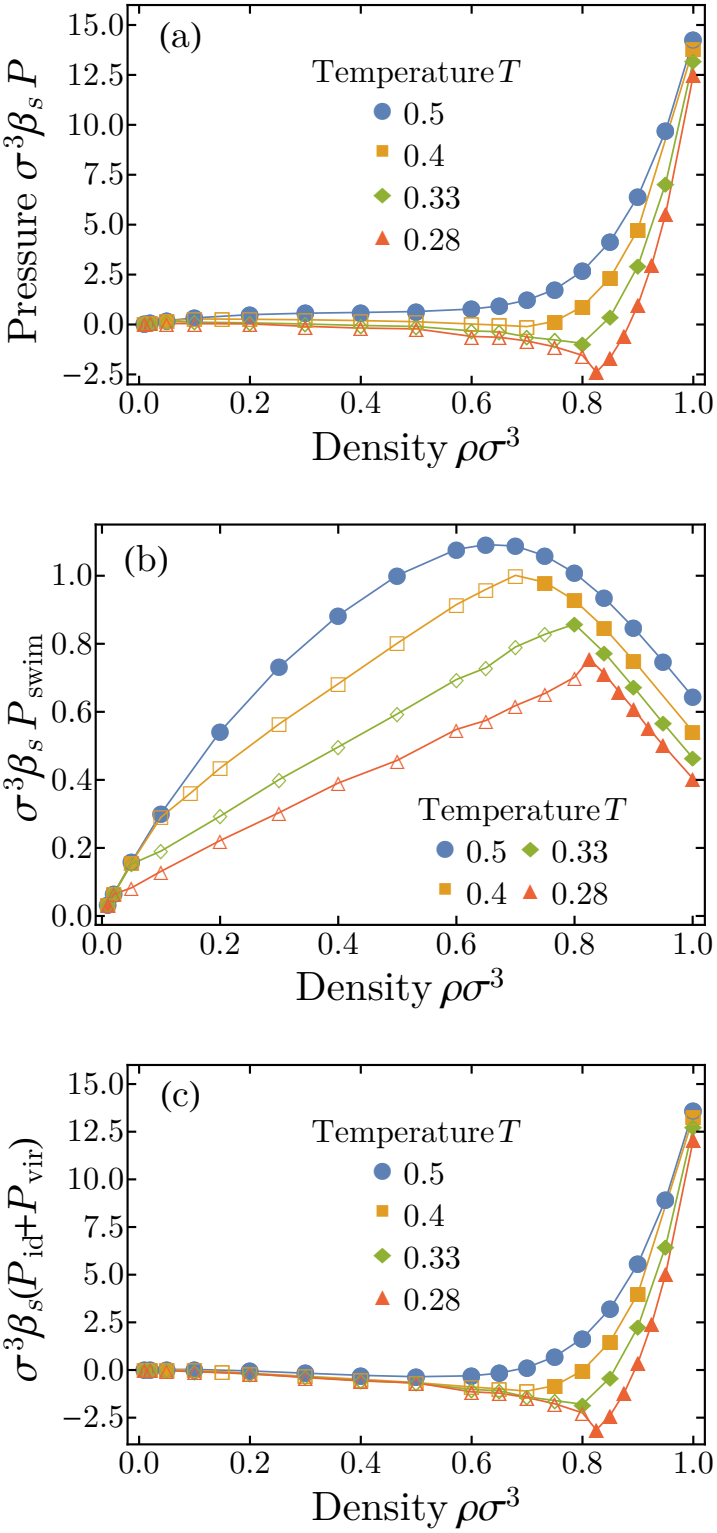

Figure 3.1: Equations of state for a system with propulsion speed $v_0\tau/\sigma = 20$ and rotational diffusion coefficient $D_r\tau = 20$. (a) shows the total pressure of the system as a function of the density, (b) shows the swim pressure contribution (Eq. 3.9) and (c) shows the sum of the ideal and the virial contribution (Eqs. 3.7 and 3.8 respectively). Full symbols correspond to state points where the system is in a homogeneous state while open symbols denote vapour-liquid phase coexistence. Full lines are simply guides to the eye.

of both the gas and the liquid phase stays fixed throughout the coexistence region, hence this linear growth of the total swim pressure arises due to the lever rule. Note that in our system the swim pressure of the dense phase is higher than that of the dilute phase in the coexistence region, while the opposite is true in the case of motility-induced phase separation [91].

Subsequently, in Fig. 3.1(c) we show the contribution coming from the ideal and the virial part of the pressure. Note that these two contributions alone cannot account for the observed phase behaviour, as the high temperature curve (colored blue) is non-monotonic even though the system is in a fluid state for all densities shown.

3.3.2 Vapour-liquid coexistence

In this section we map out the phase diagram for the LJ fluid. To this end, we conducted simulations in a long simulation box with dimensions $L_z = 6L_x = 6L_y$, containing a liquid slab coexisting with vapour, as shown in Fig. 3.2(a). The overall number density of the system was fixed at $\rho\sigma^3 = 0.1333$. We then measured the density profile along the long axis by dividing the box into slabs of width $\simeq 0.3\sigma$ along the z direction and taking the time average of the number of particles in a given slab. Subsequently, we calculated the local number densities of the vapour phase ρ_v and the liquid phase ρ_l by fitting the density profile $\rho(z)$ around each interface to the function

$$\rho(z) = \frac{1}{2}(\rho_l + \rho_v) - \frac{1}{2}(\rho_l - \rho_v)\tanh\left[\frac{2(z - z_0)}{w}\right], \tag{3.10}$$

where z_0 and w are the location and width of the vapour-liquid interface, and are also determined from the fit. Fig. 3.2(b) shows an example of a measured density profile as well as the fitted Eq. 3.10. We find that the hyperbolic tangent provides an excellent fit to the interface and that we can accurately determine the local densities of the vapour and the liquid phase.

We systematically obtained the coexisting densities for a wide range of parameters following two different paths that drive the system out of equilibrium. First, we varied the rotational diffusion coefficient while keeping the self-propulsion fixed at a non-zero value. Second, we varied the propulsion speed while keeping the rotational diffusion rate of the particles fixed. The measured coexisting densities are summarized in Fig. 3.3. Clearly, both routes produce a series of phase diagrams that are highly consistent with a simple passive attractive fluid, such as a LJ fluid. Note that these two paths are not equivalent as the $D_r \to \infty$ limit does not coincide with the $v_0 \to 0$ limit: the first one corresponds to a passive system with a higher effective temperature than the second one, which corresponds to the equilibrium LJ system with temperature $T = 1/\beta_s\epsilon$. Also, we set a rather high rotational diffusion coefficient when we varied the self-propulsion speed. This choice was made in order to minimize the area of the percolating state regime in the state diagram [121] (see also Chapter 2).

In the following subsections, we compare the obtained phase diagrams more closely to the equilibrium case by exploring the temperature dependence of $\Delta\rho = \rho_l - \rho_v$, and examining whether the law of rectilinear diameters and law of corresponding states still hold.

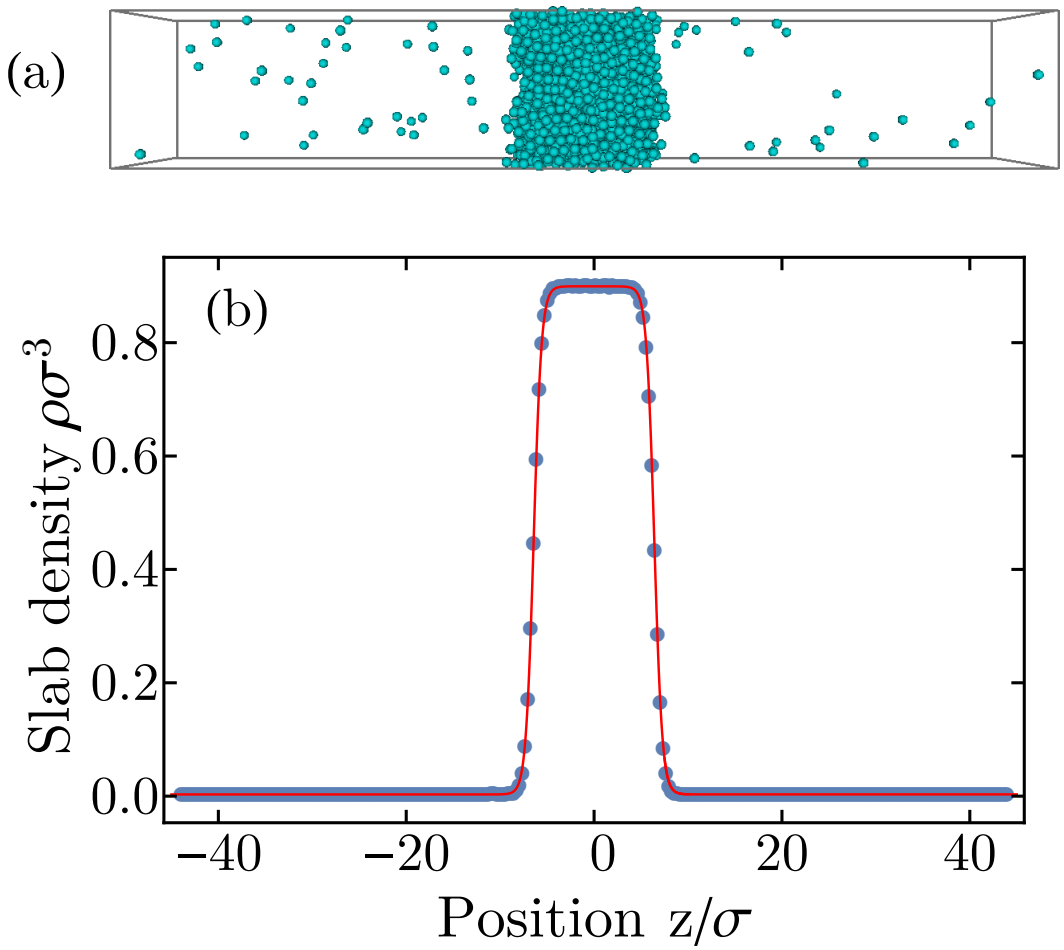

Figure 3.2: (a) Snapshot of a long box simulation. (b) Average number density $\rho\sigma^3$ as a function of position. Data points are the time averages obtained from simulations while the red curve is a fit of Eq. 3.10.

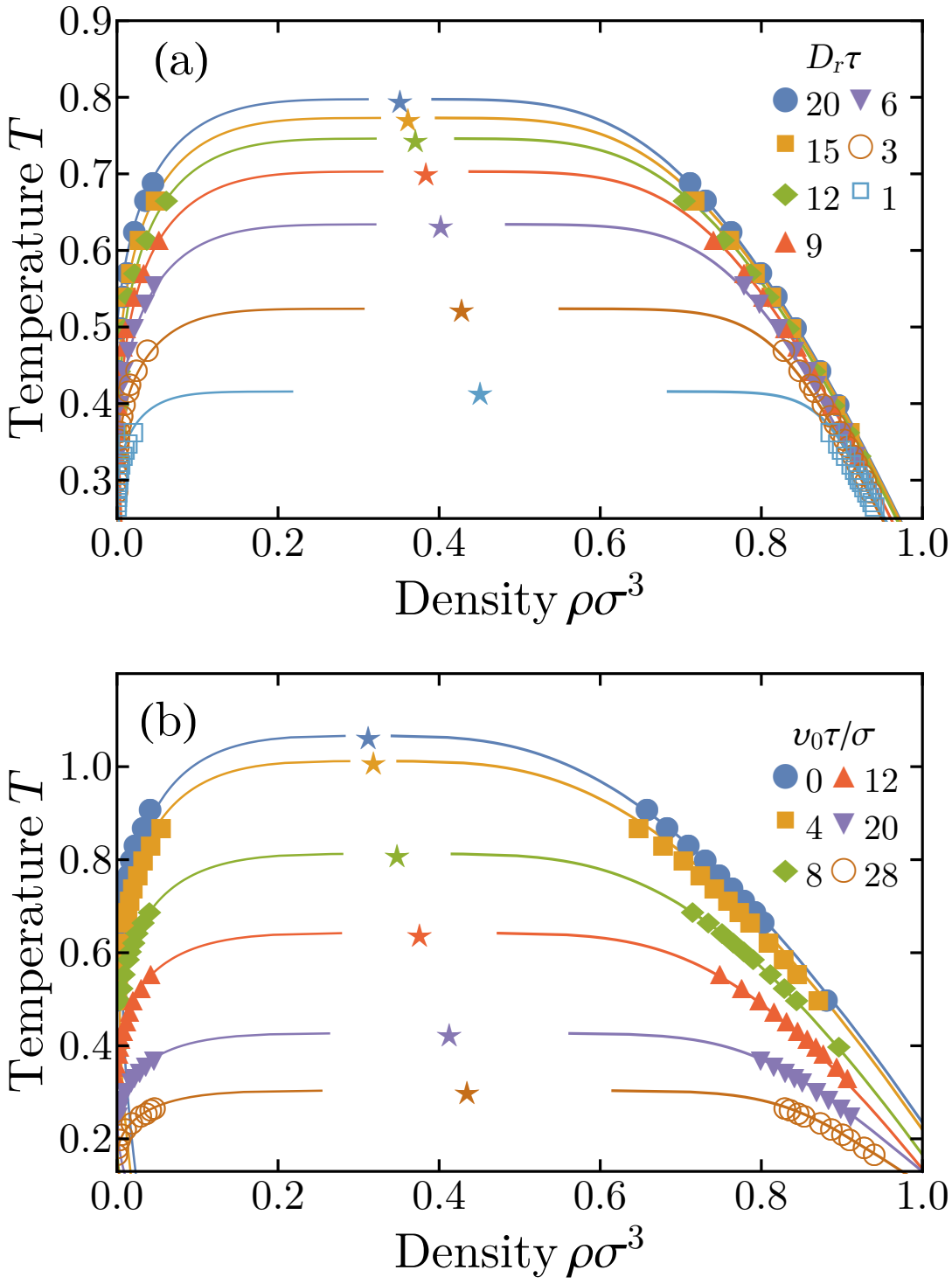

Figure 3.3: Binodal lines of the system for a system of (a) constant propulsion speed $v_0\tau/\sigma = 8$ and varying rotational diffusion coefficient and (b) constant rotational diffusion coefficient $D_r\tau = 20$ and varying propulsion speed. Simulation results are denoted by points. Full lines are fits, obtained by using the exponential fits for the parameters $T_c, \beta, A, \rho_c, \alpha$ and B (Tables 3.1 and 3.2) on Eqs. 3.11 and 3.14. Stars denote the calculated critical points.

3.3.3 Temperature dependence of $\Delta\rho$

The order parameter that governs the vapour-liquid phase transition in equilibrium is the difference between the two coexisting densities $\Delta\rho = \rho_l - \rho_v$. In equilibrium, $\Delta\rho$ follows a power law given by

$$\sigma^3 \Delta\rho = A\,(T_c - T)^{\beta}\,, \tag{3.11}$$

where T_c is the critical temperature, β is the (critical) exponent and A is a proportionality constant. Here we examine whether the scaling of $\Delta\rho$ with temperature follows the same behaviour for our active system, and treat T_c, A, and β as free fitting parameters.

In Figs. 3.4(a) and 3.5(a) we show the order parameter $\Delta\rho$, as a function of the scaled temperature (Eq. 3.11) for different values of rotational diffusion rate and self-propulsion speed, respectively. Interestingly, the simulation data fall on straight lines, indicating that Eq. 3.11 accurately describes the active system in the examined parameter space.

Next, we examine the scaling of the fitted critical temperature T_c, the exponent β and the constant A as the system is driven away from equilibrium. The results are plotted in Figs. 3.4(b-c) and 3.5(b-c). Error bars are the standard errors from fitting and in the majority of cases they are smaller than the plotted markers. As expected, the critical temperature decreases with decreasing rotational diffusion coefficient/increasing propulsion speed, as stronger attraction is needed to bring together swimmers with larger persistence lengths. This is in accordance with the predictions of Farage *et al.* for the same model [88]. We also find that the exponent β decreases as our particles become more active. The parameter A stays quasi-constant as a function of the rotational diffusion (Fig. 3.4(c) inset), but clearly increases with increasing propulsion speed (Fig. 3.5(c) inset).

For the systems where the rotational diffusion coefficient is varied, the scaling of T_c and β is well captured by simple exponential functions, for instance

$$T_c(D_r) = a_1 + a_2 e^{-a_3 D_r \tau}, \tag{3.12}$$

is an excellent fit for the critical temperature, where the values of the dimensionless parameters a_1, a_2 and a_3 can be found in Table 3.1. We also fit the parameter A with an exponential function, even though its variation is minimal and the fit is clearly not optimal.

For the systems where the propulsion speed is varied, we similarly find that the scaling

$$T_c(v_0) = b_1 + b_2 e^{-b_3 \sigma/(v_0 \tau)}, \tag{3.13}$$

describes our data fairly well. The same holds for the exponent β and the constant A. The numerical coefficients can be found in Table 3.2. Note that the difference between Eqs. 3.13 and 3.12 is simply the replacement of $D_r\tau$ with $\sigma/(v_0\tau)$. As the Péclet number is simply the ratio of these two, it might be tempting to ask whether the phase behaviour can be completely described by the Péclet number $\mathrm{Pe} = D_r\sigma/v_0$. However, this turns out not to be the case as these two separate paths out of equilibrium cannot be collapsed *via* the Péclet number.

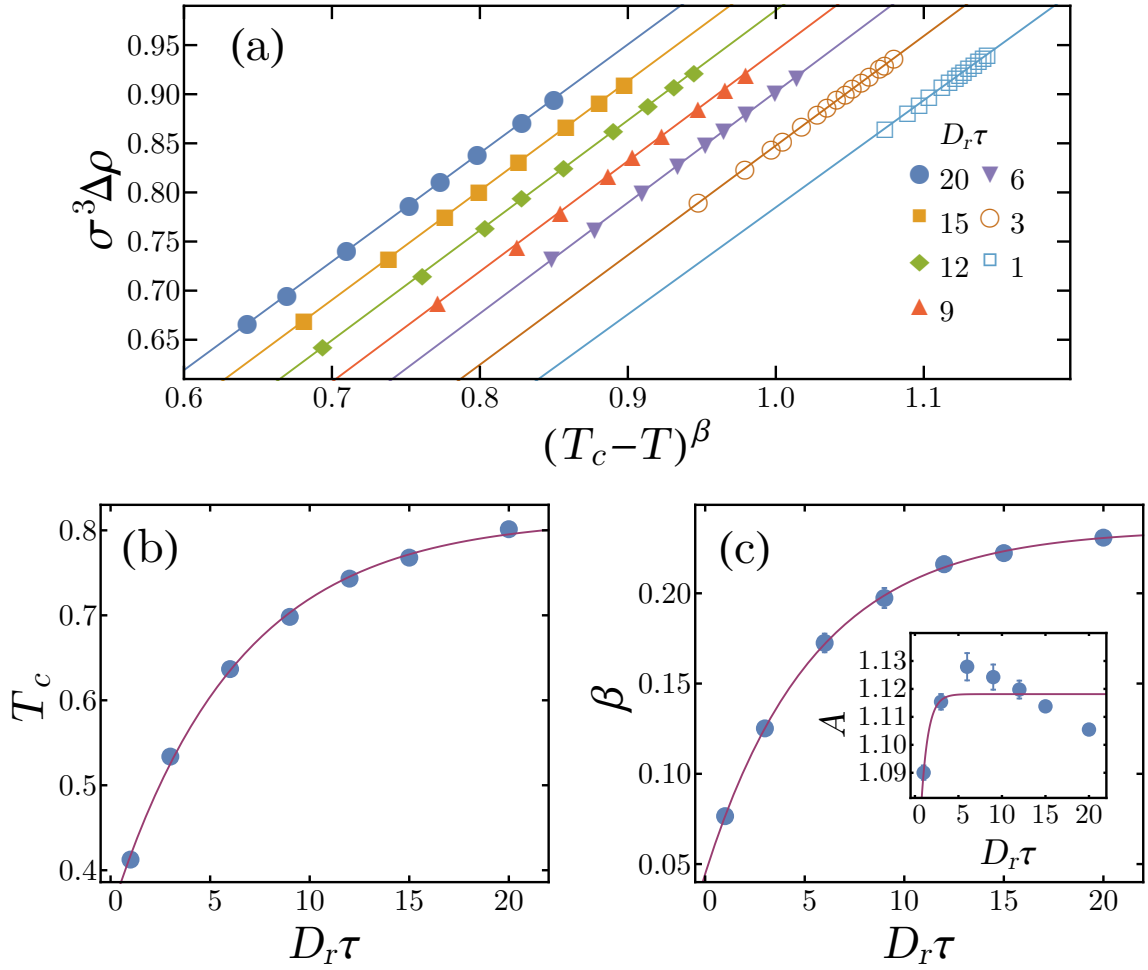

Figure 3.4: (a) $\Delta\rho$ as a function of the scaled temperature for systems of different rotational diffusion rates and constant propulsion speed $v_0\tau/\sigma = 8$. Data points correspond to simulation results while the lines denote the fits (Eq. 3.11). Results for different rotational diffusion rates are offset for clarity. (b) Critical temperature T_c as a function of the rotational diffusion rate. The continuous line shows the fit from Table 3.1 . (c) Critical exponent β and constant A (inset) as a function of the rotational diffusion rate. The continuous line shows the fit from Table 3.1.

Table 3.1: Fitting parameters of the function $a_1+a_2e^{-a_3D_r\tau}$ to the parameters of Eqs. 3.11 and 3.14 for systems of different rotational diffusion rates and constant propulsion speed $v_0\tau/\sigma = 8$.

	T_c	β	A	$\rho_c\sigma^3$	α	B
a_1	0.818	0.237	1.118	0.339	1.04	0.252
a_2	-0.47	-0.194	-0.081	0.126	1.122	1.336
a_3	0.156	0.18	1.004	0.114	0.229	0.79

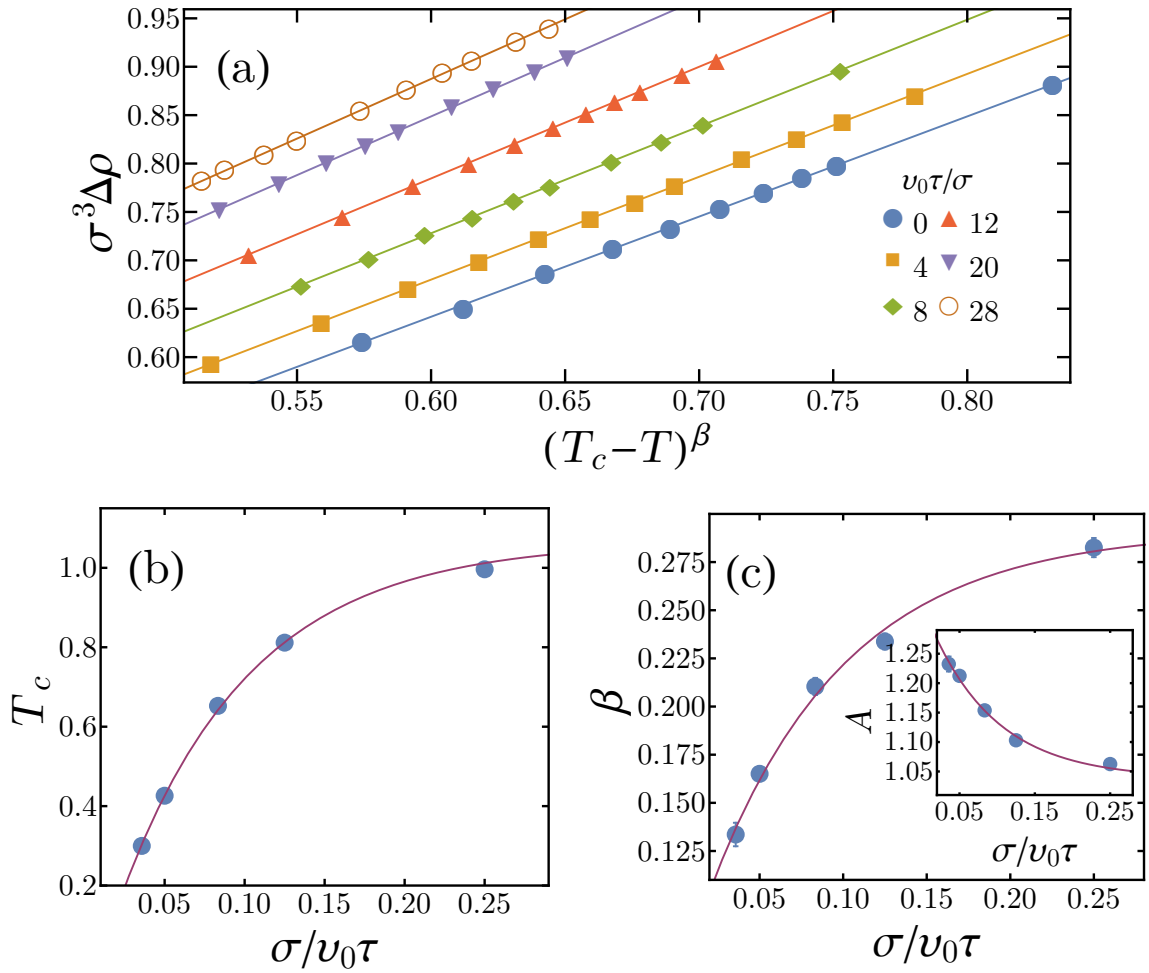

Figure 3.5: (a) $\Delta\rho$ as a function of the scaled temperature for systems of different propulsion speeds and constant rotational diffusion $D_r\tau = 20$. Data points correspond to simulation results while the lines denote the fits (Eq. 3.11). Results for different propulsion speeds are offset for clarity. (b) Critical temperature T_c as a function of the self-propulsion speed. The continuous line shows the fit from Table 3.2. (c) Critical exponent β and constant A (inset) as a function of the self-propulsion speed. The continuous line shows the fit from Table 3.2.

Table 3.2: Fitting parameters of the function $b_1 + b_2 e^{-b_3\sigma/(v_0\tau)}$ to the parameters of Eqs. 3.11 and 3.14 for systems of different propulsion speeds and constant rotational diffusion $D_r\tau = 20$.

	T_c	β	A	$\rho_c\sigma^3$	α	B
b_1	1.066	0.291	1.038	0.312	0.971	0.234
b_2	-0.184	-0.241	0.297	0.201	2.132	8.082
b_3	12.33	12.382	11.384	13.795	33.406	69.521

3.3.4 Law of rectilinear diameters

Next, we investigate whether the law of rectilinear diameters holds for our system. Specifically, we study the properties of the sum of the coexisting densities which in equilibrium typically scales as [106, 124]

$$\frac{1}{2}\left(\rho_v + \rho_l\right)\sigma^3 = B\left(T_c - T\right)^{\alpha} + \rho_c\sigma^3. \tag{3.14}$$

with B a proportionality constant, α an exponent and ρ_c the density at the critical point. According to the law of rectilinear diameters, the exponent $\alpha = 1$. Note that in Eq. 3.14 we have omitted corrections that are needed in order to capture the behaviour near the critical point, as we are unable to study this regime in the present chapter. Using T_c as calculated in the previous section, we determine the proportionality constant B, the exponent α and the critical density ρ_c by fitting the coexisting densities to this expression. In Figs. 3.6(a) and 3.7(a) we show that Eq. 3.14 can indeed accurately reproduce the behaviour of our out-of-equilibrium system as we vary the rotational diffusion rate and self-propulsion speed respectively.

Next, in Figs. 3.6(b-c) and 3.7(b-c) we plot the fitted parameters critical density ρ_c, exponent α and constant B. In Figs. 3.6(b) and 3.7(b) one can see that the critical density increases with decreasing rotational diffusion coefficient/increasing propulsion speed, indicating that higher densities are necessary in order to have coexistence when particles swim faster. Interestingly, we also find that the exponent α deviates substantially from unity as we drive the system away from equilibrium. Thus, sufficiently far from equilibrium the law of rectilinear diameters is clearly violated. Lastly, the parameter B also increases with decreasing rotational diffusion coefficient/increasing propulsion speed.

In addition, the three parameters ρ_c, α and B can be fitted again with a simple exponential of the form of Eq. 3.12 or 3.13, depending on whether the rotational diffusion or the propulsion speed is varied. The measured fits can be found in Tables 3.1 and 3.2. The fact that all fitting parameters $T_c, \beta, A, \rho_c, \alpha$ and B scale in a similar fashion in the active system is remarkable, and may suggest that a simple, comprehensive description of the phase transition is indeed possible for our model.

It is tempting to identify the aforementioned fitting parameters with the true critical point and the critical exponents of the system. However, currently we do not have enough evidence to establish the existence of a critical point for the active system, as we are unable to access the region close to the fitted critical point due to the small system sizes considered here. Also, we cannot be certain that the calculated power laws still hold in this region, and that the values of the critical temperature, the critical density and the exponents remain unchanged as one approaches the transition region. Hence, we cannot safely link the measured fitting parameters to the critical properties of the transition. Nonetheless, it is interesting to compare the equilibrium limit of the fits presented in Tables 3.1 and 3.2 (the equilibrium limit corresponds to the limits $D_r\tau \to \infty$ and $v_0\tau/\sigma \to 0$ respectively), with their equilibrium counterpart. We find that our estimations for the critical point and exponents are rough, yet reasonable. Specifically, we estimate the equilibrium critical point at $T_c = 1.066$ and $\rho_c\sigma^3 = 0.312$, while recent finite size scaling studies report $T_c = 1.187$ and $\rho_c\sigma^3 = 0.32$ [125, 126]. Moreover, we find for the exponent $\beta = 0.291$, while literature reads $\beta = 0.3285$ [116]. Also, even though the extrapolated equilibrium

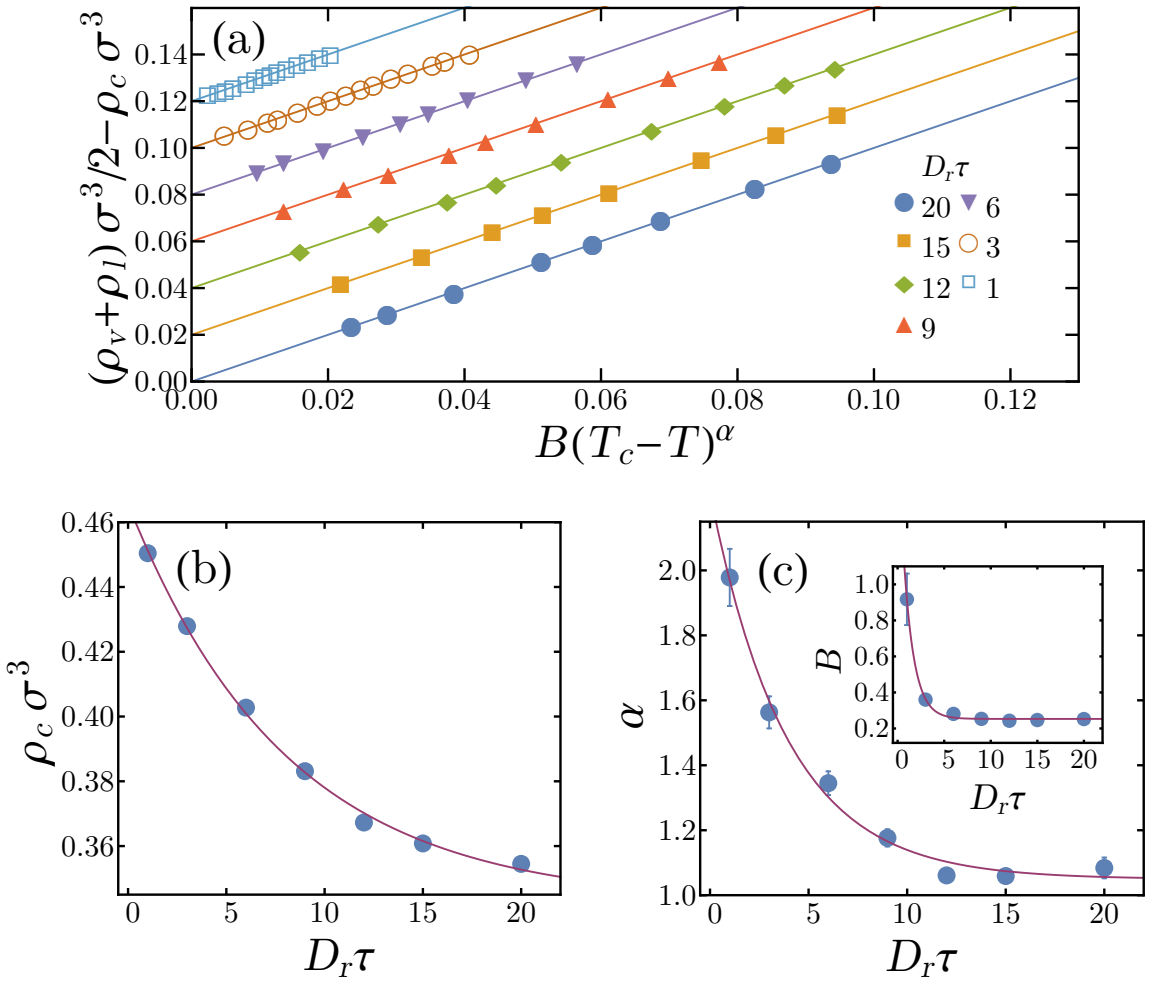

Figure 3.6: Distance of the average of the coexisting densities from the critical density $\frac{1}{2}(\rho_v + \rho_l) - \rho_c$ as a function of the scaled temperature for different rates of rotational diffusion and constant self-propulsion speed $v_0\tau/\sigma = 8$. Data points correspond to simulation results while the lines denote the fits of Eq. 3.14. Results for different rotational diffusion rates are offset for clarity. (b) Critical density ρ_c as a function of the rotational diffusion coefficient D_r. The continuous line shows the fit from Table 3.1. (c) Critical exponent α and constant B (inset) as a function of the rotational diffusion coefficient D_r. The continuous line shows the fit from Table 3.1.

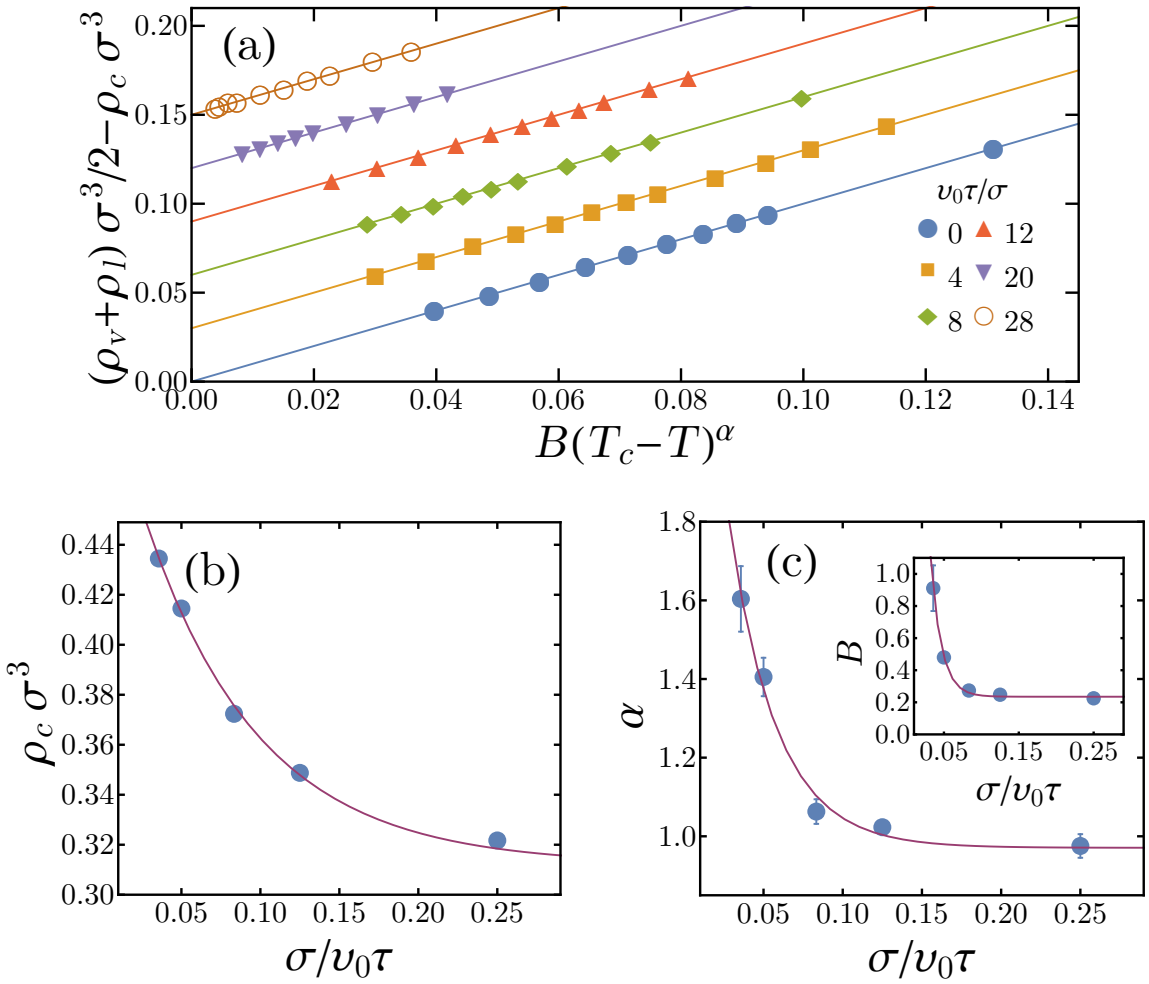

Figure 3.7: Distance of the average of the coexisting densities from the critical density $\frac{1}{2}(\rho_v + \rho_l) - \rho_c$ as a function of the scaled temperature for different propulsion speeds and constant rotational diffusion coefficient $D_r\tau = 20$. Data points correspond to simulation results while the lines denote the fits of Eq. 3.14. Results for different propulsion speeds are offset for clarity. (b) Critical density ρ_c as a function of the self-propulsion speed. The continuous line shows the fit from Table 3.2.(c) Critical exponent α and constant B (inset) as a function of the self-propulsion speed. The continuous line shows the fit from Table 3.2.

exponents α of Tables 3.1 and 3.2 are in reasonable agreement ($\alpha = 1.04$ and 0.971 respectively), there is a discrepancy between the values of the exponent β ($\beta = 0.237$ and 0.291).

3.3.5 Binodal lines and law of corresponding states

Finally, one can now combine Eqs. 3.11 and 3.14 in order to express the coexisting densities ρ_v and ρ_l as a function of the parameters $T_c, \beta, A, \rho_c, \alpha$ and B. In Fig. 3.3 we compare the binodals of the system from the directly measured coexisting densities to the fits for the aforementioned parameters (Tables 3.1 and 3.2). We find that the agreement between measurements and fits is excellent. We note that in Ref. [121] a percolating network state separated the fluid from the vapour-liquid coexistence region when the system was sufficiently far from equilibrium (see also Chapter 2). Consequently, this extra state may well result in a metastable critical point for our system. However, we have performed simulations at all the predicted critical temperatures and observed no signatures of a percolating state within the predicted coexistence regions.

Last but not least, we checked whether our system obeys a simple law of corresponding states. That is, whether the binodal lines fall on top of each other if one scales the temperature and the density with the corresponding quantities at the critical point. Such a collapse of the binodals can be made, for example, for various real substances [124], or for different cutoff radii of the equilibrium LJ fluid [120]. However, as shown in Fig. 3.8, the active LJ fluid obeys no such law of corresponding states for different values of rotational diffusion and self-propulsion. Naturally, the fact that the active LJ fluid does not obey this simplified law of corresponding states does not prove that it does not obey a more general Noro-Frenkel law of corresponding states, which compares the thermodynamic properties at the same reduced density and second virial coefficient. However, a more general test is out of the scope of the present work.

3.4 Conclusions

We studied a system of self-propelled spheres that interact *via* the Lennard-Jones potential using Brownian Dynamics simulations. We calculated equations of state for different temperatures and verified that, as the system transitions from a homogeneous to a phase separated state with decreasing temperature, the pressure curve as a function of density shows the expected transition from monotonic to non-monotonic. Moreover, we observed a linear growth of the swim pressure in the coexistence region.

Subsequently, we studied the phase coexistence regime using long box simulations. We showed that the scaling of the coexisting densities with temperature follows classic power laws. As mentioned in Section 3.3.4, the limitations of the present work do not allow for an identification of the fitting parameters of these power laws with the critical point and critical exponents of the system. Specifically, we have neither demonstrated explicitly that a critical point exists for the active system, nor that the calculated power laws coincide with the binodal lines close to the transition region. Nonetheless, the power

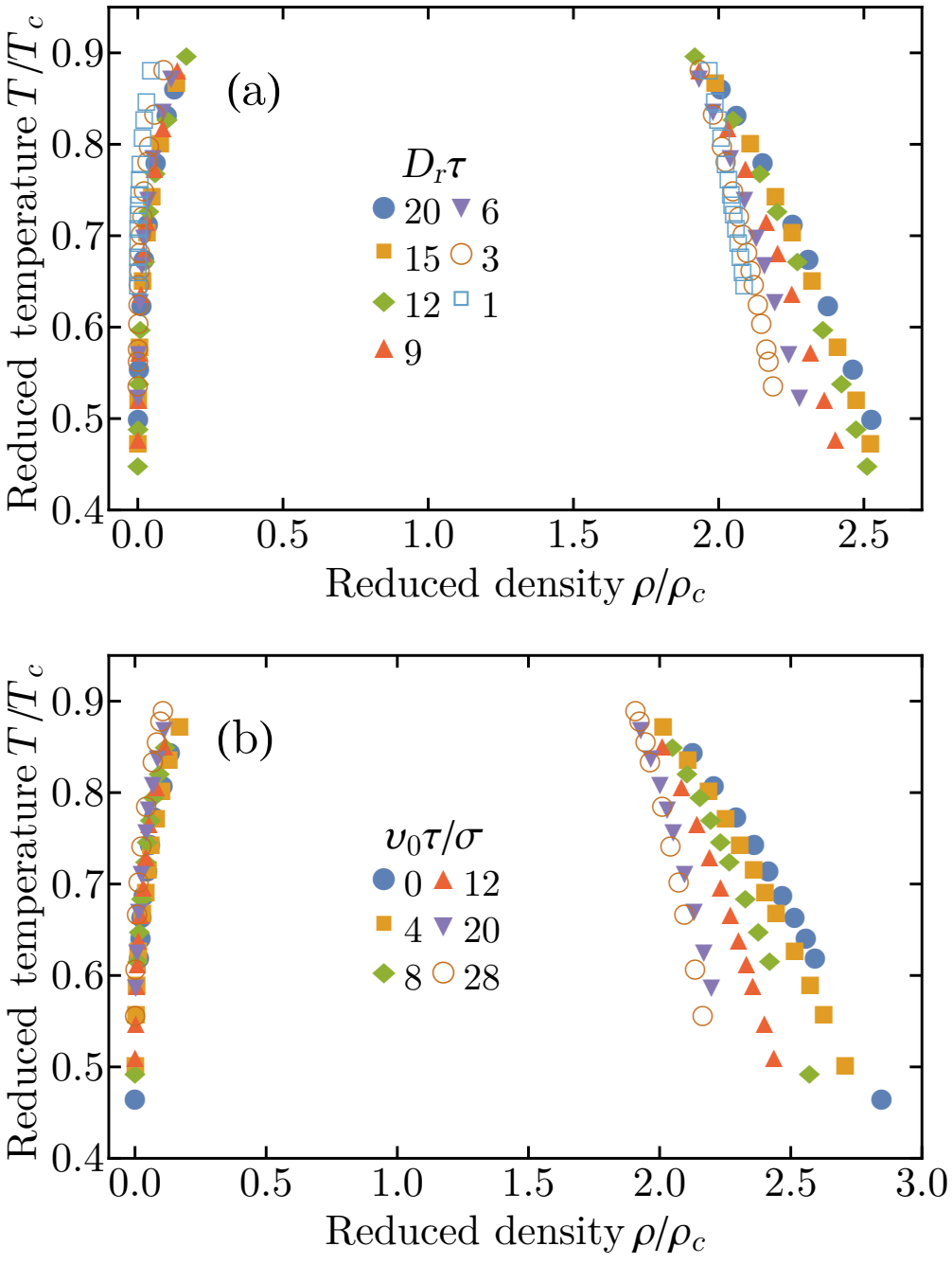

Figure 3.8: Reduced binodal lines of the active LJ system (a) for systems of different rotational diffusion rates and constant propulsion speed $v_0\tau/\sigma = 8$ and (b) for systems of different propulsion speeds and constant rotational diffusion coefficient $D_r\tau = 20$. Points correspond to directly observed coexisting densities, scaled by the fitted critical temperatures and densities.

laws we present describe extremely well the binodal envelope far away from the transition region and should provide guidance for future studies of the system.

Noticeably, we also showed that all the various parameters of the power laws vary with the propulsion speed or the rotational diffusion rate in a similar fashion, namely their scaling is well captured by simple exponential functions. These parameters include the critical temperature and density as well as the exponents of the power laws. Thus, a unified description of the binodal lines for both the passive and the active Lennard-Jones system may be within reach.

Acknowledgments

The results presented in this chapter are part of a collaboration with Siddharth Paliwal. Siddharth performed all the simulations for constant rotational diffusion coefficient and analysis of the corresponding results. We would also like to thank Robert Evans for useful discussions.

4

Vapour-liquid interfaces and surface tension of an active Lennard-Jones fluid

In this chapter we study a three-dimensional system of self-propelled Brownian particles interacting *via* the Lennard-Jones potential. Using Brownian Dynamics simulations in an elongated simulation box, we investigate gas-liquid phase coexistences of active Lennard-Jones particles with planar interfaces. We measure the normal and tangential component of the pressure tensor along the direction perpendicular to the interface and verify mechanical equilibrium of the two coexisting phases. In addition, we determine the non-equilibrium interfacial tension by integrating the difference of the normal and tangential component of the pressure tensor, and show that the surface tension as a function of activity is well-fitted by simple power laws. Finally, we measure the interfacial stiffness and find a simple linear relation between the surface tension and interfacial stiffness with a proportionality constant given by an effective temperature.

4.1 Introduction

In the last two chapters we have explored the self-assembly of attractive, self-propelled particles. Specifically, in Chapter 2 we presented state diagrams for systems of self-propelled and attractive particles and studied properties of the different states we found the system in, while in Chapter 3 we focused solely on the vapour-liquid transition of the system and studied the validity of various equilibrium scalings and laws for the out-of-equilibrium system. In the present chapter we perform a study of the same system and we focus again on the vapour-liquid regime of the phase diagram. However, here we examine the properties of the interface and demonstrate mechanical equilibrium of a system that has undergone phase separation between a dense liquid and a dilute gas. The present chapter can then naturally be seen as a continuation of Chapters 2 and 3. Also, in this chapter we will use for the first time the notion of a local pressure of active systems, a concept which we will use thoroughly in the rest of this thesis.

A working definition of pressure for systems of self-propelled particles has been a major topic of current research and many different approaches have been adopted in order to arrive at it. A popular approach assumes as a starting point the Fokker-Planck equation of a probability density and obtains the microscopic stress tensor through a continuum theory or by calculating the force exerted on a surrounding wall [89, 127]. Other approaches have utilized a virial route in order to define and calculate an expression for the bulk pressure [92, 122, 123], an expression which has been studied immensely for a variety of systems in recent literature [90, 91, 128–130]. Moreover, it has been shown that in order to write down an expression for the mechanical equilibrium of different parts of an active system, one needs to include extra contributions with respect to equilibrium systems due to the swim force [91, 130]. Solon and co-workers have shown that in the case of a contained system, surprisingly, pressure depends upon the exact interactions of the contents of the system with its confining walls, which naturally implies that pressure is generally not a state function in active systems [127].

Many of the studies in the literature of active systems, especially those that examine the notion of active pressure, consider soft repulsive or excluded volume interactions among the self-propelled particles [59, 90, 91, 122, 123, 127]. The reason for this specific choice of the model is that when such a system is in the far out-of-equilibrium regime of very fast self-propulsion speeds, a so-called motility-induced phase separation (MIPS) takes place, which is an intrinsically out-of-equilibrium and athermal phenomenon [61, 62, 74]. If the local pressure is calculated for a system that has undergone MIPS, mechanical equilibrium between the coexisting phases can be shown. However, a negative surface tension is present at the interface if the mechanical definition for the surface tension is considered [91]. A negative surface tension is of course impossible for equilibrium systems in phase coexistence as it directly implies that the system can minimize its free energy by maximizing the area of the interface, thus rendering the interface unstable [94]. The failure of standard equilibrium interpretations to explain this surprising result is a consequence of the out-of-equilibrium character of the transition and the so far incomplete understanding of the thermodynamics of active systems [93].

In this chapter we study a different active system that undergoes phase separation and test whether properties of the interface such as the surface tension and the stiffness

can still be defined or whether such definitions lead to unintuitive results, as in the case of MIPS. To this end, we use the model studied in the previous Chapters 2 and 3, that is a system comprised of self-propelled and Brownian particles that interact *via* the Lennard-Jones (LJ) potential. Many reasons justify the choice of the system. First of all, the passive counterpart of the model is well studied and properties of its phase transitions as well as values of associated thermodynamic quantities can be found in a large number of scientific articles [105, 106, 116, 119, 120]. Secondly, the computational efficiency of the model makes it very convenient and attractive for computer simulations. Furthermore, and perhaps more importantly, the system undergoes a vapour-liquid phase transition due to particle attractions for very low but also even high persistence lengths of the active motion of the particles, which correspond to both quasi-equilibrium and fairly out-of-equilibrium regimes, and forms stable interfaces between the coexisting phases (see Chapters 2 and 3). It is thus an ideal system to study the effect of self-propulsion on the properties of the phase transition and of the interface as one can slowly switch on the activity of the system, contrary to the case of MIPS.

The structure of this chapter is as follows. In Section 4.2.1 we describe the dynamics and model used in our numerical study along with the simulation setup. In Section 4.2.2 we present the expression we use in order to calculate the local pressure of the system. We then discuss the density and pressure profiles in Sections 4.3.1 and 4.3.2 respectively. We obtain the surface tension in Section 4.3.3 and perform fits to its scaling. Section 4.3.4 contains the calculation for the stiffness coefficient and a discussion on its relation to the surface tension measured in Section 4.3.3. Conclusions are given in Section 4.4.

4.2 Methods

4.2.1 Model and dynamics

The model used in this chapter is identical to the one used in Chapters 2 and 3. We will also present it here for completeness.

We consider a three-dimensional system consisting of self-propelled spherical particles (colloids) immersed in a molecular solvent, in a periodic box with dimensions L_x, L_y and L_z. The position of the center of mass of the i-th particle at time t is given by the vector $\boldsymbol{r}_i(t)$. With particle i, we associate a three-dimensional unit vector $\boldsymbol{u}_i(t)$ that indicates the direction of the self-propelling force. The particles interact with each other *via* a Lennard-Jones potential

$$U(r_{ij}) = 4\epsilon \left[\left(\frac{\sigma}{r_{ij}} \right)^{12} - \left(\frac{\sigma}{r_{ij}} \right)^{6} \right], \tag{4.1}$$

truncated and shifted at 2.5σ, where σ is the particle length scale, $r_{ij} = |\boldsymbol{r}_j - \boldsymbol{r}_i|$ and the parameter ϵ controls the strength of the interaction.

To describe the translational and rotational motion of the individual colloidal particles inside the solvent we use the overdamped Langevin equations

$$\frac{d\boldsymbol{r}_i}{dt} = -\frac{1}{\eta}\sum_{j\neq i}\frac{\partial U(r_{ij})}{\partial \boldsymbol{r}_i} + \upsilon_0 \boldsymbol{u}_i + \sqrt{2D_{tr}}\boldsymbol{\xi}_i^{tr}, \tag{4.2}$$

$$\frac{d\boldsymbol{u}_i}{dt} = \sqrt{2D_r}\,(\boldsymbol{u}_i \times \boldsymbol{\xi}_i^{r})\,. \tag{4.3}$$

Note that after each iteration of Eq. 4.3 we normalize the unit vectors $\boldsymbol{u}$ in order to prevent their drift. The translational diffusion coefficient is given by the Einstein-Smoluchowski relation $D_{tr} = 1/(\beta_s \eta)$, with η the damping coefficient and $\beta_s = 1/k_B T_s$ the inverse temperature of the surrounding solvent with k_B the Boltzmann coefficient and T_s the temperature of the surrounding solvent. D_r denotes the rotational diffusion coefficient and υ_0 the propulsion speed. The vectors $\boldsymbol{\xi}_i^{tr}$ and $\boldsymbol{\xi}_i^{r}$ are unit-variance random vectors, with mean value and variation

$$\langle \boldsymbol{\xi}_i^{tr,r}(t)\rangle = 0, \tag{4.4}$$

$$\langle \boldsymbol{\xi}_i^{tr,r}(t)\boldsymbol{\xi}_j^{tr,r}(t')\rangle = \mathbb{I}_3\,\delta_{ij}\,\delta(t-t'), \tag{4.5}$$

where $\mathbb{I}_3$ is the unit matrix in three dimensions. Lengths are given in units of σ, time in units of $\tau = \sigma^2/D_{tr}$, and energy in units of $1/\beta_s$. We also denote $T = 1/\beta_s\epsilon$ as the dimensionless temperature of our system. This notation is adopted as it facilitates direct comparison to a passive LJ system. Throughout this chapter we choose the simulation parameters such that the system is always in the region of the phase diagram where a gas coexists with a liquid. The density of the system has been kept fixed for all simulations at $\rho\sigma^3 = 0.1333$.

We implemented the aforementioned equations of motion (Eqs. 4.2 and 4.3) using an Euler-Maruyama integration scheme [107]. A maximum time step of $dt = 2 \times 10^{-5}\tau$ was used for the numeric integration of the equations of motion. For our simulations we used the steady state particle configurations obtained in Chapter 3. Thus, the number of particles in our simulations was approximately $N = 2500$ and the dimensions of the simulation box are $L \times L \times 6L$ in all simulations except the ones presented in Section 4.3.4. Periodic boundary conditions in all three dimensions are always applied. For each set of simulation parameters, we let the simulations run and collect data for 300τ. We also fix the center of mass of the system at the origin of the z-axis in order to prevent the drift of the liquid slab that coexists with the gas by regularly shifting the coordinates of the particles at fixed time intervals.

4.2.2 Local pressure

We use the definition of the local pressure of the system derived in Ref. [127] (see also the discussion in Appendix A).

For the purpose of our simulations, we always assume a slab geometry with the long axis of the simulation box being along the z dimension, such that the $\hat{z}$ axis is normal to all interfaces and the system is isotropic in the xy plane. In order to write down an

expression for the diagonal components of the local pressure, first we define the moments

$$\rho(\boldsymbol{r}) = \sum_{k=1}^{N} \delta(\boldsymbol{r} - \boldsymbol{r}_k), \tag{4.6}$$

$$\boldsymbol{m}_i(\boldsymbol{r}) = \sum_{k=1}^{N} \boldsymbol{u}_{k,i}\delta(\boldsymbol{r} - \boldsymbol{r}_k), \tag{4.7}$$

$$\boldsymbol{s}_{ij}(\boldsymbol{r}) = \sum_{k=1}^{N} \boldsymbol{u}_{k,i}\boldsymbol{u}_{k,j}\delta(\boldsymbol{r} - \boldsymbol{r}_k), \tag{4.8}$$

where i, j denote the spatial components of the corresponding vectors and tensors. $\rho(\boldsymbol{r})$ is the local density of particles while $\boldsymbol{m}(\boldsymbol{r})$ is the corresponding local polarization. The diagonal ii-th component of the local pressure tensor $P_{ii}(z)$ can then be calculated using the equation

$$P_{ii}(z) = P_{\text{ideal},ii}(z) + P_{\text{virial},ii}(z) + P_{\text{swim},ii}(z), \tag{4.9}$$

where

$$P_{\text{ideal},ii}(z) = \langle\rho(z)\rangle\, k_B T_s = \frac{k_B T_s}{L_x L_y} \int dx \int dy \, \langle\rho(\boldsymbol{r})\rangle \,, \tag{4.10}$$

is the ideal component of the pressure, where we have spatially integrated over the dimensions that are perpendicular to the $\hat{z}$ dimension and divided by the surface $L_x L_y$ that we integrated over, and brackets denote an average at the steady state over noise realizations,

$$P_{\text{virial},ii}(z) = \frac{1}{L_x L_y} \int dx \int dy \int_{\boldsymbol{r}_i'' < \boldsymbol{r}_i} d\boldsymbol{r}_i'' \int d\boldsymbol{r}' \, \langle\rho(\boldsymbol{r}'')\rho(\boldsymbol{r}')\rangle \, \partial_{\boldsymbol{r}_i''} U(|\boldsymbol{r}' - \boldsymbol{r}''|), \tag{4.11}$$

is the standard local virial term, where the vector $\boldsymbol{r}''$ has the same components as the vector $\boldsymbol{r}$ except for the i-th component, and

$$P_{\text{swim},ii}(z) = \frac{\eta \upsilon_0}{(d-1)D_r} \frac{1}{L_x L_y} \int dx \int dy \Bigg[-\frac{1}{\eta} \int d\boldsymbol{r}' \partial_{\boldsymbol{r}_i} U(|\boldsymbol{r}' - \boldsymbol{r}|) \, \langle \boldsymbol{m}_i(\boldsymbol{r})\rho(\boldsymbol{r}')\rangle + \upsilon_0 \, \langle \boldsymbol{s}_{ii}(\boldsymbol{r})\rangle - D_{tr}\partial_i \, \langle \boldsymbol{m}_i(\boldsymbol{r})\rangle \Bigg] \tag{4.12}$$

is the local swim pressure.

In our particle simulations, we divide the simulation box into slabs and measure the different local quantities Eqs. 4.6-4.12 for each slab. The contributions to each slab of the ideal and swim components of the pressure can be calculated straightforwardly, while for the virial component we use Ref. [131].

Herein we refer to the diagonal elements of the pressure tensor with respect to the dimension spanned by the vapour-liquid interface. In this light, we denote $P_N(z) = P_{zz}(z)$ the normal component along the direction perpendicular to the vapor-liquid interface (z-direction) and $P_T(z) = (P_{xx}(z) + P_{yy}(z))/2$ the tangential component as the average of the x and y components due to the symmetry of the system in the xy plane. The non-diagonal components in the pressure tensor vanish due to hydrostatic equilibrium, which we have also verified by directly measuring them in our simulations.

4.3 Results

4.3.1 Density and orientation profiles

As a starting point of our study of the phase separated system, we measure the local density $\rho(z)$ across the simulation box. A similar investigation was presented in Chapter 3, but we will repeat it here for the sake of completeness. A typical snapshot of a phase separated system is shown in Fig. 4.1(a), and the measured density profile is shown in Fig. 4.1(b). We find that the density profiles are similar to equilibrium profiles and can be well fitted to a hyperbolic tangent function:

$$\rho(z) = \frac{1}{2}\left(\rho_l + \rho_v\right) - \frac{1}{2}\left(\rho_l - \rho_v\right)\tanh\left[\frac{2(z - z_0)}{D}\right], \tag{4.13}$$

where ρ_l and ρ_v are the corresponding bulk liquid and vapor densities, z_0 is the location of the plane satisfying an equal area construction and D represents the thickness of the interface. We fit the above equation to the right and left half of the box ($z > 0$ and $z < 0$) separately using z_0 and D as fitting parameters and obtain the bulk densities ρ_l and ρ_v from the mean of the two fits.

In Fig. 4.1(c) we plot the local average orientation of particles $\boldsymbol{u}(z) = \langle \boldsymbol{m}(z) \rangle \,/\, \langle \rho(z) \rangle$. It is evident that the particles tend to orient themselves along the normal direction at the interfaces, and the peak of the orientation profile does not coincide with the estimated position of the interface z_0 (dotted lines). On average, the particles tend to orient themselves with the direction of self-propulsion towards the less-dense (vapor) phase. This asymmetry in the average orientation is easily explained by assuming a zero net velocity at the interface: particles at the interface that point towards the dense phase have a larger average velocity than particles that point towards the dilute phase due to the net attractive force towards the liquid. Thus, more particles need to point outwards in order to balance the asymmetry in velocities. It is also important to note that this preferential ordering is only along the normal (z) direction. There is no net orientation along the tangential plane (xy) as the system is isotropic in this plane. We note that in the case of MIPS, where the activity drives the phase separation, the orientations tend to be exactly reverse, with the preferred orientation of particles at the interfaces being towards the denser phase.

We also find that at fixed activity, which for our system translates to fixed self-propulsion speed and rotational diffusion coefficient, the shape of the orientation profile along the interface as well as the interfacial width D becomes broader upon increasing T, or equivalently upon decreasing the strength of attraction between particles. The broadening of the interface as the system moves towards its "critical point" is completely analogous to what is observed in the passive LJ system [106]. Also, at fixed temperature T, the interfacial region becomes broader as the activity increases. This observation is compatible with the results of Chapters 2 and 3, which show that higher attraction strength is needed to induce phase separation upon increasing activity, which can be seen for example in the shifting of the binodal lines shown in Chapter 3 and also in other studies [32, 88, 104].

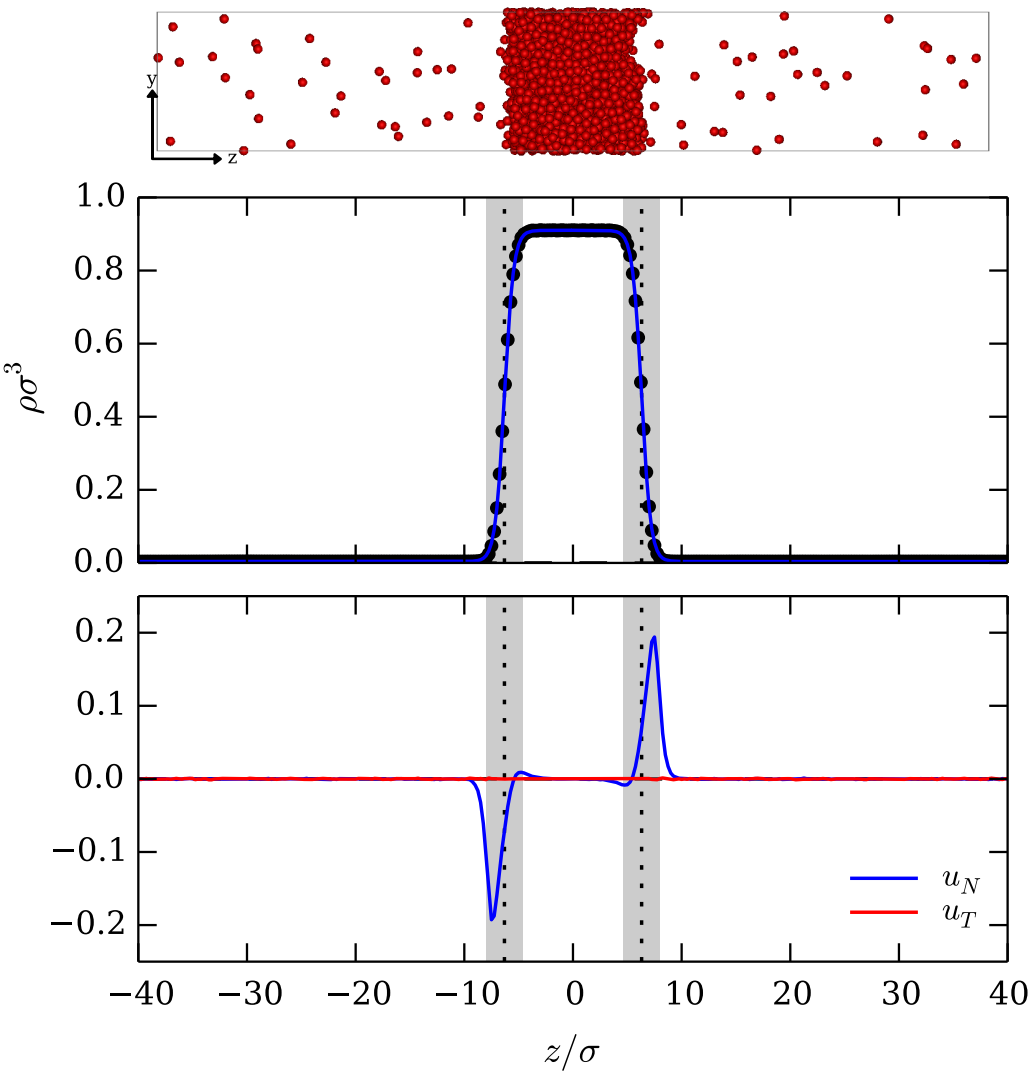

Figure 4.1: (a) A snapshot of a yz projection of the simulation box showing a system in its steady state, where a liquid and a gas coexist. The dense liquid slab is in the middle of the box and two planar interfaces separate it from the vapour phase on each side. (b) Local density profile. Data points correspond to simulation measurements and the continuous line is the fit of Eq. 4.13. Dotted lines indicate the location z_0 of the interface according to Eq. 4.13 and the shaded area shows the interfacial region $(z_0 - D/2, z_0 + D/2)$. (c) Profile of the components of the orientation vector $\boldsymbol{u}(z) = \langle \boldsymbol{m}(z) \rangle \,/\, \langle \rho(z) \rangle$ ($u_N = u_z$ and $u_T = (u_x + u_y)/2$). The simulation parameters for the system shown in this figure are $v_0 \tau \sigma^{-1} = 28, T = 0.2$, $D_r \tau = 20$.

4.3.2 Pressure profiles

We now calculate the normal and tangential components of the terms that contribute to the local pressure, Eqs. 4.10-4.12, for our phase separated systems. Figure 4.2 shows typical profiles of the different components. Below we discuss the various contributions as well as the total pressure profile separately.

In passive systems, mechanical equilibrium requires a constant normal component of the total pressure, which simply consists of the ideal and virial contributions. However, a net imbalance of the interaction forces along the tangential plane causes the tangential component of the pressure to be smaller on average than the normal component along the interfacial region. This inequality of the pressure components at the interface leads to the surface tension [132, 133]. In the case of our active system, Fig. 4.2(a) shows that the normal component of the sum of the ideal and the virial pressure is not constant across the system and that the liquid has a smaller bulk pressure than the gas. Thus, mechanical equilibrium is not established simply by considering the virial and the ideal components of the pressure. Moreover, the tangential component is also not equal at the bulk of the two coexisting phases, though it is reassuringly equal to the normal component in the bulk. It is also smaller on average than the normal component of the pressure along the interface, similar to the passive case. Note that the behaviour of the sum of the ideal and the virial components of the pressure is inversed with respect to their respective profiles in the case of MIPS [91]; in that case the ideal and virial component are higher in the dense phase than in the dilute one.

The swim pressure, as we see in Fig. 4.2(b), is also not equal in the two phases for both the normal and tangential components. Its magnitude is larger in the liquid phase than the gas phase where it is essentially zero. Also, both components show peaks along the interfaces. Again, the pressure profile is inversed with respect to the case of MIPS; the swim pressure in that case is higher in the dilute phase than in the dense one [91].

In Fig. 4.2(c) we show the total pressure, that is the sum of the ideal, the virial and the swim pressure. Reassuringly, the normal component now becomes constant throughout the system, as it is required for mechanical equilibrium. We would like to emphasize here that the gradient term of the form $\partial_i \boldsymbol{m}_i$ in the swim pressure, Eq. 4.12, needs to be included in the total pressure to obtain a perfectly flat normal component at the interface. This term is obviously zero in the bulk of the system but its magnitude along the interface is increased as the activity of the system is increased. The tangential component of the total pressure is also equal in the two bulks but has negative peaks at the interfaces. This is again similar to the case of equilibrium systems and leads to a positive surface tension, as we discuss in Section 4.3.3. In the case of MIPS the total pressure profiles are again reversed in the y-axis with respect to the ones shown in Fig. 4.2(c) [91]. The tangential component in that case has positive peaks which translate into a negative surface tension of the interface.

4.3.3 Surface tension

In the case of equilibrium fluids, the surface tension γ of an interface that separates two coexisting bulk phases can be defined in various ways [134]. The surface tension can be

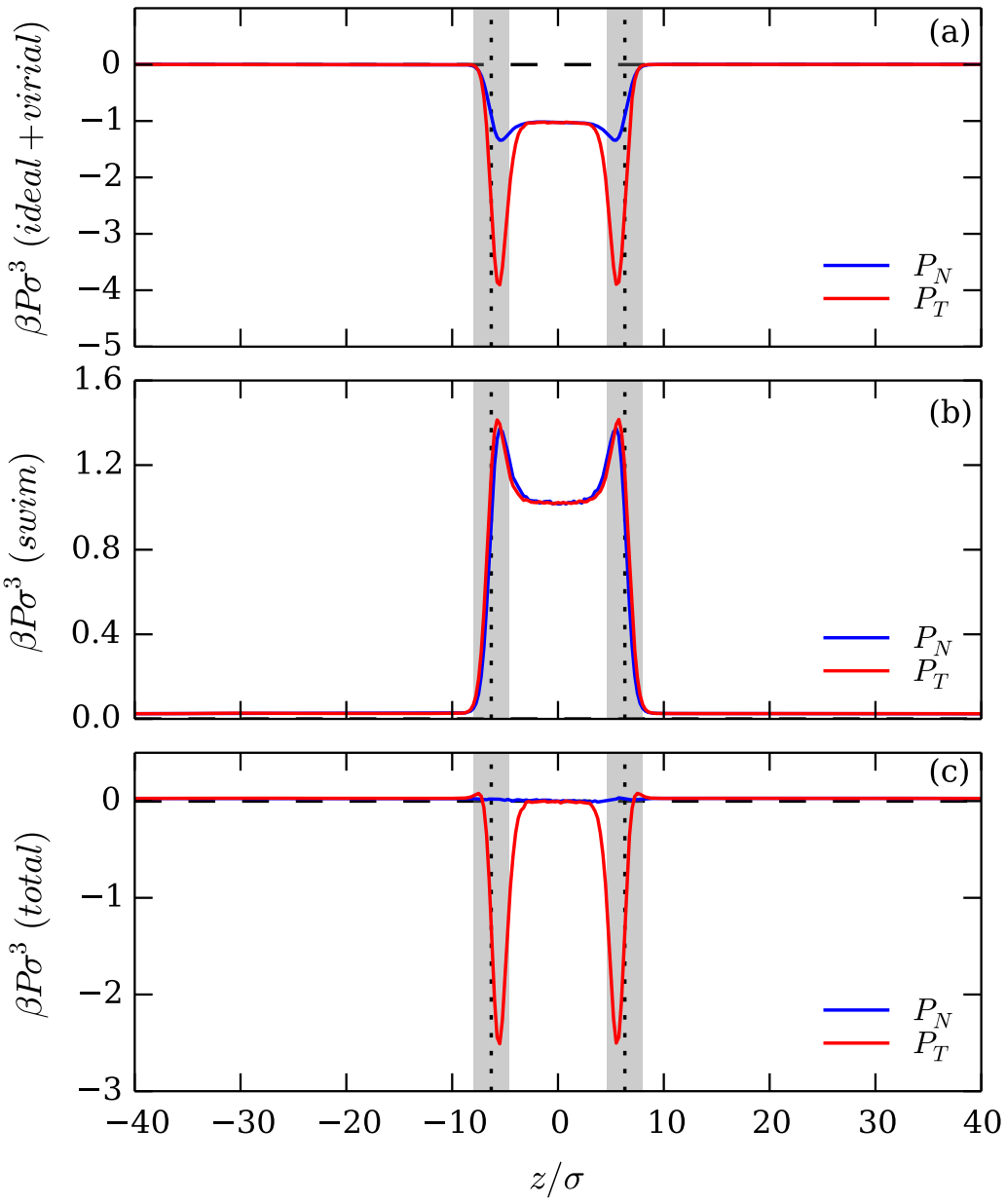

Figure 4.2: Normal and tangential components of (a) the ideal (Eq. 4.10) plus the virial pressure (Eq. 4.11), (b) the swim pressure (Eq. 4.12), and (c) the total pressure (Eq. 4.9). The normal component is constant throughout the system, indicating mechanical equilibrium. The tangential component has negative peaks at the two interfaces due to the surface tension. Similarly to Fig. 4.1 dotted lines indicate the location z_0 of the interface according to Eq. 4.13 and the shaded area shows the interfacial region $(z_0 - D/2, z_0 + D/2)$. The simulation parameters are the same as in Fig. 4.1.

defined thermodynamically as the difference in grand potential between a phase-separated system with an interface and a homogeneous bulk system, which are both at the same coexisting bulk chemical potential divided by the surface area of the interface. Using this definition, the gas-liquid interfacial tension can be determined in simulations by measuring the grand canonical probability distribution function of observing N particles in a volume V at fixed chemical potential μ and temperature T. This probability distribution function can be measured very accurately using successive umbrella sampling in grand canonical Monte Carlo simulations [135]. Using the histogram reweighing technique, one can then determine the chemical potential corresponding to bulk coexistence using the equal area rule for the gas and liquid peak [134, 135]. The interfacial tension can be determined from the difference in the maximum of the peaks and the minimum [136–138]. Alternatively, one can also determine the surface tension by measuring the width of the interface, which is determined by an intrinsic width and a broadening due to capillary wave fluctuations. Using the equipartition theorem, one can relate the mean-square fluctuations due to capillary waves to the interfacial tension, and hence the interfacial tension can be determined by measuring the capillary wave broadening [134, 139–142] . It is important to note that the method of determining the interfacial tension from the probability distribution is based on grand canonical Monte Carlo simulations, and relies on knowledge of the statistical weight corresponding to the grand canonical ensemble. The second method employs the equipartition theorem, which is derived by assuming a Boltzmann distribution. Finally, the interfacial tension can be defined as the mechanical work required to enlarge the interface. Using the condition of hydrostatic equilibrium, the surface tension can be defined as the integral of the difference of the two pressure tensor components

$$\gamma = \frac{1}{2}\int_{-L_z/2}^{L_z/2} \left[P_N(z) - P_T(z)\right] dz, \tag{4.14}$$

where we assume that the system is only inhomogeneous in the z-direction with the two planar interfaces parallel to the xy-plane. The factor $\frac{1}{2}$ comes from the presence of two interfaces in a simulation with periodic boundary conditions. For equilibrium fluids, all these definitions for the interfacial tension coincide. In the case of non-equilibrium systems such as the active LJ system, the statistical weights of the different ensembles are unknown, which precludes the use of Monte Carlo simulations for determining the interfacial tension from a probability distribution function. We therefore resort to the mechanical definition of the surface tension by employing Eq. 4.14. In addition, in Section 4.3.4 we measure the interfacial width in Brownian dynamics simulations, and naively assume the equipartition theorem to hold even though it is based on a statistical ensemble average.

Following Ref. [91], in this section we determine the surface tension using the mechanical route (Eq. 4.14), where we also include the contribution from the swim pressure in the total pressure in order to satisfy the hydrostatic equilibrium condition. Note that the gradient term of the form $\partial_\alpha \boldsymbol{m}_\alpha$ in the swim pressure (Eq. 4.12), which is essential in order to obtain a flat profile of the normal pressure component across the interface, does not contribute to the surface tension. Using Eq. 4.14 and the total pressure profiles as shown in Fig. 4.2(c) we determine the surface tension γ for a wide range of parameters of the active system following two paths that drive the system out of equilibrium. To

this end, we either increased the self-propulsion speed at fixed rate of rotational diffusion ($D_r\tau = 20$) or we decreased the rotational diffusion coefficient at fixed self-propulsion speed ($v_0\tau\sigma^{-1} = 8$). For the first path, the high value of the rotational diffusion coefficient was chosen as such in order to minimize the area of the percolating state regime in the state diagram (see Chapter 2). Note that the equilibrium limits of these two paths are not equivalent as the $D_r \to \infty$ limit does not coincide with the $v_0 \to 0$ limit. The second limit corresponds to the equilibrium LJ system with temperature $T = 1/\beta_s\epsilon$ while the first limit corresponds to a passive system with a higher effective temperature. The systems we examine have a Péclet number in the range $0 - 8$, where the Péclet number is defined as $Pe = v_0/D_r\sigma$, so that we probe the equilibrium limit as well as systems where self-propulsion plays a much more important role in the dynamics than translational diffusion. However, in all cases we are well below the onset of MIPS ($Pe \sim 50$ [62]).

The results of the measurements of the surface tension are shown in Figs. 4.3(a) and 4.4(a) for constant rotational diffusion coefficient and constant speed of self-propulsion respectively. Note that we always measure a positive surface tension, contrary to the case of MIPS [91] and the magnitude of the surface tension is in the same range as in the equilibrium system (~ 1) [106]. Also, as the temperature is increased, that is as the attraction between particles is weakened, the surface tension assumes smaller values, similarly to the equilibrium scenario.

Next, we examine the scaling of the surface tension γ with the temperature T as the system departs from the equilibrium regime and the activity is increased. It is known that in the equilibrium system γ scales with temperature as:

$$\gamma = A(1 - T/T_c)^c, \tag{4.15}$$

where A is a constant and T_c is the critical temperature of the system. The exponent c is related to the critical exponent of the correlation length of the system ν, where for equilibrium systems $\nu = 0.63$ [116], such that $c = 2\nu$. Here, we examine whether the surface tension for our active system follows a scaling with temperature similar to Eq. 4.15 and treat A, T_c and the exponent c as fit parameters.

In Figs. 4.3(a) and 4.4(a) we plot the resulting fits and find that they fit well to the measured data in the examined parameter space. We thus find that the scaling of the surface tension with temperature can be captured *via* Eq. 4.15 even for the active system. Note that these fits also give us an estimate for the critical temperature of the system in the limit $\gamma = 0$ for different degrees of activity.

Similar to Chapter 3, we now examine the scaling of the fit parameters A, T_c and c with the strength of activity. The results are plotted in Figs. 4.3(b), 4.3(c), 4.4(b) and 4.4(c). We find that for constant rotational diffusion coefficient, as the propulsion speed is increased and the system departs from equilibrium, the value of the exponent c as well as the critical temperature of the system T_c decrease as well, while the parameter A increases. The exponent c moves away from its equilibrium value ($c = 1.21 - 1.26$ [106, 143]) to values less than unity. The scaling of the critical temperature with the propulsion force is in accordance to the findings of Chapter 3. Furthermore, in Fig. 4.3(c) we also plot the critical temperature as found from the scaling of the order parameter $\Delta\rho = \rho_l - \rho_v$ (see Chapter 3). We find that the two values of the critical temperature as

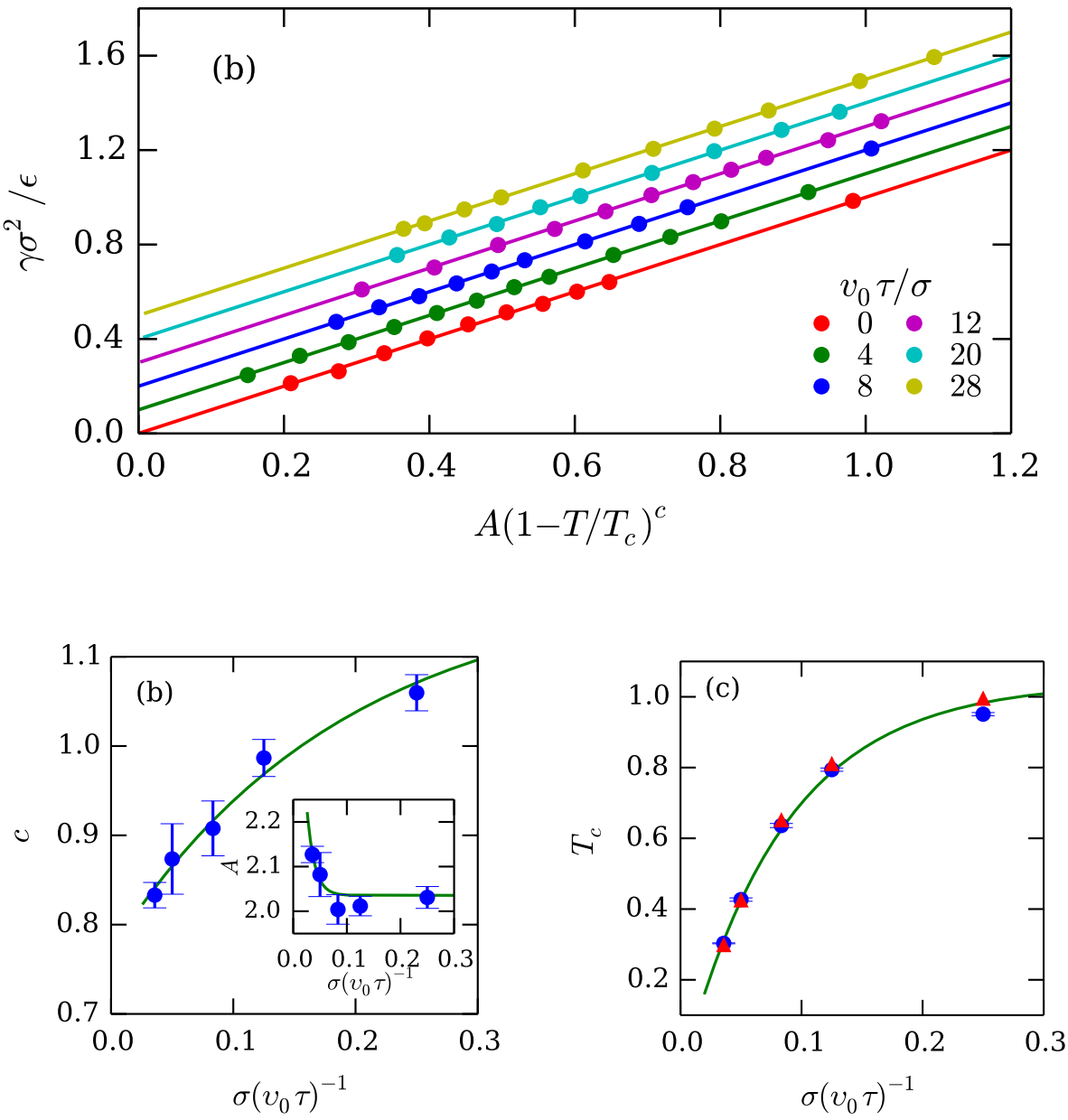

Figure 4.3: (a) Surface tension as a function of the temperature for systems of different self-propulsion speeds and constant rotational diffusion coefficient $D_r\tau = 20$. Data points correspond to simulation results while the lines denote the fits (Eq. 4.15). Note that data points and fits are offset for clarity. (b) Exponent c and constant A (inset) as a function of the propulsion speed. The continuous lines show the fits from Table 4.1. (c) Critical temperature T_c as a function of the propulsion speed obtained from the scaling of the surface tension Eq. 4.15 (blue circles ●) and from the scaling of the order parameter (red triangles ▲, see Chapter 3). The continuous line shows the fit from Table 4.1. Error bars in (b) and (c) are the standard errors from fitting.

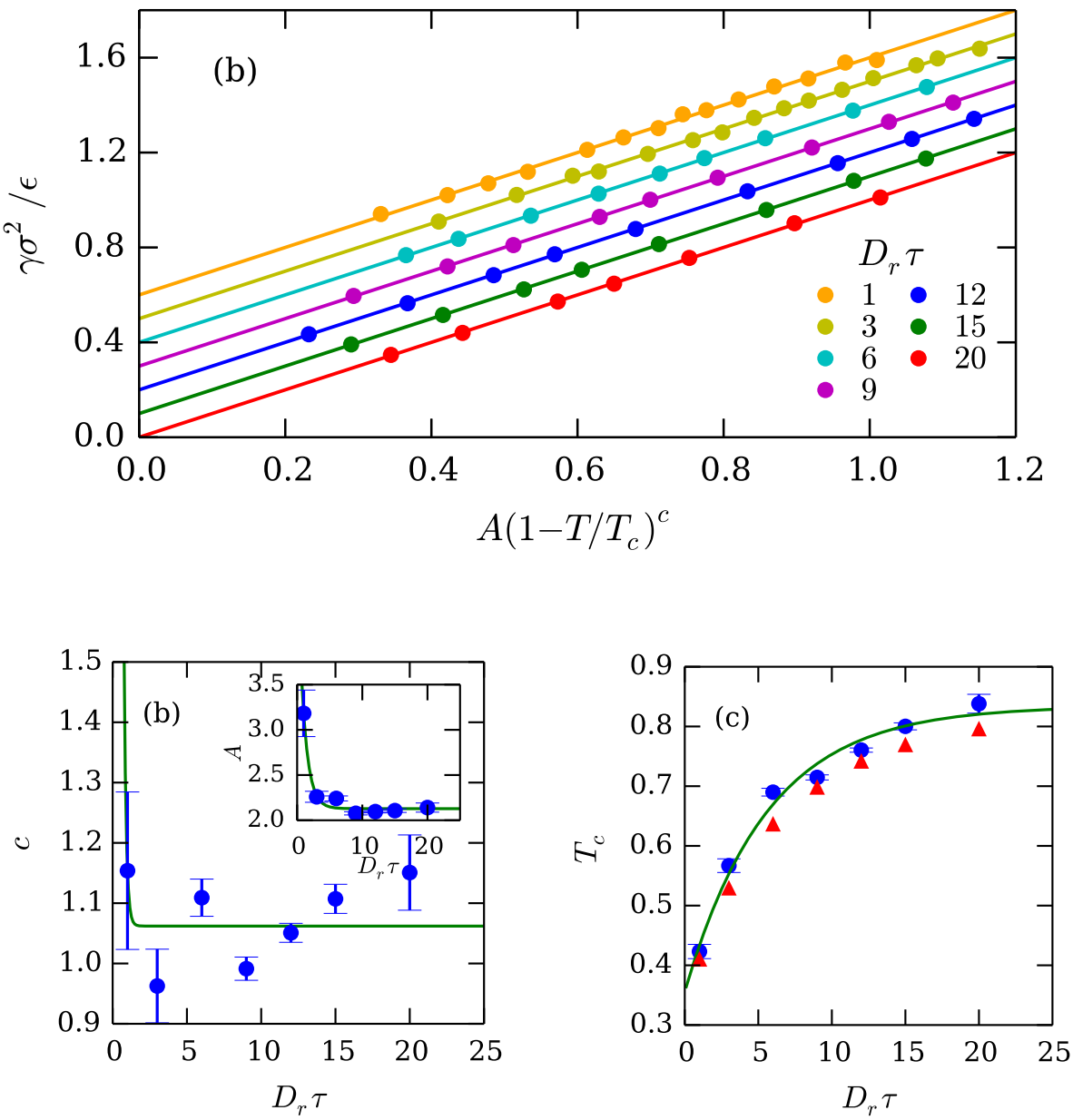

Figure 4.4: (a) Surface tension as a function of the temperature for systems of different rotational diffusion rates and constant propulsion speed $v_0\tau\sigma^{-1} = 8$. Data points correspond to simulation results while the lines denote the fits (Eq. 4.15). Note that data points and fits are offset for clarity. (b) Exponent c and constant A (inset) as a function of the rotational diffusion coefficient. The continuous lines show the fits from Table 4.2. (c) Critical temperature T_c as a function of the rotational diffusion coefficient obtained from the scaling of the surface tension Eq. 4.15 (blue circles •) and from the scaling of the order parameter (red triangles ▲, see Chapter 3). The continuous line shows the fit from Table 4.2. Error bars in (b) and (c) are the standard errors from fitting.

evaluated from the two different routes (*via* the scaling of the order parameter and the scaling of the surface tension with temperature) are very close to each other. Moreover, for constant propulsion force and varying rotational diffusion coefficient, we find scalings for the three parameters A, T_c and c in accordance to the case of varying propulsion force. That is, as the rotational diffusion coefficient is decreased and the system moves further out of equilibrium, c and T_c decrease, while A increases. However, the exponent c appears to increase again for very low values of the rotational diffusion coefficient (Fig. 4.4(b)). Unfortunately, large error bars in the fits for this regime prevent us from making definite conclusions on the dependence of the exponent c on the activity of the system for high Péclet numbers. Lastly, note that the agreement between the values of the critical temperature as obtained from the scaling of the order parameter and the scaling of the surface tension is not as good as in the case of constant propulsion speed (Fig. 4.4(c)). Nonetheless, the two values are still close to one another and follow a similar scaling.

Similar to our previous work in Chapter 3, in Fig. 4.3(b)-(c) and Fig. 4.4(b)-(c) we show empirical fits for the dependence of the parameters A, c and T_c on the propulsion speed v_0 and the rotational diffusion coefficient D_r respectively. All three parameters are fitted *via* simple exponential scalings, namely

$$A(v_0), c(v_0), T_c(v_0) = \quad a_1 e^{-a_2 \sigma / v_0 \tau} + a_3 \tag{4.16}$$

$$A(D_r), c(D_r), T_c(D_r) = \quad b_1 e^{-b_2 D_r \tau} + b_3, \tag{4.17}$$

where a_1, a_2, a_3 and b_1, b_2, b_3 are again fit parameters. These fits capture the scaling of the critical temperature T_c and the parameter A (Figs. 4.3(b)-(c) and 4.4(b)-(c)) for varying propulsion speed v_0 (Eq. 4.16) and rotational diffusion coefficient D_r (Eq. 4.17) as well as the scaling of the exponent c for the case of varying propulsion speed (Fig. 4.3(b)). The fit for c obviously fails for varying rotational diffusion coefficient (Fig. 4.4(b)), but we still present it for consistency. The fit parameters are given in Table 4.1 and 4.2 for varying self-propulsion speeds and rotational diffusion coefficient respectively. Similar to the findings in Chapter 3, the two separate paths cannot be collapsed *via* the Péclet number.

Before closing this section, let us comment on the applicability of the language of critical phenomena to the results that we presented in this section. Note that so far we have not demonstrated the existence of a critical point and we also have not probed the region close to a possible critical point, due to the small system sizes that we consider here. See also the relevant discussion in Chapter 3. Consequently, we cannot be certain that the power law Eq. 4.15 still holds as the system approaches its possible critical point. It also follows that the values of the fitted critical temperature T_c and exponent c should not necessarily remain unchanged in the critical region. Nonetheless, it is instructive to compare the equilibrium limit of our measurements to their known equilibrium values, with the equilibrium limit corresponding to the limits $v_0\tau/\sigma \to 0$ and $D_r\tau \to \infty$ for the results presented in Tables 4.1 and 4.2 respectively. We find that, similarly to Chapter 3, our estimations for the critical temperature and exponent are rough, yet reasonable; we estimate the equilibrium $T_c = 1.041$, while recent finite size scaling studies report $T_c = 1.187$ [125]. Furthermore, we find the exponent $c = 1.181$ and 1.1062, while literature reads $c = 1.21 - 1.26$ [106, 143].

Table 4.1: Fitting parameters a_1, a_2, a_3 of Eq. 4.16 to the parameters A, c, T_c of Eqs. 4.15 for systems of different propulsion speeds and constant rotational diffusion rate $D_r\tau = 20$. The column T_c^1 shows the corresponding values for the critical temperature obtained in Chapter 3.

	A	c	T_c	T_c^1
a_1	1.159	-0.410	-1.113	-0.184
a_2	70.01	5.257	11.810	12.33
a_3	2.035	1.181	1.041	1.066

Table 4.2: Fitting parameters b_1, b_2, b_3 of Eq. 4.17 to the parameters A, c, T_c of Eqs. 4.15 for systems of different rotational diffusion rates and constant propulsion speed $v_0\tau\sigma^{-1} = 8.0$. The column T_c^1 shows the corresponding values for the critical temperature obtained in Chapter 3.

	A	c	T_c	T_c^1
b_1	2.840	109.99	-0.478	-0.470
b_2	0.993	7.095	0.178	0.156
b_3	2.128	1.062	0.834	0.818

4.3.4 Interfacial fluctuations and stiffness

In this section we study the scaling of the interfacial width as a function of the area of the interface, which will allow us to measure the stiffness of the interface. Subsequently we attempt to connect the estimated value for the stiffness to the values of the surface tension obtained in Section 4.3.3.

For equilibrium systems capillary wave theory provides a connection between the fluctuations of an interface, its stiffness coefficient, and subsequently its surface tension [139–142]. Capillary wave theory [144] describes the broadening of an intrinsic interface of width w_0 due to thermal fluctuations. The capillary wave broadening depends primarily on the interfacial tension and the area of the interface, and can be calculated by using equipartition theorem and summing over the mean-square fluctuations of all allowed excitation modes of the interface. We refer the reader to Refs. [139, 140] for more details, and present here only the result. According to capillary wave theory [139, 140] the total interfacial width w can be written as the sum of an intrinsic part w_0 and a contribution due to capillary wave fluctuations

$$w^2 = w_0^2 + \frac{1}{\kappa} \ln\left(\frac{L}{B_0}\right), \tag{4.18}$$

where w_0 and B_0 are constants and κ is the stiffness coefficient, which parametrizes the energy penalty for deformations of the interface with dimensions $L \times L$. Equation 4.18 implies that the width of an interface is determined by an intrinsic contribution w_0 that depends only on intensive variables and a term that explicitly depends on the area of the

interface. For equilibrium systems, the stiffness coefficient of an interface that separates two fluids is related to the surface tension *via* the simple relation $\gamma = k_B T_s \kappa$.

First, we test the applicability of Eq. 4.18 to our out-of-equilibrium system. To this end, we performed simulations with phase-separated systems of different sizes such that the area of the planar interface is set at L^2, $2L^2$, $4L^2$, $9L^2$ and $16L^2$, with L ranging from 14.7σ to 58.8σ. The smaller area corresponds to the system of 2500 particles that we studied in Sections 4.3.1-4.3.3, while the bigger system has approximately 40000 particles. As we increase the system size we find that the value of the surface tension reassuringly does not change, indicating that the results presented in the previous Section 4.3.3 are free from large finite size effects. In order to measure the width of the interface we first measure the density profile of the various systems. We find that, as the system size is increased, Eq. 4.13 does not describe our simulation data as accurately as the error function fit

$$\rho(z) = \frac{1}{2}\left(\rho_l + \rho_v\right) - \frac{1}{2}\left(\rho_l - \rho_v\right) \mathrm{erf}\left[\frac{\sqrt{\pi}(z - z_0)}{w}\right], \tag{4.19}$$

where the various parameters have the same interpretation as in Eq. 4.13. This observation has been made for the passive LJ system as well [145]. Thus, in this section we use Eq. 4.19 in order to fit the density profiles $\rho(z)$ and estimate the width of the interface w for different systems.

We performed simulations for systems of different sizes for various combinations of the self-propulsion speed v_0, the rotational diffusion coefficient D_r and temperature T. Interestingly, we find that the width of the interface indeed scales linearly with the logarithm of the interfacial area, as Eq. 4.18 prescribes. In Fig. 4.5(a) we plot typical results for two sets of simulation parameters as well as the fitted Eq. 4.18. These fits allow us to extract the stiffness coefficient. Note that an equilibrium-like scaling of the width of the interface as a function of the interfacial area has previously been observed in the case of MIPS in a two-dimensional system [91].

Next, we compare the value of the stiffness coefficient to the values of the surface tension for the same system. The values of the two quantities have been acquired *via* independent measurements, namely the stiffness coefficient is extracted from the scaling of the width of the interface with the area of the interface, while the surface tension values are obtained by integrating the pressure profiles along the system (Eq. 4.14). Remarkably, we find that the two values can be related for all the systems studied *via* the simple relation

$$\begin{aligned} \gamma &= \left(k_B T_s + \frac{v_0^2}{6 D_r}\right) \kappa \\ &= k_B T_{eff} \kappa, \end{aligned} \tag{4.20}$$

where we have defined an effective temperature $T_{eff} = T_s + \frac{v_0^2}{6 k_B D_r}$. Note that this quantity has already been discussed in literature as a means to connect active systems to their equilibrium counterparts [94, 128, 146]; ideal passive particles with temperature T_{eff} would share on average the same translational diffusion rates as ideal active Brownian particles with self-propulsion force v_0 and rotational diffusion D_r immersed in a solvent of temperature temperature T_s. In Fig. 4.5(b) we show the comparison between the

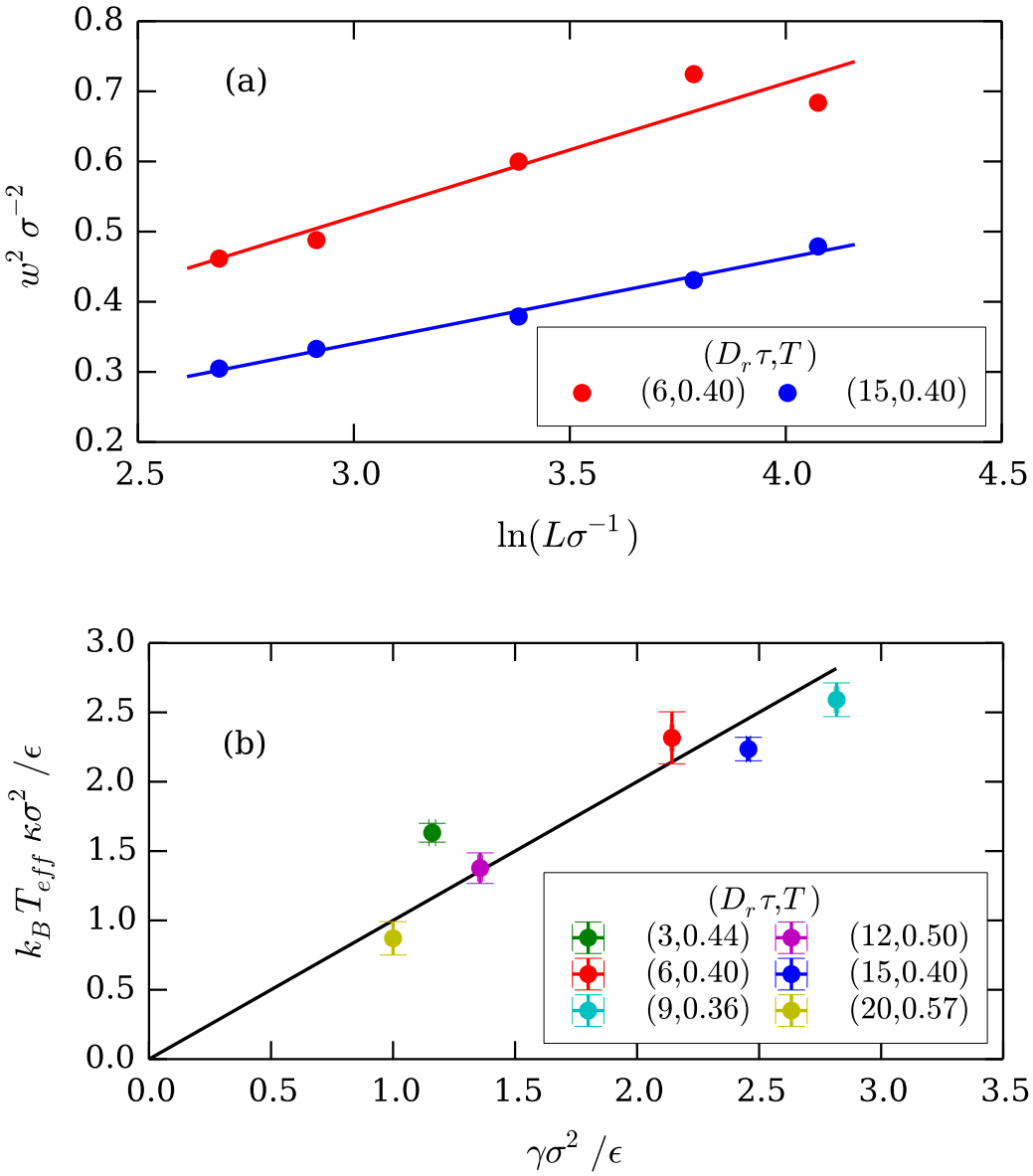

Figure 4.5: (a) Interfacial width w as a function of the length L of the interface. Data points correspond to simulation results and the continuous lines are fits of Eq. 4.18. (b) Comparison between the surface tension values measured *via* Eq. 4.20 and *via* Eq. 4.14 for a range of different temperatures T and rotational diffusion coefficients $D_r\tau$. The black line shows the expected scaling $\gamma = k_B T_{eff}\kappa$. The speed of the self-propulsion is $v_0\tau\sigma^{-1} = 8$ for all systems shown in this figure. Errors bars denote the error in the calculation of κ from the fit of the width Eq. 4.18.

scaled stiffness coefficient and the surface tension for different system parameters. The figure confirms the applicability of Eq. 4.20 to our system, which we have further verified for various other system parameters (not shown here) and whose effective temperature T_{eff}/T_s ranges from ~ 1 up to ~ 100. As a final remark, note that Bialké *et al.* argue that a similar relation to Eq. 4.20 holds also in the case of MIPS [91], where $\gamma = -\kappa v_0^2/D_r$ in two dimensions. However, an extra minus sign has to be included in this relation since the stiffness coefficient is positive while the surface tension is negative.

4.4 Conclusions

In this chapter we performed Brownian dynamics simulations of a three-dimensional system of self-propelled particles interacting with Lennard-Jones interactions at state points that are well-inside the vapour-liquid phase coexistence region. We examine systems with a Péclet number $0 \leq \mathrm{P}e = v_0/D_r\sigma \leq 8$, so that we probe the equilibrium limit as well as systems that are out-of-equilibrium. However, in all cases the phase separation is driven by the cohesive energy of the particles.

We studied the phase coexistence of a vapour and a liquid phase in an elongated simulation box and investigated the properties of the system and the interface. By employing a local expression of the pressure tensor for active systems, we measured the normal and tangential components of the pressure tensor in the direction perpendicular to the interface. We verified mechanical equilibrium of the two coexisting phases by measuring a constant normal component of the pressure tensor in the direction perpendicular to the interface. The tangential component showed negative peaks at the interface, behaviour reminiscent of equilibrium systems and indicative of a positive non-equilibrium interfacial tension of the interface as measured by integrating the difference of the normal and tangential component of the pressure tensor.

We calculated the non-equilibrium surface tension for different combinations of self-propulsion speed and rotational diffusion rate, and demonstrated that the trends of the surface tension can be fitted by simple power laws similar to equilibrium systems. These scaling laws enabled us to obtain an estimate for the critical temperature of the system as well. Interestingly, the resulting critical temperature of the active system was in close agreement with the values of the critical temperature obtained from the scaling of the order parameter (see Chapter 3). This agreement suggests on the one hand that the definitions of pressure and surface tension that were used constitute useful tools for the study of the physics of the phase transition and on the other hand hints to a deeper but not yet understood connection between the physics of the passive and the active system.

Furthermore, we calculated the stiffness coefficient of the interface and found a simple equation that relates it to the surface tension. This relation had the same form as in equilibrium systems, assuming an effective temperature of the interfacial fluctuations. Our results show many similarities between bulk and interfacial properties of active and passive Lennard-Jones systems for state points in the vapour-liquid coexistence region. We hope that, by bringing these similarities into light, we inspire and assist theoretical work in the direction of building a statistical physics of active matter and its associated phase transitions.

Acknowledgements

The results presented in this chapter are part of a collaboration with Siddharth Paliwal. Siddharth performed all the simulations for constant rotational diffusion coefficient and analysis of the corresponding results. We would also like to thank Robert Evans for useful discussions.

5

Mechanical and chemical equilibrium in mixtures of active spherical particles

In this chapter we study the phase coexistence in mixtures of active particles using Brownian dynamics simulations. We measure the pressures and the compositions of liquid-gas coexistences and show that they collapse in the pressure-composition plane onto a single binodal in the phase diagram. This confirms that the two phases are in mechanical equilibrium. Additionally, we demonstrate that the coexisting phases are in chemical equilibrium by bringing each phase into contact with particle reservoirs, and showing that for each species these reservoirs are characterized by the same density in both phases. Hence, we show explicitly that the phase separation is governed by bulk properties. Lastly, we show that phase coexistences can be *predicted* quantitatively for torque-free active systems simply by measuring these bulk properties - the same as in equilibrium.

5.1 Introduction

While active systems often exhibit behaviour fully prohibited in equilibrium systems, such as motility-induced phase separation in purely repulsive systems (see *e.g.* [61, 147]) and symmetry-breaking motion [148, 149], the steady-state behaviour of active systems can often be summarized by phase diagrams similar to their passive counterparts, *i.e.* consisting of single-phase regions and coexistence regions where the lever rule holds. For instance, fairly classic phase diagrams have recently been observed in the attraction-induced liquid-gas phase coexistence of active Lennard-Jones particles (see Chapters 2 and 3) [121, 150], the motility-induced phase separation observed in repulsive, self-propelled spheres [61], and even squares (see Chapter 6) [118], as well as binary mixtures [151].

In equilibrium, phase boundaries and coexistences are inherently tied to bulk thermodynamic properties. Since coexisting phases have equal pressures and equal chemical potentials, the bulk properties of the individual phases provide a direct route to predicting phase coexistences - a strategy commonly used to draw phase diagrams. However, for active particles no such rules exist and it remains an open question whether their phase behavior can be predicted from bulk (thermodynamic) quantities. In other words, is it possible to determine whether two phases of active particles coexist purely by measuring their bulk properties?

Perhaps the most studied bulk property in active systems is the pressure [90–93, 122, 123, 127]. Recently, Solon and coworkers have shown that there is a well-defined equation of state for torque-free, self-propelled particles [90, 127]. Specifically, for this class of active particles the pressure is purely a function of the bulk density and does not depend *e.g.* on the interaction with a surrounding wall. In this chapter, we take this as a starting point and explore the phase behaviour of two systems that are part of this class: an out-of-equilibrium mixture of passive and active attractive particles that undergoes a liquid-gas transition, and an active-active mixture of purely repulsive particles that undergoes motility-induced phase separation. Using computer simulations, we show that, similar to equilibrium, the phase behaviour of these binary mixtures collapses onto a single binodal. We also demonstrate mechanical equilibrium by directly measuring the local pressure and showing that it holds the same value for coexisting phases, as shown previously in Ref. [91] and Chapter 4.

Moreover, for the first system, we demonstrate that the coexisting phases are in chemical equilibrium by bringing each phase into contact with particle reservoirs, and showing that for each species these reservoirs are characterized by the same density in both phases. Hence, we show explicitly that the phase coexistence is governed by bulk properties, which are the pressure and a chemical potential-like bulk variable for each individual species, as represented by the reservoir density. Note that this has been assumed in several approximate theoretical treatments (see *e.g.* [79, 80, 89, 128, 152]). However, to date, no simulations have directly addressed this question, nor verified the existence of a chemical potential-like variable. Furthermore, using the requirement of three sets of equal thermodynamic potentials we *predict* the phase diagram for the latter active system simply by measuring bulk properties.

The chapter is organized as follows. We start by presenting our methods in Section 5.2. In more detail, first we describe the models studied and the dynamics of the simulations

in Section 5.2.1, we present the formulation of the local pressure for a binary system in Section 5.2.2 and finally we discuss the setup for the simulations that involve particle reservoirs in Section 5.2.3. In Section 5.3.1 we present our results for the passive-active mixture of attractive particles, followed by the results for the active-active mixture of repulsive particles in Section 5.3.2. We conclude in Section 5.4.

5.2 Methods

5.2.1 Models and dynamics

In this chapter we study two different binary mixtures. The first one is a three-dimensional system of N spherical particles that interact *via* the Lennard-Jones potential:

$$\beta U(r) = 4\beta\epsilon_{LJ}\left(\left(\frac{\sigma}{r}\right)^{12} - \left(\frac{\sigma}{r}\right)^{6}\right) \tag{5.1}$$

truncated and shifted at $r_c = 2.5\sigma$ with σ the particle diameter, $\beta\epsilon_{LJ} = 1.2$ the energy scale, and $\beta = 1/k_BT$, where k_B is the Boltzmann constant and T is the temperature. Out of the N particles, we "activate" a subset of N_a particles by introducing a constant self-propulsion force f_a along the axis $\hat{\mathbf{u}}_i$. This axis indicates the direction of self-propulsion for each particle. We denote the fraction of active particles by $x = N_a/N$.

The second binary mixture that we consider is a two-dimensional system of N purely repulsive particles that interact *via* the Weeks-Chandler-Andersen potential, that is given again by Eq. 5.1 but with the interaction cutoff radius $r_c = 2^{1/6}\sigma$ and the energy scale $\beta\epsilon_{WCA} = 40$. For this system, we consider an active-active mixture with the self-propulsions of fast and slow species being f_f and f_s, respectively.

The same equations of motion were used for both systems, adapted to their corresponding dimension. The translational and rotational motion of the position $\mathbf{r}_i$ and orientation $\hat{\mathbf{u}}_i$ of particle i follows from the overdamped Langevin equations

$$\dot{\mathbf{r}}_i(t) = \beta D_0\left[-\nabla_i U(t) + f_i\hat{\mathbf{u}}_i(t)\right] + \sqrt{2D_0}\boldsymbol{\xi}_i(t) \tag{5.2}$$

$$\dot{\hat{\mathbf{u}}}_i(t) = \sqrt{2D_r}\hat{\mathbf{u}}_i(t) \times \boldsymbol{\eta}_i(t), \tag{5.3}$$

where $\boldsymbol{\xi}_i(t)$ and $\boldsymbol{\eta}_i(t)$ are stochastic noise terms with zero mean and unit variance. The translational diffusion coefficient D_0 and the rotational diffusion constant D_r are linked *via* the Stokes-Einstein relation $D_r = 3D_0/\sigma^2$. Naturally, for a passive particle $f_i = 0$. We measure time in units of the short-time diffusion $\tau = \sigma^2/D_0$. Equations 5.2 and 5.3 were numerically integrated using an Euler-Maruyama integration scheme [107]. A time step of $dt = 10^{-5}\tau$ was used for the numeric integration of the equations of motion.

5.2.2 Pressure

For the purpose of our simulations, we always assume a slab geometry with the long axis of the simulation box being along the z dimension, such that the $\hat{z}$ axis is normal to all

interfaces. In order to write down an expression for the z (normal component) of the local pressure, first we define the moments

$$\rho_\alpha(\boldsymbol{r}) = \sum_{k=1}^{N_\alpha} \delta(\boldsymbol{r} - \boldsymbol{r}_k), \tag{5.4}$$

$$\boldsymbol{m}_{\alpha,i}(\boldsymbol{r}) = \sum_{k=1}^{N_\alpha} \hat{\mathbf{u}}_{k,i}\delta(\boldsymbol{r} - \boldsymbol{r}_k), \tag{5.5}$$

$$\boldsymbol{s}_{\alpha,ij}(\boldsymbol{r}) = \sum_{k=1}^{N_\alpha} \hat{\mathbf{u}}_{k,i}\hat{\mathbf{u}}_{k,j}\delta(\boldsymbol{r} - \boldsymbol{r}_k), \tag{5.6}$$

where i, j denote the spatial components of the corresponding vectors and tensors. $\rho_\alpha(\boldsymbol{r})$ is the local density of species α while $\boldsymbol{m}_\alpha(\boldsymbol{r})$ is the corresponding local polarization. The z (normal) component of the local pressure of the system $P_N(z)$ can then be calculated using the equation

$$P_N(z) = P_{\mathrm{id},zz}(z) + P_{\mathrm{vir},zz}(z) + \sum_\alpha P^{(\alpha)}_{\mathrm{swim},zz}(z), \tag{5.7}$$

where

$$P_{\mathrm{id},zz}(z) = \langle\rho(z)\rangle\, k_B T = \frac{1}{L^{d-1}} \int d\boldsymbol{r}^{d-1} \langle\rho(\boldsymbol{r})\rangle\, k_B T, \tag{5.8}$$

is the ideal component of the pressure, where we have spatially integrated over the dimensions that are perpendicular to the $\hat{z}$ dimension and divided by the surface L^{d-1} that we integrated over, $\rho(\boldsymbol{r}) = \sum_\alpha \rho^{(\alpha)}(\boldsymbol{r})$ is the total density at point $\boldsymbol{r}$, and brackets denote an average at the steady state over noise realizations,

$$P_{\mathrm{vir},zz}(z) = \frac{1}{L^{d-1}} \int_{z''<z} d\boldsymbol{r}'' \int_{z'>z} d\boldsymbol{r}' \langle\rho(\boldsymbol{r}'')\rho(\boldsymbol{r}')\rangle\, \partial_{z''} U(|\boldsymbol{r}' - \boldsymbol{r}''|), \tag{5.9}$$

is the standard local virial term, and

$$P^{(\alpha)}_{\mathrm{swim},zz}(z) = \frac{D_0 f^{(\alpha)}}{(d-1)D_r} \left[-\beta\partial_z U(z) \left\langle \boldsymbol{m}^{(\alpha)}_z(z)\right\rangle + \beta f^{(\alpha)} \left\langle \boldsymbol{s}^{(\alpha)}_{zz}(z)\right\rangle - \partial_z \left\langle \boldsymbol{m}^{(\alpha)}_z(z)\right\rangle\right] \tag{5.10}$$

is the local swim pressure of species α. In Eq. 5.10 $U(z), \boldsymbol{m}^{(\alpha)}_z(z)$ and $\boldsymbol{s}^{(\alpha)}_{zz}(z)$ have been averaged similar to Eq. 5.8. For a derivation of Eq. 5.7 we refer the reader to Appendix A.

In our particle simulations, we divide the simulation box into slabs, and measure the normal component of the pressure for each slab. The contributions to each slab of the ideal and swim components of the pressure can be calculated straightforwardly, while for the virial component we follow Ref. [131].

5.2.3 Reservoir simulations

The standard method for showing chemical equilibrium in passive systems is to directly measure the chemical potential of the coexisting phases. For a passive system, this can be

done in a number of different ways depending on the exact circumstance - ranging from *e.g.* grand canonical simulations to thermodynamic integration [153]. However, for active systems the situation is much more complex and currently there is no well-established method to measure the chemical potential. To avoid this issue, we go back to more basic definitions of the chemical potential. In a textbook derivation of the chemical potential, one typically attaches the system in question to a large particle reservoir, and allows the particles of a given species to travel between the subsystem in question, and the particle reservoir. The subsystem is then in a grand-canonical (μVT) ensemble, with μ set by the chemical potential of the reservoir. Hence, if two systems have the same chemical potential, one must be able to connect them to the same particle reservoir, *i.e.* one with the same particle density. Here, we follow a similar procedure with our simulations.

Specifically, we connect a binary phase consisting of two different species of particles to particle reservoirs that only contain a single species. To this end, we divide our simulation box into two sections, one which contains the "bulk" binary phase, with the other part of the box acting as a particle reservoir of one species only, which we call species R. We place a semi-permeable membrane at the division, which only allows particles of species R to pass through at no energy cost. For the other species, the wall is impenetrable with the wall-particle interaction given by a purely repulsive Weeks-Chandler-Andersen-like wall potential:

$$\beta U(z) = 4\beta\epsilon_{WCA}\left(\left(\frac{\sigma}{z}\right)^{12} - \left(\frac{\sigma}{z}\right)^{6} + \frac{1}{4}\right), \tag{5.11}$$

where z is the distance of a particle in the bulk to the nearest semi-permeable wall, $\beta\epsilon_{WCA} = 40$, and the interaction is cut off at a distance $z = 2^{1/6}\sigma$. For snapshots of such simulations see Fig. 5.3(a-d).

At the beginning of the simulation, the binary phase consists of the desired partial densities for the two species. The reservoir contains a gas of the appropriate species R with a randomly chosen initial density. During the simulation, particles of species R travel from the bulk to the reservoir and *vice-versa*, thus altering the density of the species in the bulk (*i.e.* away from the semi-permeable membrane) as well as the density of the reservoir. Also, a small fraction of the bulk phase builds up on the semi-permeable membrane, and sometimes depletes the bulk region of the confined species.

During the course of the simulation, we measure in regular intervals the partial density of each species in the center of the bulk phase. To correct for the deviations from the desired partial densities we tune the number of particles of both species during equilibration. This tuning is done by either deleting or adding particles randomly inside the part of the box that contains the binary phase. Eventually, the partial densities of both species in the bulk region reach the desired constants and the density of the reservoir assumes a constant value. After a steady state is obtained we stopped tuning, *i.e.* removing and adding particles, and checked that the reservoir density remained constant. This way we have ensured that the reservoir and the bulk phase were in chemical equilibrium. Thus, even though we cannot directly measure the chemical potential, this method allows us to measure the density of the reservoir, a quantity that uniquely characterizes the single phase reservoir.

5.3 Results

5.3.1 Lennard-Jones active-passive binary mixture

To start our investigation, we construct a liquid-gas coexistence in an active-passive mixture of Lennard-Jones particles, in the regime where the system phase separates due to attractions [121]. To this end, we set the energy scale of the attraction strength to $\beta\epsilon_{LJ} = 1.2$, which for a purely passive system (composition of active particles $x = 0$) results in a well-characterized liquid-gas coexistence at intermediate densities [105]. We fix the self-propulsion force $f_a = 10k_BT/\sigma$ for all active particles, such that the Péclet number of the active particles is $\mathrm{Pe} = 3\beta D_0 f/\sigma D_r = 10$.

We studied the phase diagram of the binary mixture by performing direct coexistence simulations. We simulated approximately 8000 particles in a three-dimensional elongated box with dimensions $L_{\hat{z}} = 12L_{\hat{y}} = 12L_{\hat{x}}$. This choice for the dimensions of the box ensures that two flat interfaces form that span the shorter dimension [91]. For the highest density (smallest simulation box) we consider, the dimensions of the box are approximately $12\sigma \times 12\sigma \times 144\sigma$. Thus, the short axis of the box is much larger than the persistence length of the active particles, which is $\beta D_0 f/2D_r \approx 1.67\sigma$. We performed direct coexistence simulations for compositions of active particles $x = 0 - 0.4$, and total densities $\rho\sigma^3 = N/L_{\hat{x}}L_{\hat{y}}L_{\hat{z}} = 0.20, 0.30$ and 0.40. These simulations were initiated from a configuration where all particles are located within a dense slab and ran for approximately 3500τ. We collected data only for the last 500τ.

In Fig. 5.1(a), we show a typical snapshot of an active-passive mixture exhibiting a liquid-gas coexistence. Here, the active and passive particles are coloured red and blue, respectively. In Fig. 5.1(b), we plot the corresponding density $\rho(z)$, active particle fraction $x(z)$, and the normal pressure $P_N(z)$ along the long axis of the box. Note that in the bulk regime of either phase, this normal pressure P_N will be equal to the bulk pressure P of the phase in question. Fig. 5.1(b) shows that, in this case, the system exhibits a gas-liquid coexistence with the gas characterized by density ρ^G and composition x^G, and the liquid characterized by density ρ^L and composition x^L. Note that in all of our simulations, the pressure is the same in both coexisting phases indicating that the system is in mechanical equilibrium.

Using composition and pressure profiles, similar to those shown in Fig. 5.1(b), we map out the coexisting compositions and pressures of our active-passive mixtures, for a wide range of overall system densities ρ and compositions x. The results are plotted in Fig. 5.2(a). Similar to passive systems, we find that the phase behaviour collapses in this representation, *i.e.* the lever rule holds within the coexistence region.

The validity of the lever rule is also evident when plotting the phase diagram in the active density - passive density (ρ_a-ρ_p) representation, as shown Fig. 5.2(b). This is consistent with the recent simulation results of Ref. [151] where they summarized the phase behaviour of a different active-passive mixture in the ρ_a-ρ_p representation. We also investigate the pressure dependence of the partial densities of each species in the coexisting liquid and gas phases. In Fig. 5.2(c) we plot these partial densities ρ_i^γ vs. pressure P with i denoting the species (active or passive) and γ denoting the phase (liquid (L) or gas

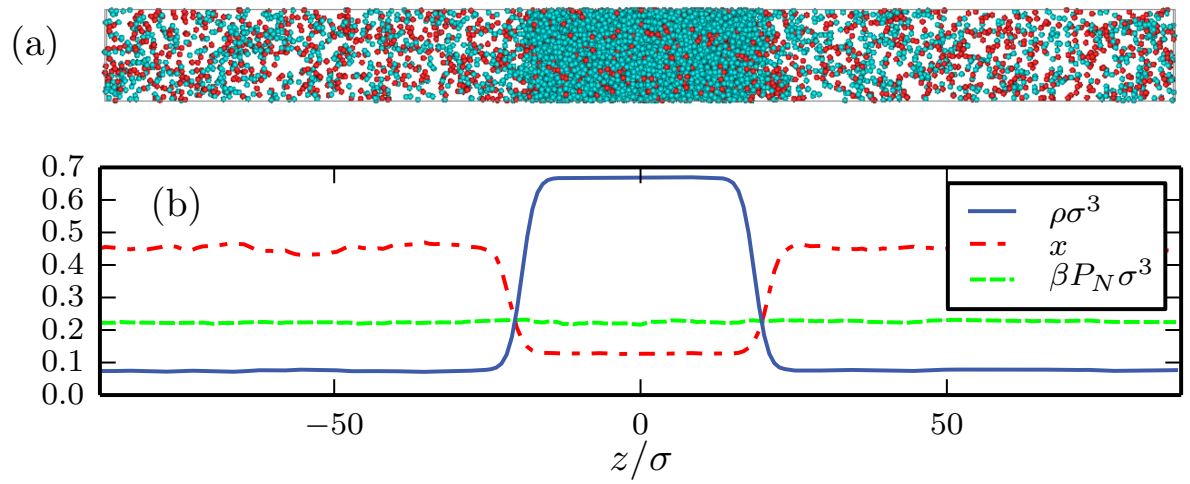

Figure 5.1: (a) Liquid-gas coexistence of an active-passive mixture with an overall active fraction $x = 0.22$ at an overall density $\rho\sigma^3 = 0.20$. For the active particles the self-propulsion force equals $f_a = 10k_BT/\sigma$. Active particles are coloured red and passive particles are coloured blue. (b) The corresponding density, composition, and pressure profile along the long direction z of the box. The system contains $N = 8192$ particles.

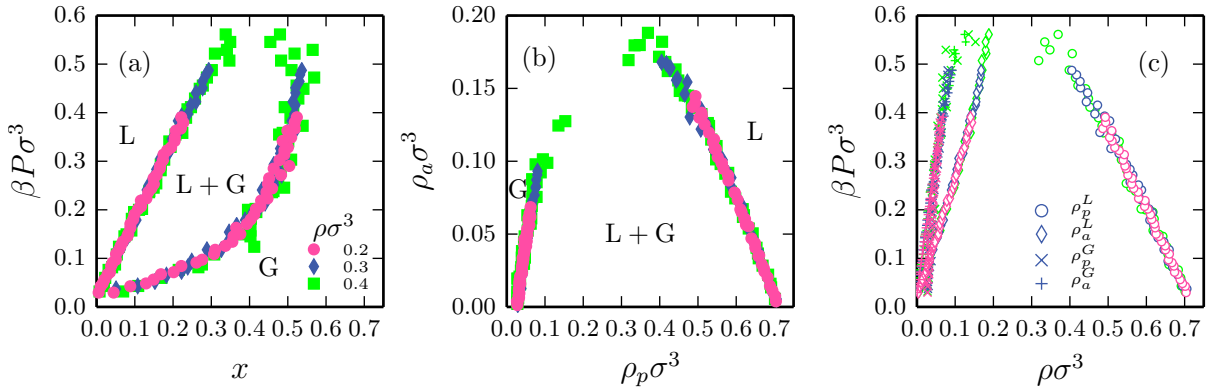

Figure 5.2: (a) Phase diagram of the Lennard-Jones active-passive mixture in the P-x representation. (b) The same phase diagram in the ρ_a-ρ_p representation. (c) Coexistence lines in the P-ρ_a and P-ρ_p representations.

(G)). Interestingly, we find that in the gas phase, the partial densities of the active and passive species are approximately the same along the entire coexistence curve.

Our results so far clearly demonstrate that the pressure is a key variable in controlling phase coexistences in our active-passive mixture: all phase coexistences are characterized by equal bulk pressures in the two phases. However, phase coexistence in an equilibrium binary system requires not only equal pressures between the two phases, but also equal chemical potentials for both species. This raises the question whether we can identify bulk properties analogous to the chemical potential in active-passive mixtures which similarly control the phase coexistence.

To this end, we study single binary phases in contact with a particle reservoir as described in Section 5.2.3. Specifically, by referring to the phase diagram Fig. 5.2(b)

we select a binary gas and liquid that coexist, and connect them individually to particle reservoirs that only contain a single species of particles. Note that in total we will need four simulations per coexistence point, namely: the gas in contact with a passive particle reservoir, the gas in contact with an active particle reservoir, the liquid in contact with a passive particle reservoir, and the liquid in contact with an active particle reservoir (see Fig. 5.3(a-d)). The goal will be to determine whether the active (and passive) reservoirs associated with the coexisting phases are the same. If they are, then we can infer that there exists a chemical potential-like variable that governs the coexistence.

For the reservoir simulations we simulated approximately 4000 particles in the bulk binary phase in contact with a reservoir that contains a gas of a random initial density. As described in Section 5.2.3, during equilibration a small fraction of the bulk phase builds up on the semi-permeable membrane (see in Fig. 5.3 (e,f)). This adsorption is counteracted by tuning the number of particles of both species during equilibration. Eventually, the average partial densities of both species in the bulk region reach the targeted constants, and also the density of the reservoir reaches a constant value.

In Fig. 5.4(a), we show the time evolution of the densities in the active particle reservoirs for the coexisting liquid and gas phases at $\beta P\sigma^3 = 0.34$. Note that although we chose a high initial density of the reservoirs in both cases, both reservoir densities quickly converged to the same density. In Fig. 5.4(b), we plot the densities of both the active and passive reservoirs as a function of the coexistence pressure $\beta P\sigma^3$. Clearly, for all coexisting liquid-gas pairs we find the same reservoir densities: $\rho_p^{\mathrm{res},L} = \rho_p^{\mathrm{res},G}$ and $\rho_a^{\mathrm{res},L} = \rho_a^{\mathrm{res},G}$. Hence, while we still cannot directly measure the chemical potential of our active system, this demonstrates the existence of a bulk variable that is conjugate to the number of particles, therefore providing clear simulation evidence of an active chemical potential.

5.3.2 Weeks-Chandler-Andersen binary mixture

So far, we have shown that gas-liquid coexistence for an active-passive mixture of Lennard-Jones particles is entirely controlled by properties which can be measured purely from the individual coexisting phases, namely the bulk pressure and reservoir densities per species. This of course raises the interesting question whether or not such phase coexistence rules can also be found for systems undergoing a purely out-of-equilibrium phase transition, namely motility-induced phase separation (MIPS), and whether or not they can be used to *predict* the phase diagram.

To this end, we use the Weeks-Chandler-Andersen potential to model the interaction between particles, with constant interaction strength $\beta\epsilon_{WCA} = 40$. We consider a two-dimensional active-active mixture with the self-propulsions of fast and slow species being $f_f = 160k_BT/\sigma$ and $f_s = 120k_BT/\sigma$, respectively. The Péclet numbers of the fast and slow active particles are $\mathrm{Pe}_{f,s} = 3\beta D_0 f_{f,s}/\sigma D_r = 160$ and 120. We chose such a set of forces for two reasons. First of all, such a choice ensures that even the slow species

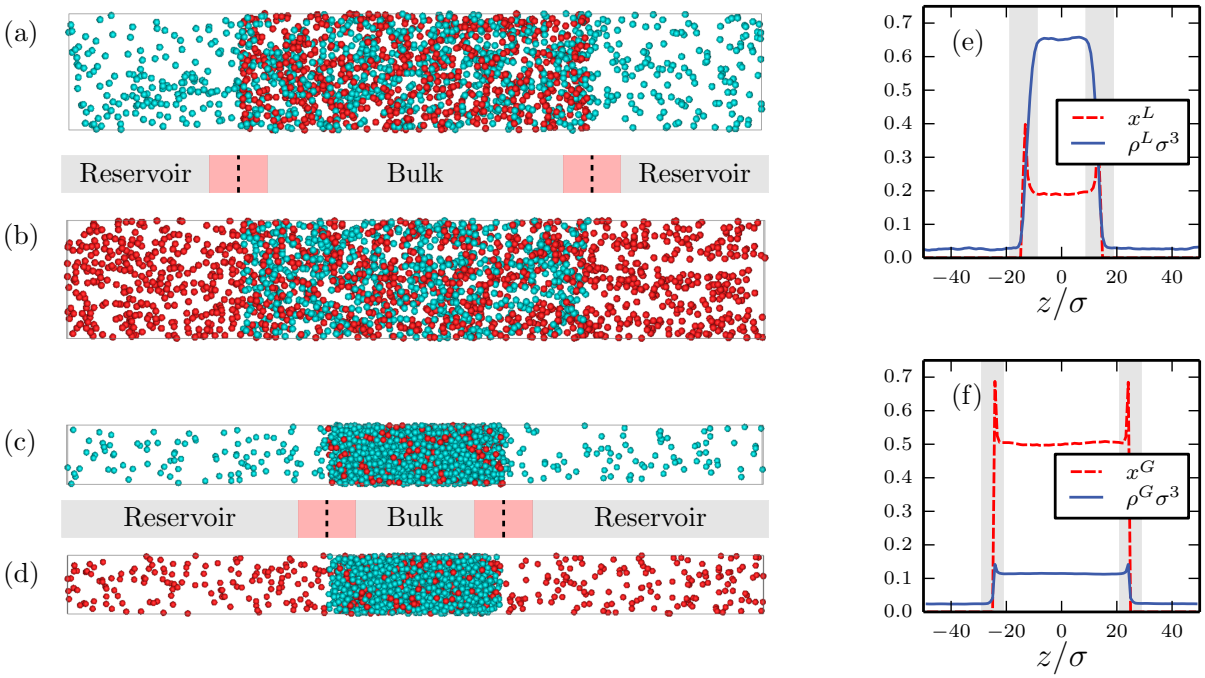

Figure 5.3: (a) The gas in contact with a passive particle reservoir. (b) The gas in contact with an active particle reservoir. (c) The liquid in contact with a passive particle reservoir. (d) The liquid in contact with an active particle reservoir. (e,f) Density and composition profiles of the liquid (e) and gas (f) in contact with a passive reservoir. The partial densities of the binary phases were chosen to correspond to the coexistence at pressure $\beta P\sigma^3 = 0.34$. Note that some active particles adsorb at the wall. We thus exclude these interfacial regions (shaded areas) in the determination of the bulk density and composition, as well as in the determination of the reservoir density.

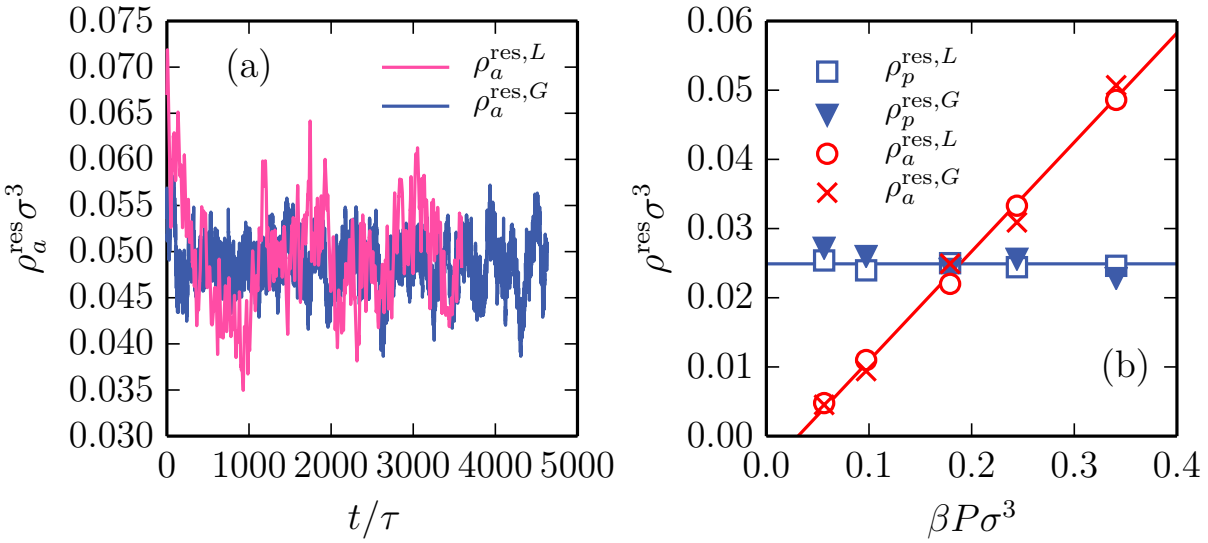

Figure 5.4: (a) The density in the active particle reservoir over time for both the liquid and the gas that coexist at pressure $\beta P\sigma^3 = 0.34$. Both phases converge to the same reservoir density of active particles. (b) The reservoir densities as a function of the coexistence pressure $\beta P\sigma^3$. The liquid and gas phase are in contact with the same reservoirs, showing that there is chemical equilibrium between the phases, for each species.

undergoes MIPS into a fluid and a crystal phase (see *e.g.* the state diagram of MIPS in Ref. [61]). As a result, we can probe the full spectrum of compositions of the binary mixture. Secondly and more importantly, such high self-propulsions result in relatively fast dynamics for the system, so that our reservoir simulations can access a large number of configurations within reasonable computational time.

We start our study for this binary mixture by constructing the phase diagram. To this end, we performed direct coexistence simulations between the fluid and the crystal phases by simulating approximately 30000 particles in a two-dimensional elongated box with dimensions $L_{\hat{z}} = 5L_{\hat{y}}$. This choice for the dimensions of the box was done such that two flat interfaces are created that span the box perpendicular to its long axis. Note that we also observe the formation of gas bubbles in the crystal phase, which have been reported in Ref. [91]. The direct coexistence simulations were performed for compositions of fast particles $x = 0 - 1$ with an interval of 0.1, and total densities $\rho\sigma^2 = 0.45, 0.6$ and 0.75. For the highest density we consider, the dimensions of the box are approximately $90\sigma \times 450\sigma$. Thus, the short axis of the box is larger than the persistence lengths of the active particles, which are $\beta D_0 f_f/D_r \approx 53.3\sigma$ and $\beta D_0 f_s/D_r = 40\sigma$, for the fast and slow species respectively. The simulations were initiated from a configuration where all particles are part of a hexagonal crystal and ran for approximately 1500τ. We collected data only for the last 500τ. The long running times are necessary for the relaxation of the compositions of the coexisting phases.

We then measured the local densities of the two species and the normal component of the pressure by dividing the box into slabs of length σ across the long z-axis and measuring the corresponding quantities for each slab. Typical results for such measurements, as well as a snapshot of the system in direct coexistence, are shown in Fig. 5.5. From the results

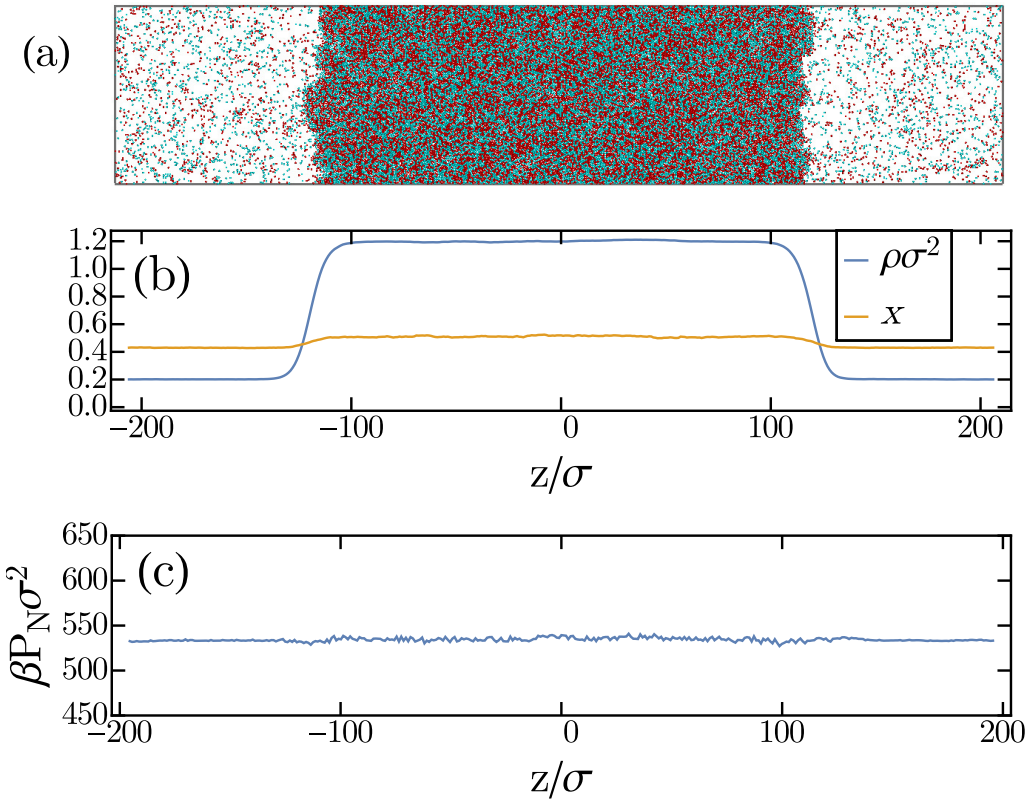

Figure 5.5: (a) Motility-induced phase separation of an active-active binary mixture with overall fraction $x = 0.5$ and overall density $\rho\sigma^2 = 0.75$. Red particles are "fast" swimmers with self-propulsion force $f_f = 160k_BT/\sigma$ and blue particles are "slow" swimmers with self-propulsion force $f_f = 120k_BT/\sigma$. The system contains approximately 30000 particles. (b) The corresponding density (ρ) and composition profile (x) along the long direction z. (c) The corresponding normal pressure profile along the long direction z.

of these direct coexistence simulations we constructed the phase diagram, as shown in Fig. 5.6(a). As in the case of the active-passive binary mixture of Lennard-Jones particles, for this active-active mixture we observe a clear collapse of the direct coexistence data onto a single binodal.

As a next step we predict the phase boundaries by calculating the pressure P and reservoir densities ρ_f^{res} and ρ_s^{res} for a wide range of binary crystal and gas phases (shaded area in Fig. 5.6(a)). Accordingly, we performed simulations of a binary phase in contact with a particle reservoir. As described in Section 5.2.3, the two parts of the system were separated by a semipermeable wall that repels the species that is absent in the reservoir. In addition to the repulsion, we also apply a torque to the particles of this species that reorients these particles away from the wall. This torque was applied in order to minimize the accumulation of particles on the wall. Reassuringly, we find that the applied torque does not affect the bulk part of the binary phase, since the orientation of the particles relaxes rapidly as we move away from the wall.

First, we ran simulations of a binary gas phase in contact with a reservoir in order to acquire the bulk pressure and the reservoir densities for fast and slow swimmers. The

gas phases we considered had compositions in the regime $x \in (0.1 - 0.9)$ and densities $\rho\sigma^2 = 0.05 - 0.5$ (see shaded area in Fig. 5.6(a)). The interval between the points we considered was 0.1 for the composition and $0.02 - 0.05$ for the density. We find that for total density $\rho\sigma^2 > 0.4$ the system spontaneously phase separates so we cannot probe this high-density regime. For each gas phase, which corresponds to a point in the (x, ρ) grid, we ran two simulations, one in contact with a reservoir of fast swimmers and one in contact with a reservoir of slow swimmers. Each simulation provided us with a value for the density of the corresponding reservoir and also a value for the normal pressure in the bulk. The two measured values for the pressures were reassuringly in close agreement, since we simulated the same binary bulk phase in both simulations. Thus a pair of such simulations provided us with a hypersurface $(\rho_f^{\text{res}}, \rho_s^{\text{res}}, P)$, which is a function of the variables x and ρ. The value of the pressure P was the average from the two simulations. This surface was then fitted by a second degree polynomial. The red surface shown in Fig. 5.6(b) is the fitted polynomial.

For the crystal phase we followed a similar approach. We simulated the binary bulk crystal in contact with a reservoirs of slow and fast particles separately. The points we simulated were in the interval of compositions $x \in (0.1 - 0.9)$ and densities $\rho\sigma^2 = 1 - 1.30$, with intervals 0.1 for the composition and 0.02 for the density (see shaded area in Fig. 5.6(a)). Again, the results of the simulations produced a hypersurface $(\rho_f^{\text{res}}, \rho_s^{\text{res}}, P)$ which we again fitted with a second degree polynomial. This polynomial is the blue surface shown in Fig. 5.6(b).

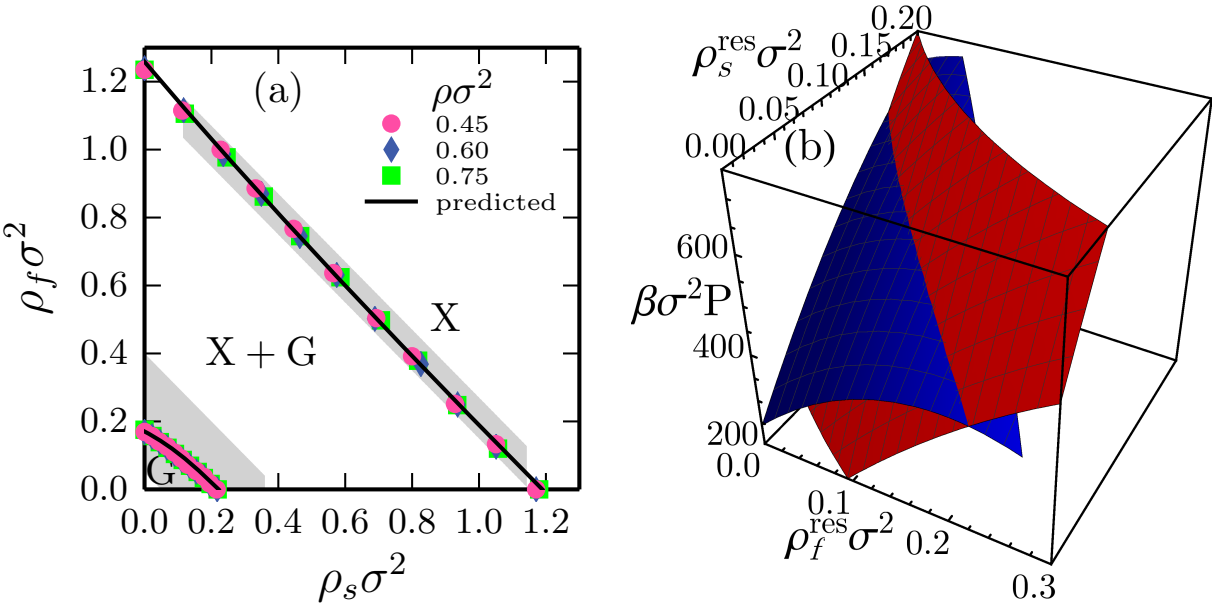

Figure 5.6: (a) Direct coexistence results for the phase diagram of the active-active mixture of WCA particles (markers), and the predicted phase diagram (line). Note that X denotes the crystal phase while G denotes the gas phase. (b) Surface plots of the gas (red) and crystal (blue) reservoir densities vs pressure. From the intersection between the two surfaces we obtain the predicted binodals in (a).

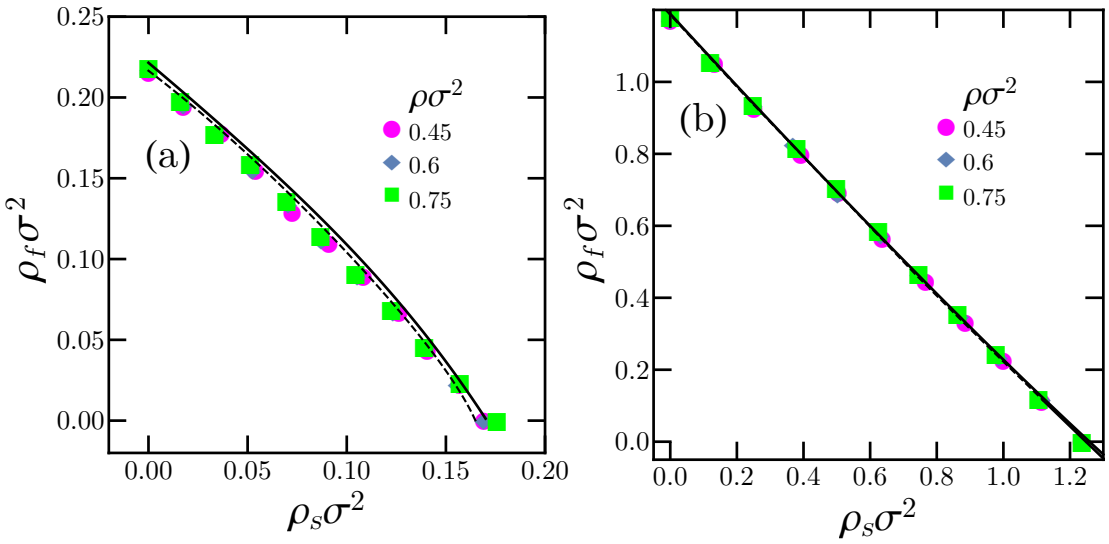

Figure 5.7: Predicted binodal lines of the active-active mixture of WCA particles before (full lines) and after (dashed lines) applying a correction to the pressure of the reservoir simulations. Markers denote the results from direct coexistence simulations. (a) covers the low-density region of the phase diagram and (b) the high-density region.

The intersection of the two surfaces is the line where the reservoir densities of both species and pressures of the binary crystal and gas phases are equal. Thus, it should correspond to the binodals of the phase diagram. The lines on each of the two $(\rho_f^{res}, \rho_s^{res}, P)$ surfaces can be converted back into lines in the (x, ρ) and subsequently the (ρ_f, ρ_s) representation of the phase diagram. The resulting phase boundaries are drawn in Fig. 5.6(a) in order to compare them with the results from the direct coexistence simulations. A more detailed view can be seen in Fig. 5.7.

We find that the predicted high-density binodal (full black line in Fig. 5.7(b)) is in excellent agreement with the points from the direct coexistence simulations. We have thus in this section quantitatively *predicted* for the first time the binodal lines for a system that undergoes motility-induced phase separation from bulk properties only. Note that the low-density binodal (full black line in Fig 5.7(a)) slightly deviates to higher densities. We attribute this discrepancy to finite-size effects in our simulations. We find that on average, the reservoir simulations measure a higher pressure of the binary crystal than the direct coexistence simulation despite having equal densities and compositions. This difference is caused by the different tangential dimensions of the box between the reservoir and the direct coexistence simulations. A typical direct coexistence simulation has a box length in the tangential dimension three times larger than the reservoir simulations. Note that the pressure difference is minute: on average we measure a pressure difference $\Delta P\beta\sigma^2 \sim 4$, while the pressure of the system in coexistence is in the range $\beta P\sigma^2 \sim 400 - 700$. In order to estimate the magnitude of this finite size effect on the binodals, we make a crude correction by vertically shifting the crystal (blue) surface of Fig. 5(b) of the main text by a constant which is equal to the average pressure difference. This correction subsequently

alters the intersection of the two surfaces, and shifts the initially predicted binodals to the full lines shown in Fig. 5.7. This indeed appears to reduce the discrepancy between the predicted and measured coexistence lines. It should be noted that this correction is not included in the coexistence lines reported in Fig. 5.6(a).

5.4 Conclusions

In conclusion, in this chapter we studied phase coexistences of two different active systems using Brownian dynamics simulations, and focused on the mechanical and chemical equilibrium of the coexisting phases. The first system was a binary mixture of attractive active and passive spherical particles that undergoes a liquid-gas, attraction-induced phase transition. Using direct coexistence simulations, we calculated the phase diagram of this system for different compositions and directly showed mechanical equilibrium by measuring the bulk pressure of the coexisting phases. Subsequently, by bringing each of two coexisting binary phases into chemical equilibrium with a reservoir of particles of a given species, we showed that the connected reservoirs of each particle species are identical for the two phases. We thus numerically demonstrated chemical equilibrium between coexisting phases for this system by measuring a quantity analogous to the chemical potential of passive systems: the density of the reservoir.

The latter system we studied was a binary mixture of purely repulsive active spherical particles of two different self-propulsion speeds, that undergoes a motility-induced phase separation into a fluid and a crystalline region. First, we calculated the phase diagram of the system using direct coexistence simulations. Next, we performed a series of simulations where a pure binary phase, either a fluid or a crystal, was brought into contact with a reservoir of particles of each species, and measured the densities of the two reservoirs as well as the pressure of the bulk binary phase. Assuming mechanical and chemical equilibrium between the gas and the crystalline phases, we were then able to *predict* the phase diagram that we previously obtained using direct coexistence simulations.

We have therefore highlighted two important features of active systems that do not experience torques: first, we demonstrated the existence of a quantity conjugate to the number of particles, which we identified here as the density of the connected reservoir, and second, we established that phase diagrams can be quantitatively predicted by simply measuring properties of the individual phases, that is the bulk pressure and reservoir densities per species. Note that other theoretical methods have so far failed to quantitatively predict phase diagrams from bulk properties alone [86, 90, 103]. Though our work does not demonstrate an analytical way to such a prediction, it does provide numerical evidence that such a task is achievable. We thus believe that have have taken an important step towards the thermodynamics of active matter.

Acknowledgments

The results presented in this chapter are part of a collaboration with Berend van der Meer. Berend performed the simulations and analysis for the Lennard-Jones system, and

also helped with the analysis of the WCA system. We thank Frank Smallenburg and Michiel Hermes for many useful discussions.

6

State behaviour and dynamics of self-propelled Brownian squares

In this chapter we study the state behaviour of self-propelled Brownian squares as a function of the speed of self-propulsion and density. We find that the system undergoes a transition from a fluid state to phase coexistence with increased self-propulsion and density. Close to the transition we find oscillations of the system between a fluid state and phase coexistence that are caused by the accumulation of forces in the dense phase. Finally, we study the coarsening regime of the system and find super-diffusive behaviour.

6.1 Introduction

In Chapters 2-5 we studied systems of spherical particles that interact with one another *via* isotropic interactions. This class of active matter systems is special since an equation of state exists and mechanical pressure is well defined for such systems [90]. Associated to these theoretical results is the observation that phase diagrams of systems of isotropic and self-propelled particles share many similarities with phase diagrams of equilibrium, non-active systems, as we have clearly demonstrated in Chapters 2, 3 and 5. However, in order to arrive at a general description of active matter one needs to study active matter systems with more complex interactions between particles than the simple case of isotropic interactions. As a small step towards this direction, in the present chapter we thus shift our attention to a system of square self-propelled particles.

Determining how the shape of a particle can affect collective behaviour is an important challenge in understanding the physics of active matter [113]. To date, only a few shapes have been explored in combination with active motion. Some notable examples include the self-propelled L-shaped particle that has been created and studied by Kümmel and collaborators [37], self-propelled dumbbells [32, 76, 154] and self-propelled rods [77, 155–157]. In all of these studies significant results have been reported; the L-shaped swimmer performs gravitactic motion and can swim against the direction of gravity [39], active dumbbells assemble in rotating clusters [76], and rods can form swarms and lanes due to the emergent aligning interaction between the particles [155, 158]. The plethora of dynamic phenomena shows that the shape of an active particle can dramatically change the single particle and many particle dynamics.

Here we explore the behaviour of a very simple particle, namely a repulsive square that self-propels in the direction perpendicular to one of its edges. It is already known that repulsive, active spheres and discs can phase separate due do their activity, a phenomenon known as motility-induced phase separation (MIPS) [61, 62, 74] (see also Chapters 1 and 5). However, how such behaviour might manifest in the case of anisotropic particles with four-fold symmetry is not *a priori* evident. Here, we explore the state diagram of self-propelled squares for a wide range of densities and speeds of self-propulsion, in order to fully map out the behaviour of such a geometry. We explicitly compare our results with existing literature on self-propelled discs and rods with respect to the state behaviour, the phase coexistence and the coarsening properties of the different systems.

This chapter is organized as follows. We start by introducing the model and the parameters of our simulations in Section 6.2.1, and in Section 6.3.1 we present the state diagram and give a general overview of the different states of the system. In Section 6.3.2 we quantify certain properties of the phase coexistence regime, while in Section 6.3.3 we focus on what we identify as state oscillations of the system. Finally, we look into the coarsening process in Section 6.3.4. Conclusions are given in Section 6.4.

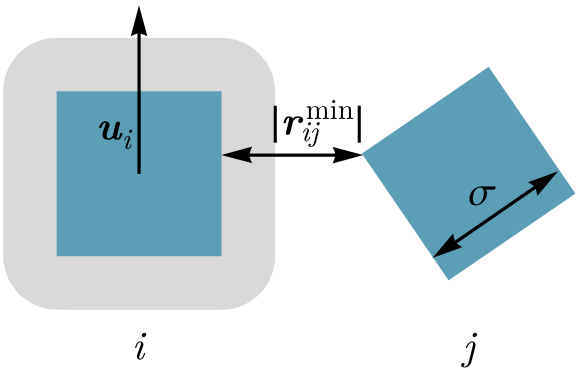

Figure 6.1: A schematic overview of the model. Particles i and j are coloured blue, and the gray area around particle i stands for the area in which particle j must enter in order for the two particles to interact. The distance $|\boldsymbol{r}_{ij}^{\min}|$ is the minimum distance between the surfaces of the two particles.

6.2 Methods

6.2.1 Model

We consider a two-dimensional system, consisting of squares of length σ in a periodic square box of length L. The position of the center of mass of the i-th particle at time t is given by the vector $\mathbf{r}_i(t)$ while its orientation is given by the unit vector $\boldsymbol{u}_i(t) = (\cos\theta_i(t), \sin\theta_i(t))$, where $\theta_i(t) \in [0, 2\pi)$ is the angle between a fixed axis in the lab frame and a fixed axis on the particle. The axis on the particle is chosen such that the vector $\boldsymbol{u}_i$ is perpendicular to one of the edges of the square. A schematic overview of the model can be found in Fig. 6.1.

The interaction between two particles is modeled as a soft repulsion between their points of closest approach. To this end, we first find the minimum distance vector between the surfaces of the two squares i and j, which we denote here as $\boldsymbol{r}_{ij}^{\min}$. The force that acts between the two particles is then given by

$$\boldsymbol{F}_{ij} = -\frac{\partial U(|\boldsymbol{r}_{ij}^{\min}|)}{\partial \boldsymbol{r}_{ij}^{\min}}, \tag{6.1}$$

where $U(r)$ is a soft, yet steep, repulsive potential, specifically a slight modification of the Weeks-Chandler-Andersen potential:

$$\beta U(r) = \begin{cases} 4\beta\epsilon\left(\left(\frac{1}{r/\sigma+0.8}\right)^{12} - \left(\frac{1}{r/\sigma+0.8}\right)^{6} + \frac{1}{4}\right) & r/\sigma + 0.8 \leq 2^{1/6}, \\ 0 & r/\sigma + 0.8 > 2^{1/6}. \end{cases} \tag{6.2}$$

Here ϵ parametrizes the strength of repulsion and $\beta = 1/k_B T_s$ is the inverse temperature of the system, with k_B the Boltzmann constant and T_s the temperature of the system. In

this chapter, for all our simulations we set $\beta\epsilon = 40$. Note that in Eq. 6.2, the shortest surface-to-surface distance $|\boldsymbol{r}_{ij}^{\min}|$ is increased by 0.8σ so that particles will repel each other only if their surface-to-surface distance is smaller than $(2^{1/6} - 0.8)\sigma \simeq 0.322\sigma$. This reduces the effective roundness of our particles, so that the effects of the non-isotropic shape become more prominent. The corner rounding to length ratio (see Ref. [159]) for our soft squares is approximately 0.14.

We then apply the force $\boldsymbol{F}_{ij}$ on the surface point of particle i that is closest to the surface of particle j, which we denote here as $\boldsymbol{r}_i^j$. This creates a torque

$$\boldsymbol{T}_{ij} = (\boldsymbol{r}_i^j - \boldsymbol{r}_i) \times \boldsymbol{F}_{ij}, \tag{6.3}$$

that acts on particle i, causing it to rotate around the axis $\boldsymbol{z}$, that is perpendicular to the plane of movement. This torque tends to align the particles such that they become parallel when they are pushed towards one another.

6.2.2 Dynamics

To make the particles active, we include a self-propelling speed of constant magnitude v_0 that acts along $\boldsymbol{u}$. Thus, the particles are self-propelled along one of their edges. Additionally, we consider our particles immersed in a solvent whose damping coefficient is given by η. Since we are interested in the regime that applies to the colloidal world, we use overdamped Langevin dynamics for the equations of motion, which include the solvent-particle interactions implicitly and neglect the inertia of the particles. Thus, the translational and rotational equations of motion are

$$\frac{d\boldsymbol{r}_i(t)}{dt} = \beta \boldsymbol{D}_{tr} \sum_{j \neq i} \boldsymbol{F}_{ij}(t) + v_0 \boldsymbol{u}_i(t) + \sqrt{2}\boldsymbol{D}_{tr}^{1/2} \boldsymbol{\xi}_i^{tr}(t), \tag{6.4}$$

$$\frac{d\theta_i(t)}{dt} = \beta D_r \sum_{j \neq i} \boldsymbol{T}_{ij}(t) \cdot \boldsymbol{z} + \sqrt{2D_r}\xi_i^r(t). \tag{6.5}$$

Here, the translational diffusion matrix $\boldsymbol{D}_{tr} = D_{tr}(\boldsymbol{u}_i\boldsymbol{u}_i + \boldsymbol{u}_{i,\perp}\boldsymbol{u}_{i,\perp})$ is a diagonal matrix in the particle frame of reference with $D_{tr} = 1.08/(8\pi\eta\delta\beta)$, where δ is the radius of a disk with area σ^2 [160]. Similarly, $D_r = 1.32/(8\pi\eta\delta^3\beta)$ is the rotational diffusion coefficient of a single square [161]. The unit vector $\boldsymbol{u}_{i,\perp}$ is perpendicular to $\boldsymbol{u}_i$. Thermal noise is modeled *via* two white noise Gaussian terms denoted by $\boldsymbol{\xi}_i^{tr}$ and ξ_i^r, which both have zero mean and unit variance. We define the unit of time τ as the time it takes a free particle to diffuse over its length, *i.e.* $\tau = \sigma^2 D_{tr}^{-1}$. Finally, $\boldsymbol{D}_{tr}^{1/2} = D_{tr}^{1/2}(\boldsymbol{u}_i\boldsymbol{u}_i + \boldsymbol{u}_{i,\perp}\boldsymbol{u}_{i,\perp})$.

Equations 6.4 and 6.5 are integrated using an Euler-Maruyama integration scheme [107], with a time step of $dt = 10^{-5}\tau$. In the initial configuration of our simulations, particles are placed on a square lattice spanning the entire simulation box, with their orientations randomly distributed.

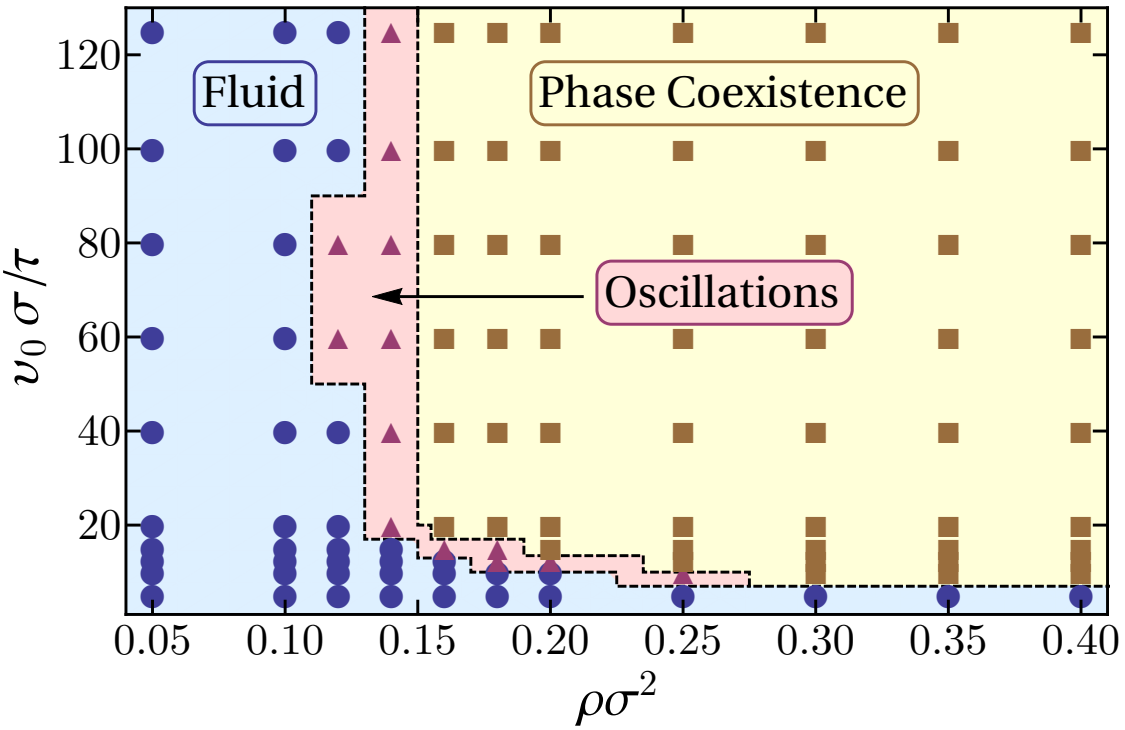

Figure 6.2: State diagram of soft active squares, as a function of system density $\rho\sigma^2$ and propulsion speed $v_0\sigma/\tau$. Blue circles (●) denote points where the system is found in a homogeneous fluid state, brown squares (■) denote phase coexistence, and red triangles (▲) points where the system oscillates between the two aforementioned states. The dotted lines are approximate boundaries between the different regimes.

6.3 Results

6.3.1 State behavior

To investigate the state behavior of our system we performed Brownian Dynamics simulations of $N = 4900$ particles for a range of reduced densities $\rho\sigma^2 = N\sigma^2/L^2$ and propulsion speeds $v_0\sigma/\tau$. The results of our simulations are summarized in the state diagram in Fig. 6.2.

We identify three distinct regions: a homogeneous fluid regime, a regime where there is coexistence between a dense and a dilute phase, and a region where the system oscillates between a homogeneous fluid state and a phase coexistence. In the regime where the density and the speed of self-propulsion are relatively small, the system is found in a homogeneous fluid state. Note that in this fluid, small and short-lived clusters can form due to collisions between the particles. In contrast, at sufficiently high densities and speeds of self-propulsion a kinetic trapping mechanism takes place, similar to that seen in self-propelled discs [61, 74]. Particles slow down significantly in dense regions due to frequent collisions with one another, which leads to a further increase in the local density. Ultimately, this leads to phase coexistence between a high-density *crystalline* region and a low density fluid, a phenomenon known as motility-induced phase separation (see Fig. 6.3(a)). We also found that at low densities, the high density cluster sometimes breaks up into smaller clusters (see Fig. 6.3(b)) and then reforms. Note that this breakup is not typically observed in coexistences of passive systems once the system has thermally equilibrated.

Interestingly, between the homogeneous phase and the coexistence regime, we find an additional region where we observe "oscillation" between a homogeneous fluid state and a phase coexistence (an oscillation whose frequency we will attempt to determine in Section 6.3.3). Specifically, in this region if we start with a homogeneous fluid state, the system appears to undergo nucleation and growth, resulting in a single large cluster. However, as we explore in more detail in Section 6.3.3, at some point the cluster disintegrates completely and the system returns to a homogeneous fluid state. This process repeats itself continuously. In the following, we refer to this region as the oscillatory regime of our state diagram.

In order to further clarify the differences between the three regimes in our state diagram, we plot in Fig. 6.4 the time evolution of two quantities: i) the fraction of particles associated with the largest cluster in the system $f_{\mathrm{lc}} = N_{\mathrm{lc}}/N$, with N_{lc} the number of particles in the largest cluster and N the total number of particles, and ii) the degree of clustering $\Theta = 1 - N_{\mathrm{c}}/N$ [104], where N_{c} is the average number of clusters. Θ goes to zero for a system composed of single-particle clusters while it approaches unity when the mean cluster size becomes comparable to the total number of particles. We assign two particles to the same cluster if they exert non-zero forces on one another. Also, we assign a parameter space point to the phase coexistence regime if, for the whole course of the performed simulation, the largest cluster fraction stays higher than 10%.

As expected, the homogeneous state shows minimal clustering ($\Theta \simeq 0.3$, $f_{\mathrm{lc}} \simeq 0$), while in the case of phase coexistence the system is highly clustered ($\Theta \simeq 0.9$, $f_{\mathrm{lc}} \simeq 0.9$). Following the time evolution of the curve that corresponds to the phase coexistence regime

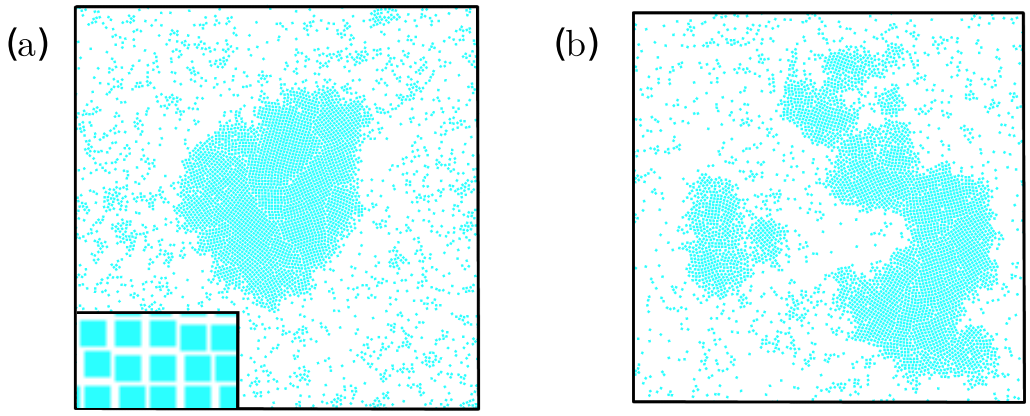

Figure 6.3: (a)-(b): Snapshots of the system for $\rho\sigma^2 = 0.18$ and $v_0\sigma/\tau = 60$ at different times. On the left bottom side of (a) we have zoomed in on the center of the cluster.

(coloured green), we find that the sudden drops in $f_{\rm lc}$ (Fig. 6.4(a)) are not simultaneously accompanied by a significant drop in Θ (Fig. 6.4(b)), and correspond to temporary breaking of the largest cluster into smaller pieces (for example see Fig. 6.3(b)). In contrast, from the curves that represent the oscillatory regime (coloured yellow), a correlation between the two quantities is clearly visible. This correlation suggests that the clustering of the whole system is dictated by the behaviour of the largest cluster in the system. The peaks observed in both quantities indicate nucleation, growth and breaking of a single cluster.

Moreover, in the phase coexistence regime all functions tend to their steady-state value immediately after the simulation begins, thus no nucleation time is required. This feature is shared for all points that we identify as phase coexistence states. This hints that these points may lie inside the spinodal lines of the system, if such a correspondence with equilibrium physics can be made. However, in the yellow curve of Fig. 6.4(a), which corresponds to the oscillatory regime, one can see distinct plateaus where the largest cluster in the system is very small ($f_{\rm lc} \sim 0$), accompanied by growth and destruction of the cluster. These features are shared by all the simulations that we identify to be in the oscillatory regime. Thus, we infer that what we identify as an oscillatory regime may coincide with the region between the binodal and the spinodal lines of the system. What remains unclear is whether the system would ever fully nucleate. Specifically, whether for a sufficiently large system and sufficiently long time, the oscillations would stop. We note that we have seen no sign of such stopping in our systems for any of the state points we have examined.

Comparison between our state diagram (Fig. 6.2) and the diagram of self-propelled discs (see for example Fig 2(a) in Ref. [61]), shows that phase coexistence in our system requires much smaller propulsion speeds. We attribute this to the augmented average duration of a collision event between squares compared to discs, which arises due to the different shape of the particles: squares cannot slip past each other when they collide as their flat surfaces tend to align the particles. This hinders their movement, especially when particles with anti-parallel self-propulsion axes collide. Moreover, the oscillatory

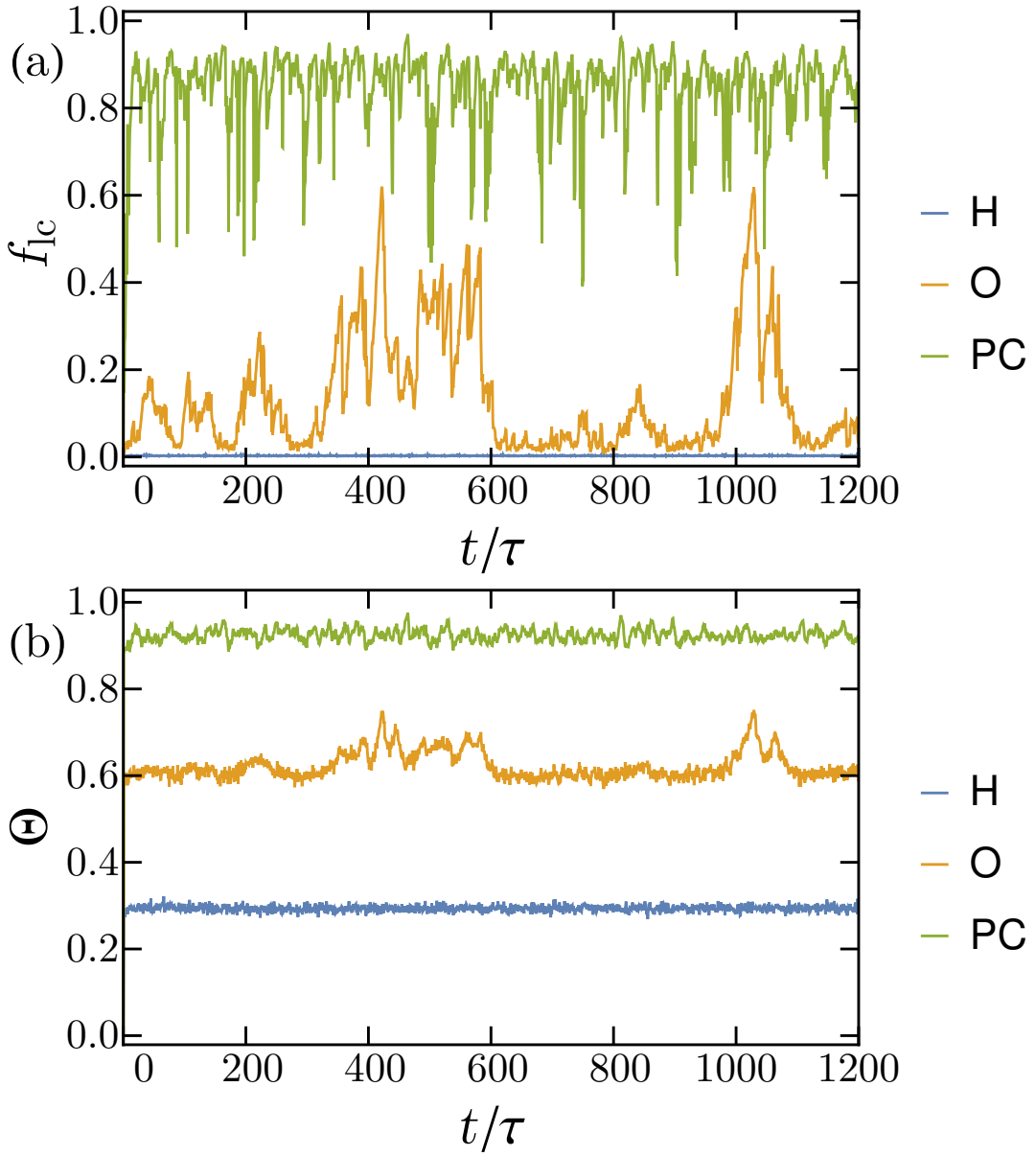

Figure 6.4: Time evolution of (a) the largest cluster fraction f_{lc} and (b) the degree of clustering Θ, for three systems with constant self-propulsive speed $v_0\sigma/\tau = 100$ and densities $\rho\sigma^2 = 0.05, 0.14$ and 0.3, corresponding to systems in the homogeneous (H), oscillatory (O) and phase-coexistence (PC) regimes of the phase diagram respectively.

regime is absent in the case of the isotropic discs. We will discuss how the anisotropic shape of the squares gives rise to this regime in Section 6.3.3.

We also note that we have observed no formation of lanes or swarms in our simulations. These dynamic states are seen in models where interparticle interactions tend to align the axes of self-propulsion of the colliding particles [77, 162]. For example, when two self-propelled rods collide, their axes of self-propulsion will tend to become parallel or anti-parallel. In the case of two squares colliding, even though the particles do become parallel after the collision, their axes of self-propulsion can also be perpendicular to one another. We conclude that the four-fold symmetry of squares, instead of the two-fold symmetry of rods, is enough to lead to the absence of lanes or swarms. A more detailed comparison between active squares and rods will be given in Section 6.3.3.

6.3.2 Phase separation regime

By inspection of the dense cluster that forms when phase separation takes place, we find that the cluster is composed of regions that resemble a square crystal phase. These regions are separated from one another by linear defects. See Fig. 6.5(a) for a closeup of such a cluster. Here, individual particles are coloured according to the absolute value of the bond orientational parameter

$$q_4(k) = \frac{1}{\mathcal{N}_k} \sum_{l=1}^{\mathcal{N}_k} e^{i4\theta_{kl}}, \tag{6.6}$$

where $\mathcal{N}_k$ is the total number of neighbors of particle k, and θ_{kl} is the angle between the vector $\boldsymbol{r}_k - \boldsymbol{r}_l$ and an arbitrary lab axis. Neighboring particles are defined such that their center-to-center distance is smaller than 1.5 σ. This bond order parameter detects local four-fold symmetry in the neighborhood of each particle.

In Fig 6.5(b) we plot the bond orientational order averaged over all particles and many independent configurations

$$Q_4 = \frac{1}{N} \sum_{i=1}^{N} \langle q_4(i) \rangle, \tag{6.7}$$

as well as the global orientational order parameter

$$\Phi_4 = \frac{1}{N} \sum_{i=1}^{N} \langle e^{i4\theta_i \bmod(2\pi/4)} \rangle, \tag{6.8}$$

that detects global orientational order in the system. The modulus function takes into account the four-fold symmetry of the squares. We find that Q_4 takes non-zero values even in the homogeneous regime, as a result of the small clusters that form, and higher values in the phase coexistence regime. On the other hand, Φ_4 stays close to zero in the homogeneous regime and sharply assumes non-zero values once phase separation occurs and a system size cluster forms.

We now study the local densities of the coexisting phases in the phase coexistence regime. We determine the densities of the two phases by identifying the peaks of the local density histogram of the system (not shown here), similar to previous studies of active matter systems [61, 121] (see also Chapter 2). The local densities for the fluid (ρ_g) and the

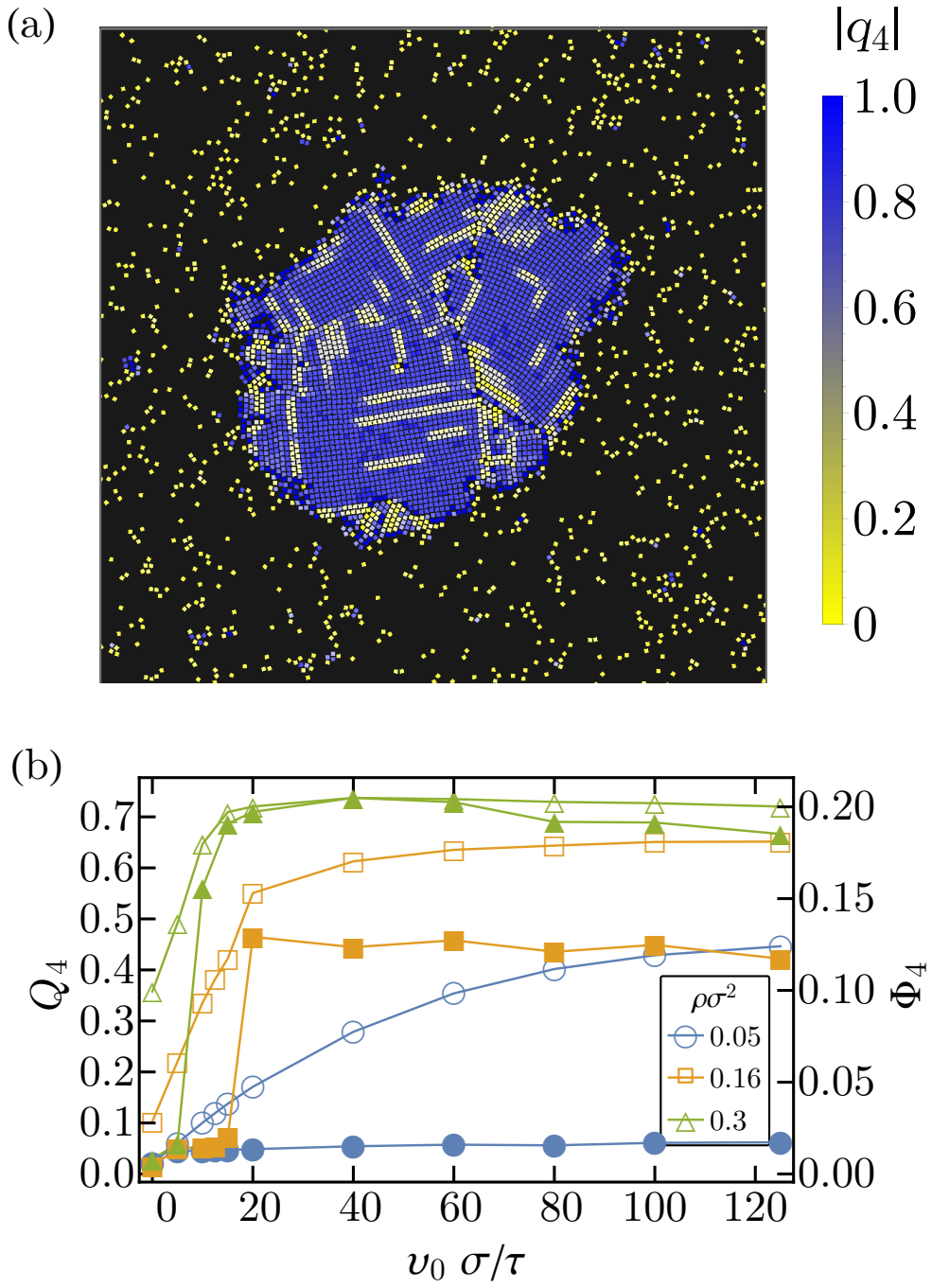

Figure 6.5: (a) Snapshot of the system for $\rho\sigma^2 = 0.18$ and $v_0\sigma/\tau = 60$. Particles are coloured according to their $|q_4|$ value. (b) Average local order parameter Q_4 (open symbols) and global orientational parameter Φ_4 (full symbols) as a function of $v_0\sigma/\tau$ for various system densities. Lines are simply guides to the eye.

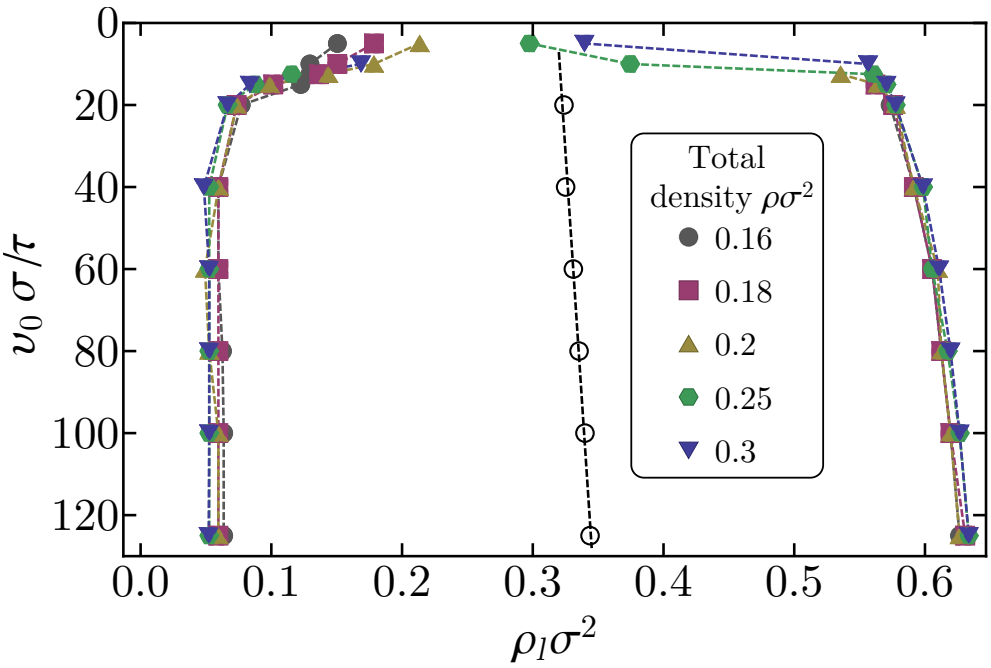

Figure 6.6: Local densities $\rho_l\sigma^2$ of the coexisting phases in the phase separation regime for different speeds of self-propulsion $v_0\sigma/\tau$. Data points correspond to maxima of the local density histograms and different symbols refer to different total densities. Black open circles denote the mean of the two coexisting densities $(\rho_x + \rho_g)/2$ and the black dotted line is a linear fit. Coloured dotted lines are guides to the eye. Note that the vertical axis of this plot is inversed with respect to Fig 6.2.

crystalline region (ρ_x) are plotted in Fig. 6.6. This figure suggests that the speed of self-propulsion alone determines the time averaged local densities of the dense and the dilute phase, irrespective of the total system density. This property also holds for the motility-induced phase separation of active self-propelled discs and the liquid-gas coexistence of attractive self-propelled spheres [61, 121] (see also Chapter 2). However, self-propelled squares pack better than self-propelled discs as the squares assemble in a square crystal rather than a hexagonal crystal. We would like to note that the seemingly lower values of the densities of the crystalline phase compared to the values reported for passive squares (Ref. [159]) do not necessarily imply a less efficient packing of self-propelled squares. The lower values are in fact caused by the range of our soft repulsive potential.

Moreover, in Fig. 6.6 we plot $(\rho_x + \rho_g)/2$ averaged over the different system densities. We find that, away from the critical point, this quantity follows linear scaling as a function of the self-propulsion speed $v_0\sigma/\tau$. This linear scaling is also found in equilibrium systems, where it is known as the law of rectilinear diameters [117]. Close to the critical point, we cannot safely determine the local densities of the coexisting phases, as the peaks of the local density histograms flatten due to fluctuations in the density.

We have checked that the qualitative properties of the system reported in this section still hold for other system sizes. In particular, we have simulated a small number of the

parameter space points for systems of 2500 and 8000 particles and found that the resulting state diagrams and coexisting densities remain essentially unchanged.

Moreover, we have also performed simulations for dense systems ($\rho\sigma^2 = 0.55$ and 0.6) for a limited number of self-propulsion speeds $v_0\sigma/\tau$. We have validated that the local density of the dense phase for these simulations remains in close proximity with the values found in the simulations of more dilute systems. Hence, the high densities part of the envelope shown in Fig. 6.6, which would correspond to a binodal envelope in an equilibrium system, is indeed collapsing onto one curve. Since the interaction between particles is anisotropic and thus pressure is not an equation of state for the system [90], this collapse constitutes a surprising result.

6.3.3 Oscillatory regime

In Fig. 6.7 we show a time series of snapshots of a system in the oscillatory regime. On each snapshot we superimpose the displacement field, unnormalized by the density. To calculate this field, we divided the simulation box into a square lattice of cell length 7σ, and summed the displacement of the particles in each cell, see Eq. 6.4. Note that we have ignored the contribution from translational diffusion.

This figure shows two instances where the system transitions from a homogeneous fluid to a phase coexistence and back to the fluid. The two snapshots that show phase coexistence ($t/\tau = 610, 1089$) are taken slightly before the largest cluster breaks apart. In these two subfigures the displacement field clearly shows collective rotation of the cluster and formation of vortices. Inspection of the majority of breaking events in the simulations, using the displacement field as a guide for the collective dynamics, reveals that rotation of the cluster is a general feature that precedes cluster destruction. Note that the packing of squares in the crystalline clusters of the oscillatory regime is similar to the phase separated regime as described in Section 6.3.2. That is, all clusters are composed from square crystalline domains. Also, the local densities of the clusters in the oscillatory regime have similar values to the local densities in Fig. 6.6, which correspond to the phase separated regime.

In an effort to quantify and understand the destruction of a large cluster, we plot three different quantities in Fig. 6.8: the fraction of particles which belong to the largest cluster f_{lc}, the angular momentum L_{lc} of the largest cluster and the total potential energy of the system U_{tot}. The angular momentum $L_{\mathrm{lc}}(t)$ is given by

$$L_{\mathrm{lc}}(t) = \sum_{i=1}^{N_{\mathrm{lc}}} [d\boldsymbol{r}_i(t) \times (\boldsymbol{r}_i(t) - \boldsymbol{r}_{\mathrm{lc}}(t))] \cdot \boldsymbol{z}, \tag{6.9}$$

where N_{lc} denotes the total number of particles in the largest cluster of the system, $\boldsymbol{r}_{\mathrm{lc}}$ is the center of the cluster and the displacement $d\boldsymbol{r}_i$ is calculated from Eq. 6.4 while omitting the term that accounts for translational diffusion. The potential energy of the system is calculated using Eqs. 6.1 and 6.2.

In Fig. 6.8 we see that the growth of a cluster (growth of f_{lc}) is accompanied by an oscillation of its angular momentum. When the cluster obtains its maximum size, the angular momentum also has a maximum in its absolute value. The growth of the cluster

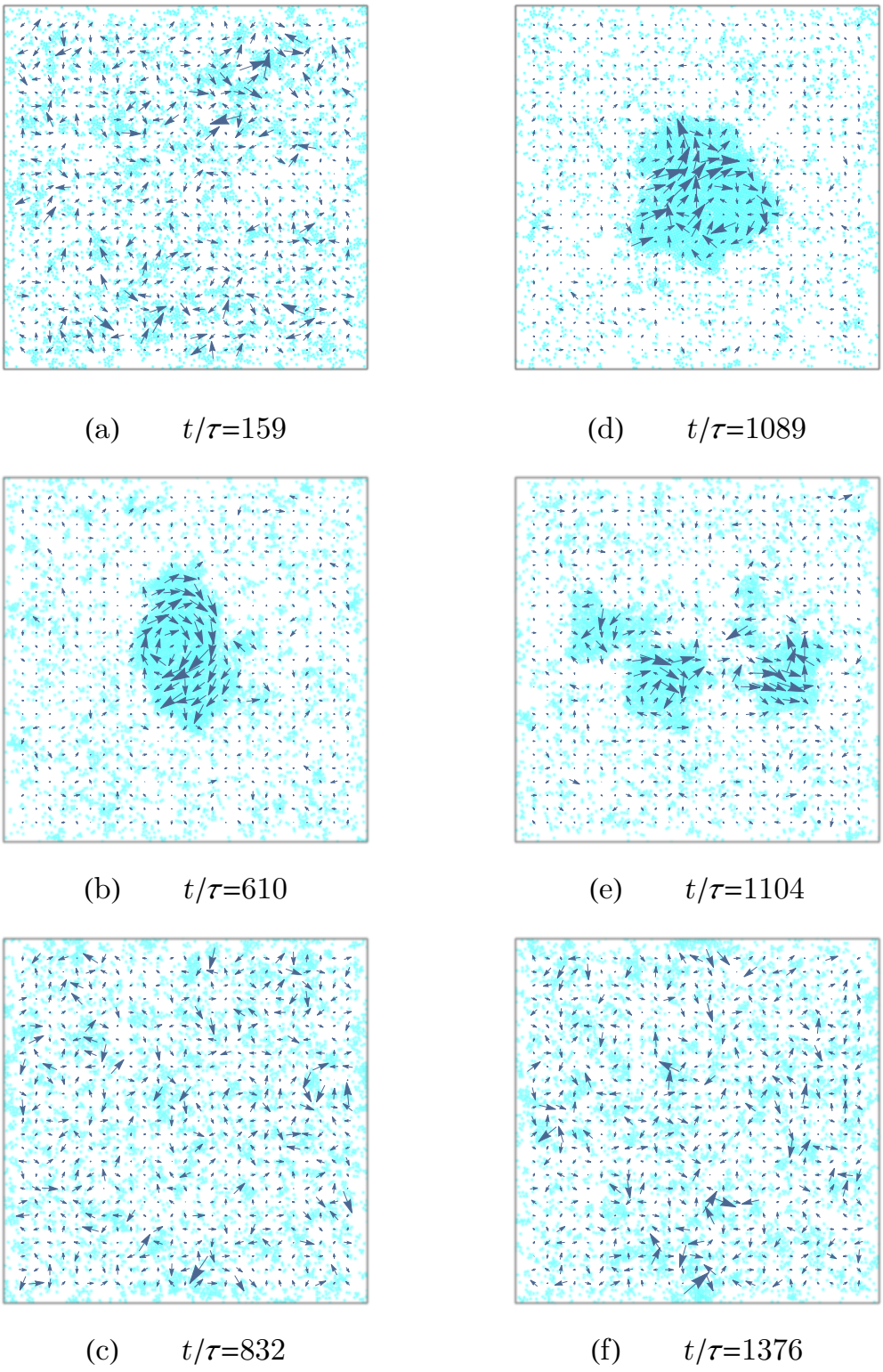

(a) t/τ=159 (d) t/τ=1089

(b) t/τ=610 (e) t/τ=1104

(c) t/τ=832 (f) t/τ=1376

Figure 6.7: Snapshots of the system at different times. The arrows indicate the direction and relative magnitude of the displacement field. The parameters for this system are $\rho\sigma^2 = 0.14$ and $v_0\sigma/\tau = 100$.

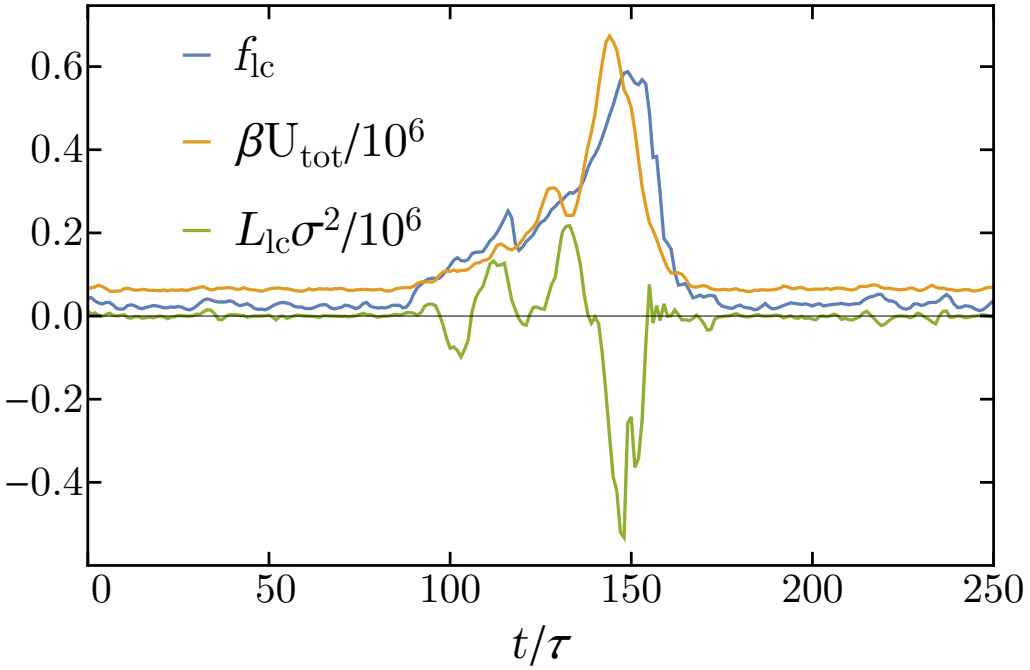

Figure 6.8: Time evolution of the degree of clustering $f_{\rm lc}$, the total potential energy of the system $U_{\rm tot}$ and the angular momentum of the system's largest cluster $L_{\rm lc}$ during nucleation, growth and destruction of a cluster (for this system $\rho\sigma^2 = 0.14$ and $v_0\sigma/\tau = 100$).

also causes a sharp increase in the potential energy of the system. This increase indicates that strong forces are present in the interior of the formed cluster. Afterwards, the cluster swiftly disintegrates ($f_{\rm lc} \simeq 0$) and the potential energy of the system returns to low values. We stress that the features shown in the plot and described above hold in general for all the nucleation and breaking events we studied.

The above results lead us to the following picture for the clustering of active squares in the oscillatory and phase coexistence regime: once a small cluster appears, it keeps growing by absorbing the incoming particles from the gas. Naturally, the particles that attach to the cluster will have on average their axes of self-propulsion pointing at the center of the cluster. However, since the square particles that belong to the cluster cannot change their orientation, an anisotropy of forces will eventually create one (Fig.6.7(b)) or more (Fig. 6.7(d)) vortices that rotate the cluster as a whole.

Once a vortex appears, particles relocate and are free to collectively escape the cluster in large groups. In the oscillatory regime, the remaining pieces of the cluster may disintegrate completely so that the system returns to a homogeneous state, while in the phase coexistence regime at least one cluster survives due to the fast absorption of gas particles.

The behaviour of the squares can be contrasted with the behaviour of active discs, where no oscillations have been reported. In the case of discs, the particles that accumulate at the surface of a cluster also point towards the center of the cluster, but can leave the cluster once their axis of self-propulsion points outwards due to rotational diffusion. The cluster is then stabilized by an influx and outflux of particles at its surface [61]. Moreover, particles in the inner layers can relax their orientation and hence no large

torques accumulate. On the other hand, squares in the cluster are unable to rotate freely due to interactions with neighboring particles. This leads to accumulating internal forces and torques, that rotate and eventually destabilize the cluster.

Oscillations between states have also been found in other active systems. Self-propelled dumbbells show very similar behaviour, and close to the binodal lines this system continuously moves from a clustered state to a uniform state [76]. Furthermore, a system of self-propelled rods can also oscillate between an orientationally ordered state (phase coexistence between a band-like structure with nematic order and a uniform, low density fluid) and an aggregated state (phase coexistence between a dense cluster with no global orientational order and a fluid) [77]. Also, when the aggregated state is stable, large polar clusters continuously escape the cluster. What is common in the aforementioned systems and the system of self-propelled squares is that, once an orientationally disordered aggregate forms, large stresses develop due to the inability of the clustered particles to relax their orientation. These large stresses will induce either the destruction of the aggregate, or the constant ejection of large groups of particles. As mentioned in Ref. [77], the presence of large stresses and oscillations is not consistent with the phase separation of self-propelled discs, which is well captured by a classical description.

An open question, with regard to the state oscillations in all the aforementioned systems, is whether there is a characteristic frequency related to these oscillations. To fully answer such a question, one would have to study the time evolution of a system in the oscillatory regime (see for example Fig. 6.4) for a long period, which is currently outside of our computational capabilities. However, it should be noted that our system did not oscillate between two clearly distinctive states, but rather the crystalline cluster disintegrates at disparate stages of the growth process. This is evident in Fig. 4(a), as the height of the different peaks, which corresponds to different cluster sizes, differs significantly for different disintegration points. Our results suggest that there is a broad distribution of phase separated states that lead to cluster disintegration and that, in all likelihood, the oscillations are not associated with a characteristic frequency.

6.3.4 Coarsening

As we have already seen in Section 6.3.2, in the phase coexistence region we find static statistical properties similar to the properties of self-propelled discs and equilibrium systems. On the other hand, in Section 6.3.3, the study of the cluster dynamics demonstrated striking differences between self-propelled squares and discs. The differences in cluster dynamics motivate us to study the coarsening dynamics. Our main tools for this study are the structure factor $S(k)$ and the averaged cluster size $\langle N_{\mathrm{cs}} \rangle$. $S(k)$ is the orientational average of the full structure factor

$$S\left(\boldsymbol{k}\right) = \frac{1}{N} \sum_{i,j=1}^{N} e^{-i\boldsymbol{k}\cdot\left(\boldsymbol{r}_i - \boldsymbol{r}_j\right)}, \tag{6.10}$$

and $\langle N_{\mathrm{cs}} \rangle = \sum_{A=1}^{N} A p_A$, where p_A is the normalized probability of finding a cluster of size A in the system.

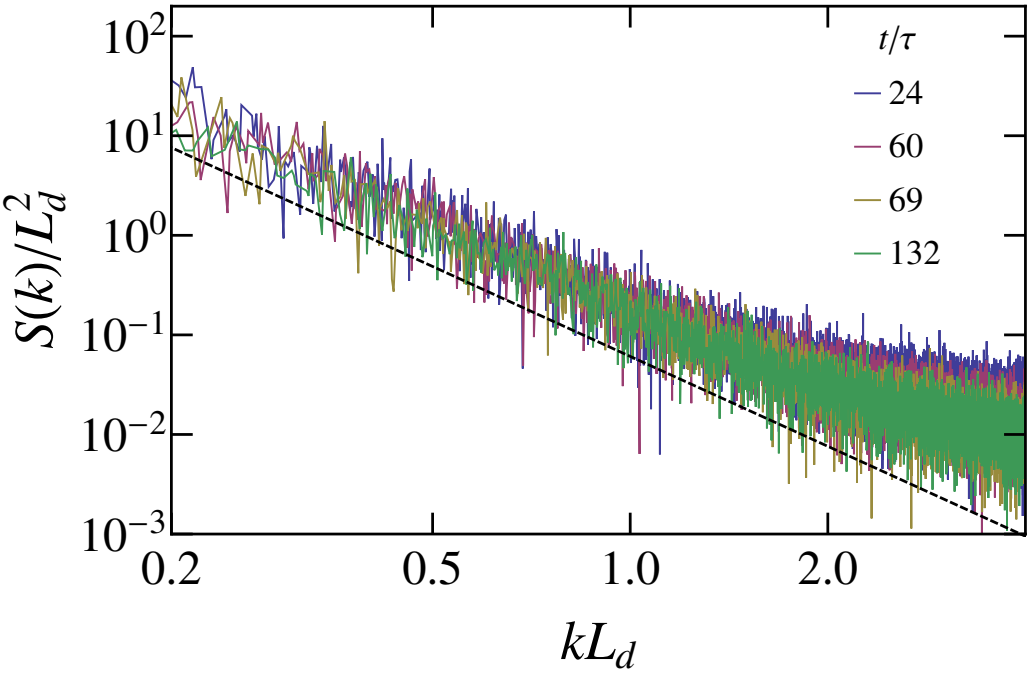

Figure 6.9: Scaled structure factor $S(k)/L_\mathrm{d}^2$ as a function of kL_d for different time instances. The black dashed line follows the scaling k^{-3}. For this system $\rho\sigma^2 = 0.2$ and $v_0\sigma/\tau = 80$.

To achieve better statistics and longer coarsening times, we used a system of 250000 particles. Then, we computed the characteristic domain length $L_\mathrm{d}(t)$ [62] using

$$L_\mathrm{d}(t) = 2\pi \left[\frac{\sum_{2\pi/L}^{k_\mathrm{cut}} kS(k,t)dk}{\sum_{2\pi/L}^{k_\mathrm{cut}} S(k,t)dk} \right]^{-1}, \tag{6.11}$$

where k_cut is taken as the first minimum of $S(k,t)$ and L is the length of the simulation box.

Using the structure factor and the characteristic domain length we test the dynamical scaling hypothesis for our system [163, 164]. According to this hypothesis, in two dimensions, the time behavior of the structure factor in the coarsening regime follows from the relation

$$S(k,t) = [L_\mathrm{d}(t)]^2 \, f(kL_\mathrm{d}), \tag{6.12}$$

where f is a time independent function. In Fig. 6.9 we plot $S(k)/L_\mathrm{d}^2$ for different (late) times, and we find that it indeed shows dynamical scaling behaviour, as the different curves fall onto each other for small wavelengths. Thus, we find that the domain structure in our system is actually time independent in the late time coarsening regime. On top of this, we see that the tail of the structure factor scales as $L_\mathrm{d}^{-1}k^{-3}$, in accordance with Porod's law in two dimensions [164].

We also study the coarsening dynamics by following the average cluster size $\langle N_\mathrm{cs}\rangle$ with time, shown in Fig. 6.10. This figure shows that cluster coarsening scales slightly faster than t, up to the latest times we could simulate, and surpasses the $t^{1/2}$ scaling that

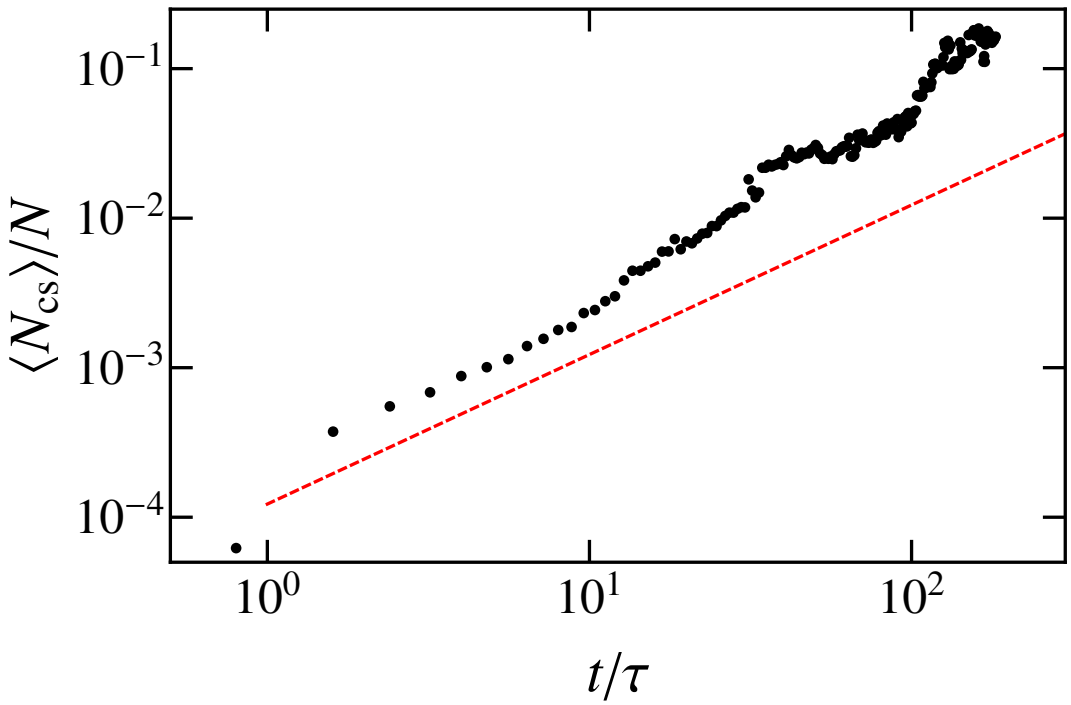

Figure 6.10: Evolution of the average cluster size $\langle N_{cs} \rangle$ with time. The red dashed line scales as t. For this system $\rho\sigma^2 = 0.2$ and $v_0\sigma/\tau = 80$.

active discs [61] and polar systems [112] show. We have verified that the same super-diffusive coarsening scaling holds for other parameter space points. We speculate that the rapid coarsening might be caused by the peculiar dynamics of the individual clusters, as inspection of our simulations shows that the clusters, apart from continuously breaking apart and reassembling, also move in space. This movement boosts the frequency of cluster collisions. The two aforementioned effects may cause a ballistic growth of the average cluster size for all the time scales examined.

However, we would like to note that our results may be limited due to the finite size of our system, and in the infinite system size limit one may recover the scaling $t^{1/2}$ for late times that should hold for diffusive systems with no hydrodynamic interactions, for example, a system of passive Brownian particles or self-propelled particles with no aligning interactions [165]. Thus, further study needs to be done in this aspect.

6.4 Conclusions

We have studied the state behaviour of self-propelled Brownian squares using computer simulations. We find that for low densities and slow swimming speeds the system is in a uniform fluid phase, while for high densities and fast swimmers the system phase separates into a high density and a low density phase. In between these two regimes, there is a third regime where the system oscillates continuously between the two aforementioned states.

By studying the phase coexistence regime, we found that the dense phase is made of square crystalline domains and that the time averaged local densities of the coexisting crystal and fluid are independent of the overall system density. Next, we demonstrated that the rupture of a crystalline cluster in the oscillatory regime is accompanied by a rotational motion of the cluster. This rotation originates from the large stresses that are developed in the interior of the cluster. Furthermore, we find that the system coarsens at a much faster rate than a purely diffusive system, which may be caused by the intriguing dynamics of individual clusters.

Comparing our results with existing literature for self-propelled discs, we discover that the two systems share many similarities, as they both undergo phase separation due to a kinetic trapping mechanism and the coexisting local densities are a function of the swimming speed alone. However, there are also striking differences, including the oscillatory regime and the fast, super-diffusive coarsening rates, which are possibly caused by the large stresses developed in a crystalline cluster of self-propelled squares. It is also important to note that the collapse of the binodal lines for different total densities of the system is a direct consequence of the existence of an equation of state in the case of discs but is a surprising result in the case of squares, where mechanical pressure is not a function of the state of the system. We will discuss in more detail this interesting point in the next chapter.

On the other hand, the peculiar dynamics of clusters formed by self-propelled squares resembles the dynamics found in systems of self-propelled dumbbells and rods, where system spanning clusters can also continuously form and disintegrate, and large groups of particles can frequently escape large clusters. Future work should look into the stability of the oscillatory behaviour in the infinite system size limit, as well as measuring a possible periodicity of such clustering and disintegration events. Lastly, a more detailed comparison between the dynamic behaviour of different self-propelled and anisotropic particles may shed light to universal features of the coarsening dynamics and the state behaviour near the phase separation regime.

Acknowledgments

The work presented in this chapter was performed in collaboration with Sela Samin. Sela helped with the interpretation of the results and suggested directions of research that were proven useful. Additionally, we would like to thank Bram Bet for providing the value of the rotational diffusion coefficient for a square particle.

7

Phase coexistence of spherical self-propelled particles with anisotropic interactions

We study phase coexistence in a system of purely repulsive and anti-aligning self-propelled Brownian particles that undergoes motility-induced phase separation. We quantify the force balance and show that the mechanical equilibrium of the coexisting phases cannot be captured *via* a local pressure definition, even when the swim pressure is considered. However, we show that chemical equilibrium of the coexisting phases can be shown by bringing the system in contact with a particle reservoir and showing that the reservoirs that correspond to coexisting phases are identical.

7.1 Introduction

During the first four research chapters of this thesis, Chapters 2-5, we studied active matter systems whose components interact with one another *via* purely isotropic (radially symmetric) interactions. We found that many properties that govern phase coexistences for this subgroup of active matter systems bore similarities to the corresponding properties of equilibrium systems. Arguably, the most important and surprising result we reported was a numerical method to construct the phase diagram of an active system by quantifying conditions for the mechanical and chemical equilibrium of coexisting phases (see Chapter 5). In the subsequent Chapter 6 we studied the self-assembly of particles with an anisotropic (square) shape and again found a fairly equilibrium-like phase diagram for the system. Motivated by these two results, in the present chapter we study a system comprised of spherical particles, but with explicit anisotropic interactions between them. Our ultimate goal is to investigate whether one can predict the phase diagram of the system utilizing numerical methods such as the one presented in Chapter 5.

One of the great successes of equilibrium statistical physics is its ability to predict phase diagrams for the self-assembly of particles of any given shape and interaction potential [22]. Phase diagrams are constructed by demanding the same set of intensive variables for coexisting phases. The intensive variables of an equilibrium bulk system uniquely characterize it and for a traditional thermodynamics system these are the temperature, the pressure and the chemical potential and are conjugate to the entropy, the volume and the number of particles of the system respectively.

Currently, these three intensive variables have not yet uniquely been defined for active matter systems. Temperature in active systems is in many cases defined only as an effective quantity that maps the properties of the out-of-equilibrium system, for example its equation of state, to a corresponding equilibrium system [99–101]. However, for the purpose of constructing phase diagrams, the temperature can be considered as a function of only the propulsion speed and the translational and rotational diffusion of particles, so that is by definition equal in coexisting phases of the same species (see for example Refs. [86, 102] and Chapter 5). Moreover, the definition of a mechanical pressure for active matter systems has been addressed in various approaches [86, 89, 91, 93, 94]. Most relevant to our discussion,while it has been shown that pressure can be well defined for systems that involve only isotropic interactions, interparticle and particle-wall anisotropic interactions lead to the absence of an equation of state [90, 127]. Lastly, a definition of the chemical potential has been also proposed following different paths, for example either following a generalized free-energy theory or a dynamic density functional theory approach [62, 86, 103]. In Chapter 5 we used a numerical method in order to measure a variable conjugate to the number of particles, namely the density of a reservoir in contact to a single phase. We showed that this variable is enough, together with the known definition of a pressure in the absence of anisotropic interactions, to successfully predict the phase diagram. This result hinted to the existence of a chemical potential for active systems.

On the other hand, given the lack of an equation of state for the case of active systems with anisotropic interactions, it may appear that predicting phase diagrams is impossible in this case. However, note that even though the pressure as defined in Ref. [127] may not be a state function, that is it will depend on the potential of a surrounding wall, it is

unclear whether it assumes the same value in coexisting phases of a spontaneously phase separated system. Furthermore, given the complications that arise for the pressure in the presence of torques, it is uncertain whether our numerical method to show chemical equilibrium of coexisting phases for systems with purely isotropic interactions, shown in Chapter 5, could be used to demonstrate chemical equilibrium for systems with anisotropic interactions as well. If such a numerical method could indeed be used, it would suggest that a chemical potential exists for a larger class of active matter systems than the results of Chapter 5 solely imply.

In the present chapter we address these two important questions by studying a system that undergoes motility-induced phase separation (MIPS) and whose particles explicitly exert torques onto one another. Applying a numerical method similar to the one presented in Chapter 5, we show that coexisting phases share the same value for the reservoir density. Our study thus suggests that chemical equilibrium can be directly shown for coexisting phases. However, we find that two coexisting phases do not share the same values for the bulk pressure, when using the current formalism for the pressure of active systems. Whether this inequality is due to the formalism itself or it is a general property of active systems with anisotropic interactions is still unclear to us.

The structure of the chapter is as follows: in Section 7.2.1 we describe the model and the dynamics implemented for our simulations and in Section 7.2.2 we describe two different formulations for the pressure of an active system and give an equation for the force balance. We present the method of quantifying a variable conjugate to the number of particles in Section 7.2.3. In Section 7.3.1 we study phase coexistences using direct coexistence simulations, discuss the various components of the force balance of the phase separated system and present state diagrams. We test whether our numerical method can capture chemical equilibrium in Section 7.3.2 and we conclude in Section 7.4.

7.2 Methods

7.2.1 Model and dynamics

We consider a two-dimensional system, consisting of disc-like particles of diameter σ. The position of the center of mass of the i-th particle at time t is given by the vector $\mathbf{r}_i(t)$ while its orientation is given by the unit vector $\boldsymbol{u}_i(t) = (\cos\theta_i(t), \sin\theta_i(t))$, where $\theta_i(t) \in [0, 2\pi)$ is the azimuthal angle between a fixed axis in the lab frame and the vector $\boldsymbol{u}_i$.

Particles interact *via* the radially symmetric Weeks-Chandler-Andersen potential:

$$U(r_{ij}) = 4\epsilon \left[\left(\frac{\sigma}{r_{ij}} \right)^{12} - \left(\frac{\sigma}{r_{ij}} \right)^{6} + \frac{1}{4} \right] \tag{7.1}$$

truncated and shifted at $r_c = 2^{1/6}\sigma$, where $r_{ij} = |\mathbf{r}_i - \mathbf{r}_j|$ and ϵ controls the strength of the interaction. On top of the radially symmetric potential, particles also apply torques to one another, such that the torque applied to particle i is

$$\Gamma_i = -\frac{\kappa}{\mathcal{N}_i} \sum_{j=1}^{\mathcal{N}_i} \sin\left(\theta_i - \theta_j\right), \tag{7.2}$$

where κ controls the strength of the interaction and $\mathcal{N}_i$ is the number of particles within a distance $2^{1/6}\sigma$ from particle i. This torque reorients particle i away from the orientations of particles that are in close proximity to it and tends to make them anti-parallel. Note that Eq. 7.2 is of the form of the Vicsek interaction, but with an extra minus sign [63]. We find that such an anti-aligning interaction between particles leads to relatively stable interfaces when motility-induced phase separation takes place in the system. Thus, our motivation for the use of the specific anisotropic interaction is merely practical, as the two requirements for a suitable model for our investigation are that the particles should interact *via* anisotropic interactions and that the system can undergo motility-induced phase separation. As a point of interest, these two requirements were also satisfied by the model we studied in Chapter 6. However, we did not select the model of self-propelled squares for our investigation since it turns out that is not possible to construct a motility-induced phase separated system in a slab geometry with this model. Specifically, when the dense crystalline phase spans completely one dimension of the box, we find that it is not able to rotate, thus the particles that are part of this phase cannot relax their orientation. As a consequence, eventually all particles become part of the dense crystalline phase. This problem arises due to the finite size of the system combined with periodic boundary conditions. Hence, to avoid this issue we chose a model of spherical particles with explicit torques.

To make the particles active, we include a self-propelling speed of constant magnitude v_0 that acts along $\boldsymbol{u}$. Following Ref. [62], we impose a constant ratio between the self-propulsion speed and the strength of the interparticle interactions $v_0/\beta\epsilon = 24$ in order to set a constant "effective" diameter between particles that collide at a 90° angle. Additionally, we consider our particles immersed in a solvent whose damping coefficient is given by η_{tr} for the translational and η_r for the rotational motion of the particles. Since we are interested in the regime that applies to the colloidal world, we use overdamped Langevin (Brownian) dynamics for the equations of motion, which includes the solvent-particle interactions implicitly and neglects the inertia of the particles. Thus, the translational and rotational equations of motion are

$$\frac{d\boldsymbol{r}_i}{dt} = -\frac{1}{\eta_{tr}} \sum_{j \neq i} \nabla_{\boldsymbol{r}_i} U(r_{ij}) + v_0 \boldsymbol{u}_i + \sqrt{2D_{tr}}\boldsymbol{\xi}_i^{tr}, \tag{7.3}$$

$$\frac{d\theta_i}{dt} = \frac{1}{\eta_r}\Gamma_i + \sqrt{2D_r}\xi_i^r, \tag{7.4}$$

where $D_{tr} = 1/(\beta\eta_{tr})$ is the translational diffusion coefficient and $\beta = 1/k_BT$, where k_B is the Boltzmann constant and T is the temperature of the surrounding solvent. $D_r = 1/(\beta\eta_r)$ denotes the rotational diffusion coefficient and is related to the translational diffusion coefficient *via* the Stokes-Einstein relation $D_r = 3D_{tr}/\sigma^2$. The stochastic terms $\boldsymbol{\xi}_i^{tr}$ and ξ_i^r are respectively a two-dimensional vector and scalar with zero mean and unit variance.

We measure time in units of the short-time diffusion $\tau = \sigma^2/D_{tr}$. Equations 7.3 and 7.4 were numerically integrated using an Euler-Maruyama integration scheme [107]. A time step of $dt = 10^{-5}\tau$ was used for the numeric integration of the equations of motion.

7.2.2 Force balance and pressure

Below we define the local and the virial pressure for systems of self-propelled particles and give an equation for the local force balance. In this section we restrict ourselves in a brief presentation of the expressions and refer the reader to Appendix A for their derivation and an extensive discussion of the force balance equation.

Perhaps the first attempt to define a pressure for active systems appeared in the work of Takatori *et al.*, where the direct contribution of self-propulsion to the mechanical pressure of a system containing self-propelled particles was given by the expression [123]

$$P^{\mathrm{vir}}_{\mathrm{swim}} = \frac{\eta_{tr} v_0}{dV} \left\langle \sum_i \boldsymbol{r}_i \cdot \boldsymbol{u}_i \right\rangle, \tag{7.5}$$

where the sum is over all particles and the brackets can be seen as a configurational average or an average over time, d is the number of dimensions and V is the total volume of the system. Note that Eq. 7.5 only prescribes the direct contribution of self-propulsion to the pressure of the system, and the total pressure of the system also includes the ideal $P^{\mathrm{vir}}_{\mathrm{id}}$ and interaction $P^{\mathrm{vir}}_{\mathrm{inter}}$ components of the pressure which are given by

$$P^{\mathrm{vir}}_{\mathrm{id}} = \rho/\beta \tag{7.6}$$

$$P^{\mathrm{vir}}_{\mathrm{inter}} = -\frac{1}{2dV} \left\langle \sum_i \sum_{j \neq i} \boldsymbol{r}_{ij} \cdot \nabla_{\boldsymbol{r}_i} U(r_{ij}) \right\rangle, \tag{7.7}$$

where ρ is the total density of the system and $\boldsymbol{r}_{ij} = \boldsymbol{r}_j - \boldsymbol{r}_i$. Equation 7.5 was confirmed by other theoretical treatments of active matter as the direct contribution of self-propulsion to the pressure [92, 122], and has been used in order to demonstrate mechanical equilibrium between coexisting phases of self-propelled particles [91]. We will refer to the quantity that is described by the sum of Eqs. 7.5-7.7 as the virial pressure of the system P^{vir}. A theoretical derivation of this expression can be found in Appendix A. Note that for systems with periodic boundary conditions the absolute positions of the particles must be used in Eq. 7.5, so that the swim virial pressure will depend on the history of the system. Also, note that the expression for the virial pressure holds for any homogeneous system of self-propelled particles with periodic boundary conditions irrespective of the interparticle interactions.

A different approach to the problem, which has culminated in the work of Solon and coworkers [127], starts by constructing the Fokker-Planck equation of the system and studying the force balance locally. We present a complete overview of this approach in Appendix A but summarize the results in the following.

Let us assume a slab geometry with the long axis of the two-dimensional simulation box along the $\hat{x}$ dimension, such that the x-axis is normal to all interfaces, which will span the $\hat{y}$ dimension of the box. In order to write down an expression for the x (normal

component) of the local pressure, first we define the moments

$$\rho(\boldsymbol{r}) = \sum_k \delta(\boldsymbol{r} - \boldsymbol{r}_k), \tag{7.8}$$

$$\boldsymbol{m}_i(\boldsymbol{r}) = \sum_k \boldsymbol{u}_{k,i}\delta(\boldsymbol{r} - \boldsymbol{r}_k), \tag{7.9}$$

$$\boldsymbol{s}_{ij}(\boldsymbol{r}) = \sum_k \boldsymbol{u}_{k,i}\boldsymbol{u}_{k,j}\delta(\boldsymbol{r} - \boldsymbol{r}_k), \tag{7.10}$$

where i, j denote the spatial components of the corresponding vectors and tensors and the sum is over all particles. $\rho(\boldsymbol{r})$ is the local density of particles while $\boldsymbol{m}(\boldsymbol{r})$ is the corresponding local polarization. The x (normal) component of the local pressure of the system $P^{\text{local}}(x)$ for particles that do not experience any torques can then be calculated using the equation

$$P^{\text{local}}(x) = P^{\text{local}}_{\text{id}}(x) + P^{\text{local}}_{\text{inter}}(x) + P^{\text{local}}_{\text{swim}}(x), \tag{7.11}$$

where

$$P^{\text{local}}_{\text{id}}(x) = \langle\rho(x)\rangle\, k_BT = \frac{1}{L_y}\int dy\, \langle\rho(\boldsymbol{r})\rangle\, k_BT, \tag{7.12}$$

is the ideal component of the pressure, where we have spatially integrated over the $\hat{y}$ dimension and divided by the length of the box L_y that we integrated over and brackets denote an average at the steady state over noise realizations. Additionally,

$$P^{\text{local}}_{\text{inter}}(x) = \frac{1}{L_y}\int dy \int_{x''<x} dx'' \int_{x'>x} d\boldsymbol{r}'\partial_{x''}U(|\boldsymbol{r}' - \boldsymbol{r}''|)\, \langle\rho(\boldsymbol{r}'')\rho(\boldsymbol{r}')\rangle\,, \tag{7.13}$$

is the standard local virial term and $\boldsymbol{r}'' = (x'', y)$, and finally

$$P^{\text{local}}_{\text{swim}}(x) = \frac{1}{L_y}\int dy \frac{\eta_{tr}\upsilon_0}{(d-1)D_r}\Big[\upsilon_0\, \langle\boldsymbol{s}_{xx}(\boldsymbol{r})\rangle + D_{tr}\partial_x\, \langle\boldsymbol{m}_x(\boldsymbol{r})\rangle - \frac{1}{\eta_{tr}}\int d\boldsymbol{r}'\partial_x U(|\boldsymbol{r}' - \boldsymbol{r}|)\, \langle\boldsymbol{m}_x(\boldsymbol{r})\rho(\boldsymbol{r}')\rangle\Big] \tag{7.14}$$

is the local swim pressure.

In our particle simulations we divide the simulation box into slabs, and measure the normal component of the pressure for each slab. The contributions to each slab of the ideal and swim components of the pressure can be calculated straightforwardly, while for the virial component we follow Ref. [131]. Note that in the case of purely isotropic interactions between particles, the local bulk pressure will be equal to the virial pressure of bulk phases [122] (see also Chapters 3 and 5).

In the general case where particles also exert torques onto one another, the force balance along the x-axis can be written as (periodic boundary conditions are applied, see Appendix A)

$$\partial_x P^{\text{local}}(x) - F^{\text{ani}}(x) = 0, \tag{7.15}$$

where the local anisotropic force $F^{\text{ani}}(x)$ is defined by

$$F^{\text{ani}}(x) = \frac{1}{L_y}\int dy \frac{\upsilon_0}{(d-1)D_{tr}} \int d\Omega \partial_\Omega \boldsymbol{u}_x(\Omega) \int d\boldsymbol{r}' \int d\Omega' \Gamma(\boldsymbol{r}, \boldsymbol{r}', \Omega, \Omega') \left\langle \Psi(\boldsymbol{r}', \Omega')\Psi(\boldsymbol{r}, \Omega)\right\rangle , \tag{7.16}$$

with

$$\Psi(\boldsymbol{r}, \theta) = \sum_{i=1}^{N} \delta(\boldsymbol{r} - \boldsymbol{r}_i)\delta(\theta - \theta_i) \tag{7.17}$$

the probability of finding a particle at position $\boldsymbol{r}$ with orientation θ. Note that Eq. 7.16 cannot be written as a spatial derivative, thus it cannot be incorporated in the pressure term. Integrating Eq. 7.15 over a region with boundaries x_1 and x_2 gives

$$P^{\text{local}}(x_2) - P^{\text{local}}(x_1) = \int_{x_1}^{x_2} dx F^{\text{ani}}(x) = P^{\text{ani}}(x_2, x_1), \tag{7.18}$$

where, for later convenience, we have defined the local pressure difference between points x_1 and x_2 due to the presence of the anisotropic force as $P^{\text{ani}}(x_2, x_1)$.Thus, the local pressure difference is equal to the integral over the anisotropic local force. As we show in Appendix A, for a bulk phase we have $F^{\text{ani}}(x) = 0$, or equivalently the local pressure remains constant. However, from the form of Eqs. 7.15 and 7.16 it is not *a priori* evident whether there is a non-zero contribution of the anisotropic force in the case of an interface between bulk phases. We will set out to investigate this in this chapter. Also, we will use the virial pressure P^{vir} (Eqs. 7.5-7.7) for the sole purpose of verifying the values of the local pressure P^{local} (Eqs. 7.11-7.14) when appropriate.

7.2.3 Chemical equilibrium and reservoir simulations

In this chapter we extend the method of connecting a bulk phase to a reservoir, which we presented in Chapter 5 for binary systems, to systems of a single species. Below we describe the modified method in detail.

To quantify the properties of a bulk phase associated with chemical equilibrium, we connect a bulk phase of a single species of particles to a reservoir that contains the same species of particles. However, in order to employ the same method we used in Chapter 5, we artificially divide the particles of the bulk phase into two species by simply colouring them with two different colours, creating in this way a binary mixture. Note that the particles of the two species are actually identical when it comes to their interparticle interactions and dynamics. Moreover, we divide our simulation box into two sections, one which contains the "bulk" binary phase, and the other part of the box acting as a particle reservoir of one species only, which we call species R. We place a semi-permeable membrane at the division, which only allows particles of species R to pass through at no energy cost. For the other species, the wall is impenetrable with the wall-particle interaction given by a purely repulsive Weeks-Chandler-Andersen-like wall potential:

$$\beta U_{\text{wall}}(x) = 4\beta\epsilon_{\text{wall}} \left(\left(\frac{\sigma}{x}\right)^{12} - \left(\frac{\sigma}{x}\right)^{6} + \frac{1}{4} \right), \tag{7.19}$$

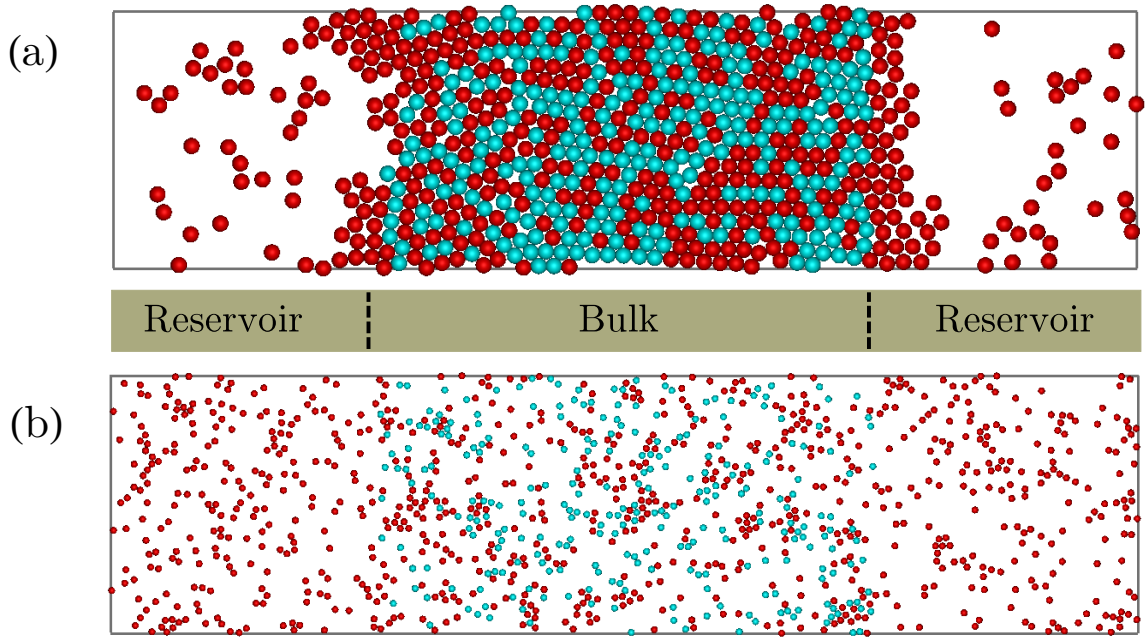

Figure 7.1: (a) The crystal in contact with a reservoir. (b) The gas in contact with a reservoir. The location of the semipermeable membrane is denoted by the dotted lines. The colouring of the particles in red and blue is artificial, which means that there is no difference in the dynamics or the interactions of the two species. The only difference is that the red particles can travel through the membrane at no energy cost while the blue particles are confined in the bulk part of the simulation box. This enables us to freely choose the composition of the binary mixture. We fix the composition at 0.5 for all the points in the parameter space such that a given density of the bulk binary phase corresponds to a unique density of the reservoir. Also, note that in this figure we show small systems of a few hundred particles while for the results presented in Section **??** each simulation involves approximately 15000 particles.

where x is the distance of a particle to the nearest semi-permeable wall, $\beta\epsilon_{\text{wall}} = 40$, and the interaction is cut off at a distance $x = 2^{1/6}\sigma$. Thus, effectively the only difference between the two species is that one of them can pass through the wall while the other species cannot. In addition to the wall repulsion, we also apply a torque to the particles of the confined species that reorients these particles away from the wall. This torque was applied in order to minimize the accumulation of particles at the wall. Reassuringly, we find that the applied torque does not affect the bulk part of the simulation, since the orientation of the particles relaxes rapidly as we move away from the wall. For snapshots of such simulations see Fig. 7.1.

At the beginning of the simulation, the bulk phase consists of the desired total density of particles and half of the particles are assigned to species R while the other half are assigned to the confined species. Note that in principle any value for the composition of the binary phase can be chosen since the colouring of particles in the bulk and their division into two species is arbitrary. We chose a composition of 0.5 since it leads to a binary phase that is less susceptible to fluctuations of the number of particles of both species. The reservoir contains a gas of species R with a randomly chosen initial density.

During the course of the simulation, particles of species R travel from the "bulk" part of the simulation box to the reservoir and *vice-versa*, while the confined particles move only between the walls. We measure the density of each species in the central area of the bulk phase in regular intervals and to correct for the deviations from the targeted total density and the desired composition 0.5 of species R, we tune the number of particles of both species during equilibration by randomly adding or removing particles, as described in Chapter 5. Eventually, the partial densities of both species in the bulk region reach the desired constants and the density of the reservoir assumes a constant value.

7.3 Results

7.3.1 Direct coexistence simulations

To start our investigation, we perform a series of simulations for different values of the torque coefficient κ in the regime where the system undergoes motility-induced phase separation. To this end, we simulated 15000 particles in a two-dimensional elongated box with dimensions $L_x = 5L_y$. This choice for the dimensions of the box ensures the formation of two flat interfaces that span the box perpendicular to its long axis when phase separation takes place. The direct coexistence simulations were performed for torque coefficients $\beta\kappa = 0, 5, 10$ and 15, total densities $\rho\sigma^2 = 0.5, 0.65$ and 0.8 and different propulsion speeds v_0. The simulations were initiated from a configuration where all particles are part of a hexagonal crystal and ran for approximately 750τ. We collected data only for the last 250τ. During the data collection period of our simulation we divide the box into slabs of length σ across the long x-axis and measure the density of particles in each slab as well as the different contributions to the local force balance Eq. 7.15. Note that during the course of our simulation we kept the center of mass of the system fixed at position $x = 0$, such that the dense phase was always located at the center of our box.

In Fig. 7.2 we show typical results for the measurements as well as a snapshot of the phase separated system. A dense phase, located at the middle of the simulation

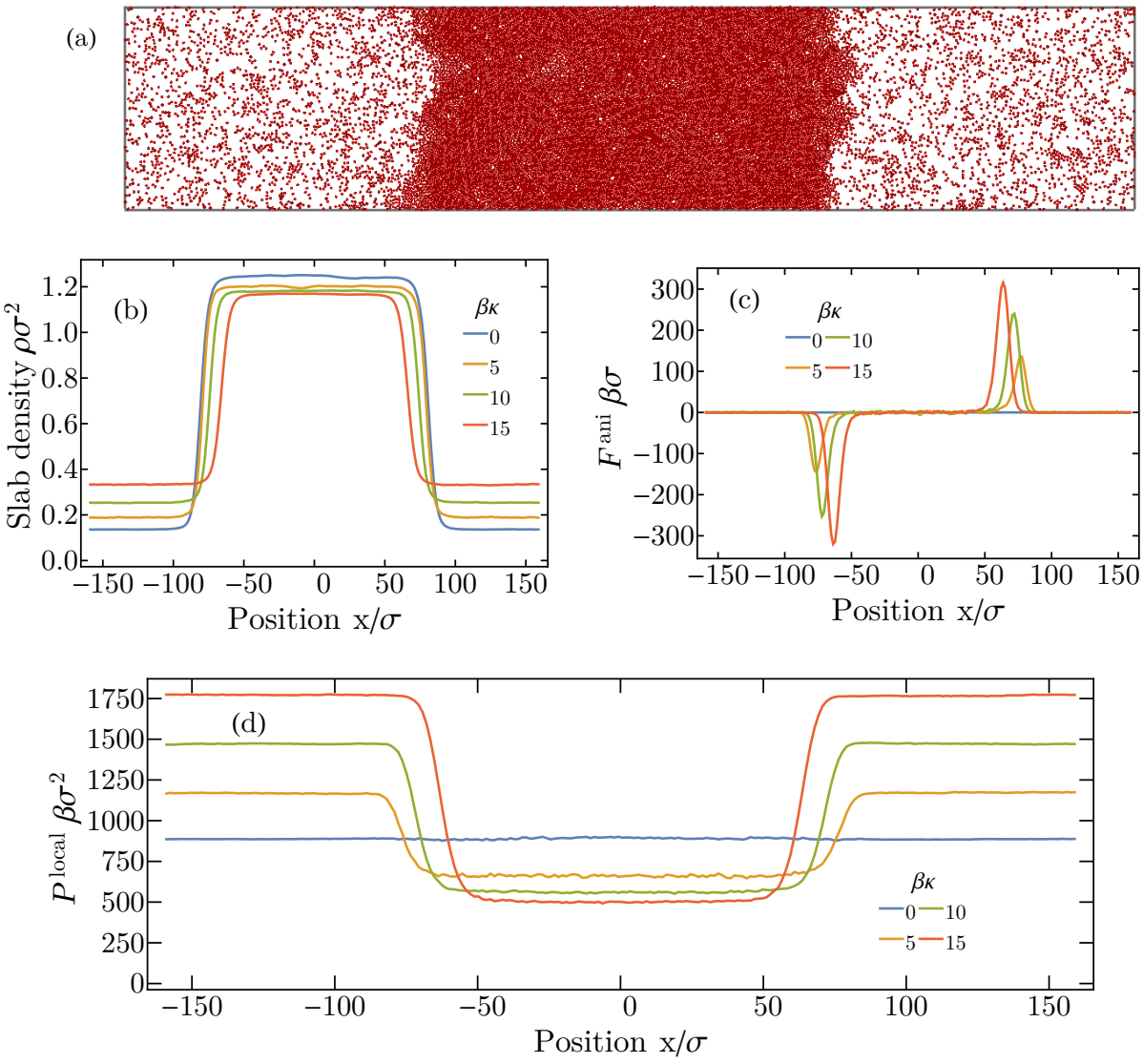

Figure 7.2: (a) Snapshot of a system with 15000 particles that has undergone MIPS. The simulation parameters of the system are $\rho\sigma^2 = 0.65$, $v_0 = 210$, $\kappa = 10$. (b) Local density $\rho(x)$, (c) anisotropic force (Eq. 7.16) and (d) normal component of the local pressure (Eq. 7.11) profiles for systems with $\rho\sigma^2 = 0.65$, $v_0 = 210$ and various torque coefficients.

box and coexisting with a gas is shown in Fig. 7.2(a). Figure 7.2(b) shows the local density profiles of four different phase-separated systems that share the same values for total density and propulsion speed of particles and differ only in the value of the torque coefficient κ. Clearly, an increase of the torque coefficient κ is accompanied by a decrease in the density difference of the coexisting phases. Furthermore, in Fig. 7.2(c) we show typical measurements for the anisotropic force $F^{\rm ani}$. We find that $F^{\rm ani}$ assumes a non-zero value at interfaces in systems with anisotropic interactions, while it is zero in the bulk phases and away from the interfaces, as we argue in Appendix A. Moreover, profiles for the normal component of the local pressure are shown in Fig. 7.2(d). This figure clearly demonstrates that the local pressure as defined by Eq. 7.11 does not assume the same values when measured at the bulk of two coexisting phases when anisotropic interactions are present. On the other hand, the pressure profile in the case of purely isotropic interactions ($\kappa = 0$) remains constant throughout the simulation box. The non-equality of the local pressures in the coexisting phases is a direct consequence of the non-zero anisotropic force along the interface, as it is dictated by Eq. 7.18.

Before moving on to study the phase diagram of the system, it is instructive to investigate further the validity of the values for the local pressure that we present in Fig. 7.2. To this end we have performed simulations of single phases, either gaseous or crystalline. The densities for these single-phase, bulk simulations were chosen to be the local densities of the coexisting phases, which can be read for example from Fig. 7.2(b). We then measure the pressure of the whole system by using the virial pressure which is the sum of Eqs. 7.5-7.7. We find that the values of the local pressure that we measure in the direct coexistence simulations coincide with the values that we obtain from using Eqs. 7.5-7.7 on bulk systems where no phase separation takes place.

Next, we construct the phase diagram of the system for different torque coefficients κ using the results from the direct coexistence simulations. The densities of the coexisting phases are obtained by fitting the density profiles (as shown for example in Fig. 7.2(b)) to hyperbolic tangent functions, similar to Chapters 3 and 5. The resulting phase diagrams are shown in Fig. 7.3(a). The effect of the strength of the anisotropic interaction on the phase behaviour of our system, already reported in the discussion of Fig. 7.2, now becomes even more transparent: an increasing torque coefficient decreases the density difference between the coexisting phases for the same propulsion speed and thus shifts the onset of motility-induced phase separation to higher propulsion speeds. Also, note that the binodal lines for different total densities of the system fall on top of each other, which indicates that no large finite size effects have affected our measurements. It also shows that even when anisotropic interactions take place, the phase diagram of our system collapses onto a fairly equilibrium-like phase diagram, in the sense that the lever rule is obeyed in the coexistence region. We have already demonstrated this in Chapter 6 for a very different model that undergoes motility-induced phase separation.

In Fig. 7.3(b) we plot the local pressures of the coexisting phases, which can be directly extracted from the local pressure profiles (see for example Fig. 7.2(d)). As we already reported in the discussion of Fig. 7.2, the dilute gaseous phases have systematically higher values of local pressure than the dense crystalline ones when anisotropic interactions are present. Of course, in the absence of anisotropic interactions ($\kappa = 0$) the measured local pressures coincide. Once again, we find that results for different total densities

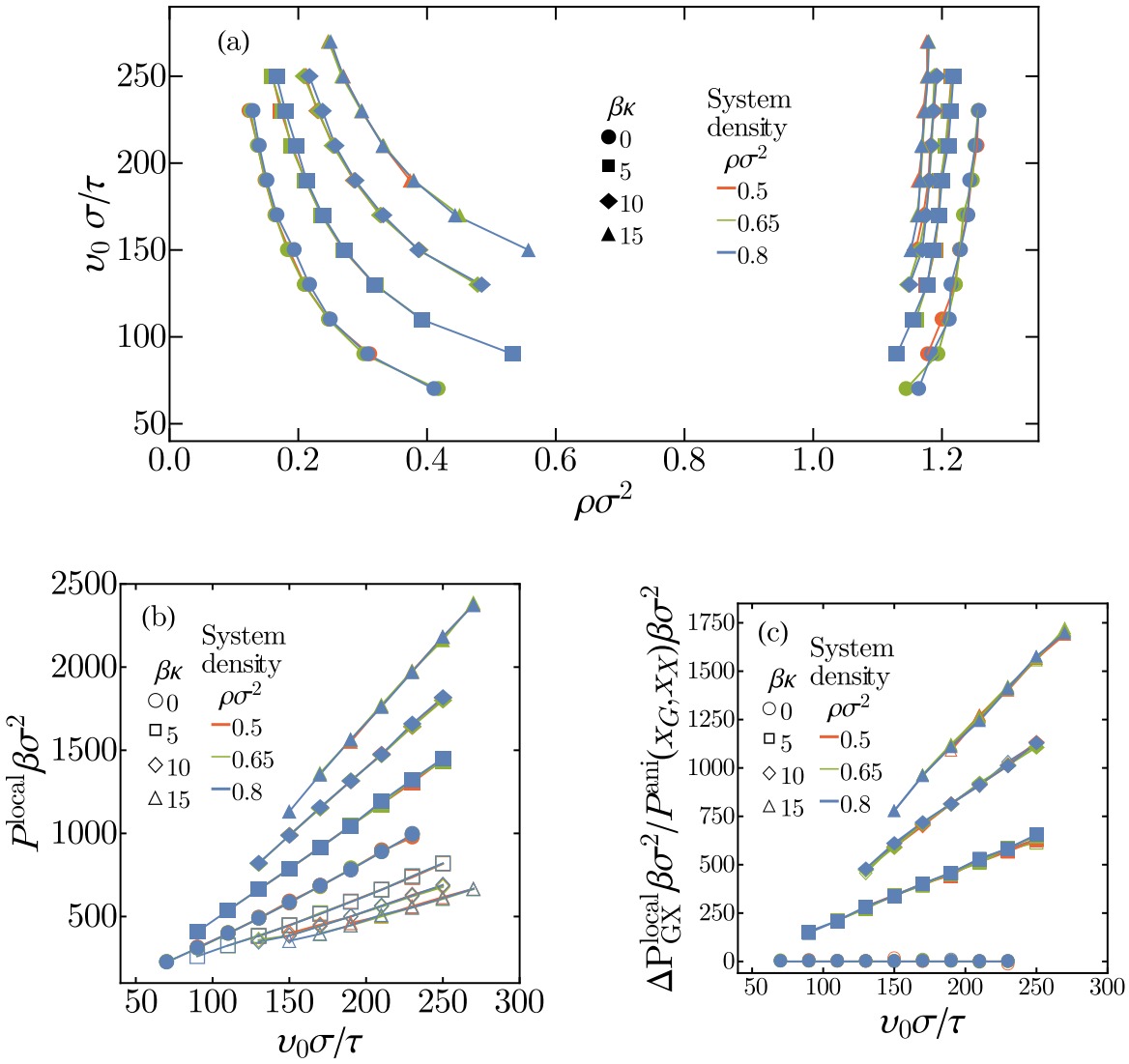

Figure 7.3: (a) Phase diagram of the system for different torque coefficients and total system densities. Markers denote simulation results while continuous lines are simply guides to the eye. (b) Local pressure (Eq. 7.11) of the coexisting phases presented in phase diagram (a) as a function of the propulsion speed. Open symbols correspond to the dense crystalline phase and full symbols denote the dilute gaseous phase. Note that for the case of purely isotropic interactions ($\kappa = 0$) open and full symbols coincide. Continuous lines are simply guides to the eye. (c) Difference of the local pressures of the coexisting phases $\Delta P^{\mathrm{local}}_{GX} = P^{\mathrm{local}}(x_G) - P^{\mathrm{local}}(x_X)$ (full symbols) and spatial integral of the anisotropic force across the interface $P^{\mathrm{ani}}(x_G, x_X) = \int_{x_X}^{x_G} dx F^{\mathrm{ani}}(x)$ (open symbols) as a function of the propulsion speed, where x_X and x_G denote arbitrary positions located in the bulk of the dense crystalline and dilute gaseous phase accordingly. Note that open and full symbols are practically indistinguishable as they fall perfectly on top of each other. Continuous lines are simply guides to the eye. This figure can be seen as a direct validation of Eq. 7.18.

are indistinguishable, which suggests only minor finite size errors in our measurements. Moreover, in Fig. 7.3(c) we plot the difference in the local pressures of the coexisting phases (that is the gap between the local pressures of the dilute and the dense phase, Fig. 7.3(b)) and the integral of the measured anisotropic force over the interfacial region, Eq. 7.18. Reassuringly, we find perfect agreement between these two quantities, which confirms the validity of Eq. 7.18.

7.3.2 Chemical equilibrium of coexisting phases

In the previous section we demonstrated that, in the case of particles exerting torques onto one another, the local pressure as defined in Eq. 7.11 does not assume the same value when measured in the bulk of coexisting phases and thus the mechanical equilibrium of the coexisting phases cannot directly be shown. One then naturally asks whether such a breakdown also takes place for the chemical equilibrium, as demonstrated by the methods of Chapter 5.

To this end, we bring single phases in chemical equilibrium with particle reservoirs as described in Section 7.2.3 (see Fig. 7.1). After the whole system, which comprises of the bulk phase and the reservoir, reaches a steady state, we measure the density of the reservoir. The simulated bulk phases corresponded to the points measured on the binodal lines of the phase diagram that were acquired by direct coexistence simulations (Fig. 7.3(a)). We then compare the densities of the reservoirs for the two single phases (dilute and dense) that were found to coexist in direct coexistence simulations.

In Fig. 7.4 we show the results of this comparison. We find that the corresponding reservoirs are identical for coexisting phases, that is we find the same densities for the reservoirs connected independently to two coexisting phases, within the accuracy of our measurements. Also, there are no significant differences between the four curves that correspond to different values of the torque coefficient κ and, more importantly, there are no signs of a trend as the coefficient κ is increased. We can thus infer from this figure that the chemical equilibrium of coexisting phases can be demonstrated using particle reservoirs *even for systems with non-isotropic interactions*. Naturally, slight deviations from the expected behaviour are present, even for the case of purely isotropic interactions ($\kappa = 0$). We attribute these deviations to systematic errors due to the finite size of the simulated systems (see also the relevant discussion in Chapter 5).

7.4 Conclusions

In this chapter we studied a system of spherical, self-propelled particles that interact with one another *via* radially repulsive and anisotropic, anti-aligning interactions using Brownian dynamics simulations. We performed simulations in an elongated box, in the regime of high propulsion speeds where the system undergoes motility-induced phase separation for various strengths of the anisotropic interaction, and studied properties of the coexisting phases.

Initially, we studied the components of the force balance, derived from the Fokker-Plank equation, in the phase separated system. We found that the quantity we associated

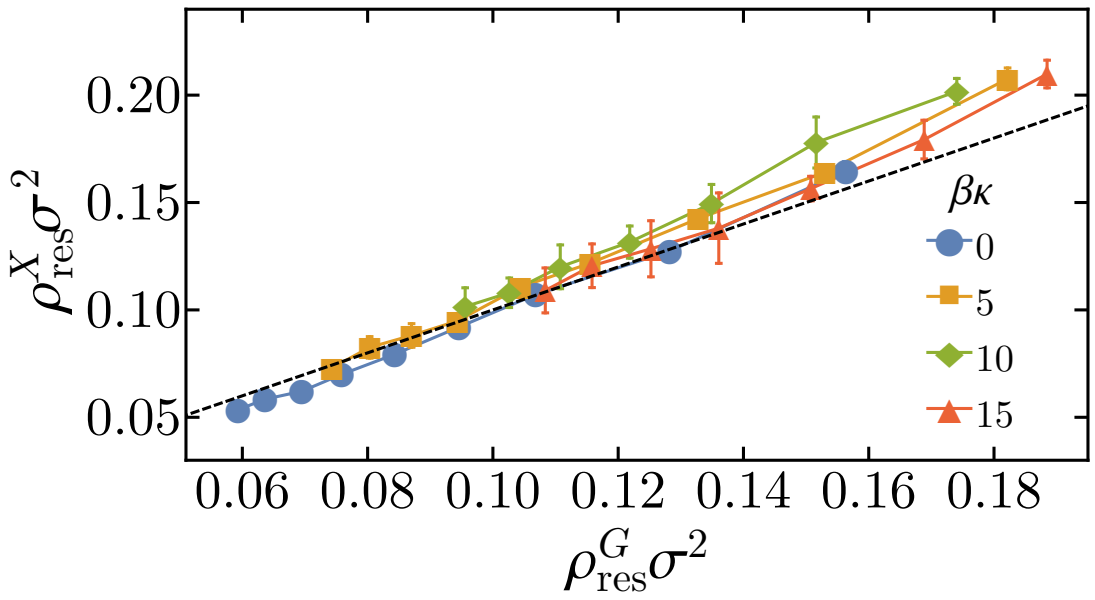

Figure 7.4: Comparison between the resulting reservoir densities for coexisting crystalline $\rho^X_{\rm res}$ and gaseous phases $\rho^G_{\rm res}$. Each data point corresponds to the results of two simulations where a bulk phase was brought into chemical equilibrium with a particle reservoir. For each simulation with a reservoir we performed four runs with different initial densities of the reservoir. The error bars are the standard deviation of these independent runs. Note that the error bars for the gaseous phases are typically smaller than the plotted symbols. The black dotted line follows the scaling $\rho^G_{\rm res} = \rho^X_{\rm res}$ and coloured continuous lines are simply guides to the eye.

with the local pressure, which does not incorporate explicitly the torques, assumes a constant profile along the interface only in the absence of anisotropic interactions. When the particles exert torques onto one another the local pressures in the two coexisting bulk phases are not equal due to a term that explicitly depends on the anisotropic interactions and is non-zero at the interfaces. Note that this term cannot be written as a spatial derivative, thus it does not stem from a pressure-like term. Also, we have further verified the pressure difference of the coexisting phases by performing single phase simulations and measuring the virial pressure of the homogeneous system. Thus, we are left to infer that either a new formulation is needed for the case of active systems with anisotropic interactions, where a quantity conjugate to volume would assume the same value in the bulk of coexisting phases, or perhaps such a quantity does not exist for this general class of active matter systems, an absence that would manifest the out-of-equilibrium nature of the system.

Moreover, we investigated whether chemical equilibrium between coexisting phases can be shown by means of connecting the individual phases to particle reservoirs. The system was connected to particle reservoirs using a modified version of the numerical method presented in Chapter 5. Interestingly, we found that coexisting phases are in chemical equilibrium with the *same* particle reservoir, irrespectively of the presence or absence of anisotropic interactions. This conclusion indicates the existence of a bulk quantity analogous to the chemical potential of equilibrium systems for a wide range of active systems.

Acknowledgments

We thank Berend van der Meer, Frank Smallenburg and Michiel Hermes for many useful discussions. Siddharth Paliwal is gratefully acknowledged for a critical reading of this chapter.

A

Force balance and pressure in active systems

In this appendix we present an equation for the force balance of active Brownian systems utilizing the Fokker-Planck equation and derive an expression for the mechanical pressure of active systems under specific conditions. Moreover, we perform a separate calculation for the mechanical pressure of active systems using the virial route and then compare the two resulting expressions. Note that the calculations presented follow closely Refs. [90], [127] and [122] and are given here in full detail only so that the reader has a comprehensive view of recent literature. Results presented in this appendix are used in Chapters 3, 4, 5 and 7.

A.1 Model and dynamics

The model we consider for our theoretical calculation is a d-dimensional system that contains N self-propelled Brownian particles immersed in a molecular solvent whose viscosity is parametrized by the damping coefficient η. The particles interact with one another *via* pairwise interactions that be decomposed in center-of-mass to center-of-mass forces and explicit torques. We also assume that the system is confined by a wall in the $\hat{z}$ dimension. The position of particle i is given by the vector $\boldsymbol{r}_i$ and its direction of self-propulsion by the vector $\boldsymbol{u}_i$. We also define the (solid) angle between the axis of self-propulsion and a fixed coordinate system as Ω_i. The equations of motion for particle i are then

$$\frac{d\boldsymbol{r}_i}{dt} = -\frac{1}{\eta}\sum_{j\neq i}\nabla_{\boldsymbol{r}_i}U(r_{ij}) - \frac{1}{\eta}\nabla_{\boldsymbol{r}_i}U_w(r_i) + \upsilon_0\boldsymbol{u}_i + \sqrt{2D_{tr}}\boldsymbol{\xi}_i^{tr}, \tag{A.1}$$

$$\frac{d\boldsymbol{u}_i}{dt} = \frac{1}{\eta_r}\left(\boldsymbol{u}_i \times \boldsymbol{\Gamma}_i\right) + \sqrt{2D_r}\left(\boldsymbol{u}_i \times \boldsymbol{\xi}_i^r\right), \tag{A.2}$$

where $U(r)$ is a pairwise potential, $r_{ij} = |\boldsymbol{r}_i - \boldsymbol{r}_j|$, U_w is the potential of the wall, υ_0 is the constant self-propulsion speed of particles, $D_{tr} = 1/(\beta\eta)$ is the translational diffusion coefficient and $\beta = 1/k_BT$, where k_B is the Boltzmann constant and T is the temperature of the surrounding solvent. $\boldsymbol{\Gamma}_i = \sum_{i\neq j}\boldsymbol{\Gamma}(\boldsymbol{r}_i, \boldsymbol{r}_j, \Omega_i, \Omega_j)$ is the sum of torques exerted on particle i by all other particles, η_r is the damping coefficient associated with rotational motion and $D_r = 1/\beta\eta_r$ denotes the rotational diffusion coefficient. The stochastic terms $\boldsymbol{\xi}_i^{tr}$ and $\boldsymbol{\xi}_i^r$ are d-dimensional vectors with zero mean and unit variance.

A.2 The Fokker-Planck equation

For the calculation presented in this section we follow closely Refs. [90] and [127].

Let us define the microscopic density, which we denote as $\Psi(\boldsymbol{r}, \Omega)$, such that

$$\Psi(\boldsymbol{r}, \Omega) = \sum_{i=1}^{N}\delta(\boldsymbol{r} - \boldsymbol{r}_i)\delta(\Omega - \Omega_i). \tag{A.3}$$

Starting from the equations of motion (Eqs. A.1 and A.2) and following standard procedures [166, 167], we find that the time evolution of the microscopic density follows from the equations

$$\begin{aligned}\partial_t\Psi(\boldsymbol{r}, \Omega) = -\nabla\cdot\Bigg[\Bigg(&-\frac{1}{\eta}\int\int\nabla U(|\boldsymbol{r}' - \boldsymbol{r}|)\Psi(\boldsymbol{r}', \Omega')d\boldsymbol{r}'d\Omega' - \frac{1}{\eta}\nabla U_w(r)\\ &+ \upsilon_0\boldsymbol{u}(\Omega)\Bigg)\Psi(\boldsymbol{r}, \Omega) - D_{tr}\nabla\Psi(\boldsymbol{r}, \Omega)\Bigg]\\ &-\partial_\Omega\left[\frac{1}{\eta_r}\int\int\Gamma(\boldsymbol{r}, \boldsymbol{r}', \Omega, \Omega')\Psi(\boldsymbol{r}', \Omega')\Psi(\boldsymbol{r}, \Omega)d\boldsymbol{r}'d\Omega' - D_r\partial_\Omega\Psi(\boldsymbol{r}, \Omega)\right].\end{aligned} \tag{A.4}$$

For later convenience, we now define the moments

$$\rho(\boldsymbol{r}) = \int d\Omega \Psi(\boldsymbol{r}, \Omega), \tag{A.5}$$

$$\boldsymbol{m}(\boldsymbol{r}) = \int d\Omega \boldsymbol{u}(\Omega) \Psi(\boldsymbol{r}, \Omega), \tag{A.6}$$

$$\boldsymbol{s}_{ij}(\boldsymbol{r}) = \int d\Omega \boldsymbol{u}_i(\Omega) \boldsymbol{u}_j(\Omega) \Psi(\boldsymbol{r}, \Omega), \tag{A.7}$$

where i, j denote the spatial components of the corresponding vectors and tensors. $\rho(\boldsymbol{r})$ is the local density of particles while $\boldsymbol{m}(\boldsymbol{r})$ is the local polarization.

Assuming that our system is in a steady state, such that time derivatives vanish, we obtain an equation for the flow of particles by integrating Eq. A.4 over the angle Ω and performing an average over noise:

$$0 = -\nabla \cdot \Bigg[-\frac{1}{\eta} \int \nabla U(|\boldsymbol{r}' - \boldsymbol{r}|) \left\langle \rho(\boldsymbol{r}') \rho(\boldsymbol{r}) \right\rangle d\boldsymbol{r}' - \frac{1}{\eta} \nabla U_w(r) \left\langle \rho(\boldsymbol{r}) \right\rangle + \upsilon_0 \left\langle \boldsymbol{m}(\boldsymbol{r}) \right\rangle - D_{tr} \nabla \left\langle \rho(\boldsymbol{r}) \right\rangle \Bigg], \tag{A.8}$$

where the brackets denote the average over noise. The above equation can be rewritten in the form $\nabla \cdot \boldsymbol{J}(\boldsymbol{r}) = 0$, where $\boldsymbol{J}(\boldsymbol{r})$ is the particle current. We now consider a system that is isotropic in the dimensions perpendicular to $\hat{z}$, such that no swirls are present and Eq. A.8 can be written in the form

$$\partial_{\boldsymbol{r}_i} \boldsymbol{J}_i(\boldsymbol{r}) = 0 \Rightarrow$$

$$\partial_{\boldsymbol{r}_i} \Bigg[-\frac{1}{\eta} \int \partial_{\boldsymbol{r}_i} U(|\boldsymbol{r}' - \boldsymbol{r}|) \left\langle \rho(\boldsymbol{r}') \rho(\boldsymbol{r}) \right\rangle d\boldsymbol{r}' - \frac{1}{\eta} \partial_{\boldsymbol{r}_i} U_w(\boldsymbol{r}) \left\langle \rho(\boldsymbol{r}) \right\rangle + \upsilon_0 \left\langle \boldsymbol{m}_i(\boldsymbol{r}) \right\rangle - D_{tr} \partial_{\boldsymbol{r}_i} \left\langle \rho(\boldsymbol{r}) \right\rangle \Bigg] = 0, \tag{A.9}$$

where the derivative $\partial_{\boldsymbol{r}_i}$ denotes spatial differentiation of the i-th component of the vector $\boldsymbol{r}$. We will now proceed to rewrite various terms of Eq. A.9 for later convenience.

The first term in the left hand side of Eq. A.9 is associated to the virial term of equilibrium systems that results from the interactions between particles. This term can be written in the form [90]

$$\int \partial_{\boldsymbol{r}_i} U(|\boldsymbol{r}' - \boldsymbol{r}|) \left\langle \rho(\boldsymbol{r}') \rho(\boldsymbol{r}) \right\rangle d\boldsymbol{r}' =$$

$$\partial_{\boldsymbol{r}_i} \int_{\boldsymbol{r}_i'' < \boldsymbol{r}_i} d\boldsymbol{r}_i'' \int d\boldsymbol{r}' \partial_{\boldsymbol{r}_i''} U(|\boldsymbol{r}' - \boldsymbol{r}''|) \left\langle \rho(\boldsymbol{r}'') \rho(\boldsymbol{r}') \right\rangle = \partial_{\boldsymbol{r}_i} P_{ii}^{\text{int}}(\boldsymbol{r}), \tag{A.10}$$

where the vector $\boldsymbol{r}''$ has the same components as the vector $\boldsymbol{r}$ except for the i-th component and we have defined the virial pressure due to interactions as $P^{\text{int}}(\boldsymbol{r})$. For the case of pairwise interactions between particles such as the ones considered in this thesis, the contribution of the virial pressure in a local volume V is [131]

$$P_{ii}^{\text{int}} = \frac{1}{V} \sum_k \sum_{l<k} \int_{C_{kl} \in V} \partial_{\boldsymbol{r}_{k,i}} U(r_{kl}) d\boldsymbol{\lambda}_i, \tag{A.11}$$

where the index i denotes the spatial component of the corresponding tensors and vectors while the indices k and l denote particle identities. $\boldsymbol{\lambda}$ is a position on the integration contour C_{kl} from $\boldsymbol{r}_k$ to $\boldsymbol{r}_l$. The constraint $C_{kl} \in V$ means that the force between particles k and l contributes to the virial pressure only with the part of C_{kl} that lies inside V.

Next, we relate the last term in the left hand side of Eq. A.9 to the ideal gas contribution to the pressure tensor

$$P_{ii}^{\mathrm{id}}(\boldsymbol{r}) = \langle \rho(\boldsymbol{r}) \rangle / \beta. \tag{A.12}$$

Last but not least, by multiplying Eq. A.4 with the vector $\boldsymbol{u}_i(\Omega)$ and integrating over the angle Ω, we obtain an equation for the polarization in a noise-averaged steady state that is isotropic in the directions perpendicular to $\hat{z}$ [90, 127]:

$$\langle \boldsymbol{m}_i(\boldsymbol{r}) \rangle = -\frac{1}{\eta \upsilon_0} \partial_{\boldsymbol{r}_i} P_{ii}^{\mathrm{swim}}(\boldsymbol{r}) + \frac{1}{(d-1) D_r \eta} \partial_{\boldsymbol{r}_i} \left(\partial_{\boldsymbol{r}_i} U_w(\boldsymbol{r}) \langle \boldsymbol{m}_i(\boldsymbol{r}) \rangle \right) + \frac{1}{\eta \upsilon_0} \boldsymbol{F}_i^{\mathrm{ani}}(\boldsymbol{r}), \tag{A.13}$$

where we have defined the swim pressure as

$$P_{ii}^{\mathrm{swim}}(\boldsymbol{r}) = \frac{\eta \upsilon_0}{(d-1) D_r} \left[\upsilon_0 \langle \boldsymbol{s}_{ii}(\boldsymbol{r}) \rangle + D_{tr} \partial_{\boldsymbol{r}_i} \langle \boldsymbol{m}_i(\boldsymbol{r}) \rangle - \frac{1}{\eta} \int d\boldsymbol{r}' \partial_{\boldsymbol{r}_i} U(|\boldsymbol{r}' - \boldsymbol{r}|) \langle \boldsymbol{m}_i(\boldsymbol{r}) \rho(\boldsymbol{r}') \rangle \right], \tag{A.14}$$

and the force contribution from the anisotropic interactions as

$$\boldsymbol{F}_i^{\mathrm{ani}}(\boldsymbol{r}) = \frac{\upsilon_0}{(d-1) D_{tr}} \int d\Omega \partial_\Omega \boldsymbol{u}_i(\Omega) \int d\boldsymbol{r}' \int d\Omega' \Gamma(\boldsymbol{r}, \boldsymbol{r}', \Omega, \Omega') \langle \Psi(\boldsymbol{r}', \Omega') \Psi(\boldsymbol{r}, \Omega) \rangle . \tag{A.15}$$

Thus, we can now rewrite Eq. A.9 in the form

$$\begin{aligned} \partial_{\boldsymbol{r}_i} \boldsymbol{J}_i(\boldsymbol{r}) = 0 \Rightarrow \\ \partial_{\boldsymbol{r}_i}^2 \left[-P_{ii}^{\mathrm{id}}(\boldsymbol{r}) - P_{ii}^{\mathrm{int}}(\boldsymbol{r}) - P_{ii}^{\mathrm{swim}}(\boldsymbol{r}) + \frac{\upsilon_0}{(d-1) D_r} \partial_{\boldsymbol{r}_i} U_w(\boldsymbol{r}) \langle \boldsymbol{m}_i(\boldsymbol{r}) \rangle \right] \\ + \partial_{\boldsymbol{r}_i} \left(\partial_{\boldsymbol{r}_i} U_w(\boldsymbol{r}) \langle \rho(\boldsymbol{r}) \rangle \right) + \partial_{\boldsymbol{r}_i} \boldsymbol{F}_i^{\mathrm{ani}}(\boldsymbol{r}) = 0. \end{aligned} \tag{A.16}$$

Note that for any confined system the above equation can be simplified to $\boldsymbol{J}_i(\boldsymbol{r}) = 0$. Also, in the case of periodic boundary conditions and the absence of a wall, if there exists a spatial region where the system is in a bulk, isotropic state (that is $\partial_{\boldsymbol{r}_i} P_{ii}^{\mathrm{id}}(\boldsymbol{r}) = \partial_{\boldsymbol{r}_i} P_{ii}^{\mathrm{int}}(\boldsymbol{r}) = 0$ and $\langle \boldsymbol{m}(\boldsymbol{r}) \rangle = 0$) then Eq. A.9 dictates $\boldsymbol{J}_i(\boldsymbol{r}) = 0$ as well. For the systems that we study in this thesis either one of these two conditions will always be satisfied, such that we arrive at an equation that describes the force balance at any point of the system:

$$\begin{aligned} J_i(\boldsymbol{r}) = 0 \Rightarrow \\ \partial_{\boldsymbol{r}_i} \left[-P_{ii}^{\mathrm{id}}(\boldsymbol{r}) - P_{ii}^{\mathrm{int}}(\boldsymbol{r}) - P_{ii}^{\mathrm{swim}}(\boldsymbol{r}) + \frac{\upsilon_0}{(d-1) D_r} \partial_{\boldsymbol{r}_i} U_w(\boldsymbol{r}) \langle \boldsymbol{m}_i(\boldsymbol{r}) \rangle \right] \\ + \partial_{\boldsymbol{r}_i} U_w(\boldsymbol{r}) \langle \rho(\boldsymbol{r}) \rangle + \boldsymbol{F}_i^{\mathrm{ani}}(\boldsymbol{r}) = 0. \end{aligned} \tag{A.17}$$

This equation will be the starting point for all the special cases we consider in the following.

A.2.1 Local pressure in the absence of anisotropic interactions

In the absence of torques, Eq. A.17 in the $\hat{z}$ dimension is simplified to

$$\partial_z \left[-P_{zz}^{\mathrm{id}}(\boldsymbol{r}) - P_{zz}^{\mathrm{int}}(\boldsymbol{r}) - P_{zz}^{\mathrm{swim}}(\boldsymbol{r}) + \frac{v_0}{(d-1)D_r} \partial_z U_w(\boldsymbol{r}) \left\langle \boldsymbol{m}_z(\boldsymbol{r}) \right\rangle \right] + \partial_z U_w(\boldsymbol{r}) \left\langle \rho(\boldsymbol{r}) \right\rangle = 0. \tag{A.18}$$

Let us assume that a wall is located at $z = 0$ that confines the particles in the $z > 0$ region of the box, and that the particles feel the potential of the wall only for a limited range, such that we can define a bulk of the system for some $z = z_0 \gg 0$ where $U_w(z_0) = 0$. Then the pressure exerted on the wall by the active particles is simply

$$P^{\mathrm{wall}} = \frac{1}{V^{d-1}} \int_{0^-}^{z_0} dz \int d^{d-1}\boldsymbol{r} \partial_z U_w(\boldsymbol{r}) \left\langle \rho(\boldsymbol{r}) \right\rangle, \tag{A.19}$$

where V^{d-1} denotes here the surface of the box in the dimensions perpendicular to $\hat{z}$. Substituting Eq. A.18 into the above equation yields

$$P^{\mathrm{wall}} = P_{zz}^{\mathrm{id}}(z_0) + P_{zz}^{\mathrm{int}}(z_0) + P_{zz}^{\mathrm{swim}}(z_0), \tag{A.20}$$

where we have defined $P_{zz}^{\mathrm{id}}(z_0) = \frac{1}{V^{d-1}} \int d^{d-1}\boldsymbol{r_0} P_{zz}^{\mathrm{id}}(\boldsymbol{r_0})$, with $\int d^{d-1}\boldsymbol{r_0}$ the integral over the plane $z = z_0$, and similarly for the interaction and swim pressure. Thus, isotropic particles exert a pressure on the wall that can be directly measured in the bulk of the system. This calculation has already been given in literature [90, 127].

Note that in the absence of any walls, *i.e.* when periodic boundary conditions are applied, one can still write a force balance in the form of Eq. A.18, such that

$$\begin{aligned} \partial_{\boldsymbol{r}_i} \left[P_{ii}^{\mathrm{id}}(\boldsymbol{r}) + P_{ii}^{\mathrm{int}}(\boldsymbol{r}) + P_{ii}^{\mathrm{swim}}(\boldsymbol{r}) \right] = 0 \Rightarrow \\ P_{ii}^{\mathrm{id}}(\boldsymbol{r}) + P_{ii}^{\mathrm{int}}(\boldsymbol{r}) + P_{ii}^{\mathrm{swim}}(\boldsymbol{r}) = \text{constant}, \end{aligned} \tag{A.21}$$

throughout the whole system. We have verified such a force balance in Chapters 4, 5 and 7.

In systems of self-propelled particles with only isotropic interactions one can thus define the diagonal components of the local pressure tensor at point $\boldsymbol{r}$ as

$$P_{ii}^{\mathrm{local}}(\boldsymbol{r}) = P_{ii}^{\mathrm{id}}(\boldsymbol{r}) + P_{ii}^{\mathrm{int}}(\boldsymbol{r}) + P_{ii}^{\mathrm{swim}}(\boldsymbol{r}), \tag{A.22}$$

or in the case where the system is isotropic in the dimensions perpendicular to $\hat{z}$ we can rewrite the above Eq. A.22 as

$$P_{ii}^{\mathrm{local}}(z) = P_{ii}^{\mathrm{id}}(z) + P_{ii}^{\mathrm{int}}(z) + P_{ii}^{\mathrm{swim}}(z). \tag{A.23}$$

This local pressure, when measured in the bulk of a system, coincides with the exerted mechanical pressure on the wall that contains the system. If periodic boundary conditions are applied, the local pressure remains constant throughout the whole system and its integration over the whole system reproduces the known expressions of the pressure that have been derived *via* alternative routes [92, 122]. Thus, Eqs. A.22 and A.23 can again be used as a definition of the local pressure if periodic boundary conditions are applied. We make use of this formalism in Chapters 4, 5 and 7.

A.2.2 Local pressure in the absence of anisotropic interactions for binary mixtures

The calculation for the local pressure of mixtures of active particles in the absence of torques is very similar to the calculation for a system that contains only a single species, presented in Sections A.2 and A.2.1. Thus, here we will only sketch the calculation.

Consider a binary system in d dimensions with N_1 particles of species 1 and N_2 particles of species 2, without explicit torques between the particles, whose equations of motion are given the equations by

$$\frac{d\boldsymbol{r}_i}{dt} = -\frac{1}{\eta}\sum_{j\neq i}\nabla_{\boldsymbol{r}_i}U(r_{ij}) - \frac{1}{\eta}\nabla_{\boldsymbol{r}_i}U_w(r_i) + \upsilon_i\boldsymbol{u}_i + \sqrt{2D_{tr}}\boldsymbol{\xi}_i^{tr}, \tag{A.24}$$

$$\frac{d\boldsymbol{u}_i}{dt} = \sqrt{2D_r}\left(\boldsymbol{u}_i \times \boldsymbol{\xi}_i^r\right), \tag{A.25}$$

where the various parameters of the equations have already been defined for Eqs. A.1 and A.2. The only difference between the two species is the value of the self-propulsion force, such that $\upsilon_i = \upsilon^{(1)}$ for $i \in N_1$ and $\upsilon_j = \upsilon^{(2)}$ for $j \in N_2$, with $\upsilon^{(1)} \neq \upsilon^{(2)}$.

The microscopic densities for the two species, which we denote as $\Psi^{(1)}(\boldsymbol{r},\Omega)$ and $\Psi^{(2)}(\boldsymbol{r},\Omega)$, are

$$\Psi^{(1)}(\boldsymbol{r},\Omega) = \sum_{i=1}^{N_1}\delta(\boldsymbol{r}-\boldsymbol{r}_i)\delta(\Omega-\Omega_i) \tag{A.26}$$

$$\Psi^{(2)}(\boldsymbol{r},\Omega) = \sum_{i=1}^{N_2}\delta(\boldsymbol{r}-\boldsymbol{r}_i)\delta(\Omega-\Omega_i). \tag{A.27}$$

Following standard procedures [166, 167], we find that their time evolution follows from the equations

$$\begin{aligned}\partial_t\Psi^{(\alpha)}(\boldsymbol{r},\Omega) = -\nabla\cdot\Bigg(&-\frac{1}{\eta}\int\int\nabla U(|\boldsymbol{r}'-\boldsymbol{r}|)\sum_{\gamma=1,2}\Psi^{(\gamma)}(\boldsymbol{r}',\Omega')d\boldsymbol{r}'d\Omega' \\ &-\frac{1}{\eta}\nabla U_w(r) + \upsilon^{(\alpha)}\boldsymbol{u}(\Omega)\Bigg)\Psi^{(\alpha)}(\boldsymbol{r},\Omega) \qquad \text{(A.28)}\\ &+D_{tr}\nabla^2\Psi^{(\alpha)}(\boldsymbol{r},\Omega) + D_r\partial_\Omega^2\Psi^{(\alpha)}(\boldsymbol{r},\Omega). \qquad \text{(A.29)}\end{aligned}$$

where $\alpha = 1, 2$. We now define the moments

$$\rho^{(\alpha)}(\boldsymbol{r}) = \int d\Omega\Psi^{(\alpha)}(\boldsymbol{r},\Omega), \tag{A.30}$$

$$\boldsymbol{m}^{(\alpha)}(\boldsymbol{r}) = \int d\Omega\boldsymbol{u}(\Omega)\Psi^{(\alpha)}(\boldsymbol{r},\Omega), \tag{A.31}$$

$$\boldsymbol{s}_{ij}^{(\alpha)}(\boldsymbol{r}) = \int d\Omega\boldsymbol{u}_i(\Omega)\boldsymbol{u}_j(\Omega)\Psi^{(\alpha)}(\boldsymbol{r},\Omega), \tag{A.32}$$

where i, j denote the spatial components of the corresponding vectors and tensors. $\rho^{(\alpha)}(\boldsymbol{r})$ is the local density of species α while $\boldsymbol{m}^{(\alpha)}(\boldsymbol{r})$ is the corresponding local polarization.

Repeating the steps shown in Sections A.2 and A.2.1 one can then derive the local pressure as

$$P_{ii}^{\text{local}}(\boldsymbol{r}) = P_{ii}^{\text{id}}(\boldsymbol{r}) + P_{ii}^{\text{int}}(\boldsymbol{r}) + \sum_{\alpha} P_{ii}^{\text{swim},(\alpha)}(\boldsymbol{r}), \tag{A.33}$$

where

$$P_{ii}^{\text{id}}(\boldsymbol{r}) = \langle \rho(\boldsymbol{r}) \rangle / \beta \tag{A.34}$$

is the ideal component of the pressure, where $\rho(\boldsymbol{r}) = \sum_{\alpha} \rho^{(\alpha)}(\boldsymbol{r})$ is the total density at point $\boldsymbol{r}$ and brackets denote an average at the steady state over noise realizations,

$$P_{ii}^{\text{int}}(\boldsymbol{r}) = \int_{\boldsymbol{r}_i'' < \boldsymbol{r}_i} d\boldsymbol{r}_i'' \int d\boldsymbol{r}' \partial_{\boldsymbol{r}_i''} U(|\boldsymbol{r}' - \boldsymbol{r}''|) \langle \rho(\boldsymbol{r}'') \rho(\boldsymbol{r}') \rangle \tag{A.35}$$

is the standard local virial term, where the vector $\boldsymbol{r}''$ has the same components as the vector $\boldsymbol{r}$ except for the i-th component, and

$$P_{ii}^{\text{swim},(\alpha)}(\boldsymbol{r}) = \frac{\eta \upsilon^{(\alpha)}}{(d-1)D_r} \Big[\upsilon^{(\alpha)} \left\langle \boldsymbol{s}_{ii}^{(\alpha)}(\boldsymbol{r}) \right\rangle + D_{tr} \partial_{\boldsymbol{r}_i} \left\langle \boldsymbol{m}_i^{(\alpha)}(\boldsymbol{r}) \right\rangle - \frac{1}{\eta} \int d\boldsymbol{r}' \partial_{\boldsymbol{r}_i} U(|\boldsymbol{r}' - \boldsymbol{r}|) \left\langle \boldsymbol{m}_i^{(\alpha)}(\boldsymbol{r}) \rho(\boldsymbol{r}') \right\rangle \Big], \tag{A.36}$$

is the local swim pressure of species α. Eqs. A.33-A.36 are used in Chapter 5.

A.2.3 Force balance in the presence of anisotropic interactions

When particles exert torques on one another, one must take into account all the terms in Eq. A.17. Using the definition for the local pressure, Eq. A.22, one can rewrite Eq. A.17 in the $\hat{z}$ direction as

$$J_z(\boldsymbol{r}) = 0 \Rightarrow$$
$$\partial_z U_w(\boldsymbol{r}) \langle \rho(\boldsymbol{r}) \rangle = \partial_z \left[P_{zz}^{\text{local}}(\boldsymbol{r}) - \frac{\upsilon_0}{(d-1)D_r} \partial_z U_w(\boldsymbol{r}) \langle \boldsymbol{m}_z(\boldsymbol{r}) \rangle \right] - \boldsymbol{F}_z^{\text{ani}}(\boldsymbol{r}). \tag{A.37}$$

We assume again a wall located at $z = 0$ that confines the particles in the volume $z > 0$. Also, the wall-particle interaction has a limited range such that for some $z_0 \gg 0$ there exists a bulk of the system where the particles do not feel the wall. Following the steps shown in Section A.2.1 one then finds that the pressure exerted on the wall is given by

$$P^{\text{wall}} = P_{zz}^{\text{local}}(z_0) - \int_{0^-}^{z_0} dz \boldsymbol{F}_z^{\text{ani}}(z). \tag{A.38}$$

Thus, the mechanical pressure felt by the wall is a function of the bulk pressure and also depends on the integral of the force contribution from the anisotropic interactions, which itself depends on the details of the wall potential. Thus, as previous work has demonstrated (and an identical calculation has shown), in the presence of torques pressure is not an equation of state for self-propelled particles [127].

However, note that far away from any walls and at a bulk isotropic phase, where $\boldsymbol{m} = 0$ Eq. A.13 demands $\boldsymbol{F}^{\text{ani}}(z) = 0$. Thus, the local pressure stays constant throughout the bulk isotropic phase. In Chapter 7 we examine how the components of the force balance Eq. A.37 are affected in the presence of an interface between bulk phases.

A.3 The virial route

This section follows closely the calculation performed in Ref. [122].

For an alternative derivation of the pressure, one can now multiply the equation of motion Eq. A.1 by the vector $\boldsymbol{r}_i$ (note that now $\boldsymbol{r}_i$ denotes the position of particle i), sum over all particles and take the average over the noise. The resulting equation reads

$$\frac{1}{2}\sum_{i=1}^{N}\frac{d\left\langle \boldsymbol{r}_i^2\right\rangle}{dt} = -\frac{1}{\eta}\sum_{i=1}^{N}\sum_{j\neq i}\left\langle \nabla_{\boldsymbol{r}_i}U(r_{ij})\cdot\boldsymbol{r}_i\right\rangle - \frac{1}{\eta}\sum_{i=1}^{N}\left\langle \nabla_{\boldsymbol{r}_i}U_w(r_i)\cdot\boldsymbol{r}_i\right\rangle + \upsilon_0\sum_{i=1}^{N}\left\langle \boldsymbol{u}_i\cdot\boldsymbol{r}_i\right\rangle + \sqrt{2D_{tr}}\sum_{i=1}^{N}\left\langle \boldsymbol{\xi}_i^{tr}\cdot\boldsymbol{r}_i\right\rangle \tag{A.39}$$

Now, let us assume that our system is confined by a wall, such that the mean square displacement is limited and $d\left\langle \boldsymbol{r}_i^2\right\rangle/dt = 0$. Moreover, for simple geometries of the box, such as the ones we consider in the present thesis, it is straightforward to show that the mechanical pressure exerted on the wall by the particles P^{wall} is [122]

$$P^{\text{wall}} = \sum_{i=1}^{N}\frac{1}{dV}\left\langle \nabla_{\boldsymbol{r}_i}U_w(r_i)\cdot\boldsymbol{r}_i\right\rangle, \tag{A.40}$$

where V is the volume of the confined system. Also, the last term in Eq. A.39 can be written as

$$\left\langle \boldsymbol{\xi}_i^{tr}(t)\cdot\boldsymbol{r}_i(t)\right\rangle = \int_{-\infty}^{t}\left\langle \boldsymbol{\xi}_i^{tr}(t)\cdot\dot{\boldsymbol{r}}_i(t')\right\rangle dt' = \sqrt{2D_{tr}}\int_{-\infty}^{t}\left\langle \boldsymbol{\xi}_i^{tr}(t)\cdot\boldsymbol{\xi}_i^{tr}(t')\right\rangle dt' = d\sqrt{\frac{D_{tr}}{2}}, \tag{A.41}$$

where we have used that $\langle\boldsymbol{\xi}_i^{tr}(t)\cdot\boldsymbol{r}_i(-\infty)\rangle = 0$, $\langle\boldsymbol{\xi}_i^{tr}(t)\cdot\boldsymbol{\xi}_i^{tr}(t')\rangle = d\delta(t-t')$ and $\int_{-\infty}^{t}\delta(t-t')dt' = \frac{1}{2}$.

Plugging Eqs. A.40 and A.41 in Eq. A.39 we get

$$P^{\text{wall}} = \rho k_B T - \frac{1}{2dV}\sum_{i=1}^{N}\sum_{j\neq i}\left\langle \nabla_{\boldsymbol{r}_i}U(r_{ij})\cdot(\boldsymbol{r}_i-\boldsymbol{r}_j)\right\rangle + \frac{\eta\upsilon_0}{dV}\sum_{i=1}^{N}\left\langle \boldsymbol{u}_i\cdot\boldsymbol{r}_i\right\rangle. \tag{A.42}$$

The first term in Eq. A.42 is the ideal gas contribution, the second term is the virial contribution stems from the particle interactions and the last term is the swim pressure that is a direct contribution of the self-propulsive forces to the pressure. Note that for this equation we have not assumed any particular dynamics for the orientation of the particles, so it is valid even for systems with anisotropic interactions. Eq. A.42 depends on the absolute position of particles, such that it is a global quantity that cannot be measured locally in the system.

However, in the case of only isotropic interactions between particles, it can be further simplified to [122]

$$P^{\text{wall}} = \rho k_B T - \frac{1}{2dV}\sum_{i=1}^{N}\sum_{j\neq i}\left\langle \nabla_{\boldsymbol{r}_i}U(r_{ij})\cdot(\boldsymbol{r}_i-\boldsymbol{r}_j)\right\rangle + \frac{\eta\upsilon_0}{d(d-1)D_r}\left[\rho\upsilon_0 + \frac{1}{\eta V}\sum_{i=1}^{N}\left\langle\left(-\nabla_{\boldsymbol{r}_i}U_w(r_i) - \sum_{j\neq i}\nabla_{\boldsymbol{r}_i}U(r_{ij})\right)\cdot\boldsymbol{u}_i\right\rangle\right], \tag{A.43}$$

which is a quantity that does not depend on absolute positions. Thus, one can also define the virial pressure of a volume V as

$$P^{\text{virial}} = \rho k_B T - \frac{1}{2dV} \sum_{i=1}^{N} \sum_{j \neq i} \langle \nabla_{\boldsymbol{r}_i} U(r_{ij}) \cdot (\boldsymbol{r}_i - \boldsymbol{r}_j) \rangle + \frac{\eta \upsilon_0}{d(d-1)D_r} \left[\rho \upsilon_0 + \frac{1}{\eta V} \sum_{i=1}^{N} \left\langle \left(-\nabla_{\boldsymbol{r}_i} U_w(r_i) - \sum_{j \neq i} \nabla_{\boldsymbol{r}_i} U(r_{ij}) \right) \cdot \boldsymbol{u}_i \right\rangle \right], \quad \text{(A.44)}$$

where $\rho = N/V$ and all particles $i, j \in V$.

A.4 Comparison between the two routes

In the absence of torques, a comparison between the equation for the local pressure coming from the Fokker-Plank equation Eq. A.23 (together with Eqs. A.12, A.10 and A.14) and A.44 which follows from the virial route shows that the two approaches give almost the same result (note however that one has to integrate Eq. A.23 over the volume V). The difference stems from a term that is present in the swim pressure contribution of the former equation and is proportional to the spatial derivative of the polarization $\nabla \boldsymbol{m}$. This term gives a zero contribution for all isotropic phases where by definition $\boldsymbol{m} = 0$ and is only important at an interface between bulk phases or in the presence of a wall (see also Chapter 4), that is where the system is inhomogeneous. This discrepancy is not surprising, as Eq. A.44 is derived for a closed system or a system with periodic boundary conditions where the spatial integral of $\nabla \boldsymbol{m}$ over the volume will be zero.

Note that one can also define a local pressure using Eq. A.42, as done for example in Ref. [91]. This expression has the disadvantage of not being directly applicable to inhomogeneous systems since, once particles cross an interface, the correlation between positions and velocities is lost in the dimension normal to the interface, as discussed already in Ref. [91]. It has the advantage though that it can be used even in the case of homogeneous systems with anisotropic interactions. In Chapter 7 we make a further comparison between the two routes in the case of bulk systems with anisotropic interactions.

Acknowledgments

We would like to thank René van Roij, Siddharth Paliwal and Jeroen Rodenburg for many stimulating and illuminating discussions on the contents of this Appendix.

References

[1] J. Buhl, D. J. Sumpter, I. D. Couzin, J. J. Hale, E. Despland, E. Miller, and S. J. Simpson, *From disorder to order in marching locusts.* Science, 312(5778):1402–1406, 2006.

[2] T. Feder, *Statistical physics is for the birds.* Phys. Today, 60(10):28–30, 2007.

[3] M. Ballerini, N. Cabibbo, R. Candelier, A. Cavagna, E. Cisbani, I. Giardina, V. Lecomte, A. Orlandi, G. Parisi, A. Procaccini, et al., *Interaction ruling animal collective behavior depends on topological rather than metric distance: Evidence from a field study.* Proc. Natl. Acad. Sci., 105(4):1232–1237, 2008.

[4] S. Ramaswamy, *The mechanics and statistics of active matter.* Annu. Rev. Condens. Matter Phys., 1:323–345, 2010.

[5] P. Romanczuk, M. Bär, W. Ebeling, B. Lindner, and L. Schimansky-Geier, *Active brownian particles.* Eur. Phys. J. Spec. Top., 202(1):1–162, 2012.

[6] M. Marchetti, J. Joanny, S. Ramaswamy, T. Liverpool, J. Prost, M. Rao, and R. A. Simha, *Hydrodynamics of soft active matter.* Rev. Mod. Phys., 85(3):1143, 2013.

[7] I. S. Aranson, *Collective behavior in out-of-equilibrium colloidal suspensions.* C. R. Phys., 14(6):518, 2013.

[8] J. Elgeti, R. G. Winkler, and G. Gompper, *Physics of microswimmers-single particle motion and collective behavior: a review.* Rep. Prog. Phys., 78(5):056601, 2015.

[9] A. Zöttl and H. Stark, *Emergent behavior in active colloids.* J. Phys. Condens. Matter, 28(25):253001, 2016.

[10] D. Marenduzzo, *An introduction to the statistical physics of active matter: motility-induced phase separation and the "generic instability" of active gels.* Eur. Phys. J. Spec. Top., 225(11-12):2065–2077, 2016.

[11] E. Shaw, *Schooling fishes: the school, a truly egalitarian form of organization in which all members of the group are alike in influence, offers substantial benefits to its participants.* Am. Sci., 66(2):166–175, 1978.

[12] R. Bouffanais. *Design and control of swarm dynamics.* Springer, 2016.

[13] J. L. Silverberg, M. Bierbaum, J. P. Sethna, and I. Cohen, *Collective motion of humans in mosh and circle pits at heavy metal concerts.* Phys. Rev. Lett., 110(22):228701, 2013.

[14] J. K. Parrish, S. V. Viscido, and D. Grünbaum, *Self-organized fish schools: an examination of emergent properties.* Biol. Bull., 202(3):296–305, 2002.

[15] J. Dunkel, S. Heidenreich, K. Drescher, H. H. Wensink, M. Bär, and R. E. Goldstein, *Fluid dynamics of bacterial turbulence.* Phys. Rev. Lett., 110(22):228102, 2013.

[16] J. Prost, F. Jülicher, and J. Joanny, *Active gel physics.* Nat. Phys., 11(2):111–117, 2015.

[17] F. Juelicher, K. Kruse, J. Prost, and J.-F. Joanny, *Active behavior of the cytoskeleton.* Phys. Rep., 449(1):3–28, 2007.

[18] D. Mizuno, C. Tardin, C. F. Schmidt, and F. C. MacKintosh, *Nonequilibrium mechanics of active cytoskeletal networks.* Science, 315(5810):370–373, 2007.

[19] T. Graham, *Liquid diffusion applied to analysis.* Phil. Trans. R. Soc. A, 151:183–224, 1861.

[20] I. W. Hamley. *Introduction to soft matter: synthetic and biological self-assembling materials*. John Wiley & Sons, 2013.

[21] R. A. Jones. *Soft condensed matter*, volume 6. Oxford University Press, 2002.

[22] S. C. Glotzer and M. J. Solomon, *Anisotropy of building blocks and their assembly into complex structures*. Nat. Mater., 6(8):557–562, 2007.

[23] J. Aguilar, T. Zhang, F. Qian, M. Kingsbury, B. McInroe, N. Mazouchova, C. Li, R. Maladen, C. Gong, M. Travers, et al., *A review on locomotion robophysics: the study of movement at the intersection of robotics, soft matter and dynamical systems*. Rep. Prog. Phys., 79(11):110001, 2016.

[24] W. F. Paxton, K. C. Kistler, C. C. Olmeda, A. Sen, S. K. St. Angelo, Y. Cao, T. E. Mallouk, P. E. Lammert, and V. H. Crespi, *Catalytic nanomotors: autonomous movement of striped nanorods*. J. Am. Chem. Soc, 126(41):13424–13431, 2004.

[25] J. R. Howse, R. A. Jones, A. J. Ryan, T. Gough, R. Vafabakhsh, and R. Golestanian, *Self-motile colloidal particles: from directed propulsion to random walk*. Phys. Rev. Lett., 99(4):048102, 2007.

[26] A. Bricard, J.-B. Caussin, N. Desreumaux, O. Dauchot, and D. Bartolo, *Emergence of macroscopic directed motion in populations of motile colloids*. Nature, 503(7474):95–98, 2013.

[27] J. Deseigne, O. Dauchot, and H. Chaté, *Collective motion of vibrated polar disks*. Phys. Rev. Lett., 105(9):098001, 2010.

[28] A. Kudrolli, G. Lumay, D. Volfson, and L. S. Tsimring, *Swarming and swirling in self-propelled polar granular rods*. Phys. Rev. Lett., 100:058001, 2008.

[29] R. Dreyfus, J. Baudry, M. L. Roper, M. Fermigier, H. A. Stone, and J. Bibette, *Microscopic artificial swimmers*. Nature, 437(7060):862–865, 2005.

[30] V. Narayan, S. Ramaswamy, and N. Menon, *Long-lived giant number fluctuations in a swarming granular nematic*. Science, 317(5834):105–108, 2007.

[31] V. Schaller, C. Weber, C. Semmrich, E. Frey, and A. R. Bausch, *Polar patterns of driven filaments*. Nature, 467(7311):73–77, 2010.

[32] J. Schwarz-Linek, C. Valeriani, A. Cacciuto, M. Cates, D. Marenduzzo, A. Morozov, and W. Poon, *Phase separation and rotor self-assembly in active particle suspensions*. Proc. Natl. Acad. Sci., 109(11):4052–4057, 2012.

[33] Y. Sumino, K. H. Nagai, Y. Shitaka, D. Tanaka, K. Yoshikawa, H. Chaté, and K. Oiwa, *Large-scale vortex lattice emerging from collectively moving microtubules*. Nature, 483(7390):448–452, 2012.

[34] I. Theurkauff, C. Cottin-Bizonne, J. Palacci, C. Ybert, and L. Bocquet, *Dynamic clustering in active colloidal suspensions with chemical signaling*. Phys. Rev. Lett., 108:268303, 2012.

[35] J. Palacci, S. Sacanna, A. P. Steinberg, D. J. Pine, and P. M. Chaikin, *Living crystals of light-activated colloidal surfers*. Science, 339(6122):936–940, 2013.

[36] I. Buttinoni, J. Bialké, F. Kümmel, H. Löwen, C. Bechinger, and T. Speck, *Dynamical clustering and phase separation in suspensions of self-propelled colloidal particles*. Phys. Rev. Lett., 110:238301, 2013.

[37] F. Kümmel, B. ten Hagen, R. Wittkowski, I. Buttinoni, R. Eichhorn, G. Volpe, H. Löwen, and C. Bechinger, *Circular motion of asymmetric self-propelling particles.* Phys. Rev. Lett., 110(19):198302, 2013.

[38] L. Giomi, N. Hawley-Weld, and L. Mahadevan, *Swarming, swirling and stasis in sequestered bristle-bots.* Proc. R. Soc. A, 469(2151):20120637, 2013.

[39] B. Ten Hagen, F. Kümmel, R. Wittkowski, D. Takagi, H. Löwen, and C. Bechinger, *Gravitaxis of asymmetric self-propelled colloidal particles.* Nat. Commun., 5:4829, 2014.

[40] F. C. Keber, E. Loiseau, T. Sanchez, S. J. DeCamp, L. Giomi, M. J. Bowick, M. C. Marchetti, Z. Dogic, and A. R. Bausch, *Topology and dynamics of active nematic vesicles.* Science, 345(6201):1135–1139, 2014.

[41] L. Baraban, M. Tasinkevych, M. Popescu, S. Sanchez, S. Dietrich, and O. Schmidt, *Transport of cargo by catalytic janus micro-motors.* Soft Matter, 8(1):48–52, 2011.

[42] N. Koumakis, A. Lepore, C. Maggi, and R. Di Leonardo, *Targeted delivery of colloids by swimming bacteria.* Nat. Commun., 4:2588, 2013.

[43] L. Soler, V. Magdanz, V. M. Fomin, S. Sanchez, and O. G. Schmidt, *Self-propelled micromotors for cleaning polluted water.* ACS Nano, 7(11):9611–9620, 2013.

[44] A. T. Brown, W. C. Poon, C. Holm, and J. de Graaf, *Ionic screening and dissociation are crucial for understanding chemical self-propulsion in polar solvents.* Soft Matter, 13(6):1200–1222, 2017.

[45] S. Li, H. Jiang, and Z. Hou, *Effects of hydrodynamic interactions on the crystallization of passive and active colloidal systems.* Soft Matter, 11(28):5712–5718, 2015.

[46] J. Blaschke, M. Maurer, K. Menon, A. Zöttl, and H. Stark, *Phase separation and coexistence of hydrodynamically interacting microswimmers.* Soft Matter, 12(48):9821–9831, 2016.

[47] I. Llopis and I. Pagonabarraga, *Dynamic regimes of hydrodynamically coupled self-propelling particles.* Europhys. Lett., 75(6):999, 2006.

[48] J. de Graaf, H. Menke, A. J. Mathijssen, M. Fabritius, C. Holm, and T. N. Shendruk, *Lattice-boltzmann hydrodynamics of anisotropic active matter.* J. Chem. Phys., 144(13):134106, 2016.

[49] R. Matas-Navarro, R. Golestanian, T. B. Liverpool, and S. M. Fielding, *Hydrodynamic suppression of phase separation in active suspensions.* Phys. Rev. E, 90(3):032304, 2014.

[50] R. M. Navarro and S. M. Fielding, *Clustering and phase behaviour of attractive active particles with hydrodynamics.* Soft Matter, 11(38):7525–7546, 2015.

[51] B. ten Hagen, R. Wittkowski, D. Takagi, F. Kümmel, C. Bechinger, and H. Löwen, *Can the self-propulsion of anisotropic microswimmers be described by using forces and torques?* J. Phys. Condens. Matter, 27(19):194110, 2015.

[52] P. Langevin, *Sur la théorie du mouvement brownien.* CR Acad. Sci. Paris, 146(530-533):530, 1908.

[53] W. Sutherland, *LXXV. A dynamical theory of diffusion for non-electrolytes and the molecular mass of albumin.* Philos. Mag., 9(54):781–785, 1905.

[54] A. Einstein, *Über die von der molekularkinetischen theorie der wärme geforderte bewegung von in ruhenden flüssigkeiten suspendierten teilchen.* Ann. Phys., 322(8):549–560, 1905.

[55] M. Von Smoluchowski, *Zur kinetischen theorie der brownschen molekularbewegung und der suspensionen.* Ann. Phys., 326(14):756–780, 1906.

[56] G. H. Koenderink and A. P. Philipse, *Rotational and translational self-diffusion in colloidal sphere suspensions and the applicability of generalized stokes-einstein relations.* Langmuir, 16(13):5631–5638, 2000.

[57] R. Ni, M. A. C. Stuart, and M. Dijkstra, *Pushing the glass transition towards random close packing using self-propelled hard spheres.* Nat. Commun., 4:2704, 2013.

[58] Y. Fily, S. Henkes, and M. C. Marchetti, *Freezing and phase separation of self-propelled disks.* Soft Matter, 10:2132–2140, 2014.

[59] X. Yang, M. L. Manning, and M. C. Marchetti, *Aggregation and segregation of confined active particles.* Soft Matter, 10:6477–6484, 2014.

[60] H. C. Berg. *E. coli in Motion.* Springer, 2004.

[61] G. S. Redner, M. F. Hagan, and A. Baskaran, *Structure and dynamics of a phase-separating active colloidal fluid.* Phys. Rev. Lett., 110(5):055701, 2013.

[62] J. Stenhammar, D. Marenduzzo, R. J. Allen, and M. E. Cates, *Phase behaviour of active brownian particles: the role of dimensionality.* Soft Matter, 10(10):1489–1499, 2014.

[63] T. Vicsek, A. Czirók, E. Ben-Jacob, I. Cohen, and O. Shochet, *Novel type of phase transition in a system of self-driven particles.* Phys. Rev. Lett., 75:1226–1229, 1995.

[64] J. Toner and Y. Tu, *Flocks, herds, and schools: A quantitative theory of flocking.* Phys. Rev. E, 58(4):4828, 1998.

[65] J. Toner and Y. Tu, *Long-range order in a two-dimensional dynamical xy model: how birds fly together.* Phys. Rev. Lett., 75(23):4326, 1995.

[66] H. Chaté, F. Ginelli, G. Grégoire, F. Peruani, and F. Raynaud, *Modeling collective motion: variations on the vicsek model.* Eur. Phys. J. B, 64(3-4):451–456, 2008.

[67] H. Chaté, F. Ginelli, G. Grégoire, and F. Raynaud, *Collective motion of self-propelled particles interacting without cohesion.* Phys. Rev. E, 77(4):046113, 2008.

[68] F. Ginelli and H. Chaté, *Relevance of metric-free interactions in flocking phenomena.* Phys. Rev. Lett., 105(16):168103, 2010.

[69] A. Solon and J. Tailleur, *Revisiting the flocking transition using active spins.* Phys. Rev. Lett., 111(7):078101, 2013.

[70] J.-B. Caussin, A. Solon, A. Peshkov, H. Chaté, T. Dauxois, J. Tailleur, V. Vitelli, and D. Bartolo, *Emergent spatial structures in flocking models: a dynamical system insight.* Phys. Rev. Lett., 112(14):148102, 2014.

[71] V. Dossetti and F. J. Sevilla, *Emergence of collective motion in a model of interacting brownian particles.* Phys. Rev. Lett., 115(5):058301, 2015.

[72] F. Cucker and E. Mordecki, *Flocking in noisy environments.* J. Math. Pures Appl., 89(3):278–296, 2008.

[73] H. Chaté, F. Ginelli, and R. Montagne, *Simple model for active nematics: quasi-long-range order and giant fluctuations.* Phys. Rev. Lett., 96(18):180602, 2006.

[74] Y. Fily and M. C. Marchetti, *Athermal phase separation of self-propelled particles with no alignment.* Phys. Rev. Lett., 108:235702, 2012.

[75] G. S. Redner, A. Baskaran, and M. F. Hagan, *Reentrant phase behavior in active colloids with attraction.* Phys. Rev. E, 88:012305, 2013.

[76] A. Suma, G. Gonnella, D. Marenduzzo, and E. Orlandini, *Motility-induced phase separation in an active dumbbell fluid.* EPL (Europhysics Letters), 108(5):56004, 2014.

[77] S. Weitz, A. Deutsch, and F. Peruani, *Self-propelled rods exhibit a phase-separated state characterized by the presence of active stresses and the ejection of polar clusters.* Phys. Rev. E, 92(1):012322, 2015.

[78] S. E. Ilse, C. Holm, and J. de Graaf, *Surface roughness stabilizes the clustering of self-propelled triangles.* J. Chem. Phys., 145(13):134904, 2016.

[79] J. Stenhammar, A. Tiribocchi, R. J. Allen, D. Marenduzzo, and M. E. Cates, *Continuum theory of phase separation kinetics for active brownian particles.* Phys. Rev. Lett., 111(14):145702, 2013.

[80] R. Wittkowski, A. Tiribocchi, J. Stenhammar, R. J. Allen, D. Marenduzzo, and M. E. Cates, *Scalar $\varphi 4$ field theory for active-particle phase separation.* Nat. Commun., 5:4531, 2014.

[81] T. Speck, J. Bialké, A. M. Menzel, and H. Löwen, *Effective Cahn-Hilliard equation for the phase separation of active brownian particles.* Phys. Rev. Lett., 112:218304, 2014.

[82] M. E. Cates and J. Tailleur, *Motility-induced phase separation.* Annu. Rev. Condens. Matter Phys., 6(1):219–244, 2015.

[83] J. W. Gibbs. *Elementary principles in statistical mechanics.* Courier Corporation, 2014.

[84] J. W. Gibbs. *The scientific papers of J. Willard Gibbs*, volume 1. Longmans, Green and Company, 1906.

[85] A. Wysocki, R. G. Winkler, and G. Gompper, *Cooperative motion of active brownian spheres in three-dimensional dense suspensions.* Europhys. Lett., 105(4):48004, 2014.

[86] S. C. Takatori and J. F. Brady, *Towards a thermodynamics of active matter.* Phys. Rev. E, 91(3):032117, 2015.

[87] C. Maggi, U. M. B. Marconi, N. Gnan, and R. Di Leonardo, *Multidimensional stationary probability distribution for interacting active particles.* Sci. Rep., 5:10742, 2015.

[88] T. F. Farage, P. Krinninger, and J. M. Brader, *Effective interactions in active brownian suspensions.* Phys. Rev. E, 91(4):042310, 2015.

[89] U. M. B. Marconi and C. Maggi, *Towards a statistical mechanical theory of active fluids.* Soft Matter, 11(45):8768–8781, 2015.

[90] A. Solon, Y. Fily, A. Baskaran, M. Cates, Y. Kafri, M. Kardar, and J. Tailleur, *Pressure is not a state function for generic active fluids.* Nat. Phys., 11:673, 2015.

[91] J. Bialké, J. T. Siebert, H. Löwen, and T. Speck, *Negative interfacial tension in phase-separated active brownian particles.* Phys. Rev. Lett., 115(9):098301, 2015.

[92] G. Falasco, F. Baldovin, K. Kroy, and M. Baiesi, *Mesoscopic virial equation for nonequilibrium statistical mechanics.* New J. Phys., 18(9):093043, 2016.

[93] T. Speck and R. L. Jack, *Ideal bulk pressure of active brownian particles.* Phys. Rev. E, 93(6):062605, 2016.

[94] T. Speck, *Stochastic thermodynamics for active matter.* EPL (Europhysics Letters), 114(3):30006, 2016.

[95] M. Paoluzzi, C. Maggi, U. M. B. Marconi, and N. Gnan, *Critical phenomena in active matter.* Phys. Rev. E, 94(5):052602, 2016.

[96] É. Fodor, C. Nardini, M. E. Cates, J. Tailleur, P. Visco, and F. van Wijland, *How far from equilibrium is active matter?* Phys. Rev. Lett., 117(3):038103, 2016.

[97] Z. Preisler and M. Dijkstra, *Configurational entropy and effective temperature in systems of active brownian particles.* Soft Matter, 12(28):6043–6048, 2016.

[98] C. Nardini, É. Fodor, E. Tjhung, F. van Wijland, J. Tailleur, and M. E. Cates, *Entropy production in field theories without time-reversal symmetry: Quantifying the non-equilibrium character of active matter.* Phys. Rev. X, 7(2):021007, 2017.

[99] D. Loi, S. Mossa, and L. F. Cugliandolo, *Effective temperature of active matter.* Phys. Rev. E, 77(5):051111, 2008.

[100] L. Berthier and J. Kurchan, *Non-equilibrium glass transitions in driven and active matter.* Nat. Phys., 9(5):310–314, 2013.

[101] J. Palacci, C. Cottin-Bizonne, C. Ybert, and L. Bocquet, *Sedimentation and effective temperature of active colloidal suspensions.* Phys. Rev. Lett., 105(8):088304, 2010.

[102] A. P. Solon, J. Stenhammar, M. E. Cates, Y. Kafri, and J. Tailleur, *Generalized thermodynamics of phase equilibria in scalar active matter.* arXiv preprint arXiv:1609.03483, 2016.

[103] M. Dijkstra, S. Paliwal, J. Rodenburg, and R. van Roij, *Chemical potential in active systems: Towards predicting phase equilibria from bulk equations of state using a swim potential.* arXiv preprint arXiv:1609.02773, 2016.

[104] B. M. Mognetti, A. Šarić, S. Angioletti-Uberti, A. Cacciuto, C. Valeriani, and D. Frenkel, *Living clusters and crystals from low-density suspensions of active colloids.* Phys. Rev. Lett., 111:245702, 2013.

[105] B. Smit, *Phase diagrams of Lennard-Jones fluids.* J. Chem. Phys., 96(11):8639–8640, 1992.

[106] J. Vrabec, G. K. Kedia, G. Fuchs, and H. Hasse, *Comprehensive study of the vapour–liquid coexistence of the truncated and shifted Lennard–Jones fluid including planar and spherical interface properties.* Mol. Phys., 104(09):1509–1527, 2006.

[107] D. Higham, *An algorithmic introduction to numerical simulation of stochastic differential equations.* SIAM Rev., 43(3):525–546, 2001.

[108] N. Grønbech-Jensen and O. Farago, *A simple and effective Verlet-type algorithm for simulating Langevin dynamics.* Mol. Phys., 111(8):983–991, 2013.

[109] C. H. Rycroft, *Voro++: A three-dimensional Voronoi cell library in C++.* Chaos, 19:041111, 2009.

[110] Y. Wang, S. Teitel, and C. Dellago, *Melting of icosahedral gold nanoclusters from molecular dynamics simulations.* J. Chem. Phys., 122:214722, 2005.

[111] J. Bialké, T. Speck, and H. Löwen, *Active colloidal suspensions: Clustering and phase behavior.* J. Non-Cryst. Solids, 407(0):367 – 375, 2015.

[112] S. Dey, D. Das, and R. Rajesh, *Spatial structures and giant number fluctuations in models of active matter.* Phys. Rev. Lett., 108(23):238001, 2012.

[113] C. Bechinger, R. Di Leonardo, H. Löwen, C. Reichhardt, G. Volpe, and G. Volpe, *Active particles in complex and crowded environments.* Rev. Mod. Phys., 88(4):045006, 2016.

[114] C.-N. Yang and T.-D. Lee, *Statistical theory of equations of state and phase transitions. i. theory of condensation.* Phys. Rev., 87(3):404, 1952.

[115] T.-D. Lee and C.-N. Yang, *Statistical theory of equations of state and phase transitions. ii. lattice gas and ising model.* Phys. Rev., 87(3):410, 1952.

[116] H. Watanabe, N. Ito, and C.-K. Hu, *Phase diagram and universality of the Lennard-Jones gas-liquid system.* J. Chem. Phys., 136(20):204102, 2012.

[117] S. Reif-Acherman, *The history of the rectilinear diameter law.* Quím. Nova, 33(9):2003–2010, 2010.

[118] V. Prymidis, S. Samin, and L. Filion, *State behaviour and dynamics of self-propelled brownian squares: a simulation study.* Soft Matter, 12(19):4309–4317, 2016.

[119] M. G. Noro and D. Frenkel, *Extended corresponding-states behavior for particles with variable range attractions.* J. Chem. Phys., 113(8):2941–2944, 2000.

[120] D. Dunikov, S. Malyshenko, and V. Zhakhovskii, *Corresponding states law and molecular dynamics simulations of the Lennard-Jones fluid.* J. Chem. Phys., 115(14):6623–6631, 2001.

[121] V. Prymidis, H. Sielcken, and L. Filion, *Self-assembly of active attractive spheres.* Soft Matter, 11(21):4158–4166, 2015.

[122] R. G. Winkler, A. Wysocki, and G. Gompper, *Virial pressure in systems of spherical active brownian particles.* Soft Matter, 11(33):6680–6691, 2015.

[123] S. C. Takatori, W. Yan, and J. F. Brady, *Swim pressure: stress generation in active matter.* Phys. Rev. Lett., 113(2):028103, 2014.

[124] E. A. Guggenheim, *The principle of corresponding states.* J. Chem. Phys., 13(7):253–261, 1945.

[125] W. Shi and J. K. Johnson, *Histogram reweighting and finite-size scaling study of the Lennard–Jones fluids.* FFE, 187:171–191, 2001.

[126] E. S. Loscar, C. G. Ferrara, and T. S. Grigera, *Spinodals and critical point using short-time dynamics for a simple model of liquid.* J. Chem. Phys., 144(13):134501, 2016.

[127] A. P. Solon, J. Stenhammar, R. Wittkowski, M. Kardar, Y. Kafri, M. E. Cates, and J. Tailleur, *Pressure and phase equilibria in interacting active brownian spheres.* Phys. Rev. Lett., 114(19):198301, 2015.

[128] S. C. Takatori and J. F. Brady, *A theory for the phase behavior of mixtures of active particles.* Soft Matter, 11(40):7920–7931, 2015.

[129] W. Yan and J. F. Brady, *The swim force as a body force.* Soft Matter, 11(31):6235–6244, 2015.

[130] C. F. Lee, *Interface stability, interface fluctuations, and the Gibbs–Thomson relationship in motility-induced phase separations.* Soft Matter, 13(2):376–385, 2017.

[131] T. Ikeshoji, B. Hafskjold, and H. Furuholt, *Molecular-level calculation scheme for pressure in inhomogeneous systems of flat and spherical layers.* Mol. Simul., 29(2):101–109, 2003.

[132] M. V. Berry, *The molecular mechanism of surface tension.* Phys. Educ., 6(2):79, 1971.

[133] A. Marchand, J. H. Weijs, J. H. Snoeijer, and B. Andreotti, *Why is surface tension a force parallel to the interface?* Am. J. Phys, 79(10):999–1008, 2011.

[134] A. Fortini, M. Dijkstra, M. Schmidt, and P. P. Wessels, *Wall-fluid and liquid-gas interfaces of model colloid-polymer mixtures by simulation and theory.* Phys. Rev. E, 71(5):051403, 2005.

[135] P. Virnau and M. Müller, *Calculation of free energy through successive umbrella sampling.* J. Chem. Phys., 120(23):10925–10930, 2004.

[136] K. Binder, *Monte carlo calculation of the surface tension for two-and three-dimensional lattice-gas models.* Phys. Rev. A, 25(3):1699, 1982.

[137] J. J. Potoff and A. Z. Panagiotopoulos, *Surface tension of the three-dimensional lennard-jones fluid from histogram-reweighting monte carlo simulations.* J. Chem. Phys., 112(14):6411–6415, 2000.

[138] M. Müller and L. G. MacDowell, *Wetting of polymer liquids: Monte carlo simulations and self-consistent field calculations.* J. Phys. Condens. Matter, 15(19):R609, 2003.

[139] S. W. Sides, G. S. Grest, and M.-D. Lacasse, *Capillary waves at liquid-vapor interfaces: A molecular dynamics simulation.* Phys. Rev. E, 60(6):6708, 1999.

[140] M.-D. Lacasse, G. S. Grest, and A. J. Levine, *Capillary-wave and chain-length effects at polymer/polymer interfaces.* Phys. Rev. Lett., 80(2):309, 1998.

[141] F. Buff, R. Lovett, and F. Stillinger Jr, *Interfacial density profile for fluids in the critical region.* Phys. Rev. Lett., 15(15):621, 1965.

[142] D. Beysens and M. Robert, *Thickness of fluid interfaces near the critical point from optical reflectivity measurements.* J. Chem. Phys., 87(5):3056–3061, 1987.

[143] M. A. Anisimov. *Critical Phenomena in Liquids and Liquid Crystals.* Gordon and Breach Science Publishers, 1991.

[144] J. S. Rowlinson and B. Widom. *Molecular theory of capillarity.* Courier Corporation, 2013.

[145] A. E. Ismail, G. S. Grest, and M. J. Stevens, *Capillary waves at the liquid-vapor interface and the surface tension of water.* J. Chem. Phys., 125(1):014702, 2006.

[146] F. Ginot, I. Theurkauff, D. Levis, C. Ybert, L. Bocquet, L. Berthier, and C. Cottin-Bizonne, *Nonequilibrium equation of state in suspensions of active colloids.* Phys. Rev. X, 5(1):011004, 2015.

[147] M. E. Cates and J. Tailleur, *Motility-induced phase separation.* Annu. Rev. Condens. Matter Phys., 6(1):219–244, 2015.

[148] C. Reichhardt and C. O. Reichhardt, *Active matter ratchets with an external drift.* Phys. Rev. E, 88(6):062310, 2013.

[149] R. Di Leonardo, L. Angelani, D. Dell'Arciprete, G. Ruocco, V. Iebba, S. Schippa, M. Conte, F. Mecarini, F. De Angelis, and E. Di Fabrizio, *Bacterial ratchet motors.* Proc. Natl. Acad. Sci., 107(21):9541–9545, 2010.

[150] V. Prymidis, S. Paliwal, M. Dijkstra, and L. Filion, *Vapour-liquid coexistence of an active Lennard-Jones fluid.* J. Chem. Phys., 145(12):124904, 2016.

[151] B. Trefz, S. K. Das, S. A. Egorov, P. Virnau, and K. Binder, *Activity mediated phase separation: Can we understand phase behavior of the nonequilibrium problem from an equilibrium approach?* J. Chem. Phys., 144(14):144902, 2016.

[152] J. Tailleur and M. Cates, *Statistical mechanics of interacting run-and-tumble bacteria.* Phys. Rev. Lett., 100(21):218103, 2008.

[153] D. Frenkel and B. Smit. *Understanding molecular simulation: from algorithms to applications*, volume 1. Academic press, 2001.

[154] C. Tung, J. Harder, C. Valeriani, and A. Cacciuto, *Micro-phase separation in two dimensional suspensions of self-propelled spheres and dumbbells.* Soft Matter, 12(2):555–561, 2016.

[155] F. Peruani, A. Deutsch, and M. Bär, *Nonequilibrium clustering of self-propelled rods.* Phys. Rev. E, 74(3):030904, 2006.

[156] H.-S. Kuan, R. Blackwell, L. E. Hough, M. A. Glaser, and M. Betterton, *Hysteresis, reentrance, and glassy dynamics in systems of self-propelled rods.* Phys. Rev. E, 92(6):060501, 2015.

[157] H. R. Vutukuri, Z. Preisler, T. H. Besseling, A. van Blaaderen, M. Dijkstra, and W. T. Huck, *Dynamic self-organization of side-propelling colloidal rods: experiments and simulations.* Soft Matter, 12(48):9657–9665, 2016.

[158] Y. Yang, V. Marceau, and G. Gompper, *Swarm behavior of self-propelled rods and swimming flagella.* Phys. Rev. E, 82(3):031904, 2010.

[159] C. Avendaño and F. A. Escobedo, *Phase behavior of rounded hard-squares.* Soft Matter, 8(17):4675–4681, 2012.

[160] J. B. Hubbard and J. F. Douglas, *Hydrodynamic friction of arbitrarily shaped brownian particles.* Phys. Rev. E, 47(5):R2983, 1993.

[161] B. Bet, G. Boosten, M. Dijkstra, and R. van Roij, *Efficient shapes for microswimming: From three-body swimmers to helical flagella.* J. Chem. Phys., 146(8):084904, 2017.

[162] H. H. Wensink, J. Dunkel, S. Heidenreich, K. Drescher, R. E. Goldstein, H. Löwen, and J. M. Yeomans, *Meso-scale turbulence in living fluids.* Proc. Natl. Acad. Sci., 109(36):14308–14313, 2012.

[163] P. M. Chaikin and T. C. Lubensky. *Principles of condensed matter physics*, volume 1. Cambridge Univ Press, 2000.

[164] A. J. Bray, *Theory of phase-ordering kinetics.* Adv. Phys., 51(2):481–587, 2002.

[165] F. Peruani and M. Baer, *A kinetic model and scaling properties of non-equilibrium clustering of self-propelled particles.* New J. Phys., 15(6):065009, 2013.

[166] D. S. Dean, *Langevin equation for the density of a system of interacting Langevin processes.* J. Phys. A: Math. Gen., 29(24):L613, 1996.

[167] A. M. Menzel, *Collective motion of binary self-propelled particle mixtures.* Phys, Rev. E, 85(2):021912, 2012.

Summary

In this thesis we study emergent statistical properties of many-particle systems of self-propelled particles using computer simulations. Ensembles of self-propelled particles belong to the class of physical systems labeled *active matter*, a term that refers to systems whose individual components are able to convert internal energy or energy from their environment into motion. Examples of such systems include populations of living organisms, such as birds and bacteria, but also synthetic swimmers, typically on the colloidal and granular scale. Active matter systems are intrinsically out-of-equilibrium systems due to the constant input of energy. Thanks to their out-of-equilibrium nature they can often show complex patterns of collective motion, such as turbulent flows of bacterial colonies, as well as exhibit phenomena fully prohibited to equilibrium systems, for example the motility-induced phase-separation of self-propelled purely-repulsive discs. Surprisingly, paradigms of equilibrium thermodynamics and statistical physics can be applied to active matter in many cases, suggesting that perhaps an extended thermodynamical description of such systems is possible. This possibility, along with recent advances in the fabrication of artificial swimmers and their possible applications, for example targeted cargo delivery, has led to an intensive theoretical research of active matter systems in the last decade.

The model systems that we consider here are toy models that can be associated with the world of active colloids. *Colloids* are small particles in the nanometer to micrometer scale, typically immersed in a molecular solvent. The constant collisions between colloids and solvent molecules render the inertia of the particles irrelevant for the particles' motion and also result in random displacement of particles which is known as Brownian motion. Active colloids are equipped with a propulsion mechanism that enables them to swim and are thus also referred to as microswimmers. Our models take into account only three essential components that dictate the movement of particles: the *self-propulsion* of individual particles, the *interactions* between them and the *random forces* that displace them. In brief, we employ computer simulations in order to simulate the motion of self-propelled, Brownian particles that interact with one another *via* various types of potentials and we investigate the collective behaviour of many-particle systems, as well as test the applicability of thermodynamics and statistical physics tools and notions to the active matter systems under study.

In Chapter 2 we study the *self-assembly* of a three-dimensional system of *attractive* self-propelled particles that interact *via* the Lennard-Jones potential. The term self-assembly refers to the spontaneous organization of many-particle systems in stable configurations or structures. By varying the strength of the attraction between particles as well as the rotational diffusion rate of the axes of self-propulsion, we construct various state diagrams for the system at intermediate densities. For fast rotational diffusion the self-propulsion essentially acts as a random displacement force and the state diagram of the system bears strong similarities to an equilibrium system of Brownian, Lennard-Jones particles; as the attraction between particles is increased, the system transitions from a fluid state first to a coexistence between vapour and liquid and ultimately a coexistence between vapour and crystal phases. Moreover, the lever rule, which dictates that the values of

coexisting densities should not depend on the total density of the system, is obeyed throughout the coexistence region. However, for slower rotational diffusion rates the state diagram significantly departs from the equilibrium one. In particular, the interplay between self-propulsion and attractive interactions gives rise to a *new state* between the fluid and the vapour-liquid coexistence region of the state diagram. This state consists of interconnected yet motile clusters of particles that assemble in a system-spanning network. By investigating the local correlations between the axes of self-propulsion in this novel state we discover significant local alignment of the axes of neighboring particles despite the absence of aligning interactions.

The same system is studied in the subsequent Chapter 3, where we concentrate on the *vapour-liquid phase transition* that the system undergoes with increasing strength of attraction between the particles. The mechanical pressure of the system is calculated and it is shown that, when the transition takes place, the equations of state for the system exhibit features completely analogous to the respective equations of state of the equilibrium Lennard-Jones system, provided that a direct contribution of the self-propulsion to the pressure - called swim pressure - is taken into account. Subsequently, we measure the coexisting densities of the vapour and the liquid phase for our out-of equilibrium system and find that the scaling of these densities with the strength of the attraction follows simple power laws, similar to the equilibrium system. In equilibrium, the various parameters of these laws are directly linked to the critical point of the transition and its universality class. However, we can not assert whether the active Lennard-Jones system undergoes a true second order phase-transition and thus whether a critical point exists. Nonetheless, we find that the scaling of all the aforementioned parameters with increasing activity of the system, that is either increasing self-propulsion speed or decreasing rotational diffusion rates of the particles, is captured by simple exponential functions of the same form. Last but not least, we check the validity of the law of corresponding states and the law of rectilinear diameters and find that both of them are unmistakably violated in this active matter system.

In Chapter 4 we take the next step in the study of the active Lennard-Jones system that is done in Chapters 2-3 by now solely focusing on the *vapour-liquid interface* and its statistical properties. We employ a local definition of the mechanical pressure and demonstrate mechanical equilibrium of the system across the interface by measuring a constant profile along the simulation box of the component of the pressure that is perpendicular to the interface. Subsequently, we measure the tangential component of the pressure, which enables us to calculate the tension of the interface as the mechanical work required to enlarge the interface. Our calculations result in a positive interfacial tension of the vapour-liquid interface for all the parameter space points that we consider, that is systems with different self-propulsion speeds, rotational diffusion rates and strengths of attraction. Next, we study the scaling of the interfacial tension as a function of the attraction strength by fitting it to simple power laws, similar to the treatment presented for the coexisting densities in Chapter 3. We show that the scaling of the interfacial tension can be captured *via* equilibrium-like power laws. Surprisingly, we find that the fitted values of the "critical" temperature of the system that can be obtained *via* the scaling of the tension are in close agreement with the values that are obtained in Chapter 3 using the scaling of the independently measured coexisting densities. Last but not least,

by simulating systems of different sizes we measure the scaling of the interfacial width with the interfacial area. We then naively apply results from capillary wave theory in order to associate this scaling with the stiffness of the interface. We find that the calculated interfacial stiffness is then directly proportional to the interfacial tension, same as in the equilibrium system, but with the proportionality constant given by an effective temperature of the system.

Subsequently, in Chapter 5 we simulate two different *binary mixtures* of active particles and demonstrate the *mechanical* and *chemical equilibrium* of their corresponding coexisting phases. First, we study a three-dimensional binary system of active and passive attractive particles that undergoes a vapour-liquid phase transition due to the attractions between particles. This system is similar to the system studied in Chapters 2-4, but in this mixture the passive particles are not self-propelled but simply undergo Brownian motion. Initially we demonstrate mechanical equilibrium of the coexisting vapour and liquid phases by directly measuring the normal component of the pressure, as done previously in Chapter 4. Then, by bringing independently each of the two coexisting binary phases into chemical equilibrium with a reservoir of particles of a given species, we show that the connected reservoirs of each particle species are identical for the two phases. We thus measure the density of the reservoir as a quantity analogous to the chemical potential of equilibrium systems and argue that the numerical method of attaching a binary phase to a particle reservoir can be used in order to demonstrate chemical equilibrium between coexisting phases. We then move on to study a two-dimensional binary mixture of self-propelled, purely repulsive discs. The two different species in this mixture differ only in their values of self-propulsion speed, which are chosen such that the system undergoes motility-induced phase-separation for all compositions. We then proceed to calculate the bulk properties of single binary phases by bringing them in chemical equilibrium with particle reservoirs and measuring the bulk pressure of the binary phase as well as the density of the connected reservoir. By demanding that coexisting phases have equal pressures and equal particle reservoir densities for each species we are then able to quantitatively *predict* the phase diagram of the system without having to resort to any approximations.

In Chapter 6 we depart from purely isotropic interactions between particles and we investigate the *state behaviour* and the *dynamics* of a two-dimensional system of self-propelled, purely-repulsive, *square-shaped* particles. By examining systems with different simulation parameters we construct the state diagram; for low densities and slow speeds of self-propulsion we find the system in a fluid phase, while for the regime of high densities and fast speeds we observe phase coexistence between a crystalline cluster and a gas due to the motility of the particles. Interestingly, between the two regimes we find a region where the system incessantly oscillates between a homogeneous fluid and a phase separated state. We show that in the coexistence regime the lever rule and the law of rectilinear diameters are obeyed by the system. Moreover, we monitor the nucleation, growth, and eventual rupture of crystalline clusters in the oscillatory regime and present a possible scenario that explains the system's oscillations by providing a direct link between the rupture of the clusters and the accumulation of stresses in the interior of the cluster. Lastly, we measure the coarsening rates of the system and find that it coarsens much faster than equilibrium systems, an increase that may be due to the peculiar dynamics of individual clusters.

Finally, in Chapter 7 we consider a two-dimensional system of disc-like self-propelled particles that explicitly exert *torques* on one another and render the axes of self-propulsion of neighboring particles anti-parallel. For fast speeds of self-propulsion and high densities this system undergoes motility-induced phase separation. We find that the state diagram of the system is subject to the lever rule and subsequently apply the methods employed in Chapter 5 in order to study the mechanical and chemical equilibrium of coexisting phases. We write down the *force balance equation* and we aim to investigate whether the mechanical equilibrium of coexisting phases can be shown by studying the various components of the equation in phase-separated systems. We find that the quantity associated with the local pressure of isotropic particles assumes a constant profile along the interface only in the absence of anisotropic interactions and a pressure difference is measured when particles exert torques onto one another. One possible interpretation of this result is that the out-of-equilibrium nature of the system manifests itself as an external force that acts at the interface and creates the measured pressure difference between the two coexisting phases. Moreover, the chemical equilibrium between coexisting phases is shown by connecting single phases to particle reservoirs, in a slight modification of the method introduced in Chapter 5.

In conclusion, we demonstrate that active matter systems on one hand have state diagrams with similar properties to equilibrium systems and that these state diagrams can even be predicted by studying single phases when utilizing methods similar to celebrated techniques of equilibrium statistical physics. Also, many properties related to phase transitions and interfaces separating coexisting phases can be described by laws that are generalizations of equilibrium laws. On the other hand we find that the self-propulsion of particles can lead to unexpected results with no equilibrium counterpart, such us the emergence of the state of interconnected motile clusters of attractive self-propelled particles and the oscillating state of self-propelled squares. Hopefully these results will act as a stepping stone in the effort to construct a thermodynamics of active matter but also help to set the limit up to where this thermodynamics description is valid.

Samenvatting

In dit proefschrift bestuderen we opkomende statistische eigenschappen van veel-deeltjessystemen van zelfvoortstuwende deeltjes met behulp van computersimulaties. Systemen van zelfvoortstuwende deeltjes behoren tot de klasse van fysieke systemen met de naam *actieve materie*, een term die betrekking heeft op systemen waarvan de individuele componenten interne energie of energie uit hun omgeving in beweging kunnen omzetten. Voorbeelden van dergelijke systemen zijn populaties van levende organismen, zoals vogels en bacteriën, maar ook synthetische zwemmers, doorgaans op de colloïdale en granulaire schaal. Actieve materiesystemen zijn intrinsiek buiten-evenwichtssystemen door de constante invoer van energie. Door hun buiten-evenwichtige natuur kunnen ze vaak complexe patronen van collectieve beweging tonen, zoals turbulente stromen van bacteriële kolonies, en kunnen ze fenomenen vertonen die voor evenwichtssystemen volledig verboden zijn, bijv. de motiliteitsgeïnduceerde fase-scheiding uit de zelfgedreven zuiver afstotende schijven. Verrassend genoeg kunnen paradigma's van evenwichtsthermodynamica en statistische fysica in veel gevallen op actieve materie worden toegepast, wat suggereert dat een uitgebreide thermodynamische beschrijving van dergelijke systemen wellicht mogelijk is. Samen met de recente vooruitgang in de fabricage van kunstmatige zwemmers en hun mogelijke toepassingen, zoals ladingstransport naar specifieke plaatsen, heeft dit vooruitzicht geleid tot een intensief theoretisch onderzoek van actieve materiesystemen in het afgelopen decennium.

De modelsystemen die we hier beschouwen zijn speelgoedmodellen die verbonden kunnen worden met de wereld van actieve colloiden. *Colloïden* zijn kleine deeltjes op de nanometer tot micrometer schaal, meestal ondergedompeld in een moleculair oplosmiddel. De constante botsingen tussen colloïden en oplosmiddelmoleculen zorgen ervoor dat de inertie van de deeltjes los staat van de deeltjesbeweging en resulteren ook in de willekeurige verplaatsing van deeltjes die bekend staat als Brownse beweging. Actieve colloïden zijn uitgerust met een voortstuwingsmechanisme waarmee ze kunnen zwemmen en worden ook wel microswimmers genoemd. Onze modellen houden rekening met slechts drie essentiële componenten die de beweging van deeltjes dicteren: de *zelfvoortstuwing* van individuele deeltjes, hun *interacties* en de *willekeurige krachten* die ze ondervinden. Kortom, we gebruiken computersimulaties om de beweging van zelfvoortstuwende, Brownse deeltjes te simuleren die via verschillende soorten potentialen met elkaar interacteren. We onderzoeken vervolgens het collectieve gedrag deze veel-deeltjessystemen, en toetsen de toepasselijkheid en concepten uit de thermodynamica en statistische fysica op actieve systemen.

In Hoofdstuk 2 bestuderen we de *zelforganisatie* van een driedimensionaal systeem van *aantrekkende* zelfvoortstuwende deeltjes die interacteren via de Lennard-Jones-potentiaal. De term zelforganisatie verwijst naar de spontane organisatie van veel-deeltjes systemen die liedt tot een stabiele configuratie of structuur. Door de sterkte van de aantrekkingskracht tussen de deeltjes en de snelheid waarmee de voortstuwingsas roteert te variëren, bouwen we verschillende fasediagrammen op voor het systeem. Voor snelle rotatiediffusie fungeert de zelfbeweging in wezen als een willekeurige verplaatsingskracht en ver-

toont het fasediagram van het systeem sterke overeenkomsten met een evenwichtssysteem van Brownse Lennard-Jones deeltjes: bij toenemende aantrekkingskracht tussen de deeltjes, gaat het systeem eerst van een vloeistoffase over naar een coëxistentie tussen damp en vloeistof en uiteindelijk naar een coëxistentie tussen damp- en kristalfasen. Bovendien wordt de hefboomregel, die dicteert dat de waarden van coëxistente dichtheden niet afhankelijk zijn van de totale dichtheid van het systeem, in de coëxistentie-regio gehandhaafd. Voor langzamere rotatiediffusiesnelheden wijkt het fasediagram echter aanzienlijk af van dat in evenwicht. In het bijzonder veroorzaakt de wisselwerking tussen zelfvoortstuwing en aantrekkende interacties een *nieuwe toestand* tussen het vloeistof- en het coëxistentiegebied van damp-vloeistof in het fasediagram. Deze toestand bestaat uit onderling verbonden, maar toch motiele clusters van deeltjes die zich in een systeemwijd netwerk organiseren. Door de lokale correlaties tussen de assen van zelfvoortstuwing in deze nieuwe toestand te onderzoeken, ontdekken we dat de assen van naburige deeltjes preferentied dezelfde richting hebben, ondanks de afwezigheid van interacties die hier expliciet voor zorgen.

Hetzelfde systeem wordt bestudeerd in Hoofdstuk 3, waarbij we ons concentreren op de *damp-vloeistof faseovergang* die het systeem ondergaat met een toenemende aantrekkingskracht tussen de deeltjes. De mechanische druk van het systeem wordt berekend en het wordt aangetoond dat wanneer de overgang plaatsvindt, de staatsvergelijkingen voor het systeem kenmerken hebben die volledig analoog zijn aan de respectievelijke staatsvergelijkingen van het evenwichts-Lennard-Jones systeem, mits een directe bijdrage van de zelfvoortstuwingssnelheid aan de druk - een zogenaamde zwemdruk - in acht wordt genomen. Vervolgens meten we de coëxistentiedichtheden van de damp en de vloeibare fase voor ons buiten-evenwichtssysteem en vinden we dat deze dichtheden schalen met de kracht van de aantrekking, beschreven door eenvoudige machtsfuncties, vergelijkbaar met het evenwichtssysteem. In evenwicht zijn de verschillende parameters van deze functies rechtstreeks gekoppeld aan het kritische punt van de overgang en de universaliteitsklasse. We kunnen echter niet zeggen of het actieve (buiten-evenwicht) Lennard-Jones-systeem ook een ware tweede-orde-faseovergang ondergaat en dus of er überhaupt een kritisch punt bestaat. Desalniettemin vinden wij dat de schaling van alle bovengenoemde parameters met toenemende activiteit van het systeem, d.w.z. een toenemende zelfvoortstuwingssnelheid of afnemende rotatiediffusiesnelheid van de deeltjes, goed wordt beschreven door eenvoudige exponentiële functies van dezelfde vorm. Ten slotte controleren we de geldigheid van de law of corresponding states en de law of rectilinear parameters en vinden dat ze in dit actieve materiesysteem beide onmiskenbaar worden geschonden.

In Hoofdstuk 4 nemen we de volgende stap in de studie van het actieve Lennard-Jones systeem dat in Hoofdstukken 2-3 wordt gedaan, en nu uitsluitend gericht op het *damp-vloeistof grensvlak* en diens statistische eigenschappen. Wij gebruiken een lokale definitie van de mechanische druk en tonen aan dat er mechanisch evenwicht is op het grensvlak door te laten zien dat het drukelement dat loodrecht op het grensvlak staat in de hele simulatiebox constant is. Vervolgens meten we de tangentiële component van de druk, waardoor we de oppervlaktespanning van het grensvlak kunnen berekenen, gelijk aan de mechanische arbeid die nodig is om het grensvlak te vergroten. Onze berekeningen resulteren in een positieve grensvlakspanning tussen de damp en vloeistof voor alle parameterruimtepunten die we overwegen, dat wil zeggen systemen met verschil-

lende zelfvoortstuwingssnelheden, rotatieverspreidingssnelheden en aantrekkingskrachten. Vervolgens bestuderen we de schaling van de oppervlaktespanning als functie van de aantrekkingskracht door deze te beschrijven met eenvoudige machtsfuncties, net als voor de coëxistentiedichtheden in Hoofdstuk 3 wordt voorgesteld. We laten zien dat de schaling van de grensvlakspanning kan worden beschreven door machtsfuncties die sterk lijken op die in evenwicht. Verrassend genoeg vinden we dat de gevonden waarden van de "kritische" temperatuur van het systeem, dat via de schaling van de spanning verkregen kan worden, in nauwe overeenkomst zijn met de waarden die in Hoofdstuk 3 worden verkregen, met behulp van de schaling van de onafhankelijk gemeten coëxistentie dichtheden. Ten slotte meten we, door systemen van verschillende afmetingen te simuleren, de schaling van de breedte en oppervlakte van het grensvlak. We passen de resultaten van capillaire golf theorie toe om deze schaling te relateren met de stijfheid van het grensvlak. We vinden dat de berekende stijfheid van het grensvlak direct evenredig is aan de grensvlakspanning, net als in het evenwichtssysteem, maar met een evenredigheidsconstante die wordt gegeven door een effectieve temperatuur van het systeem.

Vervolgens simuleren we in Hoofdstuk 5 twee verschillende *binaire mengsels* van actieve deeltjes en tonen aan dat coëxistente fasen van deze mengsels in *mechanisch* en *chemisch evenwicht* zijn. In de eerste plaats bestuderen we een driedimensionaal binair systeem van actieve en passieve aantrekkende deeltjes die door de attracties tussen deeltjes een damp-vloeistoffaseovergang ondergaan. Dit systeem is vergelijkbaar met het systeem dat in de Hoofdstukken 2-4 wordt bestudeerd, maar in dit mengsel zitten ook passieve (niet zelfvoortstuwende) deeltjes, die alleen zijn onderworpen aan Brownse beweging. Ten eerste tonen we mechanisch evenwicht van de coëxistente damp- en vloeibare fasen aan door de normaalcomponent van de druk direct te meten, zoals eerder in Hoofdstuk 4 is gedaan. Vervolgens brengen we elk van de twee naast elkaar aanwezige binaire fasen in chemisch evenwicht met een reservoir van deeltjes van een bepaalde soort, en laten we zien dat de aangesloten reservoirs van elke deeltjessoort identiek zijn voor de twee fasen. We meten dus de dichtheid van het reservoir als een hoeveelheid die analoog is aan de chemische potential van evenwichtssystemen en concluderen dat de numerieke methode waarin een binaire fase aan een deeltjesreservoir wordt bevestigd kan worden gebruikt om chemisch evenwicht aan te tonen tussen coëxistente fasen. Vervolgens gaan we verder met een tweedimensionaal binair mengsel van zelfvoortstuwende, zuiver afstotende schijven. De twee verschillende soorten in dit mengsel verschillen alleen in hun waarden van zelfvoortstuwingssnelheid, die zodanig gekozen worden dat het systeem bewegingsgeïnduceerde fasescheiding ondergaat voor alle samenstellingen. Vervolgens berekenen we de bulkeigenschappen van enkele binaire fasen door ze in chemisch evenwicht te brengen met deeltjesreservoirs en de bulkdruk van de binaire fase te meten, evenals de dichtheid van het aangesloten reservoir. Door te stellen dat coëxistente fasen gelijke druk en gelijke deeltjesreservoirdichtheden hebben voor elke soort kunnen we vervolgens het fasediagram van het systeem kwantitatief *voorspellen* zonder gebruik te maken van benaderingen.

In Hoofdstuk 6 laten we puur isotrope interacties tussen deeltjes achter ons en onderzoeken we het *staatsgedrag* en de *dynamiek* van een tweedimensionaal systeem van zelfvoortstuwende, zuiver afstotende, *vierkante* deeltjes. Door systemen met verschillende simulatieparameters te onderzoeken, bouwen wij het fasediagram; voor lage dichtheden en langzame snelheden van zelfvoortstuwing vormt het systeem een vloeibare fase, terwijl

we voor het regime van hoge dichtheden en hoge snelheden een coëxistentie vinden van een gasfase met een kristallijne cluster, geïnduceerd door de actieve beweging van de deeltjes. Interessant genoeg vinden we tussen deze twee regimes een gebied waar het systeem onophoudelijk oscilleert tussen een homogene vloeistof en een fasegescheiden staat. Wij tonen aan dat in het coëxistentieregime de hefboomregel en de law of rectilinear diameters worden gehandhaafd. Bovendien bekijken we de nucleatie, groei en uiteindelijke uiteenvalling van kristallijne clusters in het oscillatorische regime en presenteren we een mogelijk scenario dat de oscillaties van het systeem verklaart door een direct verband te leggen tussen de breuk van de clusters en de accumulatie van spanningen in de interne regio van de cluster. Ten slotte meten we de verandering van de gemiddelde clustergrootte als gevolg van samensmelting van individuele clusters en vinden dat deze veel sneller toeneemt dan in evenwichtssystemen, een toename die kan worden veroorzaakt door de eigenaardige dynamiek van individuele clusters.

Uiteindelijk beschouwen we in Hoofdstuk 7 een tweedimensionaal systeem van schijfachtige zelfvoortstuwende deeltjes die een *krachtsmoment* op elkaar uitoefenen en de assen van zelfbeweging van naburige deeltjes anti-parallel maken. Voor hoge snelheden van zelfvoortstuwing en hoge dichtheden ondergaat dit systeem bewegingsgeïnduceerde fasescheiding. We vinden dat het fasediagram van het systeem onderhevig is aan de hefboomregel en vervolgens passen we de in Hoofdstuk 5 beschreven methoden toe om het mechanische en chemisch evenwicht van coëxistente fasen te bestuderen. We schrijven de *krachtbalansvergelijking* op en onderzoeken of het mechanisch evenwicht van coëxistente fasen kan worden aangetoond door het bestuderen van de verschillende componenten van de vergelijking in fasegescheiden systemen. We vinden dat de grootheid geassocieerd met de lokale druk van isotrope deeltjes alleen een constant profiel over het grensvlak heeft in de afwezigheid van anisotrope interacties en dat er een drukverschil wordt gemeten wanneer deeltjes een moment op elkaar uitoefenen. Een mogelijke interpretatie van dit resultaat is dat de buiten-evenwichtige aard van het systeem zich manifesteert als een externe kracht die op het grensvlak werkt en het gemeten drukverschil tussen de twee coëxistente fasen veroorzaakt. Bovendien wordt het chemisch evenwicht tussen coëxistente fasen aangetoond door enkele fasen aan deeltjesreservoirs te verbinden, in een lichte wijziging van de in Hoofdstuk 5 geïntroduceerde methode.

In het kort, tonen we in dit proefschrift aan dat actieve materiesystemen fasediagrammen hebben met vergelijkbare eigenschappen als die van evenwichtssystemen en dat deze fasediagrammen zelfs voorspeld kunnen worden door die individuele fases te bestuderen en daarbij gebruik te maken van methoden die vergelijkbaar zijn met gevestigde technieken uit de statistische fysica van evenwichtssystemen. Ook kunnen veel eigenschappen die betrekking hebben op faseovergangen en grensvlakken tussen coëxisterende fasen, worden beschreven door wetten die generalisaties zijn van evenwichtswetten. Anderzijds vinden wij dat de zelfvoortstuwing van deeltjes tot onverwachte resultaten kan leiden zonder evenwichtstegenhanger, zoals de verschijning van de toestand van onderling verbonden motiele clusters van aantrekkende zelfvoortstuwende deeltjes en de oscillerende toestand van zelfvoortstuwende vierkanten. Hopelijk zullen deze resultaten zowel fungeren als een stap in de opbouw van een thermodynamica van actieve materie, als helpen bij het vastleggen van de grenzen van deze thermodynamische beschrijving.

List of peer-reviewed publications

This thesis is based on the following publications:

- V. Prymidis, H. Sielcken, and L. Filion, *Self-assembly of active attractive spheres*, Soft Matter **11**, 4158 (2015) (Chapter 2)
- V. Prymidis/S. Paliwal, M. Dijkstra, and L. Filion, *Vapour-liquid coexistence of an active Lennard-Jones fluid*, J. Chem. Phys. **145** (12), 124904 (2016) (Chapter 3)
- S. Paliwal/V. Prymidis, L. Filion, and M. Dijkstra, *Non-equilibrium surface tension of the vapour-liquid interface of acive Lennard-Jones particles*, manuscript submitted for publication (Chapter 4)
- B. van der Meer/V. Prymidis, M. Dijkstra, and L. Filion, *Mechanical and chemical equilibrium in mixtures of active spherical particles: Predicting phase behaviour from bulk properties alone*, manuscript submitted for publication (Chapter 5)
- V. Prymidis, S. Samin, and L. Filion, *State behaviour and dynamics of self-propelled Brownian squares: a simulation study*, Soft Matter **12**, 4309 (2016) (Chapter 6)
- V. Prymidis, and L. Filion, *Phase coexistence of spherical self-propelled particles with anisotropic interactions*, manuscript in preparation (Chapter 7)

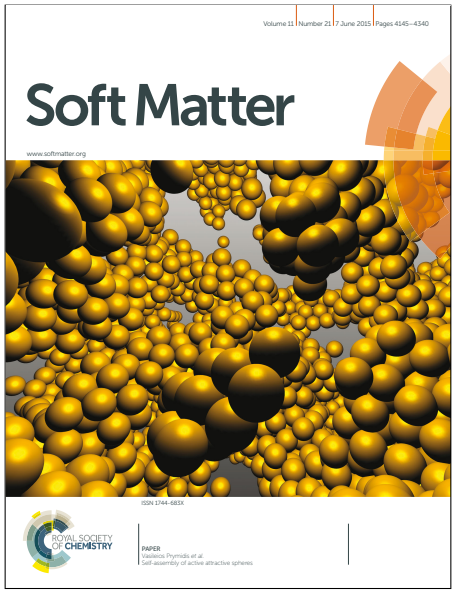

Figure: Cover featuring the research in Ref. [121]. Reprinted by permission from the Royal Society of Chemistry: Soft Matter Issue 21, copyright (2015).

Other publications by the author:

- D. Glavan, T. Prokopec, and V. Prymidis, *Backreaction of a massless minimally coupled scalar field from inflationary quantum fluctuations*, Phys. Rev. D **89**, 024024 (2014)

Oral and poster presentations

Parts of this thesis were presented at the following:

- 9th Liquid Matter Conference 2014, Lisbon (poster)
- Physics@FOM 2015, Veldhoven (poster)
- 5th International Colloids Conference 2015, Amsterdam (oral)
- Physics@FOM 2016, Veldhoven (oral)
- 4th International Soft Matter Conference 2016, Grenoble (poster)
- Physics@Veldhoven 2017, Veldhoven (poster)
- 10th Liquid Matter Conference 2017, Ljubljana (poster)